Freeze Dried Chitosan Scaffolds with Calcium Phosphate Minerals and Cerium Oxide Nanoparticles for Enhanced Osteoconductive and Antibacterial Properties

Neelam Iqbal

Submitted in Accordance with the Requirements for the Degree of Doctor of Philosophy

The University of Leeds

The School of Chemical and Process Engineering

Faculty of Engineering and Physical Sciences

October 2020

The candidate confirms that the work submitted is her own and that appropriate credit has been given where reference has been made to the work of others.

Acknowledgements

First and foremost, I am incredibly grateful to my supervisors Prof. Animesh Jha, Dr Antonios Anastasiou and Dr El Mostafa Raïf, for their guidance, invaluable advice and continuous support throughout the PhD research project. I express my gratitude to Mr Mohmamed Javed for crucial equipment training and laboratory support throughout the PhD. Special thanks to Dr Faith Bamiduro for invaluable XRD data analysis aid, Dr Simon Lloyd for microbiology training and Dr Chiranjeevi Maddi for Femtosecond laser assistance. Thank you to Dr Zaebeda Aslam and Mr Stuart Micklethwaite for their assistance with TEM and SEM respectively. I would also like to acknowledge the University of Leeds and the Engineering and Physical Sciences Research Council (EPSRC) for the opportunity and the funding for the PhD. A special thank you to Charles Chung, Sandeep Kumar, Emaan Hamad Alsubhe, Dina Abdulaziz, and Vasiliki Panagiotopoulou for their friendship and continuous support during my time at Leeds. Finally, to my parents and family for their love and encouragement throughout my academic career.

Abstract

Contemporary bone scaffolds lack the ability to address multiple requirements, i.e. osteogenic, mechanical, and antibacterial properties, for bone regeneration via a single construct. Thus, the novelty of this research project is to design and fabricate multilayered scaffolds embedded with osteoconductive minerals and antibacterial nanoparticles within a single scaffold design to address and meet the functional requirements for bone regeneration. Porous chitosan scaffolds embedded with different concentrations of Dicalcium Phosphate Dihydrate (DCPD) (0, 20, 30, 40 and 50 wt %) were fabricated using a freeze-drying approach. Cerium oxide nanoparticles (Ce^{4+} and $Ce^{3+)}$ have been selected due to their reported antibacterial potential and were synthesised via a hydroxide mediated approach. The nanoparticles were freeze-dried and furnace dried, and the calcination temperatures, e.g. 280 ˚C, 385 ˚C, and 815 ˚C, were identified using the Simultaneous Thermal Analysis technique. X-ray diffraction, Transmission Electron Microscopy, Fourier Transform Infrared, Ultraviolet-Visible, Raman and Electron Energy Loss Spectroscopy were utilised to characterise the synthesised materials.

Increasing the DCPD mineral content led to increased scaffold crystallinities and mechanical properties, while a reduction in the scaffold porosities was observed. The scaffolds' osteoconductive potential was investigated using osteoblasts from cell line G292 on days 1, 3 and 7, which was enhanced in the scaffolds containing up to 40 wt% DCPD minerals. The hydroxide mediated approach yielded spherical cerium oxide nanoparticles with particles sizes ranging from 4 nm to 53 nm. The antibacterial efficacy of nanoparticle concentrations of 50, 100 and 200 µg/ml were tested against *Escherichia coli, Staphylococcus epidermis* and *Pseudomonas aeruginosa* by

determining the half-maximal inhibitory concentration (IC_{50}). The synthesised cerium oxide nanoparticles containing a more significant amount of Ce^{3+} ions presented better antibacterial effectiveness than nanoparticles consisting solely of Ce^{4+} ions, i.e. nanoparticles calcined at 815 ˚C. Therefore, the drying method of the nanoparticles, i.e., freeze-drying or furnace drying, significantly affected the size distribution, agglomeration tendency, Ce^{3+} to Ce^{4+} ratio and the antibacterial efficacy of the synthesised nanoparticles.

Keywords: Dicalcium Phosphate Dihydrate, Freeze-Dried, Nanoparticles and Antibacterial.

TABLE OF CONTENTS

LIST OF FIGURES

LIST OF TABLES

Abbreviations

ATR	Attenuated Total Reflection
BET	Brunauer–Emmett–Teller
BHI	Brain Heart Infusion
BMPs	Bone Morphogenetic Proteins
β-TCP	β-tricalcium Phosphate
C280	Furnace dried Cerium Oxide nanoparticles calcined at 280 ˚C
C385	Furnace dried Cerium Oxide nanoparticles calcined at 385 ˚C
C815	Furnace dried Cerium Oxide nanoparticles calcined at 815 ˚C
CaP	Calcium Phosphate
Ca/P	Calcium/Phosphate Ratio
CFU	Colony Forming Unit
CH	Chitosan Freeze Dried Scaffold
CS	Chitosan
CT	Chitin
20-DCPD	Freeze dried chitosan scaffold containing 20 wt % DCPD
30-DCPD	Freeze dried chitosan scaffold containing 30 wt % DCPD
40-DCPD	Freeze dried chitosan scaffold containing 40 wt % DCPD
50-DCPD	Freeze dried chitosan scaffold containing 50 wt % DCPD
DD	Degree of Deacetylation

DNA	Deoxyribonucleic Acid
DCPD	Dicalcium Phosphate Dihydrate (Brushite Mineral)
DPBS	Dulbecco's Phosphate-Buffered Saline
DSC	Differential Scanning Calorimetry
ECM	Extracellular Matrix
EDX	Energy Dispersive X-ray
EELS	Electron Energy Loss Spectroscopy
EPS	Extracellular Polymeric Substances
FCC	Face Centre Cubic
FRNP	Freeze Dried Cerium Oxide Nanoparticles
FTIR	Fourier Transform Infrared Spectroscopy
FUNP	Furnace Dried Cerium Oxide Nanoparticles
FWHM	Full-Width Half Maximum
HA	Hydroxyapatite
HRTEM	High-Resolution Transmission Electron Microscopy
JCPDS	Joint Committee of Powder and Standards
KBR	Potassium Bromide
LOM	Lipopolysaccharide Membrane
LTA	Lipoteichoic Acids
M_W	Molecular Weight

NaOH	Sodium Hydroxide
NIR	Near-Infrared Light
OCP	Octacalcium Phosphate
OD	Optical Density
PBS	Phosphate Buffer Saline
RNP3	Commercial Cerium Oxide (CeO_4P)
RNP4	Commercial Cerium Oxide (CeO_2)
ROS	Reactive Oxygen Species
SAED	Selected Area Electron Diffraction
SEM	Scanning Electron Microscopy
STA	Simultaneous Thermal Analysis
TCP	Tricalcium Phosphate
TEM	Transmission Electron Microscopy
TGA	Thermogravimetric Analysis
TWA	Teichoic Wall Acids
UV-VIS	Ultraviolet-Visible Spectroscopy
XPS	X-ray Photoelectron Spectroscopy
XRD	X-ray Diffraction
ZS	Zeta Potential

Definitions

Adjuvant	A pharmacological or immunological agent that improves the immune response of a vaccine.
Antioxidant	A substance that protects cells from damage caused by free radicals.
Apatite	Naturally occurring minerals containing calcium and phosphorous.
Bravais Lattice	Fourteen possible three-dimensional configurations of points used to describe the orderly arrangement of atoms in a crystal.
Chelating	The chemical compound where a substance is joined to a metal atom by two or more bonds.
Electrolytes	Substances which dissociate into ions in solution and acquires the capacity to conduct electricity.
Endo Thermal	Characterized by or causing the absorption of heat.
Exo Thermal	Characterized by or causing the release of heat.
Gram-Negative	Bacteria with the relatively thin cell wall and does not retain the crystal violet dye.

Gram-Positive	Bacteria containing thick cell wall comprising of peptidoglycan which retains the crystal violet dye thus dying the cell wall purple.
Hydrolysis	Process of decomposition involving the splitting of a covalent bond.
IC_{50}	A quantitative measure which indicates the amount of inhibitory substance required to inhibit a biological response by 50 %.
Isochronal	Characterized by or occurring at equal time intervals.
In vitro	Cell studies performed outside normal biological context, i.e. in a laboratory vessel.
In vivo	Cell studies performed within living organisms.
Mesenchymal Stem Cells	Mesenchymal stem cells are multipotent stromal cells that have the capability of differentiating into a variety of lineages, including osteoblast cells, adipocytes and chondrocytes.
Monoclinic	Crystal system with three unequal axes and with one oblique intersection.
Nanoceria	Cerium oxide nanoparticles.

Necrosis	The death of living cells or tissues due to lack of blood flow.
Oligosaccharides	Carbohydrate containing three to six units of simple sugars, i.e., monosaccharides.
Osteonectin	A protein found in bone and nonmineralized tissues and is believed to play a role in mineralization.
Osteoconductive	Scaffold or matrix which stimulates bone cells to grow on its surface.
Osteoproductive	Stimulate the growth of new bone on the material away from the bone/implant interface.
Osteoinductive	Nutrients that stimulate mesenchymal stem cells to differentiate into preosteoblasts.
Osteogenesis	Formation of bone.
Phagocytosis	The process by which a cell uses its plasma membrane to engulf a large particle.
Peyer's Patches	Groups of lymphoid follicles in the mucus membrane which line the small intestine.

Peptidoglycans	Also known as murein, is a polymer consisting of sugars and amino acids which form the plasma membrane of most bacteria.
Progenitor	Cells that descend from stem cells which can differentiate into cells belonging to the same issue/organ.
Polysaccharide	A carbohydrate which contains more than three monosaccharide units per molecule.
Rietveld Analysis	XRD analysis with whole pattern fitting refinement and is a valuable method for structural analysis of nearly all classes of crystalline materials.
Solubilisation	Formation of a thermodynamically stable isotropic solution containing an insoluble/slightly soluble substance in water with the addition of a surfactant.
Tetracycline	Broad-spectrum antibiotics which are effective against a wide variety of bacteria including Haemophilus influenza, Strep and Chlamydia.
Vancomycin	An antibiotic used against resistant bacterial strains of Streptococcus and Staphylococcus.

List of Publications

Published Conference Papers Include:

- **N. Iqbal**, A. Anastasiou, M. El-Raif, and A. Jha, "CLEO®/Europe-EQEC 2017 Chitosan Membranes for Biodegradable Microfluidics," in *2017 European Conference on Lasers and Electro-Optics and European Quantum Electronics Conference*, (Optical Society of America, 2017), paper CM_P_23.

- **N. Iqbal**, A. Anastasiou, M. El-Raif, and A. Jha, "Bioglass-Brushite Membranes for Biodegradable Microfluidics", in *2017 Society of Glass Technology Annual Conference*, (Aspects of Glass, 2017).

- **N. Iqbal**, A. Anastasiou, M. El-Raif, and A. Jha, "Physicochemical and Antibacterial Properties of Freeze and Furnace Dried Cerium Oxide Nanoparticles", in *2019 The European Society of Biomaterials,* (ESB 2019).

- **N. Iqbal**, A. Anastasiou, C. Maddi, M. El-Raif, P. Giannoudis, and A. Jha, "Fabrication of Multilayered Bone Scaffolds using Femtosecond Pulsed Lasers," in *Biophotonics Congress: Optics in the Life Sciences Congress 2019*, The Optical Society (Optical Society of America, 2019), paper JT4A.45. https://doi.org/10.1364/BODA.2019.JT4A.45.

- D. Abdulaziz, **N. Iqbal**, A. Anastasiou, V. Panagiotopoulou, E.M. Raif, P. Giannoudis and A. Jha, "Novel Multilayered Scaffolds for The Treatment of Long Bone Fractures, " in *2020 European Federation of National Associations of Orthopaedics and Traumatology* (EFORT 2020), abstract number #1299.

- **N. Iqbal**, A. Anastasiou, M. El-Raif and A. Jha, "Comparative Study of Freeze and Furnace Dried Cerium Oxide Nanoparticles", in *2020 World Biomaterials Congress 2020* (WBC 2020).

Journal Papers in Preparation Include:

- **N. Iqbal**, A. Anastasiou, M. El-Raif, Z. Aslam and A. Jha, "Physicochemical and Antibacterial Properties of Freeze and Furnace Dried Cerium Oxide Nanoparticles".

- **N. Iqbal**, A. Anastasiou, M. El-Raif and A. Jha, "Freeze-Dried Synthetic Chitosan Scaffolds Embedded with Brushite For Enhanced Osteoconductive Properties".

- **N. Iqbal**, A. Anastasiou, M. El-Raif and A. Jha, "Micropatterning of Calcium Phosphate – Chitosan films using a Femtosecond pulsed laser".

Chapter 1
INTRODUCTION

1.0 Background

The metabolic and regenerative properties of bone are disrupted when the tissue is damaged from trauma and or disease. Bone grafting is the standard practice for the treatment of bone defects in orthopaedic surgeries [1], where over 2 million procedures have been performed worldwide [2]. Autologous bone grafts, such as bone marrow, cancellous and cortical bone [3, 4] are harvested from patients from anatomical sites and implanted into another, thus enabling successful integration. Although autologous grafts exhibit favourable properties, i.e., osteoconduction, osteoinduction and osteogenesis [5], concerns are raised with regards to limited viable graft quantity especially in older patients, extended surgical times [2, 6] and possible site complications [2, 7]. Bone allografts obtained from donor patients and cadavers are in limited supply due to the increasing clinical demand relating to obesity and the ageing population [8]. Allografts also carry a significant potential risk of disease in addition to eliciting an immune response [9]. Thus, there is a shift from natural grafts to synthetic bone substitutes such as bioactive ceramics, biological and synthetic polymers, and composite scaffolds [2, 6].

The dynamic and highly vascularised bone tissue has a natural regenerative ability to self-repair small defects and cracks; however, when defects are critical-sized, i.e., > 2.5 cm, the intervention of scaffolds is required. Bone is a highly specialised and complex living entity; therefore, potential bone substitutes must express multiple properties collectively. An ideal bone scaffold should exhibit: i) osteoconductive potential to aid the formation of new bone, ii) load-bearing properties, iii) appropriate microstructure to promote angiogenesis for nutrients circulation and iv) antibacterial efficacy to reduce or prevent infections which lead to failure of the surgery. In the last decade,

extensive research has been conducted to optimise biomaterials for the fabrication of suitable bone scaffolds. However, research efforts have been focused on the development of the "perfect" biomaterial, targeting to achieve all the aforementioned properties with a single component, e.g. blocks of calcium phosphates, coated titanium (Ti) implants [10], polymers [11] etc.

The osteoconductive and antibacterial properties are of particular importance to ensure successful integration and to reduce the probability of infection. Antibiotics are widely used during the implantation procedure and to treat pre-existing infections, thus have led to the manifestation of resistant bacteria and are currently a significant concern [12, 13]. Infections cause inflammation, which hinders the bone regeneration process, and if not treated, can often lead to the necrosis of tissue. Nanoparticles have emerged as novel antibacterial agents and have proven their effectiveness for treating infectious diseases [14]. The large surface area to volume ratio of nanoparticles exhibits unique properties which their bulk counterparts do not. It has been reported that factors such as size, shape, surface charge, and surface area to volume ratio affect the antibacterial potential [2].

1.1 Market Gap

Commercially available bone scaffolds lack the ability to address multiple requirements essential for the regeneration of bone tissue via a single construct. Additionally, research efforts have been focused on inducing osteogenesis or increasing the mechanical stability of synthesised scaffolds, where the antibacterial potential is often overlooked. By designing and synthesising multilayered scaffolds

embedded with osteoconductive minerals, and antibacterial nanoparticles, the scaffold has the potential to address and meet the functional requirements for bone regeneration. The antibacterial nanoparticles are likely to reduce or prevent implant-related infections. The concept relies on the fundamentals of degradation where minerals/nanoparticles are released as the scaffold degrades over time to encourage an osteoconductive and antibacterial response. The degradation rate of the scaffold should match the regeneration rate of bone, and the scaffold must remain mechanically stable during bone cell proliferation.

1.1.1 Research Focus

The focus of this research project was to develop, fabricate, characterise and test bone scaffolds inspired by the structure of natural bone. In general, the design considerations of potential bone scaffolds must include;

(i) *Biocompatibility* — Scaffolds material must not be harmful or toxic to living tissue.

(ii) Osteoconductivity — The biomaterial of the scaffold must allow bone cells to grow on its surface.

(iii) Mechanical Stability: — Synthesised scaffolds should exhibit adequate mechanical strength to enable the scaffold to retain its structure, especially handling during the implantation process and during cell growth and proliferation.

(i)	*Resorbability*	The scaffold must have the ability to degrade enhancing the void space to sure adequate space for bone cells to proliferate and differentiate.
(ii)	*Pore Size & Porosity*	Scaffold porosity provides an appropriate environment to facilitate the migration and proliferation of bone cells. Furthermore, interconnected pores are likely to encourage the transport of nutrients and removal of waste products.
(i)	*Antibacterial*	Bacterial colonisation is common for implant-related regions; thus, the presence of antibacterial components will reduce/prevent further complications such as a second surgery due to infection.

[15]

1.2 Thesis Structure

CHAPTER 1 - Introduction: This chapter outlines the significance of the investigation and includes the background information relating to bone scaffolds, an overview of the research topic and a brief explanation of the current market gap.

CHAPTER 2 - Literature Review: Critical scientific literature review which includes, (i) the composition of bone, (ii) classification of current biomaterials, (iii) bone scaffold requirements, (iv) scaffold fabrication methods, (v) the structure and properties of chitosan, calcium phosphates, and nanoparticles and (vi) the antibacterial mechanism of cerium oxide nanoparticles. Following the literature review are the aims and objectives of the research project.

CHAPTER 3 - Materials & Methods: In this chapter, detailed methods for materials synthesis, characterisation and testing are provided. The methods for materials synthesis include fabrication of freeze-dried chitosan (CS) scaffolds embedded with varying concentrations of Dicalcium Phosphate Dihydrate (DCPD) minerals (0, 20, 30, 40 and 50 wt %) and the synthesis of freeze and furnace-dried cerium oxide nanoparticles. The material characterisation techniques include X-ray Diffraction (XRD), Fourier Transform Infrared Spectroscopy (FTIR), Ultraviolet-Visible Spectroscopy (UV-Vis), Scanning Electron Microscopy (SEM), Transmission Electron Microscopy (TEM), Electron Energy Loss (EELs) and Raman Spectroscopy. The testing methods include Water Uptake (Swelling), Degradation Testing, Zeta Potential, Porosimetry, Tensile Testing, X-ray Photon Spectroscopy (XPS), Cytotoxicity Testing, Osteoblast Proliferation and Antibacterial Testing.

CHAPTER 4 and 5 - Results: The two results chapters are comprised of the synthesis, characterisation and testing results for freeze-dried scaffolds embedded with varying concentrations of DCPD minerals and cerium oxide nanoparticles. Chapter 4 includes osteoblast cellular results tested with the synthesised freeze-dried scaffolds. Chapter 5 includes the antibacterial results associated with the cerium oxide nanoparticles against Gram-positive and Gram-negative bacteria.

CHAPTER 6 - Discussion: This chapter provides an in-depth discussion and summary of the results with comparisons to current literature and includes implications and conclusions of all findings in terms of the thesis research aims and objectives as detailed in Chapter 1.

CHAPTER 7 - Conclusion & Future Work: The final chapter consists of the thesis conclusions based on the research conducted, answers to the initial research questions and possible future work.

Chapter 2
LITERATURE REVIEW

2.0 Physiology and Function of Bone

Bone is a natural composite material with a sophisticated dynamic anisotropic structure which can regenerate and self-heal when subjected to external stresses and metabolic changes. Dynamic modelling and remodelling of bone continually occur to maintain mechanical integrity. The inorganic phase of bone is composed of mainly calcium phosphate mineral, i.e., hydroxyapatite, while collagen forms the organic phase. When fractures and defects are critical-sized, the regeneration process is halted, and the intervention of bone/tissue grafts and scaffolds are required [16]. Therefore, the design and fabrication of synthetic bone scaffolds require knowledge of physical, chemical, mechanical, and biochemical properties to mimic natural bone successfully.

The structure of bone is highly specialised and dense; approximately two-thirds of bone weight is accounted for by calcium phosphate mineral ($Ca_3(PO_4)_2$). The interaction of $Ca_3(PO_4)_2$ with calcium hydroxide ($Ca(OH)_2$) leads to the formation of hydroxyapatite crystals ($Ca_{10}(PO_4)_6(OH)_2$). As the crystals form, other calcium salts and ions, i.e. calcium carbonate ($CaCO_3$), sodium (Na^+), magnesium (Mg^{2+}) and fluoride (F^-) are incorporated into the hydroxyapatite crystals. $Ca_3(PO_4)_2$ is relatively hard, inflexible and brittle; however, it is prone to fracture, especially when exposed to any bending or twisting forces. The remaining one-third of the bone weight consists of collagen fibres, where cells, proteins, lipids only account for approximately 2 % of the typical bone mass.

Collagen fibres exhibit high tensile strengths; thus, they express the ability to be robust yet flexible. However, these fibres do not have comparable strength when subjected to compressive forces. The collagen fibres provide organic structural support on which hydroxyapatite crystals form; as the crystals grow, they interlock with the collagen fibres. Therefore, a protein-crystal combination is formed which possesses the compressive strength of the hydroxyapatite crystals with the flexibility and tensile strength of the collagen fibres. This combination of materials allows the bone to exhibit outstanding properties [16, 17].

2.1 Bone Cells

2.1.1 Osteocytes

Bone contains four types of cells, i.e. osteocytes, osteoblasts, osteoclasts and osteoprogenitor cells (Figure 2.1). The osteocytes are commonly known as mature bone cells and are the most abundant cells within the bone. Osteocyte cells differentiate from osteoblast cells which are derived from Mesenchymal stem cells (MSCs). Osteocyte cells are located in lacuna pockets, sandwiched between matrix layers. The mineral and protein content of the surrounding bone matrix is maintained by these osteocyte cells. The layers within the matrix are called lamellae; the lamellae are connected via narrow passageways called canaliculi. The canaliculi spread through the matrix and thus connects all the lacunae to nutrients source, e.g. blood vessels in the central canal. Osteocytes are responsible for maintaining the protein and mineral content of the surrounding matrix, as depicted in Figure 2.1(a). There is continuous matrix components turnover as osteocytes secrete specific chemicals which dissolve the adjacent matrix, and the mineral released from the matrix enters the blood

circulation. The osteocytes then rebuild the matrix as well as stimulating new hydroxyapatite crystal depositions. Osteocytes also participate in the repair of damaged bone, and the turnover of bone depends upon the bone type and location [17]. Furthermore, if osteocytes are released from their lacuna, they can also convert into other less specialised cells such as osteoblasts or osteoprogenitor cells.

2.1.2 Osteoblasts

Osteoblasts derived from Mesenchymal stem cells are known to form new bone matrix in a process called ossification/osteogenesis. Osteoblast cells produce and release proteins and organic components to aid in the creation of new bone matrix. The organic matrix is called osteoid before the deposition of calcium salts. Osteoblast cells elevate the local $Ca_3(PO_4)_2$ levels above its solubility, thus triggering the deposition of the salts into the organic matrix. At this stage, the osteoid is converted to the bone; Figure 2.1(b) depicts the osteoblasts location. Mature osteoblast cells stop releasing proteins and organic components when surrounded by osteoids; thus, the cells become either become osteocytes or die.

2.1.3 Osteoprogenitor cells

There are also a small number of stem cells called osteoprogenitor cells, which originate from Mesenchymal stem cells. These stem cells are located in the inner periosteum layer/endosteum, which lines the medullary cavities and in the lining of passageways containing blood vessels located in the matrix of compact bone (Figure 2.1(c)). The osteoprogenitor cells can divide forming daughter cells which differentiate

into osteoblasts cells; therefore, during a fracture, the osteoprogenitor cells uphold osteoblast populations [17].

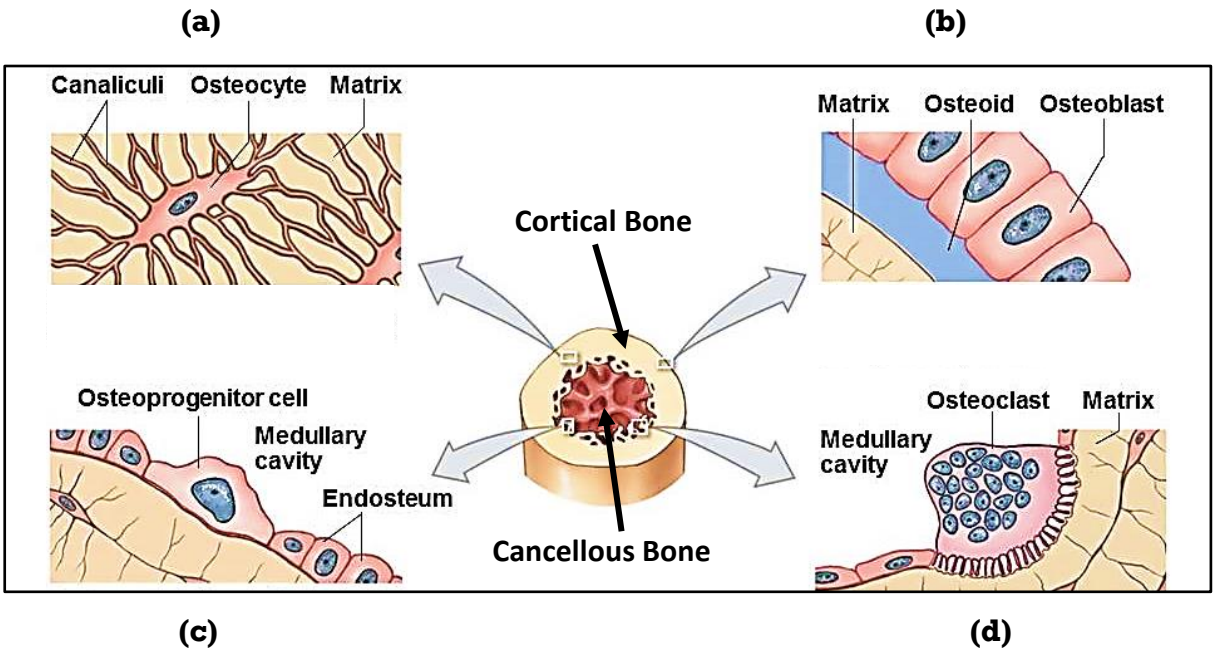

FIGURE 2.1 - Types and location of bone cells, (a) osteocyte cells, (b) osteoblast cells, (c) osteoprogenitor cells and (d) osteoclast cells. Image adapted from [17].

2.1.4 Osteoclasts

Osteoclasts cells displayed in Figure 2.1(d) are derived from Hematopoietic stem cells, and their primary purpose is to remove and recycle the bone matrix. Osteolysis is a process where the osteoclast cells excrete hydrochloric acid and digestive protein enzymes known as proteolytic enzymes which dissolve the bone matrix, thus, releasing the stored minerals. For correct bone density maintenance, there has to be a balance between removal of bone matrix and the creation of new bone matrix. If the osteoclasts remove calcium salts faster than the osteoblasts can deposit the salts, then the overall bone will weaken. With continuous exercise where bones are subjected to muscular

stress, i.e. weight training, the osteoblast activity predominates the osteoclast activity; as a result, bone and muscle strengthen [17].

2.2 Bone Structure

2.2.1 Compact Bone Structure

Compact bone is also known as cortical bone and is located on the outer surface where the lamellae are arranged in osteons. Osteons are the basic functional units which form compact bone; they are arranged around a central canal in concentric layers (Figure 2.2). Blood is carried to and from the osteons through blood vessels that lie parallel to the bone surface located in each of the central canals. Other vessels, which are known as perforating canals, supply blood to osteons located much deeper into the bone, as well as supplying blood to tissues located in the medullary cavity.

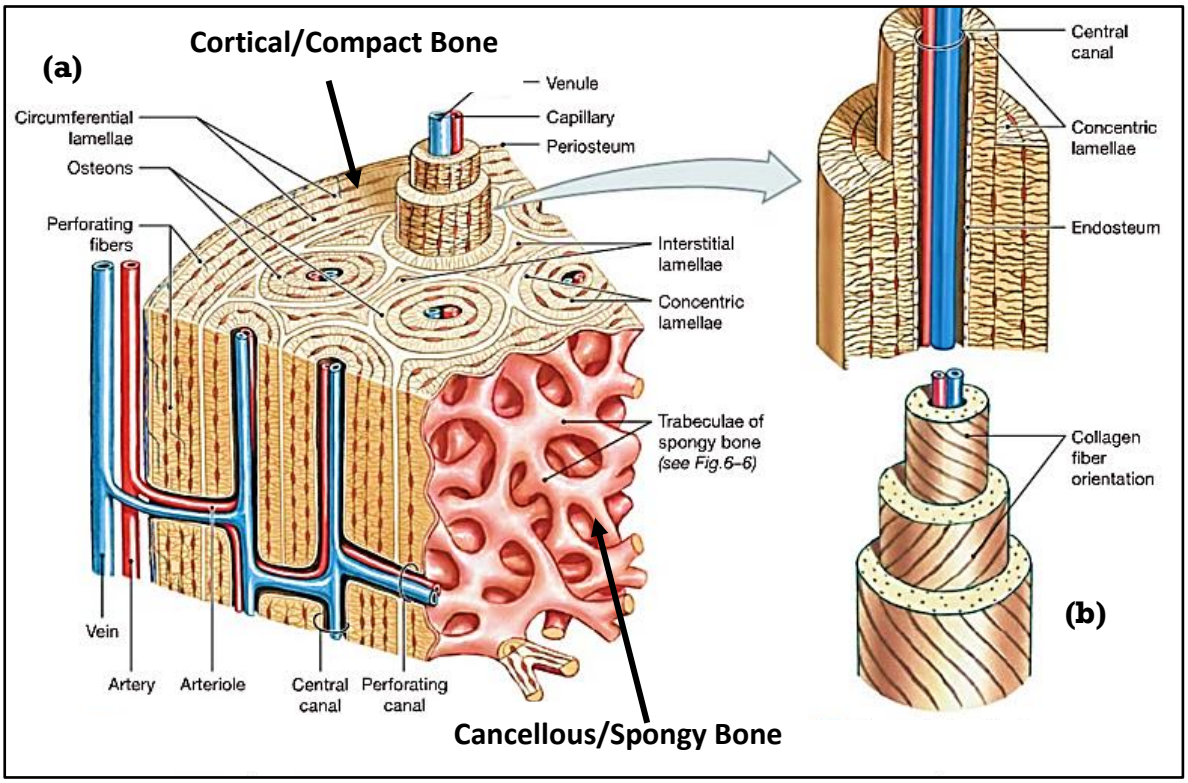

FIGURE 2.2 - The structure of compact bone, (a) osteons and lamellae organisation and (b) collagen fibres orientation. Image adapted from [17].

Compact bone is the thickest at locations where stresses are confined to a limited area. The strength of bone arises from the arrangement of osteons; thus, bone has the greatest strength when stressed along the collective osteon's alignment. However, any sideways force applied to the bone will cause fractures and breakages to occur [17].

2.2.2 Trabecular Bone Structure

Trabecular bone is also known as cancellous bone and is located internally; therefore, the structure differs significantly compared to compact bone. The internal structure of bone is porous with a structure similar to a mesh network formed from bundles of fibres known as trabeculae. The network structure does not contain any capillaries within the matrix; hence nutrients are transported via diffusion along canaliculi to reach the osteocytes (Figure 2.3). The surfaces of the trabeculae contain openings from the canaliculi, thus allowing successful diffusion to occur through the internal structure of bone. Redbone marrow is located between the bundles of fibres (trabeculae) and cancellous bone. Blood vessels are present in the redbone marrow, which transports nutrients to the trabeculae in addition to removing any waste products created from the osteocytes [17].

Unlike compact bone, cancellous bone can address stresses arising from multiple directions; however, the amount of stress that the internal structure can withstand is less compared to the outer structure of bone. The ability to withstand stresses from

multiple directions has been linked to the overall network structure of the trabeculae. The orientation of the structure is along the stress lines furthermore; the trabeculae are extensively cross-braced throughout, and this network structure also aids in the protection and growth of cells in the bone marrow [17]. Table 2.1 displays the variation of mechanical properties concerning cortical and cancellous bone.

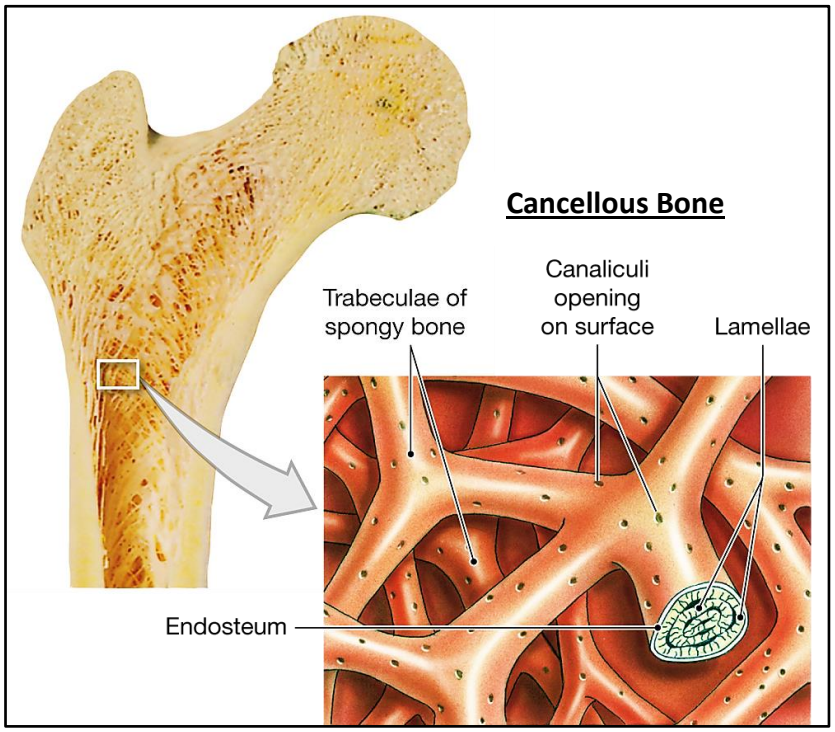

FIGURE 2.3 - The structure of spongy bone with close up of the trabeculae and canaliculi openings. Image adapted from [17].

TABLE 2.1 - An overview of the mechanical features of cortical and cancellous bone.

Bone Loading Type	Youngs Modulus	Tensile Strength	Compressive Strength

		(GPa)	(MPa)	(MPa)
Cortical	Longitudinal	17-20	79-151	131-224
	Transverse	6-13	51-56	106-133
Cancellous	Longitudinal	20	-	2-5
	Transverse	14	-	-

2.3 Biomaterials Classifications

Materials used to stimulate bone tissue can be classed as either bioactive and bioinert [18-20]. Osteoconductive and osteoproductive are the two main classes of bioactive materials [21]. Bioactive materials can stimulate the development of bone tissue by forming direct chemical bonds between the tissue and the implant material [21]. Osteoconductive materials, i.e., calcium phosphates, encourage stimulation of bone growth along the surface of the biomaterial, which consequently bonds to the bone [21]. Osteoproductive materials, i.e., bioactive glasses, stimulate new bone growth on the surface of the biomaterial away from the bone-material interface [18-22]. Most metals, including stainless steel and cobalt chrome, are classed as bioinert due to their ability only to stimulate the formation of fibrous tissue thus cannot stimulate cells for bone development. Bioinert materials do not bond to bone directly but instead form weaker interfaces between the biomaterial and bone [18, 20, 23].

2.4 Scaffold Requirements

Bone is a complex living tissue with significant metabolic and regenerative activities which are disrupted when the tissue is damaged. The biological surroundings of synthetic scaffolds evolve over time; initially implanted materials up to three days are

invaded with blood. After seven days of implantation, the blood is replaced by callus and mesenchymal tissue leading to bone resorption. Between the second and fourth week, the newly formed bone will replace the callus and mesenchymal tissue; thus, bone remodelling begins [24, 25]. Biological fluids and cells interact with the biomaterial surface; therefore; molecular and cellular surface interactions are essential to progress new bone formation [24]. Healing of fractured bone is a complicated process, where the ideal bone scaffold should have: i) exceptional osteoconductive potential to promote new bone formation; ii) load-bearing properties; iii) appropriate microstructure for promoting angiogenesis for circulation of nutrients and iv) antibacterial resistance to avoid infections which can lead to failure of the surgery. Research efforts have been focused on the development of the "perfect" biomaterial, targeting to achieve all the aforementioned properties with a single material system which has been challenging to achieve.

The porosity of potential bone scaffolds is an essential requirement to support adequate cell adhesion, proliferation, growth of blood supply, i.e., vascularisation, nutrients and oxygen supply. Smaller pore sizes increase the surface area of scaffolds allowing improved sites for cellular attachment [26]. Conversely, cell migration is restricted in scaffolds containing smaller pores < 50 μm, which have led to cellular capsules forming especially near the edge of the scaffolds [27]. In addition, necrotic regions can form in the scaffold areas where the diffusion of nutrients and waste removal is restricted. Contrary, for larger pore sizes, the surface area for cells to attach is reduced, which is found to limit the adhesion of cells [27, 28]. Additionally, the mechanical properties of scaffolds containing large pore sizes are negatively affected due to an increase in the void volume [29].

2.5 Fabrication Methods of Porous Scaffolds

Bone scaffolds vary depending upon the process and the material used to manufacture the constructs. The processing techniques used to fabricate 3D scaffolds include but are not limited to (i) solvent casting and particulate leaching, (ii) gas-foaming and (iii) freeze-drying. The solvent casting and particulate leaching procedure are the most straightforward manufacturing techniques as no special equipment such as flat sheets or tubes are required.

2.5.1 Solvent Casting and Particulate Leaching

The pore size and porosity of scaffolds fabricated using the solvent casting, and particulate leaching procedure can be easily controlled. The manufacturing process involves dissolving the polymeric material in an organic solvent mixed with a water-soluble porogen, i.e. salt, after which the mixture is cast into moulds [6, 30]. The solvent evaporates, leaving behind the scaffold matrix containing the porogen. The water-soluble porogen is leached out by submerging the scaffold in water; thus, the resulting material has porosity. The amount of porosity present in the scaffold depends on the quantity of porogen used during production [6, 30]. Usually, the scaffold formed contains between 50 % and 90 % porosity [31, 32]. In contrast, the pores' size depends on the crystal size of the porogen; thus, pore size capability is tuneable. Relatively high pore interconnectivity is achieved when 70 wt% of porogen is utilised [6, 30].

2.5.2 Gas Foaming

The gas-foaming technique involves the formation of scaffold porosity via gas expansion [33]. Carbon dioxide is the conventional gas used due to its low toxicity and non-flammable nature [30]. Pore sizes of 100 μm are created; however, the pore interconnectivity is generally low (10% to 30 %), especially on the surface of the material. Interconnected macroporous structures (100 μm to 500 μm) required for cell proliferation can be fabricated using the gas-foaming procedure [34]. Hydrophilic and glassy polymers such as chitosan (CS) are generally not processed using this procedure owing to their low solubility in carbon dioxide; perhaps a co-solvent such as a diluted acid could solve the issue [33].

2.5.3 Freeze-Drying

The freeze-drying procedure, also known as lyophilisation [31], is where ice or frozen solvents are removed through sublimation. Sublimation is a phase transition from a solid phase to a gas phase without passing through the liquid phase [35]. Polymers or ceramics are dissolved in either water or organic solvents [30], where the mixture is poured into moulds and subsequently frozen. The freeze-drying step involves placing the frozen samples under vacuum below the triple point of water, and then heat is applied to cause the frozen scaffold material to sublime from a solid phase to the gas phase [36]. The macroporosity corresponds to space which was initially occupied by ice crystals [31]. The resulting scaffolds generally contain pores located close together, ranging from 20 μm to 200 μm; a porosity of up to ~ 90 % is achieved using the freeze-drying procedure [37].

The particulate leaching method combined with the freeze-drying process consists of the addition of the porogen such as sucrose, or sodium chloride to the mixture prior to freezing. Thus, after the freeze-drying process, the porogen is removed by thoroughly rinsing with water [38]. High-temperature processing conditions associated with porous scaffold fabrication, are linked to the reduction of integrated biological factors. However, the freeze-drying procedure does not require high temperatures; thus, the created porous scaffolds retain integrated biological factors [31]. The fabrication of BG-collagen-phosphatidylserine scaffolds via freeze-drying exhibited interrelated pores in the range of 300 μm [31]. A wide variety of porous scaffolds have been fabricated using the freeze-drying processing approach, including CS nanoparticles [27], CS-alginate biocomposites [20] and formation of calcium, phosphate and hydroxyapatite (HA) complexes [9].

2.6 Bone Scaffold Biomaterials

2.6.1 First Generation

The focus of the first generation biomaterials, i.e., stainless steel, alumina and zirconia was related to physical properties and the biocompatibility [6, 39]. At the biomaterial-tissue interface, the formation of fibrous tissue which is linked to the body's non-specific immune response attacks material it has classed as foreign, inevitably encapsulating the implant [39, 40]. The encapsulation process is a result of the immune systems inability to remove the 'foreign' material via phagocytosis, leading to fibrotic tissue encapsulation to isolate the material from the surrounding tissues. Aseptic loosening of the implant is a common trait for first-generation biomaterials which has led to implant failures [39].

2.6.2 Second Generation

The second generation of biomaterials incorporated bioactive interfaces, i.e., HA coating, which promoted osteoconduction to avoid a non-specific immune response. The bioactive interfaces functionalised the implant surfaces by stimulating mineralisation via heterogeneous nucleation and crystallization of HA. Additionally; implant surfaces have been covered with bioactive ceramics, i.e. bioactive glass and β-tricalcium phosphate (β-TCP) to improve the surface chemistry of implants [39]. Natural materials, i.e., CS, hyaluronic acid and synthetic polymers, i.e. poly(ε-caprolactone and polyglycolide, are also classed as second-generation biomaterials [39, 41].

Biopolymers have the potential and the advantageous properties to be utilised for three-dimensional scaffold structures. Biodegradable polymeric materials such as poly(lactic acid), poly(glycolic acid), poly(glycerol sebacate) [42-44] and also poly(lactic-co-glycolic acid) [45, 46] have been processed to form scaffold structures. However, owing to the limited half-lives, they do not exhibit adequate mechanical strength to support bone or tissue regeneration. The properties of polymeric materials are improved by forming composites with bioactive ceramic or via chemical modification, i.e. conjugation of osteoconductive materials. Therefore, biomaterials synthesised for bone restoration must exhibit tuneable properties allowing suitable enhancements to be made to meet the biological and structural demands [47].

2.6.3 Third Generation

Third generation biomaterials integrate bioactivity and biodegradability hence are capable of inducing cellular responses [39, 48]. Modifications are being made to resorbable polymer systems at the molecular level to direct cell proliferation, differentiation and extracellular matrix (ECM) formation [6, 48-50]. The third-generation biomaterials for bone repairs are distinguished by following two routes (i) tissue engineering and (ii) *in situ* tissue engineering. Tissue engineering allows modified resorbable scaffolds seeded with progenitor cells to grow and differentiate to mimic naturally occurring tissue [48]. The engineered constructs are then subsequently implanted to replace the patient's diseased or damaged bone. Ideally, the synthetic bone constructs should resorb as bone regenerates, and a viable blood supply. The goal of tissue engineering is to design adaptable physiological 'living' scaffolds which will provide the building blocks required for bone regeneration [48, 51]. *In situ*, tissue engineering refers to an approach whereby the body's natural regeneration process is harnessed by transplanting tissue-specific biomaterials at the site of the defect [52, 53].

2.7 Biopolymers

2.7.1 Chitin

Chitin (CT) is the second most abundant renewable polysaccharide [54] found in the exoskeletal of invertebrates, cell walls and fungi [55]. The structure of CT consists of 2-acetamido-2-deoxy-D-glucose (N-acetylglucosamine) units linked via ß-(1-4) glycosidic bonds. Despite its abundance, chitin remains mainly un-utilised due to insolubility in water and common organic solvents [56]. The insolubility arises from

the CT crystalline structure, the abundance of acetylated amine groups and inter and intramolecular hydrogen bonding [57-59]. Also, the available unhydrolysed acetyl groups are likely to form hydrophobic bonds in solution, thus, causing CT to become aggregated [57, 59].

2.7.1.1 Polymorphic Forms of Chitin

There are three distinct polymorphic forms of CT expressed as α, ß and *ý* and are dependent on the origin of extraction [60, 61]. The α-CT is obtained from shells of crustaceans, i.e. crabs and lobsters, where the polysaccharide chains are aligned antiparallel as depicted in Figure 2.4(a). The antiparallel arrangement enables strong intermolecular hydrogen bonding between the chains, and this leads to the formation of organised sheets with intra-sheet hydrogen bonding. Therefore, α-CT is considered to be the most stable polymorph of CT. ß-CT is extracted from squid pens, where the polysaccharide chains have been found to align parallel (Figure 2.4(b)) leading to weaker intermolecular forces. The parallel arrangement prevents inter-sheet hydrogen bonding; hence the structure is not as compact and crystalline in comparison to α-CT. The open structure of ß-CT allows for the diffusion of smaller molecules, i.e. polar molecules, which is consistent with the increased swelling capacity as confirmed in the literature [62]. The *γ*-CT is obtained from fungi and yeast, where the structure consists of two parallel polysaccharide chains which alternate with one antiparallel aligned chain, as displayed in Figure 2.4(c). α-CT is the most widely utilised form of CT extracted and further processed due to ease of manufacturing [63, 64].

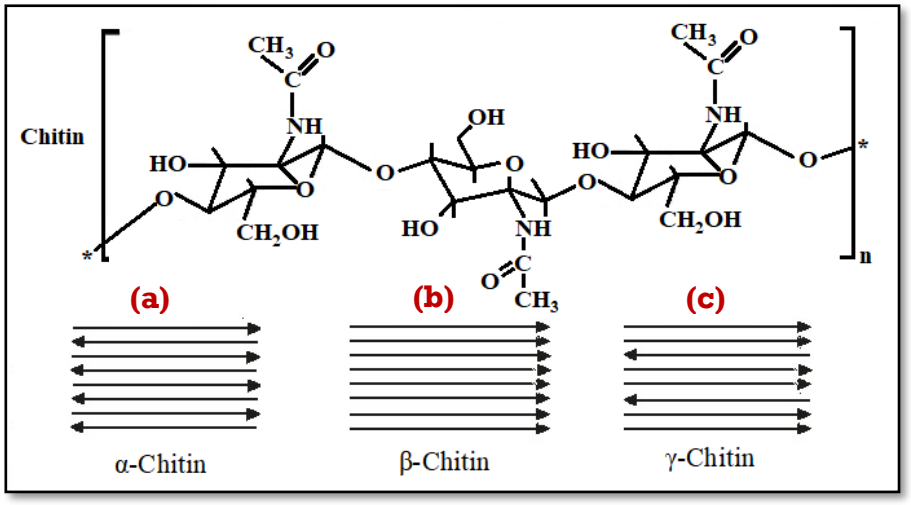

FIGURE 2.4 - The structure of different polymorphs of chitin (CT), (a) α-CT, (b) ß-CT and (c) *γ*-CT adapted from [59].

2.7.2 Chitosan

Chitosan (CS) is a copolymer obtained from a thermochemical partial deacetylation process of polysaccharide CT [65, 66]. Deacetylation involves chemical hydrolysis of the acetyl groups under alkaline conditions (concentrated NaOH) [67, 68], or by enzymatic hydrolysis via chitin deacetylase [67, 69]. The resulting structure consists of hydrophilic primary amino groups conferring positive charges [70]. The source (crab, squid, fungi etc.) [71] and processing conditions of CT affects the molecular weight (M_w), for example, the number of amino ($-NH_2$) and hydroxyl (OH) functional groups formed [70, 72]. Therefore the M_w of commercially available CS ranges from ~300 to 1000 kDa [16] with the degree of deacetylation (DD) from 30 % to 95 % [73, 74]. The DD is the ratio between glucosamine and the sum of glucosamine and N-acetyl-glucosamine units [67]; thus, DD corresponds to the free amino groups in the polysaccharide structure [75]. CS with a higher DD value corresponds to a higher

percentage of protonated primary amino groups, thus leads to an overall higher charge density [16]. For CT to be recognised as CS, the DD is required to be > 50 % [74, 76-78]. CS consists of β-(1→4) glycosidic linked D-glucosamine (deacetylated unit) and N-acetyl-D-glucosamine (acetylated unit) randomly distributed units [65, 79, 80] (Figure 2.5).

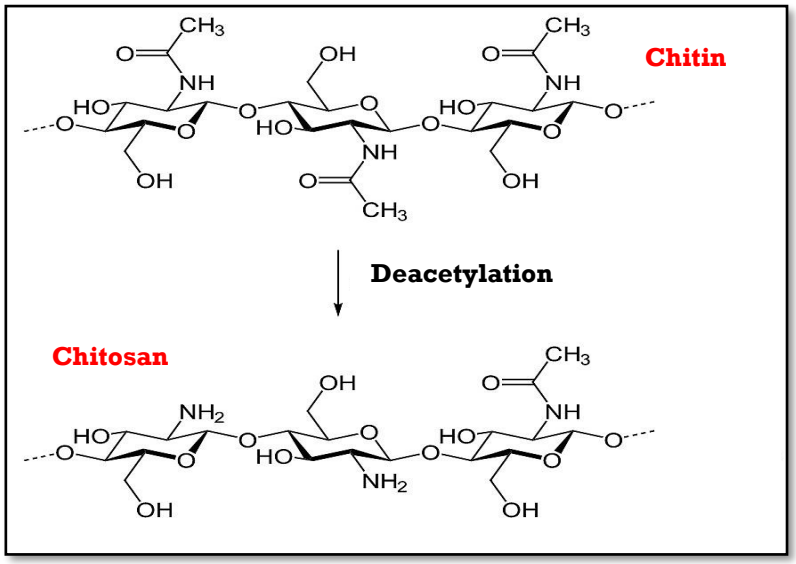

FIGURE 2.5 - The deacetylation process of chitin to obtain chitosan [81].

CS has a semi-crystalline structure [81] (Figure 2.6) where the amount of crystallinity is inversely related to the DD [70, 82]. Both DD and M_w affect the physicochemical, i.e. crystallinity, solubility and degradation [16] and biological properties of CS [60] (Table 2.2). For example, the crystallinity is maximum for CT where DD is equal to 0 % and CS where DD is equal to 100 %, and which subsequently decreases for CS with intermediate DD values [77, 81]. The decrease in crystallinity for CS with intermediate DD values is directly related to the presence of a more significant number of acetyl side

groups (-CH_3CO) on the polysaccharide chains, thus hindering close chain packing [81]. Conversely, fewer acetyl side groups in high DD CS [83] enables increased chain packing as well and further inter and intra-molecular hydrogen bonding, leading to increased crystallinity [83, 84] in comparison to CS with intermediate and low DD.

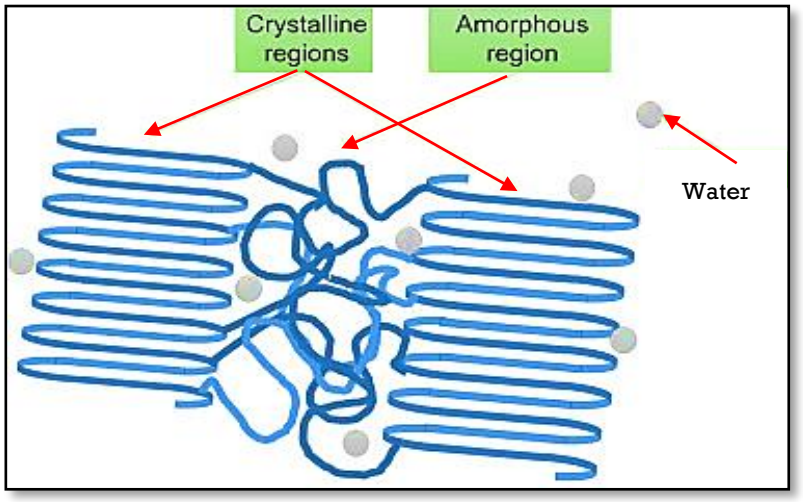

FIGURE 2.6 - Illustration of the amorphous and crystalline regions of biopolymer chitosan and the interaction of water molecules with the structure [81].

TABLE 2.2 - Chitosan (CS) relationship between structural parameters and properties [65].

Property	Structural Characteristics*	References
Solubility	↑ DD	[70, 75]
Biodegradability	↓ DD, ↓M_w	[60, 85]
Crystallinity	↓ DD	[70, 82]
Antibacterial	↑ DD, ↑ Mw	[86]

Biocompatibility	↑ DD	[70, 87, 88]
Viscosity	↑ DD	

* ↑ – signifies increase with property, ↓ – signifies decrease with property.

2.8 Chitosan in Biomedicine

CS is easily functionalised due to the presence of the reactive primary amino and hydroxyl groups which allow side groups, peptides and also amino acids to bind [16, 70]. Additionally, the functional groups can form stable covalent bonds during etherification and esterification reactions [63, 89]. CS exhibits a multitude of favourable properties including non-toxicity [37] biodegradability [60, 85], biocompatibility [60, 90, 91], antifungal, antibacterial [91] and wound healing abilities [92, 93]. Therefore, CS is widely utilised in the biomedical, biotechnology and pharmaceutical fields [62]. Applications of CS include drug delivery, wound healing, bone scaffolds, cartilage and nerve tissue engineering [65, 94]. CS systems, i.e., microspheres, nanoparticles, hydrogels and conjugates, are commonly employed to deliver pulmonary, ocular, nasal, cancer, vaccine and vaginal drugs [95].

2.8.1 Drug Delivery

Inhalation of dry powder CS nanoparticles combined with rifampicin a known antibiotic used to treat bacterial infections, i.e. tuberculosis, has been proven to have 24 hours drug delivery release with no toxic effects to neither cells nor organs [95, 96]. Nanoparticles antitubercular drugs, i.e., prothionamide (a drug used to treat tuberculosis) coated with CS, delivered via the pulmonary route has exhibited an increased improvement of the residence time the drug remained in the lungs [95, 97].

The beneficial mucoadhesive properties of CS were proven to increase the drug duration on the ocular surfaces. An *in vivo* study investigated the effects of naringenin which is commonly used as eyes drops to inhibit corneal neovascularization via anti-inflammatory and antioxidant mechanisms [95, 98]. Nasal delivery is a non-invasive procedure commonly used to deliver drugs to the respiratory system of the brain. CS increases the permeability of hydrophilic drugs; the three nasal absorption pathways include (i) transcellular, (ii) paracellular and (iii) trigeminal nerves (Figure 2.7). Nanoparticles comprising of carboxymethyl CS are functionalised to intra-nasally carry and deliver carbamazepine which is an anti-epileptic drug. The size of nanoparticles comprised of 218.76 $\pm$ 2.41 nm expressed 80 % entrapment efficiency; the *in vivo* and *in vitro* experiments confirmed an increase of the drug bioavailability, which led to enhanced targeting brain characteristics [99].

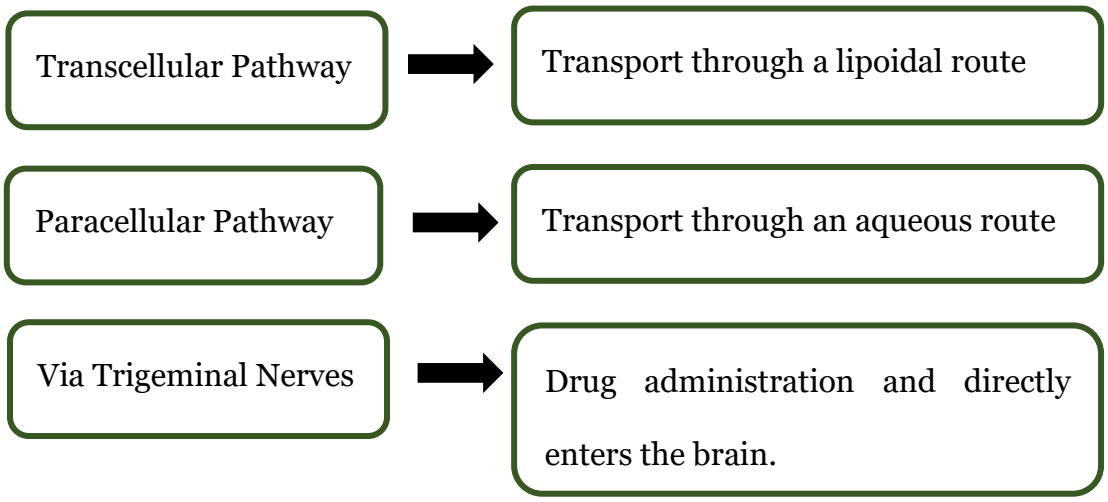

FIGURE 2.7 - The three pathways of nasal drug absorption, adapted from [95].

Cervical cancer cells are reduced via the effect of CS-ascorbate nanoparticles, where, *in vivo* and *in vitro* studies confirmed the inhibition of cervical cancer cells without affecting the viability of the surrounding cells [100]. Curcumin loaded folate CS nanoparticles are used to deliver curcumin in breast cancer therapy, confirming the use of CS as a delivery vehicle [101]. CS nanoparticles are used for mucosal and systemic vaccine delivery and can be administrated through the oral route or nasal cavity. Peyer's patches are small masses of lymphatic tissue located in the small intestine and are essential to the immune system [102]. Peyer's patches are the main target for nanoparticles which are administrated orally, CS nanoparticles containing vaccines are protected from enzymatic degradation while travelling to the mucosal tissue where they are uptaken by the intestinal epithelial microfold cells (M-cells) [95]. Conversely, CS nasal delivery vaccines containing influenza, diphtheria and pertussis antigens have proven as an effective delivery system due to CS acting as a natural adjuvant [103]. The mucoadhesive properties of CS provide an excellent pathway to facilitate the delivery of CS hydrogels or CS nanoparticles to treat vaginal co-infection [104]. Infections associated with *Candida albicans* are treated with clotrimazole which is a known antifungal medicine loaded into poly(d,l-lactide-co-glycolide) CS nanoparticles [95, 105].

2.8.2 Wound healing

The four overlapping phases associated with skin healing are, (i) hemostasis, (ii) inflammation, (iii) proliferation and (iv) tissue remodelling [106, 107]. The dynamic process of wound healing and the treatment of skin lesions requires physical protection from the external environment but also antimicrobial protection [107] to reduce the probability of the wound becoming infected. The wound healing ability of

CS is attributed to the cationic behaviour of the polysaccharide, whereby negatively charged red blood cells bind to CS; thus; the haemostatic ability leads to blood clotting [16]. Consequently, the haemostatic ability of CS is directly linked to the number of protonated amino groups [108]. CS protonated amino groups electrostatically interact with negatively charged glycolipids located on the surface of red blood cells which induces an increase of the blood viscosity allowing the transport of platelets to the wound site. The platelets adhesion leads to the formation of blood clots due to the aggregation of red blood cells at the wound site [108-110]. The haemostatic ability is related to the Mw and DD of CS and is not dependent upon the host coagulation pathway [106, 111]. CS with intermediate DD (~68%) formed a mesh-like structure facilitating blood component interactions [106]. In contrast, increased hydrogen bonding for CS containing higher DD led to increased crystallinity, thereby forming a rigid overall structure, thus limiting the interaction ability with blood-red cells [106, 112, 113].

2.8.3 Bone scaffolds

CS is an ideal polymeric biomaterial able to be mechanically and osteogenically functionalised for the fabrication of potential bone scaffolds. Potential CS bone scaffolds are created when combined with osteoconductive materials such as calcium phosphates, i.e., HA [114, 115]. Organic and inorganic material combinations have resulted in composites which are capable of stimulating bone regeneration [60, 70]. The polycationic nature of CS plays a vital role in bone tissue engineering applications, as the formation of polyelectrolyte complexes can be produced with the anionic biological macromolecules [116, 117] including but not limited to lipids, mineral, proteins, DNA and polymers, i.e. poly(acrylic acid) [67, 118, 119]. CS bone scaffolds

have demonstrated to support cell attachments and the proliferation of osteoblast cells leading to the formation of *in vitro* mineralised bone matrix [16, 120]. The proliferation of osteoblast cells improved for CS composites containing nano-HA, which led to bone regeneration after eight weeks as confirmed via micro-computed tomography [121].

The mechanical properties of CS-based scaffolds are improved by cross-linking with materials containing at least two reactive functional groups, i.e. calcium phosphates, composites (nano-zirconia and nano-calcium zirconate) and bioglass when compared to complexes containing CS solely [106]. The cross-linking provides bridges between the polymeric chains leading to structural stabilisation [70]. The reduction of the protonated amino groups via cross-linking increases the mechanical properties of CS material, i.e., CS cross-linked with DiepoxyPEG (Diepoxy-polyethylene glycol) [70, 122, 123]. The compressive strength of freeze-dried CS scaffolds is increased from 4 MPa to 11 Mpa for scaffolds containing CS- tricalcium phosphate [124]. Freeze-dried porous CS-gelatin 3D scaffolds fabricated with HA to improve the mechanical properties exhibited biomineralization after three weeks [6, 125]. Additionally, several studies have demonstrated the formation of porous CS-calcium phosphate 3D structures with improved mechanical properties [65, 126-128].

2.8.4 Cartilage and Nerve Tissue Engineering

Chondrocytes distributed into extracellular matrix form the articular cartilage; however, with increasing ageing, the repair and regeneration capability of chondrocytes reduces. Scaffolds fabricated for articular cartilage repair must exhibit

similar properties to the native tissue and adequate mechanical strength to support cellular growth. Although CS exhibits relatively low mechanical strength, when crosslinked with bioceramics, the mechanical properties are significantly improved [129]. To an extent, CS can promote the formation of cartilage tissue due to the polysaccharide presenting a similar structure to articular cartilage as depicted in Figure 2.8 [129]. *In vivo* studies found that the expression of cartilage matrix components is enhanced with the addition of CS [130].

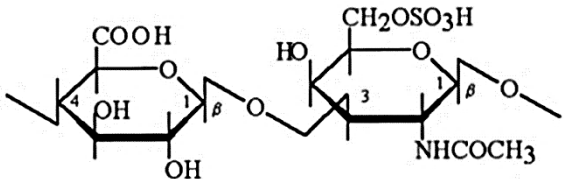

(a) Chondroitin 6-Sulfate

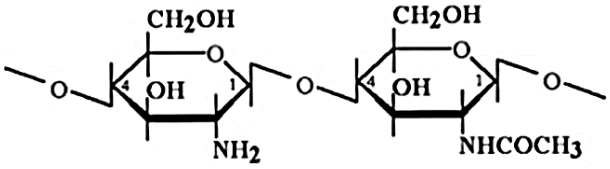

(b) Chitosan

FIGURE 2.8 - Structural comparison between (a) cartilage and (b) chitosan [129].

Damage to the nervous system causes malfunctions throughout the body and is difficult to repair [65, 131]. Mature neurons do not undergo cell division; thus, the main goal for nerve tissue engineering is to direct the regenerating nerve fibres to endoneurial tubes. The two current strategies are (i) bridging via grafting and (ii) suturing the nerve stumps end to end. CS membranes cultured with neurons is

reported to promote the repair of the peripheral nervous system [65, 132]. The adhesion, migration and proliferation of Schwann cells supported by CS fibres proved to regenerate axons [65, 133]. Laminin peptides immobilised on CS tubes facilitated the regeneration of axon bridging as well as proximal nerve sprouting [134].

2.9 Properties of Chitosan

2.9.1 Biocompatibility

Biocompatible materials cause little or no adverse reactions in the body (inflammation). CS is a known biocompatible polysaccharide which does not readily cause allergic reactions, toxicity or inflammation once implanted into the body [71, 75]. The biocompatible nature of CS is linked to the N-acetylglucosamine units, which also appears as natural components of mammalian tissues [87]. However, the biocompatibility is affected by the DD of CS. An acute inflammatory response arose for intermediate DD CS, i.e. between 69 % and 74 % when subcutaneously implanted in rats, and is likely to be a result of rapid biodegradation [70]. In comparison, CS containing high DD, i.e. between 74 % and 90 %, only a mild form of inflammation is expressed, possibly due to slower biodegradation rates. Similar results were exhibited for CS films containing $\geq$ 84 % DD are shown, which is linked to slower degradation rates; thus, the inflammation in the soft tissues was reduced [70, 88]. Osteogenesis is promoted for CS scaffolds containing immobilised adhesive peptides, e.g. tri-amino acid sequence, arginine-glycine-aspartate [39, 135].

2.9.2 Solubility

CS is insoluble in neutral solutions and has relatively poor solubility in organic solvents. The insolubility is related to crystallinity and the extensive capacity of inter and intra-molecular hydrogen bonding between CS macromolecules [90], causing the crystalline sections in CS to exhibit a rigid structure [65]. The solubilisation of CS is achieved via the soluble-insoluble transition [136], where the primary amino groups have a pKa of ~6.3 [137, 138] thus; enabling CS to form water-soluble salts in aqueous acidic conditions [16, 136]. At low pH values, i.e. < 6.3, the amino groups are protonated as expressed in Equation 2.1 due to the ionization of the acid [139], converting CS into a water-soluble polycationic material [65, 137, 140]. However, at high pH values (> 6.3), the amino groups lose their positive charges due to deprotonation, thus leading to reduced solubility [65].

$$R\,NH_2 + H_3O^+ \rightleftarrows R\,NH_3^+ + H_2O \qquad (2.1)$$

2.9.3 Swelling and Degradation

Both DD and Mw are inversely proportional to the swelling capacity and degradation of CS [65, 81, 141]. Increased DD correlates to increased crystallinity which subsequently reduces the swelling index [81, 141] and degradation rates [16, 142]. The DD plays a vital role with regards to biological *in vitro* and *in vivo* degradation, healing capacity, osteogenesis and also lysozyme degradation within biological systems [143, 144]. CS with a high DD, i.e. 84 % to 90 % has exhibited delayed degradation and presents a lower degradation index in comparison to CS DD between 65% and 82% [70]. CS containing high levels of DD have been shown to degrade slowly over several

months [143, 144], which is beneficial for bone regeneration as the degradation rate can be tuned to match bone regrowth [16]. Low M_w CS contains smaller length polysaccharide chains which in turn leads to reduced chain entanglements [145]. Therefore, the smaller CS polysaccharide chains degrade more rapidly into variable-length oligosaccharides (Figure 2.9) compared to CS with higher M_w [81, 146]. The degradation difference between low→high CS DD is related to increased crystallinity hydrogen bonding [71, 143, 144]. CS under physiological conditions provides a controlled chemical breakdown leading to inert degradation products which include non-toxic oligosaccharides [147], N-acetyl-d-glucosamine residue and water which can be utilised in metabolic pathways or excreted [69].

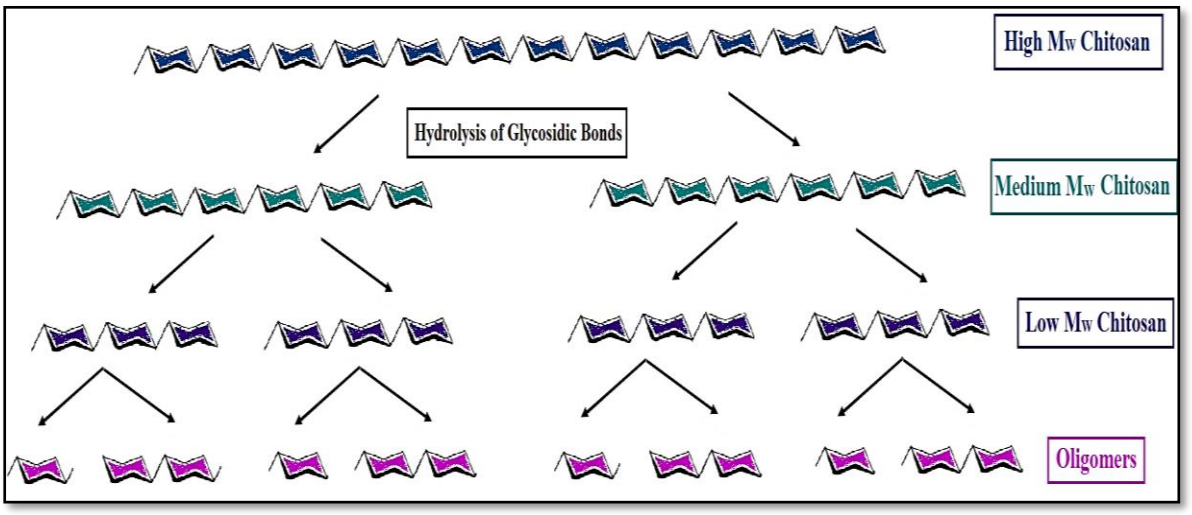

FIGURE 2.9 - Illustration of chitosan chain scission degradation in terms of molecular weight forming soluble chitosan oligomers adapted from [81].

2.9.4 Antimicrobial

The difference between Gram-positive and Gram-negative bacteria lies with the structure of the bacterial cell wall. The structural stability of the Gram-positive cell wall is attributed to the thick layers of peptidoglycan, which is modified with anionic polymers. The anionic polymers influence the membrane permeability and mediate extracellular interactions [148]. The cell wall is comprised of peptidoglycan and teichoic acid, as depicted in Figure 2.10. The teichoic acids are either covalently bonded to the peptidoglycan layer, thus are known as lipoteichoic acids (LTA) or anchored to the outer cytoplasmic membrane hence referred to as teichoic wall acids (TWA) [149]. The cell wall of Gram-positive bacteria is negatively charged due to the presence of phosphates in the structure of teichoic acids [150]. Gram-negative bacteria consists of an outer hydrophobic lipopolysaccharide membrane (LOM) which acts as a penetration barrier against macromolecules and contains anionic phosphate and carboxyl groups [151, 152]. The anionic groups can form electrostatic interactions with divalent cations, thus contributing to the stability of the lipopolysaccharide layer [153]. The lipopolysaccharides contain phosphate and pyrophosphate groups which are negatively charged, thus providing a superior overall negative charge compared to the cell wall of Gram-positive bacteria [86, 154]. However, chelating agents are known to react with the LOM causing lipopolysaccharides to be released hence destabilising the outer membrane [152].

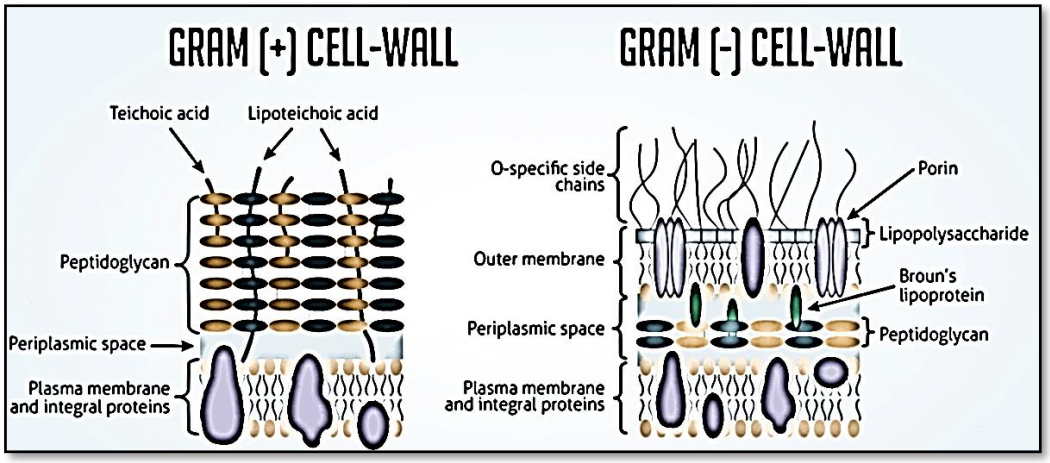

FIGURE 2.10 - Comparison of the bacterial cell wall, (a) gram-positive bacteria and (b) gram-negative bacteria adapted from [155].

CS antimicrobial and antifungal abilities are widely demonstrated in both *in vivo* and *in vitro* environments. The growth of several types of fungal and bacterial types are inhibited when CS-based materials, i.e. CS wound dressing, are applied. CS exhibits a chelating capacity due to the positive charged expressed when protonated; hence the antimicrobial action of CS is related to the electrostatic interactions of the NH_3^+ charged amino groups with negatively charged bacterial walls [86]. The interactions promote cell wall permeability which leads to internal osmotic imbalance thus, hydrolysis of the proteins (peptidoglycans) which form the bacterial cell wall occurs, causing intercellular leakage of electrolytes such as potassium ions, proteins, nucleic acids and glucose [86, 156]. The osmotic imbalance inhibits the growth of the microorganisms and often leads to cell death [157].

Several studies have found similar results for Gram-positive, and Gram-negative bacteria, where CS attached to bacterial surfaces locally causes cell wall detachment

forming vacuoles (membrane-bound sacs) invoking the internal bacterial pressure to decrease [86, 149]. The pressure decrease initiates membrane lysis, thus leads to cell death. The literature suggests that the greater the number of protonated amino groups, i.e. higher the DD, the more significant is the antimicrobial activity [86, 152]. A second CS antimicrobial mechanism is linked to the chelation capability of the biopolymer as CS is well known to bind efficiently to metal cations via the protonated amino groups [153]. The CS chelation capability, when bound to metal ions, can cause toxin production and the suppression of the binding sites of essential elements (Ca^{2+}) required for microbial growth [152, 158].

2.10 Calcium Phosphate Bioceramics

Bone osteoinductivity is due to bone morphogenetic proteins (BMPs) and osteogenic proteins including, collagen and osteonectin, which are present in the extracellular matrix. Calcium phosphates (CaP) are bioceramics known to have a high affinity for BMPs which encourage new bone tissue formation [159-161]. The capacity of CaP to form molecular interactions with surrounding tissues leading to surface apatite layer formation is referred to as osteoconductivity [162]. The rationale for the fabrication of CaP based bone scaffolds is related to the compositional similarity to natural bone mineral. CaP materials possess several advantageous properties including, biocompatibility, bioactivity, osteoconductivity and biodegradability [20]. CaP based ceramics have already gained approval for use in orthopaedic applications [163] including but not limited to, cochlear implants, coatings for metal orthopaedic implants and bone fracture defect repairs. Dental-related applications of CaPs includes dental cement, periodontal bone defect filling, coating of dental implants, maxillofacial reconstructions and sinus lift procedures [163-165]. Despite the apparent

beneficial properties exhibited by CaP materials, the low fracture strength and brittleness prevent CaP materials solely from being utilised in load-bearing applications [20]. CaP ceramics are commonly combined with other polymers (e.g. CS) to improve biological responses in terms of osteoblast response enhancement and direct mesenchymal stem cell phenotype [16, 166-168].

2.11 Composition of Calcium Phosphates

The composition of CaP ceramics is dependent on the ratio between calcium and phosphate (Ca/P) and the level of ion substitution impurities, i.e., Na^{+}, $Mg^{2+,}$ K^{+}, HPO_2^{-4}, and Cl^{-} [169]. Apatites are considered to contain an atomic Ca/P ratio between 1.5 and 1.67, of which, HA and fluorapatite are examples [169]. The lower the Ca/P ratio, the higher the solubility and the acidity of the CaP ceramics. The acidic forms of CaP are similar in chemical composition to HA but differ with regards to Ca/P ratio, crystal structure and rate of dissolution [16, 24]. Examples of acidic forms of CaPs are (i) Tricalcium Phosphate (TCP), (ii) Octacalcium phosphate (OCP) and (iii) Dicalcium Phosphate Dihydrate (DCPD) and are soluble at neutral pH (Table 2.3) [170, 171]. DCPD and OCP are known to form in solution readily; however, they are metastable precursor phases with regards to HA.

2.11.1 Hydroxyapatite

The most stable form of calcium phosphate is HA, the mineral constituent of bone which has relatively low solubility due to the Ca/P ratio (1.67). Biological HA has a hexagonal crystal structure where the calcium ions are arranged in columns with the phosphate ions located in parallel channels [172]. Sintered HA is compositionally and

crystallographically similar to bone mineral; however, is not readily resorbed [173]. Nucleating sites for bone minerals are present on the surfaces of HA; hence when applied clinically do not cause any inflammatory reactions. [174-176]. *In vivo*, regeneration of bone is improved with the addition of biocompatible HA as the mesenchymal stem cells proliferation was enhanced via the adhesion of the increased osteoblast cells [177, 178]. HA ceramic scaffolds fabricated for bone regeneration exhibited unfavourable properties such as high mechanical stiffness, low elasticity, poor resorbability, and also high brittleness due to low fracture strength [6].

2.11.2 Tricalcium Phosphate

The two crystallographic forms of Tricalcium Phosphate (TCP) are α-TCP and the partially resorbable ß-TCP, which is the most common form [165, 179]. The crystal structures of α-TCP and ß-TCP are monoclinic and rhombohedral, respectively [180, 181]. TCPs are known to support the differentiation of mesenchymal stem cells (MSCs). Bone deposition is reported for ß-TCP when utilised as a bone filler material [182, 183]. Additionally, ß-TCP combined with collagen type I and alginate gel leads to an enhanced bone formation as compared with collagen-HA scaffolds [13, 145]. However, other studies have reported fibrous tissue encapsulation of ß-TCP granules leading to lack of adequate bone growth [165, 184].

TABLE 2.3 - Comparison of different forms of calcium phosphate ceramics.

Name	Formula	Ca/P Ratio	Lattice Parameters (Å)	pH Stability	Young's Modulus (GPa)
Hydroxyapatite	$Ca_{10}(PO_4)6(OH)_2$	1.67	a,b = 9.432 c = 6.881	9-11	14.0
Tricalcium Phosphate	$Ca_3(PO_4)_2$	1.5	a,b = 10.439 c = 37.375	8	24
Octacalcium Phosphate	$Ca_8\,H_2(PO_4)_6{\cdot}5H_2O$	1.33	a = 19.69 b = 9.523 c = 6.835	5-6	-
Dicalcium Phosphate Dihydrate	$CaHPO_4{\cdot}2H_2O$	1.0	a = 5.812 b = 15.180 c = 6.239	4-6	7.4

[185]

2.11.3 Octacalcium phosphate

OCP has a triclinic crystal structure [24] consisting of alternating apatitic and hydrated layers [186]. The pH range from ~5 to 6 of OCP is the favoured metastable phase [187]. The apatitic layers act as nucleation sites for the HA phase when the pH shifts from acidic to alkaline [187]. Thus, OCP is a precursor for biological apatite formation as well as for both tooth dentin and enamel [176, 188-190], with OCP-HA transition confirmed by numerous *in vitro* studies [187, 191-194].

2.11.4 Dicalcium Phosphate Dihydrate

Dicalcium Phosphate Dihydrate (DCPD), has a monoclinic crystal structure (space group: I2/a). The structure of DCPD consists of parallel CaP chains with interlayered lattice water molecules. Below pH 6 DCPD is the dominant phase. Heat treatment of ~ 180 ˚C removes the structural water molecules leading to the transformation of an anhydrous form named Dicalcium Phosphate Anhydrous (DCPA) [195, 196]. Less stable phosphates such as DCPD, TCP and OCP precipitate biological apatite's through intermediate steps, thus are considered as precursors for bone mineralisation [197, 198]. DCPD is utilised as bone cement [196] due to being commonly found in pathological calcifications, i.e. mineralisation (osteoblast) *in vitro* [196, 199]. The synthesis of DCPD occurs via aqueous acidic conditions (pH 4-6 at 37 ˚C). Unlike HA, DCPD can be resorbed and is structurally stable at lower pH values (e.g. <5.5) [200]. Under physiological conditions, pH ~7, DCPD is metastable and converts to the more stable phases OCP and HA [201-204]. The biocompatible nature of DCPD has been demonstrated in many studies [205-207], for example, new bone formation without inflammation is observed with the addition of DCPD in sheep cranial defects sites [208].

2.12 Solubility of Calcium Phosphates

The ability for bone scaffolds to resorb is essential to ensure space is created for new bone tissue to form and integrate into the implanted scaffold [163]. CaP ceramics have demonstrated (i) predictable degradation rates, (ii) resorbability *in vivo* and (iii) the progressive replacement of lamellar bone. Degradation refers to the physical disintegration and fragmentation of materials, whereas resorption refers to biodegradation via cellular mechanisms (Figure 2.11(a)) [165]. Thus, the process of resorption is classed as cell-mediated (phagocytosis by macrophages) and solution-driven [209, 210]. The disintegration of CaP based materials causes particle formation, which leads to CaP resorption via phagocytosis by macrophages. Figure 2.11(b) depicts a solubility phase diagram of isotherms expressed as plots of (log $T_{ca}T_p$) as a function of the pH. The calcium and phosphate molar concentrations are expressed as T_{ca} and T_p, respectively. The curve positions vary with the ionic strength of the electrolyte. The thermodynamical solubility of the CaP variations at pH 7 is **DCPD > OCP > TCP > HA** from the most soluble to the least soluble [24].

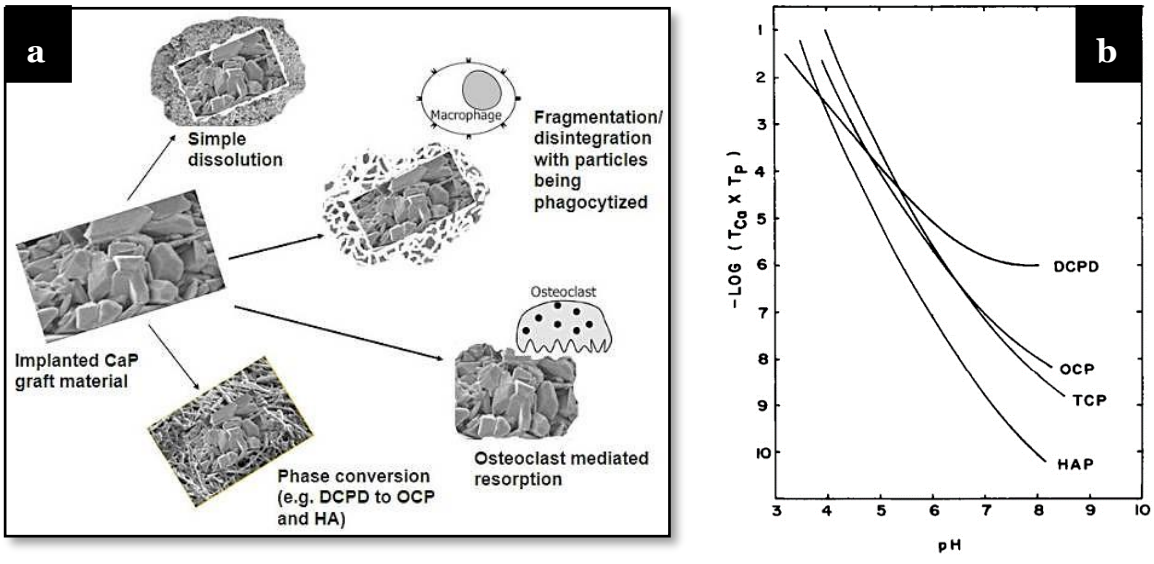

FIGURE 2.11 - Degradation and solubility diagrams (a) images of biodegradation via cellular mechanisms after implantation [163], (b) the solubility isotherms of calcium phosphate phases at 37 °C at a concentration of 0.1 M [211].

2.13 Bone Infections

Bone infections are frequent, especially concerning trauma, leading to open wound fractures [212-214]. Contamination of open wound fractures is expected, especially concerning road accidents where polluted water, dirt and other foreign materials easily infect the wound fractures site. Sources of infectious bacteria include the operating room, surgical equipment, contaminated orthopaedic/medical devices, but there are also resident bacteria already present in the patient's body or on their skin [215]. Epidemiological studies suggest between 2 %, and 5 % [216, 217] of all the implant-related procedures are likely to develop further complications due to post-operative infections leading to an increase in health-related costs, prolonged hospitalisation, revision surgeries but also morbidity [218-220]. The treatment of infection is complex involving parenteral or systemic drug administration and in extreme cases, debridement of bone and tissue due to compromised blood circulation [221]. Drug administration for infection control uses a broad range of antibiotics which has led to the emergence of multidrug-resistant bacterial strains [200, 219]. As a result, the treatment of diseases which were under control several years ago now require higher doses of multiple antibiotics which often generates intolerable toxicity.

2.13.1 Biofilm Formation

Contaminated surgical instruments or residual bacteria present on the implanted orthopaedic device introduces bacteria into the patient's body. Once an orthopaedic

device is implanted into the patient's body, tissue and proteins in the blood gradually adsorb to the surface of the device as also demonstrated extensively in the literature [20-23]. Bacteria in a planktonic state adheres to the adsorbed proteins and proliferates until a colony of bacteria is formed, enabling a change in the gene expression pattern. The genes responsible for the production of bacterial extracellular polymeric substances (EPS) are activated and expressed [222]. The excretion of EPS further facilitates the exponential growth of bacteria leading biofilm formation (Figure 2.12) [218, 223, 224]. The bacteria promoted biofilm, hinders the host's immune response and antibiotic delivery; hence biofilms are one of the major causes for the development of bacterial resistance [219].

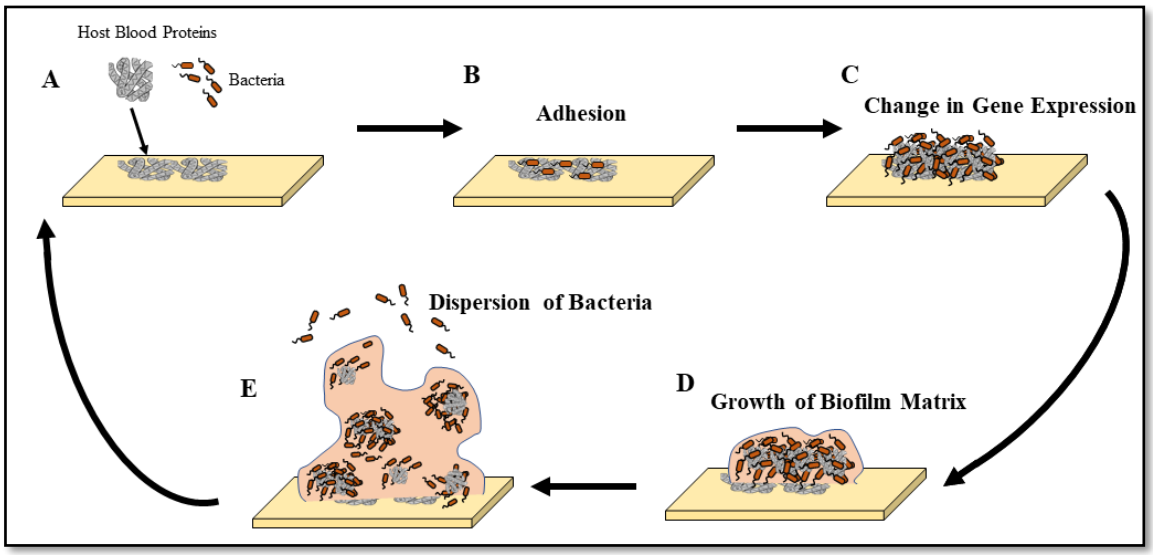

FIGURE 2.12 - Illustration of biofilm formation (a) adhesion of proteins from the host's blood, (b) adhesion ~~of~~ and proliferation of bacteria, (c) change in gene expression to form extracellular polymeric materials, (d) growth of the biofilm as well as microcolonies of bacteria and (e) sections of biofilm break leading to bacteria invading other 'clean' surfaces. (illustration not to scale: Size of proteins are ~ 10 nm and size of bacteria ~ 1 um)

2.13.2 Bacterial Resistance

The mechanism for bacterial resistance is attributed to the evolutionary processes taking place during antibiotic therapies, horizontal gene transfer by (i) conjunctions between two closely related bacterial strains, (ii) transduction and also (iii) transformation (i.e. commonly known as superbugs) [225]. Antibiotics work by attacking at least three modes of targets; cell wall, translation mechanism and DNA replication mechanism. However, many bacteria have developed a resistant gene known as New Delhi Metallo-Beta-Lactamase-1 (NDM-1), which prevents the destruction of the bacteria. Mechanisms of bacterial resistance include the expression of certain enzymes which can modify or destroy antibiotics, i.e. β-lactamases [226], modification of ribosomes and cell wall as shown with tetracycline and vancomycin resistance [218].

2.14 Nanoparticles

Due to the growing urgency to minimise the dependency on antibiotic drugs, alternative treatment strategies, including the use of nanoparticles, have attracted significant attention as these types of particles manifest unique physicochemical properties. The unique properties are only apparent on nanoscale, e.g. surface area to volume ratio, surface charge and oxidation state when compared with bulk counterparts [227]. Several types of inorganic nanoparticles (ZnO, TiO_2, Ag) are emerging as novel antibacterial agents and have proven their effectiveness in treating infectious diseases [228]. The antibacterial potential of nanoparticles is affected by factors such as size, shape, surface charge and surface area to volume ratio [227]. Nanoparticle size is essential with regards to biological functions as the morphological dimensions are comparable with (i) small biological molecules (1-10 nm), (ii) viruses

(10-100 nm) and (iii) be able to attack biological entities without changing their functions [227]. The antibacterial mechanism is likely to be attributed to their ability to enter biofilms; unlike antibiotics, nanoparticles directly attack the cell wall of bacteria attaching via (i) electrostatic interaction, (ii) Van der Waals forces as well as (iii) receptor-ligand and hydrophobic interactions [219] disrupting the integrity of the bacterial cell wall leading to cell death [229].

Nanoparticles can prevent bacteria mutating, thus replacing or even reducing the use of conventional antibiotics [230]. The antibacterial properties of metal and metal oxide nanoparticles such as silver [231], copper [232], zinc oxide [233] and titanium dioxide [234] have demonstrated to alter the metabolic activity of Gram-positive and Gram-negative bacteria [219]. Zinc oxide nanoparticles are found to inhibit *Staphylococcus aureus,* whereas concentration-dependent silver nanoparticles exhibited antimicrobial activity against *Escherichia coli* and *Pseudomonas aeruginosa* [235]. However, specific nanoparticles, i.e. silver, are toxic to cells even at low doses despite exhibiting antibacterial properties [236]. Nanosilver intraperitoneal silver injection and its dispersion through blood are found to affect the lungs, liver, gastroenterological tract and brain tissues [237]. For this reason, the use of silver in treating internal infections is now severely limited. Other studies have reported gold [238], magnesium oxide [239, 240] and copper oxide [219, 241, 242] based nanoparticles prevented the formation of biofilm; this has been linked to the high surface area to mass ratio, i.e. smaller sized <10 nm [218, 243]. Triangular-shaped silver particles exhibited higher antibacterial properties as compared with spherical or rod-shaped nanoparticles [244].

2.15 The Antibacterial Mechanism of Cerium Oxide Nanoparticles

Nanoceria has attracted a great deal of interest as antibacterial agents due to the ability to cycle between the two valence states (Ce^{3+} and Ce^{4+}) leading to the formation of oxygen vacancies in the lattice. The apparent beneficial oxygen buffering capability enables nanoceria to act as a catalyst for both oxidation and reduction reactions [245]; hence is characterised to manifest a unique antibacterial mechanism [230]. Nanoceria possesses antioxidant capabilities [246] due to its intrinsic bi-valence (catalytic oxidation and reduction) which protect cells from oxidative stress inflammation [247] and potential radiation damage [248]. Previous studies highlight nanoscale cerium presenting relatively low or no toxicity to mammalian cells [249-252] and is proven to decrease catalysts of chronic inflammation via nanotherapeutics [247] as well as demonstrating the ability to enhance neuroprotection [253]. Furthermore, cerium oxide nanoparticles exhibit pro-oxidative behaviour, depending on the environment, i.e. oxidative stresses is induced, which is directed at bacteria [254]. The redox properties of nanoceria can be tuned via materials preparation method, drying method, particle size, surface chemistry, particle shape and level of dopant materials [245].

2.15.1 Cerium Oxide Fluorite Structure

In the fluorite structure of cerium oxide, the redox equilibrium between the two valence states (Ce^{3+} : Ce^{4+}) may be explained by considering the reaction in the presence of oxygen gas, as shown in equation (2.2):

$$2CeO_2\ (s) = Ce_2O_3\ (s) + \frac{1}{2}\ O_2\ (g) \qquad \text{eq (2.2)}$$

The intrinsic presence of oxygen vacancies in the CeO_2 crystal structure renders CeO_2 into a CeO_{2-x} non-stoichiometric oxide with 'x' vacant oxygen sites [255]. The ratio of Ce^{3+} : Ce^{4+} ionic states compensates against vacant oxygen sites and may be represented by the following equation:

$$CeO_2\ (s) = CeO_{2-x}\ (s) = Ce^{4+}_{1-x}\ Ce^{3+}_{x} O^{2-}_{2-x} \blacksquare_x (s) \qquad \text{eq (2.3)}$$

In equation (2.3), the oxygen vacancy is shown by $\blacksquare_x$ where x is the fractional value of vacant sites in the fluorite structure. Oxygen deficiencies in the fluorite crystalline lattice occur when the oxygen partial pressure is less than the value predicted value from equation (2.1) enabling the vacant oxygen sites to act as a sink for oxygen, an essential step in redox reaction equilibrium in the cerium-oxygen system.

2.15.2 Regeneration Potential of Cerium Oxide

Nanoscale cerium oxide can mimic an antioxidant enzyme superoxide dismutase found in all living cells [256]. Superoxide dismutase, catalase and glutathione are considered as the body's cellular defence as they catalyse the breakdown of potentially harmful oxygen molecules known as reactive oxygen species (ROS)/free radicals thus preventing tissue damage within the body. The primary role of antioxidants is to reduce excessive amounts of ROS/free radicals hence combating oxidative stress-related diseases [257].

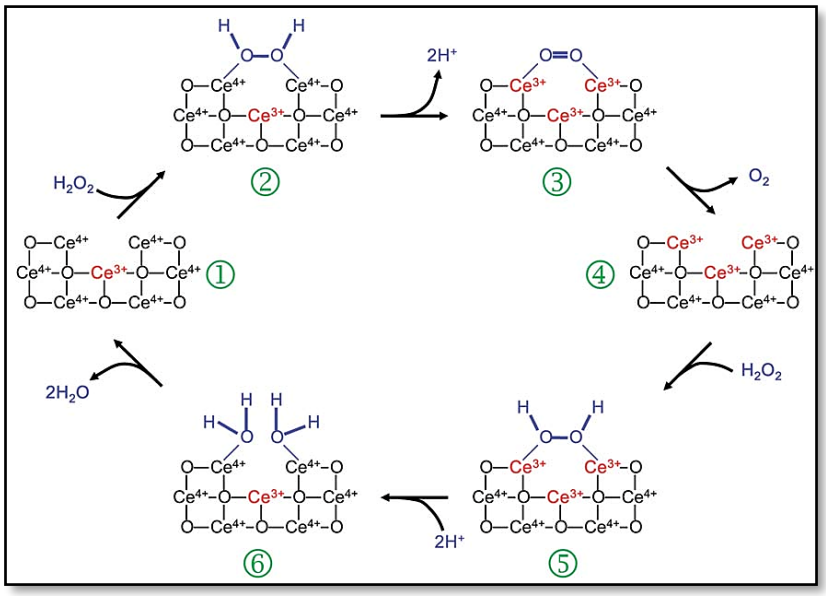

FIGURE 2.13 - Possible mechanism for self-regeneration of cerium oxide nanoparticles requiring two superoxide's reduced for each H_2O_2 oxidised. (1) $2Ce^{4+}$ binding site for H_2O_2, (2) release of two protons causing two-electron transfers to the cerium ions (3) oxygen is released, (4) fully reduced oxygen vacancy site, (5) superoxide can bind to the site and (6) single-electron transfer from one Ce^{3+} plus the addition of two protons from the solutions creates H_2O_2 [257].

Cerium oxide nanoparticles decrease catalysts of chronic inflammation via nanotherapeutics [247] as well as demonstrating the ability to enhance neuroprotection [253]. Also, there is a hypothesis regarding the potential self-regeneration of cerium oxide nanoparticles via a redox regeneration mechanism, which involves reducing hydrogen peroxide (H_2O_2), causing Ce^{3+} to be oxidised to Ce^{4+}. The Ce^{4+} reacts with further H_2O_2 hence regenerating Ce^{3+}, enabling H_2O_2 to be oxidised to oxygen (O_2); the full mechanism is depicted in Figure 2.13 [257]. The literature [253, 258] describes another possible route for the reduction of H_2O_2; the process involves a second H_2O_2 molecule oxidising Ce^{3+} (after step 4 in Figure 2.13)

therefore enabling the regeneration of Ce^{4+} which would reduce H_2O_2 to form water (H_2O). Figure 2.14 depicts the full mechanism [257].

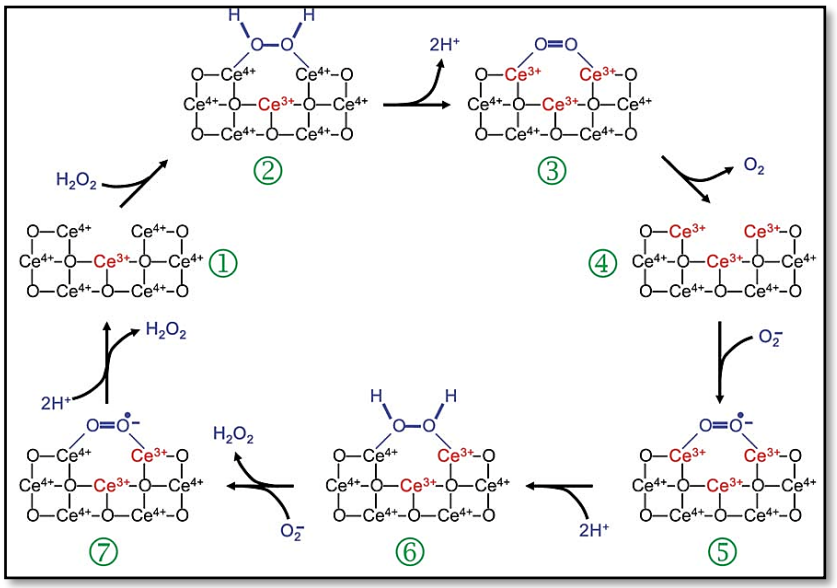

FIGURE 2.14 - A model of the reaction mechanism for the complete dismutation of hydrogen peroxide. The oxidative half-reaction is identical to the sequence shown in Figure 2.13 (1–4). (5) The binding of H_2O_2 to the $2Ce^{3+}$ and (6) water is released, thus regenerating the initial Ce^{4+} site [257].

The growth inhibition of *Escherichia coli* bacteria is related to the surface area of cerium oxide nanoparticles [259]. Also, the antioxidant activity of cerium oxide nanoparticles has demonstrated to protect cells against oxidative stresses, inflammation and potential radiation damage [248]. Several studies are concluding that there is no apparent antibacterial effect of cerium oxide nanoparticles [260, 261]. However, other findings highlight possible adverse effects of the nanoceria, where oxidative stress was induced in epithelial human lung cells [262]. The range of

conflicting data may be attributed to factors such as varying manufacturing processes, chemical solvents not entirely removed, irregular pH during production and calcination temperatures [259]. The redox properties of cerium oxide nanoparticles can be tuned via materials preparation method, drying method, particle size, surface chemistry, particle shape and level of dopant materials [245]. The drying method of nanoparticles is a vital aspect to consider as nanoparticles tend to agglomerate, which adversely affects the physicochemical properties of the particles [263]. Thus, the procedures employed to evaluate the antimicrobial and antibacterial properties associated with cerium oxide nanoparticles may also make it challenging to form significant conclusions.

2.16 Aims of the Study

The first research aim is to investigate the osteoconductive efficacy of Dicalcium Phosphate Dihydrate (DCPD) and to fabricate multilayered bone scaffolds based on the fundamentals of advanced manufacturing using a freeze-drying approach. The second research aim is the investigate whether heat treatment, particle size and Ce^{3+} : Ce^{4+} ratio affects the overall antibacterial efficacy of cerium oxide nanoparticles.

2.16.1 Objectives for Freeze-dried Scaffolds

(i) Synthesise unloaded and DCPD mineral loaded scaffolds at different concentrations (0, 20, 30, 40 and 50 wt%).

(ii) Characterise the synthesised freeze-dried scaffolds and analyse all structural changes which occur with increasing DCPD mineral content.

(iii) Investigate the mechanical properties of the synthesised scaffolds to ensure mechanical stability in terms of handling and osteoblast cellular growth.

(iv) Develop a dual-layered scaffold using freeze-drying processing techniques.

(v) Determine the optimal DCPD concentration, which enhances osteoblast proliferation.

2.16.2 Objectives for Cerium Oxide Nanoparticles

(i) Synthesise cerium oxide nanoparticles via different methods (freeze-drying, furnace-drying, and heat treatment) to investigate whether the nanoparticles drying methods affect the physicochemical properties.

(ii) Characterise all the synthesised nanoparticles to determine whether the drying method affected the particle size distribution and the Ce^{3+} : Ce^{4+} ratio.

(iii) Test the antibacterial efficacy of the nanoparticles against common Gram-negative and Gram-positive bacteria associated with common orthopaedic infections, i.e. *Escherichia coli* (-ve) [264, 265], *Pseudomonas aeruginosa* (-ve) [266, 267] and *Staphylococcus epidermis* (+ve) [215, 264, 268] respectively.

(iv) Investigate the half-maximal inhibitory concentration (IC_{50}) to determine the nanoparticle concentration, which reduces bacterial growth by 50 %.

2.16.3 Thesis Research Questions

Freeze-dried Scaffolds:

1) Does the incorporation of DCPD mineral increase the mechanical properties of the freeze-dried scaffolds?
2) How does the mineral affect the porosity of the scaffolds?
3) What is the optimal DCPD concentration, which induces enhanced proliferation?
4) Is it possible to form successful porous double-layered scaffolds where each layer differs in DCPD mineral content?

Cerium Oxide Nanoparticles:

1) Does the cerium oxide synthesis procedure form nanosized particles?
2) Does the drying method affect the size, shape and Ce^{3+} : Ce^{4+} ratio?
3) What is the optimal Ce^{3+} : Ce^{4+} ratio, which exhibits the most significant antibacterial efficacy?
4) What is the IC_{50} for the cerium oxide nanoparticles tested?

2.17 Chapter 2 Summary

This chapter reviewed the relevant literature relating to the function and structure of natural bone, current bone grafts and potential synthetic scaffold biomaterials. Biopolymer materials such as chitosan (CS) do not possess adequate mechanical properties for load-bearing applications; thus, incorporating minerals can enhance the material's modulus. The antibacterial potential of cerium oxide nanoparticles was discussed concerning the Ce^{3+} : Ce^{4+} ratio. Based on the literature review CS, DCPD and Cerium Oxide nanoparticles were selected to form synthetic bone scaffolds.

Chapter 3
MATERIALS AND METHODS

3.0 Introduction

Material synthesis of freeze-dried CS porous scaffolds embedded with DCPD minerals and synthesis of cerium oxide nanoparticles are outlined in this chapter. Characterisation techniques such as X-ray Diffraction (XRD), Fourier Transform Infrared (FTIR), Ultraviolet-Visible (UV-VIS), Transmission (TEM) and Scanning Electron Microscopy (SEM), and Raman Spectroscopy are discussed. Materials testing techniques, including Water Uptake (Swelling), Degradation, Density, Porosity measurements, Thermal Analysis (STA), Zeta Potential, and Mechanical Testing, are outlined. The *in vitro* cellular protocols relating to freeze-dried scaffolds and antibacterial experimental protocols, i.e. Optical Density (OD) and Colony Forming Unit (CFU) for cerium oxide nanoparticles are also included in this chapter.

3.0.1 Materials and Chemicals

The materials, chemicals and corresponding suppliers utilised for materials synthesis are displayed in Table 3.1. All the chemicals were of analytical grade and used without further purification.

TABLE 3.1 - Materials and chemicals used for materials synthesis with the corresponding suppliers.

Material/Chemical	Supplier
Acetic Acid Glacial, purity > 99.5%	Acros Organics, MFCD00036152
Agarose	Merck, CAS: 9012-36-6
Ammonium Phosphate ($(NH_4)_2$ HPO_4)	Acros Organics, CAS: 7783-28-0
Brain Heart Infusion agar	Sigma Aldrich, BHI Agar #70138

Brain Heart Infusion Broth	Sigma Aldrich, BHI Broth 53286
Calcium Nitrate ($Ca(NO_3)_2 \bullet 4H_2O$)	Fisher Chemicals, CAS: 13477-34-4
Cerium Nitrate Hexahydrate ($Ce(NO_3)_3 \cdot 6H_2O$)	Sigma-Aldrich, CAS: 10294-41-4
Chitosan Flakes	Sigma-Aldrich, CAS: 9012-76-4
Petri Dishes	Sigma-Aldrich, BR452005
Phosphate Buffer Saline Tablets	Sigma-Aldrich, MFCD00131855
Whatman Grade 44 filter 1 and 3 μm	Merck, WHA1444110
Quant-iT™ PicoGreen™ dsDNA Assay Kit	ThermoFisher Scientific, CAT: P7589

3.1 Freeze-Dried Scaffold Synthesis

3.1.1 Dicalcium Phosphate Dihydrate Mineral

The preparation of DCPD mineral ($CaHPO_4 \bullet 2 H_2O$) is achieved via a slow drip wet precipitation route. Briefly, 200 ml of a 0.1 M $Ca(NO_3)_2 \bullet 4 H_2O$ aqueous solution (A) was heated to 37 ˚C. Then 200 ml of a 0.1 M $(NH_4)_2 HPO_4$ aqueous solution was added dropwise under continuous stirring to the solution (A). The resulting mixture was left stirring for 2 hours at 37 °C (Figure 3.1(a)). Then, the heat-plate and the stirrer were switched off while the mixture was left to settle for 1 hour to allow precipitation (equation 3.1). The DCPD yield was filtered using Whatman Grade 44 filter paper containing 3 μm pores and washed three times using distilled water (Figure 3.1(b)). The mineral collected was dried for 24 hours at 80 °C.

$$Ca(NO_3)_2 \cdot 4 H_2O + HPO_4(NH_4)_2 \rightarrow CaHPO_4 \cdot 2 H_2O + 2 NH_4NO_3 + 2 H_2O$$

eq (3.1)

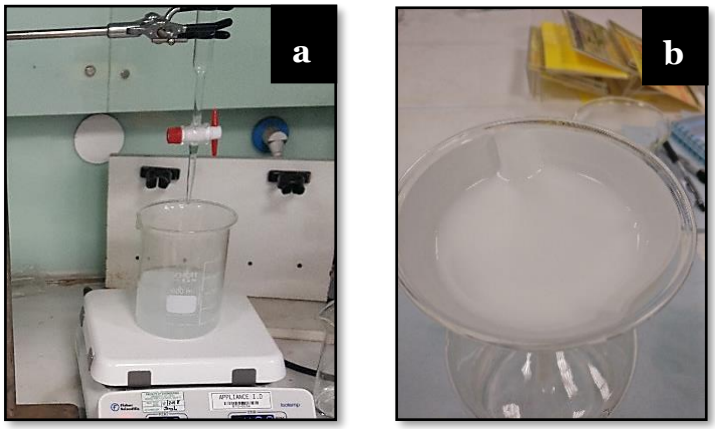

FIGURE 3.1 - Experimental setup for preparation (a) un-doped Dicalcium Phosphate Dihydrate minerals and (b) filtration process.

3.1.2 Chitosan Stock Solution

Synthesis of 3 wt.% CS stock solution was prepared by dissolving CS flakes (3100000 – 3750000 Da, > 75 % deacetylated) in a 2 (v/v)% acetic acid solution under continuous stirring for 24 hours. The resulting transparent solution was covered with aluminium foil and left to stand overnight to allow air bubble in the solution to move to the surface. The CS stock solution was stored in an airtight plastic container and was utilised within one week.

3.1.3 Dicalcium Phosphate Dihydrate Loaded Chitosan Solutions

Synthesis of CS solutions loaded with DCPD were prepared by adding different quantities (20, 30, 40 and 50 wt.%) of DCPD to CS stock solutions under continuous stirring. The solutions were left mixing for 6 hours to ensure even distribution of the mineral.

3.1.4 Freeze Drying Process

Measured amounts (1 ml) of un-loaded and DCPD loaded CS solutions were frozen at – 80 °C for 24 hours (Figure 3.2(a)). The frozen samples were then subsequently freeze-dried for 24 hours, as seen in Figure 3.2(b-c). All synthesised freeze-dried samples are displayed in Table 3.2 with corresponding sample code names.

FIGURE 3.2 - Preparation of freeze-dried chitosan samples, (a) frozen mineral loaded (20, 30, 40 and 50 wt.%) chitosan solutions, (b) image of the freezer drier utilised and (c) close-up of the freeze-drying process.

3.1.5 Alkaline Treatment

The freeze-dried samples were treated with 1M sodium hydroxide (NaOH) for 5 minutes to reduce the dissolution rate of CS. The NaOH treatment forms new hydrogen bonds leading to increased stability in aqueous environments. The samples were removed with metal tweezers and blotted onto Whatman Grade 44 filter paper to remove any excess NaOH residue. The treated samples were then washed several times with distilled water to ensure traces of NaOH were removed.

TABLE 3.2 - Summary of the synthesised Dicalcium Phosphate Dihydrate mineral and freeze-dried scaffolds.

Code	Description	Chemical Formula	CS : DCPD
DCPD	Dicalcium Phosphate Dihydrate	$CaHPO_4 \cdot 2\ H_2O$	0 : 100
CS	Chitosan	$(C_6H_{11}NO_4)_n$	100 : 0
20-DCPD	Mineral loaded scaffold	-	80 : 20
30-DCPD	Mineral loaded scaffold	-	70 : 30
40-DCPD	Mineral loaded scaffold	-	60 : 40
50-DCPD	Mineral loaded scaffold	-	50 : 50

3.2 Cerium Oxide Nanoparticles Synthesis

3.2.1 Freeze Dried Nanoparticles

The cerium oxide nanoparticles were synthesised via a hydroxide mediated method where Cerium Nitrate Hexahydrate ($Ce(NO_3)_3 \cdot 6H_2O$) was used as a precursor. Briefly, 10.85 g $Ce(NO_3)_3 \cdot 6H_2O_{(s)}$ was dissolved in 250 ml distilled water under continuous stirring for 20 minutes, resulting in a 0.1 M Cerium (solution A). Then 0.3 M NaOH solution was added dropwise under constant stirring to solution A at 50 ˚C to synthesis cerium oxide nanoparticles as shown in Figure 3.3(a) (equations 3.2 to 3.4). The solution was covered with aluminium foil and left at 50 ˚C under continuous stirring for 24 hours (Figure 3.3(b)). The nanoparticles were filtered using Whatman Grade 44 filter paper containing 1 µm pores and washed three times with distilled water and ethanol (Figure 3.3(c)). The collected nanoparticles were frozen at – 80 °C for 24 hours and then placed into a freeze drier for 24 hours.

$$Ce(NO_3)_3\ 6\ H_2O + 3\ NaOH \rightarrow Ce(OH)_3 + 3\ Na(NO_3) + 6\ H_2O \qquad \text{eq (3.2)}$$

Precipitation: $Ce^{3+} + 3\ OH^- \rightarrow Ce(OH)_{3\,(s)}$ eq (3.3)

Oxidation: $4\ Ce^{3+} + 12\ OH^- + O_2 \rightarrow 4\ CeO_{2\,(s)} + 6\ H_2O$ eq (3.4)

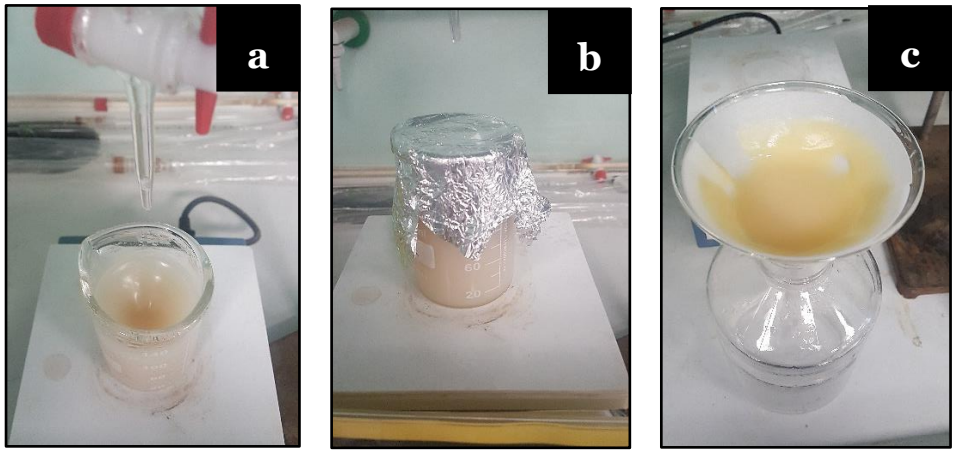

FIGURE 3.3 - Experimental setup for cerium oxide synthesis (a) addition of 0.3 M NaOH solution, (b) solution left for 24 hours under continuous stirring and (c) filtration and washing process.

3.2.2 Furnace Dried Nanoparticles

The hydroxide mediated synthesised, and washed nanoparticles were placed in a furnace at 80 °C for 24 hours to dry. Thermal analysis of the furnace dried powder was used to determine the optimal calcination temperature. All synthesised cerium oxide nanoparticles are presented in Table 3.3 with sample code names, corresponding formulas, and synthesis method.

TABLE 3.3: Summary of commercial and synthesised nanoparticles with the post-synthesis cryo and thermal treatments.

Code	Description	Chemical Formula	Synthesis
RNP3	Cerium Phosphate	CeO_4P	Alfa Aesar, CAS: 13454-71-2
RNP4	Cerium Oxide	CeO_2	Sigma-Aldrich, CAS: 1306-38-3
FRNP	Freeze Dried	-	Hydroxide mediated approach then freeze-dried
FUNP	Furnace Dried	-	Hydroxide mediated approach then dried @ 80°C
C280	Calcined @ 280°C	-	Heat treatment of FUNP (280°C, 2 hours)
C385	Calcined @ 385°C	-	Heat treatment of FUNP (385°C, 2 hours)
C815	Calcined @ 815°C	-	Heat treatment of FUNP (815°C, 2 hours)

3.3 Characterisation Methods

3.3.1 Fourier Transform Infrared Spectroscopy

Principle: Infrared spectroscopy is commonly used to investigate the functional groups of molecules by passing infrared radiation through the sample. At specific wavelengths, sample molecules selectively absorb the radiation causing a change in the dipole moments of the sample molecules. The vibrational energy levels of the sample molecules change from ground to excited state, and the vibrational energy gap is related to the frequency of the absorption peaks. The number of FTIR peaks signifies molecular vibrations that produce a change in the dipole moments and are thus observed as signals in the FTIR spectra. If there are no dipole changes, then no peaks will be formed. For Attenuated Total Reflection (ATR) FTIR, samples can be analysed

without dilution, i.e., liquids, pastes and solids. The ATR crystal has a higher refractive index than the sample being investigated. Good contact should be made between the sample and the ATR crystal. The infrared light (IR) from the FTIR is passed through the ATR crystal, causing the IR light to be reflected internally and partially absorbed by the sample. The reflected IR light contains absorption information of the sample and is collected by the detector forming the FTIR spectra.

Sample Analysis: The molecular vibration spectroscopic analysis of synthesised scaffolds and nanoparticles were analysed and characterised by using the Vertex 70 FTIR spectrometer in the attenuated total reflection mode (ATR). A KBr beam splitter and a MIR light source was utilised. Each sample was scanned 32 times in the 400 – 4000 cm^{-1} range at a spectral resolution of 4 cm^{-1}.

3.3.2 Ultraviolet-Visible Spectroscopy

Principle: UV-VIS spectroscopy is often used to determine organic and inorganic compounds in a solution. UV-VIS and FTIR are based on the principle of the interaction of light with matter and corresponds to Beer-Lambert's Law:

$$A = log\frac{I_0}{I} = \mathcal{E}CL \qquad \text{eq (3.5)}$$

The law refers to the absorbance of monochromatic light when passed through a solution. A corresponds to the absorbance, I_0 refers to the intensity of the light to the sample cell, I is the light departing from the sample cell, $\mathcal{E}$ refers to the molar absorptivity, C is the concentration of the solute and L is the length of the sample cell [269].

Sample Analysis: The PerkinElmer®, LAMDA 950 UV/VIS/NIR Spectrometer (Figure 3.4) was used to characterise unloaded and DCPD mineral loaded CH solutions and homogeneous clear suspensions of nanoparticles in deionised water. The absorption spectrum data was collected between 190 and 600 nm. The Tauc equation (equation 3.6) was used to determine the bandgap energy E_g between valence and conduction bands of the nanoparticles spectrophotometrically:

$$\alpha h v = A (h v - E_g)^{0.5} \qquad \text{eq (3.6)}$$

Where A is the absorption, α the absorption coefficient, hv the photon energy (1240/λ), and E_g is the bandgap. The bandgap energies were determined from the x-axis values of the intersections of $(\alpha hv)^2$ vs hv plots.

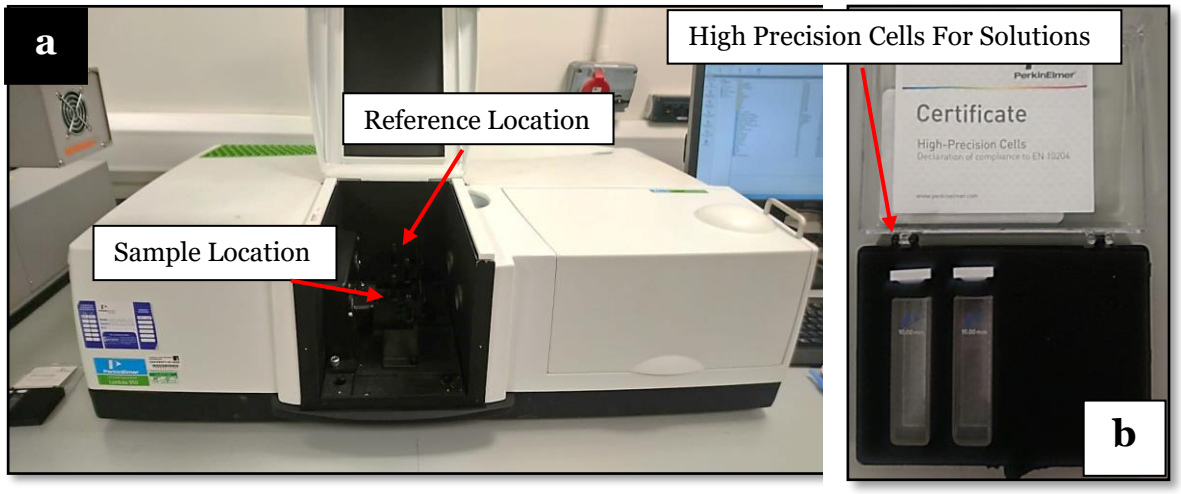

FIGURE 3.4 - The PerkinElmer®, LAMDA 950 UV/VIS/NIR Spectrometer, (a) layout of the spectrometer, (b) the reference and samples cells used for solution characterisation.

3.3.3 X-ray Diffraction

Principle: X-ray diffraction is a non-destructive analytical technique used to characterise crystalline and partially crystalline materials. XRD with Rietveld analysis is utilised for quantitative phase composition, crystallite size, microstrain, crystal structure, unit cell parameters and Bravis lattice symmetry analysis of the samples. Figure 3.5(a) shows an overview of the XRD equipment utilised. The main components of a standard XRD diffractometer consist of an (i) x-ray tube, (ii) detector and (iii) a sample holder. X-rays are formed when high-speed electrons collide with a metal target, usually copper (Cu).

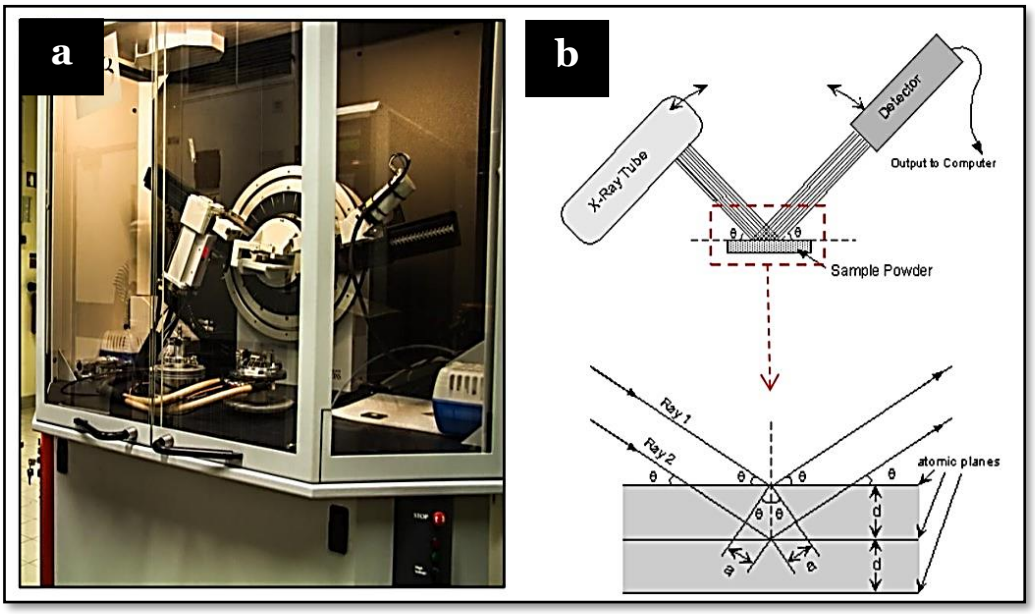

FIGURE 3.5 - X-ray diffraction analysis, (a) Bruker D8 xx-ray diffractometer, (b) constructive interference and the principle of Braggs Law [270].

The collision causes secondary electrons to be removed from the electron shells; thus, higher energy electrons move to fill the space, and the energy difference is released as

x-rays. The beam of x-rays is filtered to form monochromatic radiation required for diffraction and is focused onto the sample. If Braggs law depicted in Figure 3.5(b) (eq. 3.7) is satisfied via constructive interference, then x-ray diffractions from the sample are measured, and the data is collected in the form of a diffraction graph.

$$n\lambda = 2\,d\sin\theta \qquad \text{eq (3.7)}$$

Where n is related to the "order" of reflection, i.e., path difference in whole number of wavelengths, λ being the wavelength of the incident x-rays, d is the interplanar spacing of the crystal, and θ is the angle of incidence. Phase identification is achieved by comparing the peak positions and intensities of the experimental diffraction pattern against a library of 'standard' diffraction data of known crystalline or semi-crystalline materials.

3.3.3.1 Crystallite Size of Minerals

Principle: The crystallite size for the synthesised samples can be estimated from the line broadening of the (1 1 1) and the (0 2 0) peaks for cerium oxide nanoparticles and DCPD mineral, respectively, using the Scherrer equation. However, Scherrer's equation (B_D) (e.g. 3.9) does not consider all the XRD diffraction peaks nor the broadening due to microstrain within the crystal structure (eq 3.8). As a comparison, the Williamson-Hall method (eq 3.12) is used to calculate the average crystallite size of the samples; this method considers the peak broadening due to crystalline size B_D but also the broadening due to lattice strain and lattice defects B_E i.e:

$$B_{Total} = B_D + B_E \qquad \text{eq (3.8)}$$

Peak broadening due to crystallite size B_D is found by the Debye Scherrer equation hence:

$$B_D = \frac{K\lambda}{D\cos(\theta)} \qquad \text{eq (3.9)}$$

Where λ refers to the incident instrument Cu $k\alpha_1$ radiation wavelength, D corresponds to the crystalline size, and K is a shape factor constant ~ 0.9. Lattice strain and defect induced peak broadening are related by:

$$B_E = 4\,\varepsilon\tan(\theta) \qquad \text{eq (3.10)}$$

Where B_E is the peak broadening related to strain and ε relates to the lattice strain; therefore, combining equations (3.9) and (3.10) gives:

$$B_{Total} = \frac{K\lambda}{D\cos(\theta)} + 4\,\varepsilon\tan(\theta) \qquad \text{eq (3.11)}$$

Since we know $\tan(\theta) = \sin(\theta) / \cos(\theta)$ thus equation (4) can be reduced to the Williamson-Hall equation:

$$B_{Total}\cos(\theta) = \frac{K\lambda}{D} + 4\varepsilon\sin(\theta) \qquad \text{eq (3.12)}$$

It can be assumed that strain is uniform for all crystallographic directions; hence the lattice strain value and crystallite size for all nanoparticles and DCPD mineral can be deduced from the slope and Y-intercept of $B_{Total}\cos(\theta)$ verses $4\varepsilon\sin(\theta)$ plots, respectively.

Sample Analysis: A D8 X-ray diffractometer using the K_α radiation of Cu (λ = 0.15406 nm) was used to characterise the synthesised freeze-dried scaffolds and cerium oxide nanoparticles. The samples were analysed in the Bragg angle (2θ) scanning range of 10° to 80° at a scan speed of 0.014° s^{-1} and step size of 0.065°. All recorded patterns were analysed using the HighScore Plus software, and the Reitveld refinement was employed for peak shape and intensity analysis for ascertaining the crystallinity of samples

3.3.4 Raman Spectroscopy

Principle: Raman spectroscopy is known as a light scattering technique used to measure the vibrational energy modes of a sample. A monochromatic laser beam interacts with the molecules of the sample, causing light to scatter [271]. Inelastic scattering occurs when there is a transfer of energy between the molecule and the scattered photon; thus, the frequency of the scattered light is different compared with the incident light. The ratio of Stokes and Anti-Stokes Raman scattering is dependent upon temperature. Stokes Raman scattering occurs when the photon interacting with the molecule loses energy causing the wavelength of the scattered photon to increase.

However, Anti-Stokes Raman scattering occurs if the interacting molecule loses energy; hence, the wavelength of the scattered photon will decrease (Figure 3.6). A Raman spectrum is constructed through the inelastic scattering of light. Elastic scattering, also known as Rayleigh scattering, occurs if the molecule remains unchanged after interaction with the photon, whereby the energy and wavelength of the scattered photon are equal to the initial incident photon [272, 273].

Sample Analysis: Freeze-dried scaffolds and cerium oxide nanoparticles in solution and powder forms were analysed using a Renishaw inVia with incorporated microscope Raman spectrometer at a wavelength of 514 nm and operating at a power of 24.9 mW.

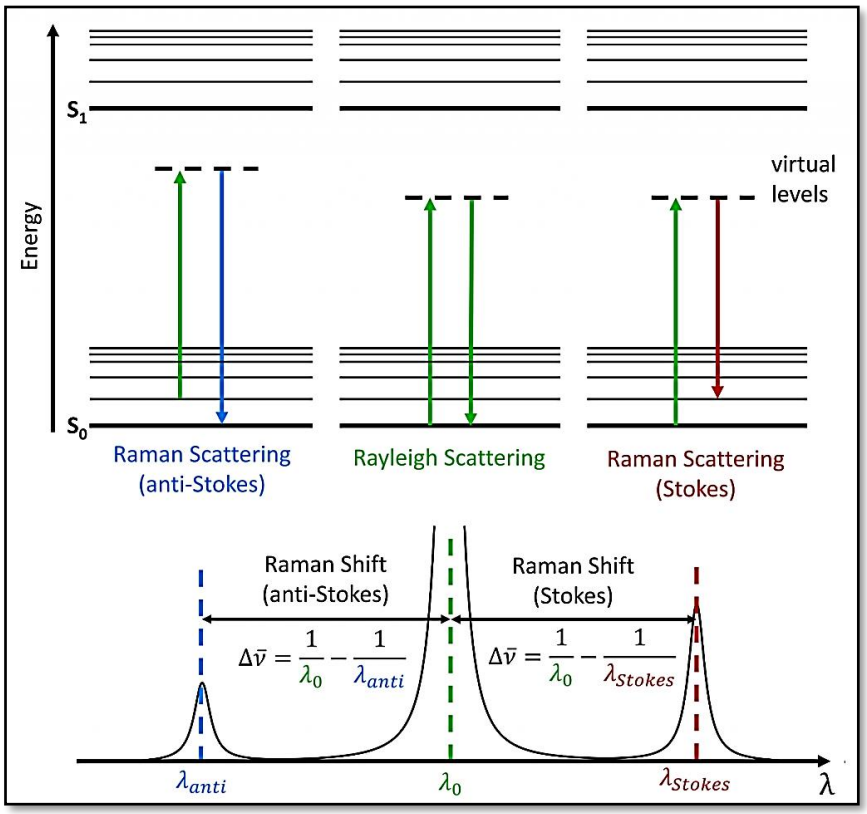

FIGURE 3.6 - Theory of Raman spectroscopy and the origin of Rayleigh, Stokes and Anti-Stokes Raman Scatter [272, 273].

3.3.5 Electron Microscopy

3.3.5.1 Scanning Electron Microscopy

Principle: SEM provides topographical, morphological, compositional and crystallographic information of materials. Electrons are accelerated and focused onto the sample by a series of lenses and apertures (Figure 3.7). Secondary and backscattered electrons create SEM images. The morphology and the topography of the samples are mapped by secondary electrons, whereas backscattered electrons illustrate the contrast in the composition. Inelastic collisions of the incident electrons with the atoms of the sample create X-rays when the excited electrons return to lower energy states. The X-rays do not lead to the volume loss of the sample; thus, SEM is considered as a non-destructive technique as the same sample can be analysed repeatedly.

Sample Analysis: The pore size and porosity of the unloaded and DCPD loaded freeze-dried scaffolds were characterised using the Hitachi SU8230 1-30kV cold field emission gun SEM. Prior to SEM, the samples were coated with 6 μm of Iridium to improve the electrical conductivity of the materials, thus enabled an improvement with regards to signal to noise ratio.

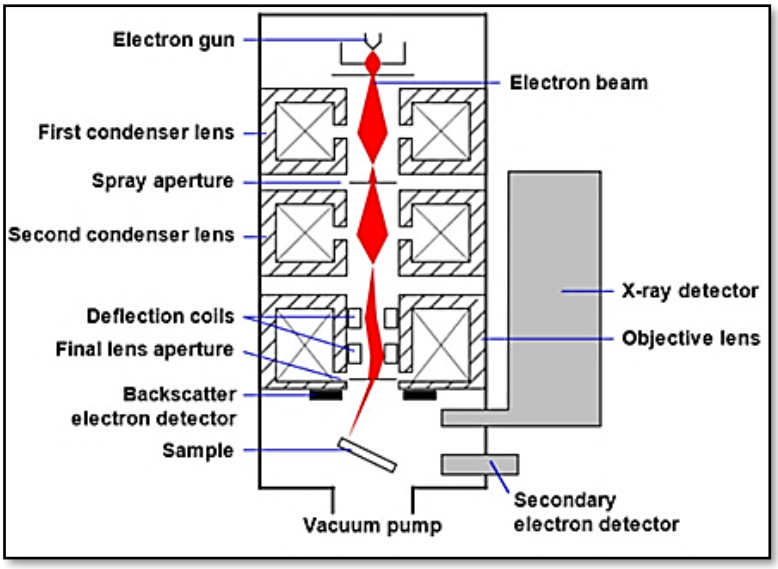

FIGURE 3.7 - Schematic of a scanning electron microscope where the main components are the electron source, a column containing electromagnetic lenses where electrons travel, detector, sample chamber and computer to display the images [274].

3.3.5.2 Transmission Electron Microscopy

Principle: Electrons are emitted from an electron gun and focused into a thin coherent Electron beam with the aid of a condenser lens. The beam of electrons is restricted by a condenser aperture where high angle electrons are excluded. The electron beam is transmitted through the sample; thus, the corresponding image is magnified and focused on a fluorescent screen, as depicted in Figure 3.8. X-rays formed from the interaction of the electron beam with the sample are detected by the energy dispersive spectrometer (EDS). The X-rays provide information relating to the elemental composition. In contrast, EELS focus on the inelastic electron scattering of the primary beam electrons with the electrons from the samples being analysed and provides information relating to the chemical bonding, valence, and condition bands within the sample.

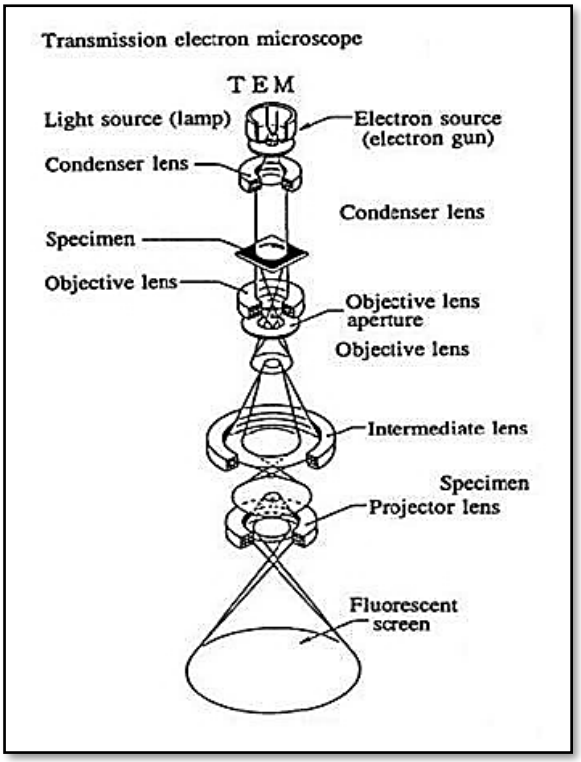

FIGURE 3.8 - Schematic of a transmission electron microscope [275].

Sample Analysis: For TEM analysis, the cerium oxide nanoparticles were prepared by ultrasonic dispersion in methanol after which several drops were placed onto holey carbon copper TEM grids. The particles suspended in methanol were then allowed to dry thoroughly using a heat lamp. The Titan Themis Cubed 300 TEM operated at 300 kV with high brightness X-FEG and Supertwin objective lens was used for the characterisation of the nano-scale size distribution and morphological analysis. The Bright field TEM images were collected using the Gatan OneView 16 Megapixel CMOS digital camera. Selected area electron diffraction (SAED) patterns, low magnification and dark-field (DF) TEM images were obtained for the analysis of the crystallinity of synthesised ceria. EELS using the Gatan GIF Quantum ER imaging

filter was used to collect low and high energy loss spectra to investigate the co-existence of two oxidation states (Ce^{3+} and Ce^{4+}) in the calcined nanoparticles.

3.4 Testing Methods

3.4.1 Thermal Properties

Principle: Thermal analysis of unloaded and DCPD mineral loaded freeze-dried scaffolds took place to investigate the decomposition of CS, and the effect of DCPD mineral addition to the thermal degradation process. Phase transformation occurs during heating as energy is required to break chemical bonds while forming bonds releases energy. Thus, bond formation and bond breakages are observed using Simultaneous Thermal Analysis (STA). STA refers to the combination of Thermogravimetry (TGA), and Differential Scanning Calorimetry (DSC) processes into a single instrument. Briefly, the reference (containing aluminium powder) and the sample (containing aluminium powder and the sample) crucibles were placed into the holders in contact with differential thermocouples used to detect temperature change. Endo and exothermal reactions take place when the sample temperature is higher or lower compared to the reference sample (Figure 3.9(a)). Figure 3.9 displays a typical thermal analysis graph (b) depicts the temperature change of the furnace, reference, and the sample against time while (c) shows the temperature difference against time with the differential thermocouple.

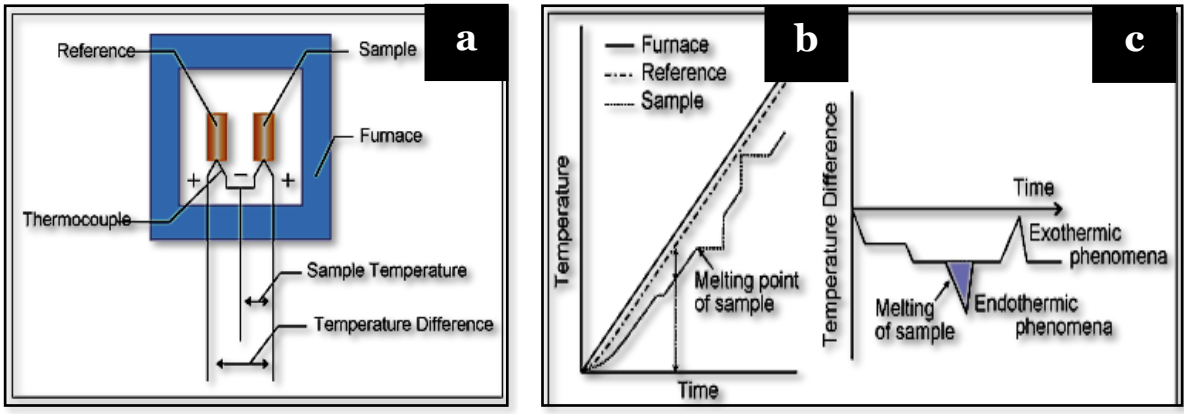

FIGURE 3.9 - Measurement principles of thermal analysis, (a) Block diagram of differential thermal analysis, (b) graph displaying the temperature change of the furnace and sample with respect to time and (c) temperature difference (ΔT) against time detected using a differential thermocouple [276].

Sample Analysis: Reactions and phase changes of freeze-dried scaffolds were investigated using the Perkin Elmer STA 8000. The thermal experiments were carried out from 30 to 600 ˚C. The Perkin Elmer STA 8000, which was used to study the phase transformation and chemical reactions covered the temperature heating range from 30˚ to 1000 ˚C. The thermal analysis characterisation of furnace dried ceria was essential for the optimisation of the calcination process without promoting the growth of nanoparticles. The isochronal heating rate of 20 ˚C min^{-1} was used to determine the optimal calcination temperature for the furnace dried nanoceria samples for comparative studies.

3.4.2 Surface Area

Principle: Brunner-Emmett-Teller theory (BET) is used to measure the surface area of solids and porous materials. The principle involves an estimation of the number of molecules required to cover the entire adsorbent surface with a single layer of adsorbed molecules, N_m. Therefore, the surface area is calculated by multiplying N_m, the cross-sectional area of the adsorbate molecules.

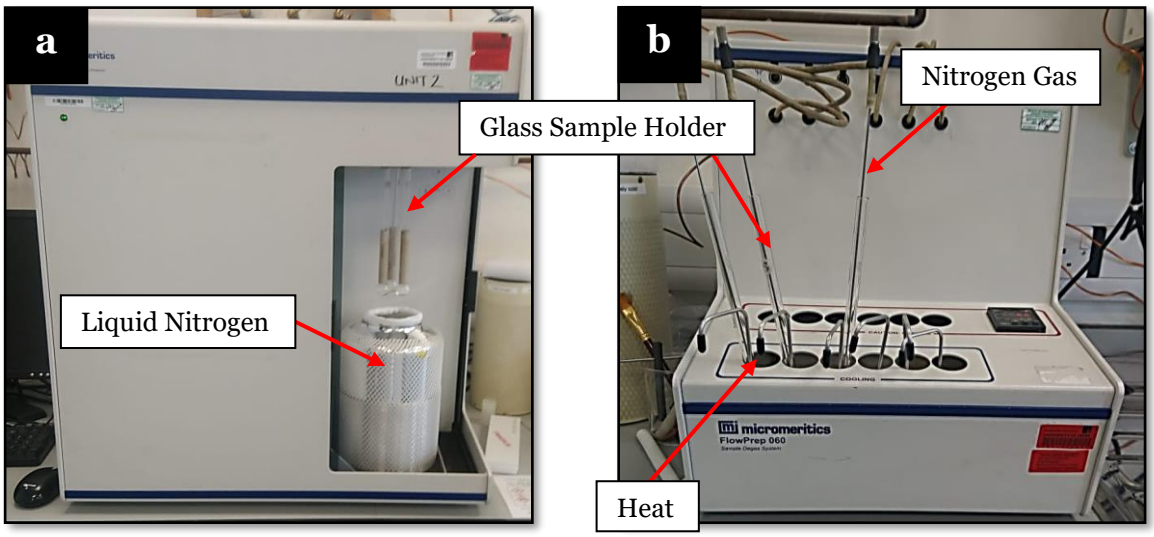

FIGURE 3.10 - Sample preparation and analysis equipment used to characterise the cerium oxide nanoparticles (a) Micromeritics Tristar 3000 equipment, (b) The FlowPrep™ 060 utilised to dry the cerium oxide nanoparticles as well as to remove any atmospheric contaminants.

Sample Analysis: Micromeritics Tristar 3000 was used to determine the BET surface area of the synthesised cerium oxide nanoparticles using the nitrogen absorption method in the powder bed. Measured amounts of nanoparticles in glass sample tubes were placed into the FlowPrep™ 060, as displayed in Figure 3.10, where

surface cleaning (degassing) was carried out; both heat and inert gas was applied to the samples for 30 minutes. This process allowed for the removal of any atmospheric contaminants, i.e. water and absorbed gas.

3.4.3 Swelling

Sample Analysis: Prior to the testing, all the freeze-dried samples were neutralised in 1 M NaOH solution for 15 minutes, after which the scaffolds were washed thoroughly using distilled water. Samples were dried at a temperature of 50 °C for 5 hours and weighed before the start of the experiment. The phosphate buffer saline (PBS) solution was formed by dissolving one tablet in 200 ml of deionised water, thus yielding a solution consisting of 0.01 M phosphate buffer, 0.0027 M potassium chloride and 0.137 M sodium chloride at a pH of 7.4. The solution was distributed into individual glass beakers, and the scaffold samples were submerged in this solution at 37 °C for 10 minutes. After removing the samples from the PBS solutions, excess liquid was removed using Whatman Grade 44 filter paper. The samples were re-weighed using an electronic balance. The swelling percentages (n = 3) of the freeze-dried scaffolds were calculated using:

$$Swelling\ \% = (\boldsymbol{W}_w - \boldsymbol{W}_d) / \boldsymbol{W}_d * 100 \qquad \text{eq (3.13)}$$

Where $\boldsymbol{W}_w$ and $\boldsymbol{W}_d$ are wet and dry weights of the samples, respectively.

3.4.4 Degradation Testing

Sample Analysis: The *in vitro* degradation of the freeze-dried scaffolds was assessed by submerging the samples into PBS solutions for four weeks at 37 °C. Each week the samples were removed from the solutions and dried for 24 hours at 50 °C. The samples were weighed and their masses recorded, fresh PBS solutions were prepared, and thus the samples were again submerged. This process continued for four weeks. The degradation percentage was calculated using:

$$\Delta W_d\,(\%) = (W_o - W_{d1})/W_{d1} * 100 \qquad \text{eq (3.14)}$$

Where W_o and W_{d1} refer to the initial sample weight and the sample weight at time *(t)*, respectively.

3.4.5 Apparent Density

Sample Analysis: Equation 3.15 determined the apparent densities *(ρ)* of 1 cm diameter and 1.5 cm height cylindrical freeze-dried scaffolds (n=3). Where *W* refers to the weight of the samples, *D* is the diameter and *H* relates to the height of the scaffolds. All measurements were taken three times using a Vernier calliper and averaged.

$$\rho = \frac{W}{\pi \left(\frac{D}{2}\right)^2 H} \qquad \text{eq (3.15)}$$

3.4.6 Porosity

Principle: The Gravimetric Principle is usually the most straightforward and quickest method to obtain a rough estimate of total porosity by determining the bulk and true densities of the material. The volume is calculated by measuring the length, width and heights of the synthesised scaffolds:

$$p_{scaffold} = \frac{Mass}{Volume} \qquad \text{eq (3.16)}$$

$$Total\ Porosity = 1 - \frac{p_{scaffold}}{p_{Material}} \qquad \text{eq (3.17)}$$

Where $p_{scaffold}$ corresponds to the apparent density of the scaffold and $p_{Material}$ corresponds to the density of the material [277]. The gravimetric method does not take into account the number and size of pores present in the scaffolds; thus can lead to significant errors [277, 278]. As a comparison, the Liquid Displacement [279] method was also utilised where the open porosity is calculated using the following equation:

$$Porosity = \frac{V_1 - V_3}{V_2 - V_3} \qquad \text{eq (3.18)}$$

Where V_1 relates to the known liquid volume, V_2 is the volume of liquid, including the impregnated scaffold, and V_3 refers to the liquid remaining when the scaffold is removed.

Sample Analysis: The displacement liquid must not be a solvent of the biopolymer; thus, ethanol was chosen as it can penetrate the pores easily without causing any shrinkage or swelling of the scaffolds. Briefly, the scaffold placed into a container of a known volume of ethanol and a series of evacuation and re-pressurisation cycles were performed to ensure the displacement liquid was forced into all the pores of the freeze-dried scaffolds. The scaffolds impregnated with ethanol were removed, and the remaining ethanol was measured.

3.4.7 Zeta Potential

Principle: Zeta potential is the electrokinetic potential measurement of colloidal systems and is affected by temperature, pH and additive concentration. The stability of the suspension is related to the magnitude of the zeta potential value. Systems with high negative or positive zeta potential values are generally stable due to the repulsive forces exceeding the attractive forces between the particles [280]. Conversely, systems with low zeta potential values are known to coagulate or flocculate due to the reduced repulsive forces.

Sample Analysis: The Melvern Zetasizer equipment with zeta potential cuvettes (cell DTS 1070) (Figure 3.11) was utilised to determine the zeta potential of unloaded and DCPD mineral loaded CH suspensions.

FIGURE 3.11 - The Melvern Zetasizer equipment used for zeta potential measurements.

3.4.8 X-ray photoelectron spectroscopy

Principle: The surface chemistry of the cerium oxide nanoparticles was analysed using x-ray photoelectron spectroscopy. X-rays irradiate the surface of the specimens causing the excitation of electrons in specific bond states. Sufficient energy causes the photoelectrons to be ejected with kinetic energy *(KE)* equal to:

$$KE = h\upsilon - BE$$

Where *BE* refers to the photoelectron binding energy and $h\upsilon$ is the energy of the photon. Many of the electrons inelastically scatter as they travel to the surface of the sample; however, some electrons undergo prompt emission and escape the surface of the material travelling into the surrounding vacuum [281]. The electron analyser measures the kinetic energy of the photo-ejected electrons and produces an energy spectrum of intensity versus binding energy. Each peak in the spectrum is related to a

specific element, and the number of atoms present in each element is proportional to the peak intensities [282, 283].

Sample Analysis: The nanoparticles (FRNP, FUNP, C280, C385 and C815) samples were prepared for XPS by sprinkling small amounts onto adhesive conductive carbon tape mounted on to the sample holders. The samples were sprayed with aerosol air to remove any loose particles before analysis. The nanoparticles were then characterised using the UHV XPS with a SPEC Phoibos 150 analyser and a SPECS XR50-M. Samples surveys were taken at pass energy of 50 Ev, and high-resolution scans were taken at 30 Ev. The data collected was analysed using Prodigy, CASAxps and Originpro.

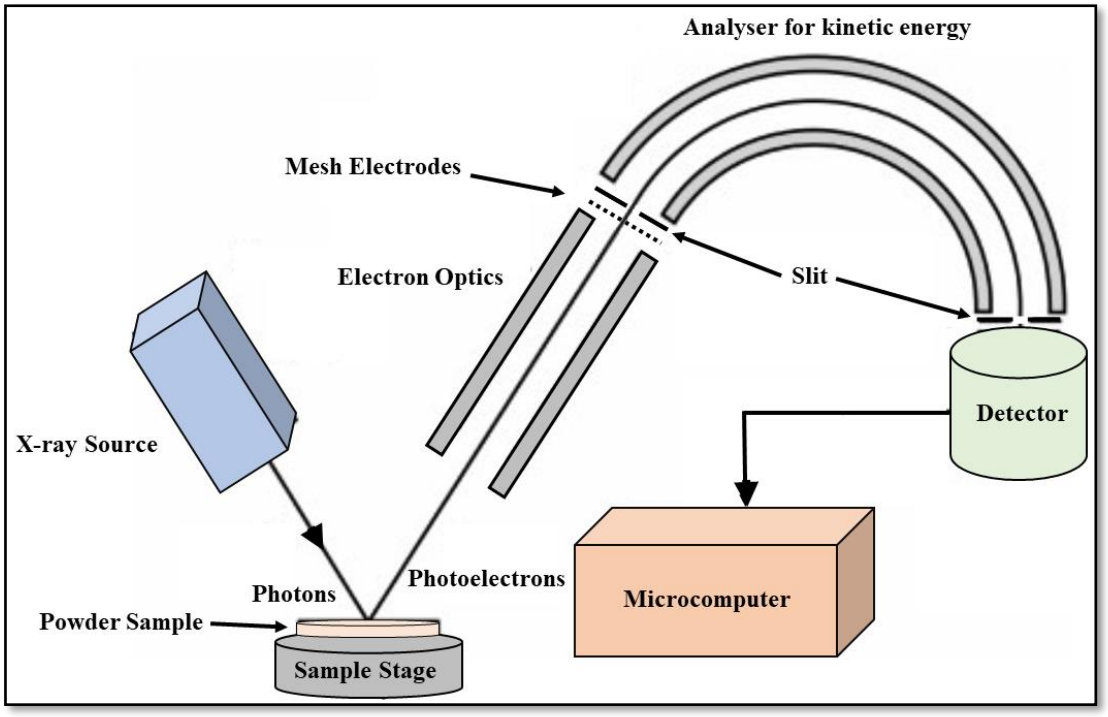

FIGURE 3.12 - Representation of the X-ray photoelectron spectroscopy components, concerning sample analysis where the material is irradiated with X-rays while the kinetic energy and the number of electrons are analysed under ultra-high vacuum conditions forming corresponding spectra adapted from [284].

3.4.9 Mechanical Testing

Sample Analysis: The Instron 5569 machine was utilised to mechanically test rectangular freeze-dried scaffolds with 5 x 1 cm dimensions (n=3). The scaffolds were sandwiched between pieces of polystyrene to prevent slipping and serve as an interface between the scaffolds and the tensile testing machine. The samples were tested with a 100 N load cell at a speed of 100mm/min with no pretension. Hence the tensile stiffness and tensile modulus were determined from stress-strain plots.

3.5 In vitro Osteoblast Studies of Freeze-Dried Scaffolds

Osteoblasts with cell line G292 were from frozen stock sourced from the Department of Oral Biology Leeds Dental School. The osteoblast cells were sustained in McCoy's 5A medium modified with L – glutamine and sodium bicarbonate liquid. The medium was additionally supplemented with 10 % foetal bovine serum (FBS) and 2 % of penicillin/streptomycin. The prepared medium was stored at 4 ˚C and used for up to one week before fresh media was prepared. Biocompatibility is an essential requirement for bone scaffolds; thus, cytotoxicity testing was performed on all freeze-dried scaffolds. See Appendix I for cell culture protocols.

3.5.1 Freeze-Dried Scaffolds Sterilisation Process

The synthesised (1 cm diameter, 0.5 cm height) freeze-dried scaffolds, i.e. CH, 20, 30, 40 and 50-DCPD tested during cell culture experiments, were initially sterilised with 70 % (v/v) ethanol and washed five times using Dulbecco's Phosphate Buffered Saline (DPBS). The second stage of sterilisation consisted of UV light exposure for 1 hour before testing. The sterilised freeze-dried scaffolds were handled aseptically throughout the testing procedures.

3.5.2 Contact Cytotoxicity Assay

The cytotoxicity testing involved attaching freeze-dried scaffolds in triplicate to 6-well culture plates with the aid of steri-strips [Medisave, cat no. R1540C]. The positive and negative controls consisted of steri-stips and 40% dimethyl sulfoxide (DMSO), respectively. DPBS-was used to wash the well plates for 10 minutes and aspirated and, to each well, 2 ml of osteoblast cell suspension containing 5 x 10^3 cells. All culture plates were incubated at 37 ˚C for 48 hours in 5 % (v/v) CO_2 in an incubator. After 24 hours, the media was aspirated from the wells and washed twice with DPBS. 1 ml of 10 % (v/v) neutral-buffered formalin (NBF) was added to each well and incubated for 15 minutes. The formalin was aspirated and, all wells were stained for 5 minutes using Giemsa solution and subsequently washed using water. The culture plates were air-dried for 24 hours and examined microscopically to record any changes in morphology, confluency, attachment and detachment of the osteoblast cells using an Olympus IX 7 Inverted Microscope under bright field illumination (CellB software; Olympus). All images were collected digitally.

3.5.3 DNA Quantification Assay

The cell attachment and proliferation testing involved adding 1 ml of 3 % (m/v) sterilised agarose gel into 24-well plates and allowed to set. Using a 1 cm diameter metal stamp the solid agarose was removed from each well; thus, restricting the remaining well area only to allow 1 cm diameter freeze-dried samples (n = 3) to fit. Freeze-dried samples added to the well plates were washed using DPBS and aspirated to ensure all the wells were free from any small regiments of agarose pieces. 1 ml of osteoblast cell suspension containing 10^4 cells, were added to each well and incubated for 1, 3 and 7 days. The media was changed every two days.

Cell proliferation examined using Quant-iT™ PicoGreen™ dsDNA Assay Kit was performed according to the manufacturer's instructions. Briefly, the samples were washed three times with DPBS, and the cells extracted with lysis solution (0.2 % (v/v) Triton x-100, 10 mM Tris-HCl, 1mM EDTA, pH 7.4) for 1 hour on a gyratory shaker. 100 µl of the PicoGreen dsDNA quantification reagent was diluted to 1:200 and added to a 96-well plate containing 100 ul of the cell lysate solutions. The DNA standard curve prepared via serial dilutions of the Lamda DNA standard in TE buffer (10mM Tris-HCl, 1mM EDTA, pH 7.4), was added to the 96-well plate instead of the sample lysis solutions in addition to 100 ul of the PicoGreen solution. The 96-well plate was incubated in the dark for 5 minutes before the absorbance was measured using a Thermo Scientific Varioskan Flash plate reader excitation 480 nm and emission at 520 nm. All the data collected were calibrated using the DNA standard curve.

3.5.4 Statistical Analysis

Triplicates of *in vitro* cellular experiments were conducted, where the data collected underwent statistical analysis and displayed as mean ± standard deviation (SD). The graphs and statistical analysis were performed using MS Excel software. Significant statistical differences were analysed using one-way analysis of variance (ANOVA) between the average of two or more results. Values of $p \leq 0.05$ were considered as statistically significant.

3.6 Antibacterial Testing of Cerium Oxide Nanoparticles

The nanoparticles tested during the bacterial experiments were sterilised inside an autoclave by suspending the particles in a Brain Heart Infusion (BHI) Broth and, once cooled were used within the hour. Optical density-and Colony Forming Units (CFUs) were carried out to assess the antibacterial characteristics of the nanoceria over 48 hours. An initial Optical Density OD_{600} of 0.015 was selected and was kept constant for all experiments to ensure reproducibility.

3.6.1 Brain Heart Infusion Agar Plates and Broth

Brain Heart Infusion (BHI) agar plates were prepared following the manufacturer's procedure which is described briefly; 52 g of BHI agar powder was mixed in 1 litre of distilled water and boiled to dissolve the medium completely. The solution was sterilised inside an autoclave at 121 ˚C for 15 minutes; once the agar solution had cooled, it was poured into a set of sterile agar plates under aseptic conditions which were left to solidify. The agar plates were then stored at < 4 ˚C until they were required. The BHI broth was prepared by dissolving 37 g of broth powder in 1 litre of distilled

water and boiled to dissolve the medium completely. The broth was autoclaved at 121 ˚C for 15 minutes to sterilise and once sufficiently cooled stored in a refrigerator < 4 ˚C for future experiments.

3.6.2 Growth of Bacterial Strains

Bacterial stock cultures of *Escherichia coli*, *Staphylococcus epidermis* and *Pseudomonas aeruginosa* were procured from a stock of 30 % glycerol solutions kept at – 80 ˚C. 10 µl sterile loops were used to streak *Staphylococcus epidermis*, *Pseudomonas aeruginosa* and *Escherichia coli* onto BHI agar plates. Inoculated plates were all incubated at 37 ˚C for 24 hours, after which a single colony was picked from each bacterium type and grown in 25 ml of BHI broth in an incubator at 37 ˚C 150 rpm for 24 hours. This process enabled the production of fresh bacterial suspension for further use by inoculation.

3.6.3 Optical Density Measurements

Optical density (OD) measurement is a widely used method to assess the number of growing bacteria in a culture; thus, the absorbance values of bacterial suspensions can be measured using a photometer [285]. The initial optical density of each bacterial type was measured using the Jenway 6305 UV/Visible Spectrophotometer at 600 nm (OD_{600}). To ensure reproducibility, each bacterium was diluted to an OD_{600} of 0.015 [286, 287] using BHI broth. Triplicate bacterial solutions for each bacterium were produced, and the growth rate without the addition of the nanoparticles was measured at 2, 4, 24 and 48 hours (OD_{600}). To investigate the antibacterial properties of selected nanoparticles (FRNP, C385 and C815) various concentrations (50, 100, and 200

µg/ml) of sterilised nanoparticles suspended in BHI broth were added to the bacterial suspensions OD_{600} of 0.015. The OD_{600} was measured after 2, 4, 24, and 48 hours and compared with the optical density measurements of bacterial suspensions containing no nanoparticles; the average values $\pm$ SD are reported.

3.6.4 Determination of Colony Forming Units

Counting colony-forming unit (CFU) was used to estimate the bacteria growth concentrations before and after exposure to the cerium oxide nanoparticles. The CFU for each bacterium without the addition of the cerium oxide nanoparticles was calculated for each time point, i.e. 2, 4, 24 and 48 hours. Serial dilution was performed by adding 900 µl of BHI broth into labelled plastic vials (1 to 8); following this, 100 µl of cultured bacteria was added to the vial labelled vial-1 (highest concertation) and vortexed to ensure even distribution of the bacteria. Next, 100 µl of the bacterial solution was taken from the highest concentration vial and placed into the vial labelled vial-2 and vortexed; the same procedure was continued until all the labelled vials had been diluted with the cultured bacteria.

BHI agar plates were labelled, and 100 µl was taken using a pipette from the lowest concentrated vial, i.e. vial-8 and placed into the centre of the labelled Petri dish-8. A plastic spreader was used to spread the bacteria solution over the surface of the set agar, and the procedure was repeated for all the serially diluted vials. All agar plates were incubated at 37 ˚C for 24 hours. Previous steps were repeated for all nanoparticle concentrations 50, 100 and 200 µg/ml. The colony-forming unit was determined for each bacterium by selecting the incubated agar plates, which contained enough

individual bacteria cultures (between 30 to 300) to be easily counted. The number of single colonies was multiplied by the agar plate concentration to determine the overall colony-forming unit of the bacteria in the original culture per ml

3.7 Chapter 3 Summary

The unloaded and DCPD mineral loaded freeze-dried scaffolds and cerium oxide nanoparticles fabrication were described, including materials characterisation and testing techniques. The osteoblast and antibacterial testing methods are also included in this chapter. Furthermore, relevant equations required for the in-depth characterisation of the synthesised materials are reviewed.

Chapter 4
SCAFFOLDS RESULTS

4.0 Characterisation Results

4.0.1 X-ray Diffraction

The experimental XRD diffraction patterns for the DCPD, CH, 20, 30, 40 and 50-DCPD synthesised scaffolds are presented in Figure 4.1. The peaks from the obtained DCPD pattern match the reference standard XRD data for DCPD (JCPDS: 00-011-0293) compiled by the Joint Committee on Powder Diffraction and Standards (JCPDS). The main 2θ peaks for the DCPD standard are 11.60°, 23.39°, 29.16°, 35.45° and 47.84° corresponding to (0 2 0), (0 4 0), (-1 1 2), (-2 3 1) and (0 8 0), respectively. Notably, Dicalcium Phosphate Dihydrate is the only detectable phase expressed in the DCPD sample.

The partially crystalline polysaccharide CS has a characteristic XRD fingerprint associated by two broad 2θ peaks at ~10˚ and ~20˚ corresponding to crystal I and crystal II phase forms, respectively [288]. The less hydrated crystal I phase exhibits higher crystallinity, while the crystal II phase has a hydrated amorphous structure corresponding to intermolecular interactions of the aligned CS polymer chains. For the CH freeze-dried scaffold, two broad peaks at 9.2˚ and 20.2˚ are observed, and the lack of other peaks in the CH diffraction pattern signifies high CS purity. Increasing DCPD concentration caused a significant decrease in the CS crystal II phase form for the freeze-dried scaffolds containing DCPD mineral, which is expected due to the high crystallinity of DCPD mineral.

The diffraction patterns for 20, 30, 40 and 50-DCPD depicts evidence for the presence of semi-crystalline CS matrix combined with the characteristic crystalline diffraction

peaks associated with DCPD. As DCPD concentration increases, the partially crystalline CS structure becomes more crystalline, where the 50-DCPD diffraction pattern is similar to the DCPD spectra, as shown in Figure 4.1(a).

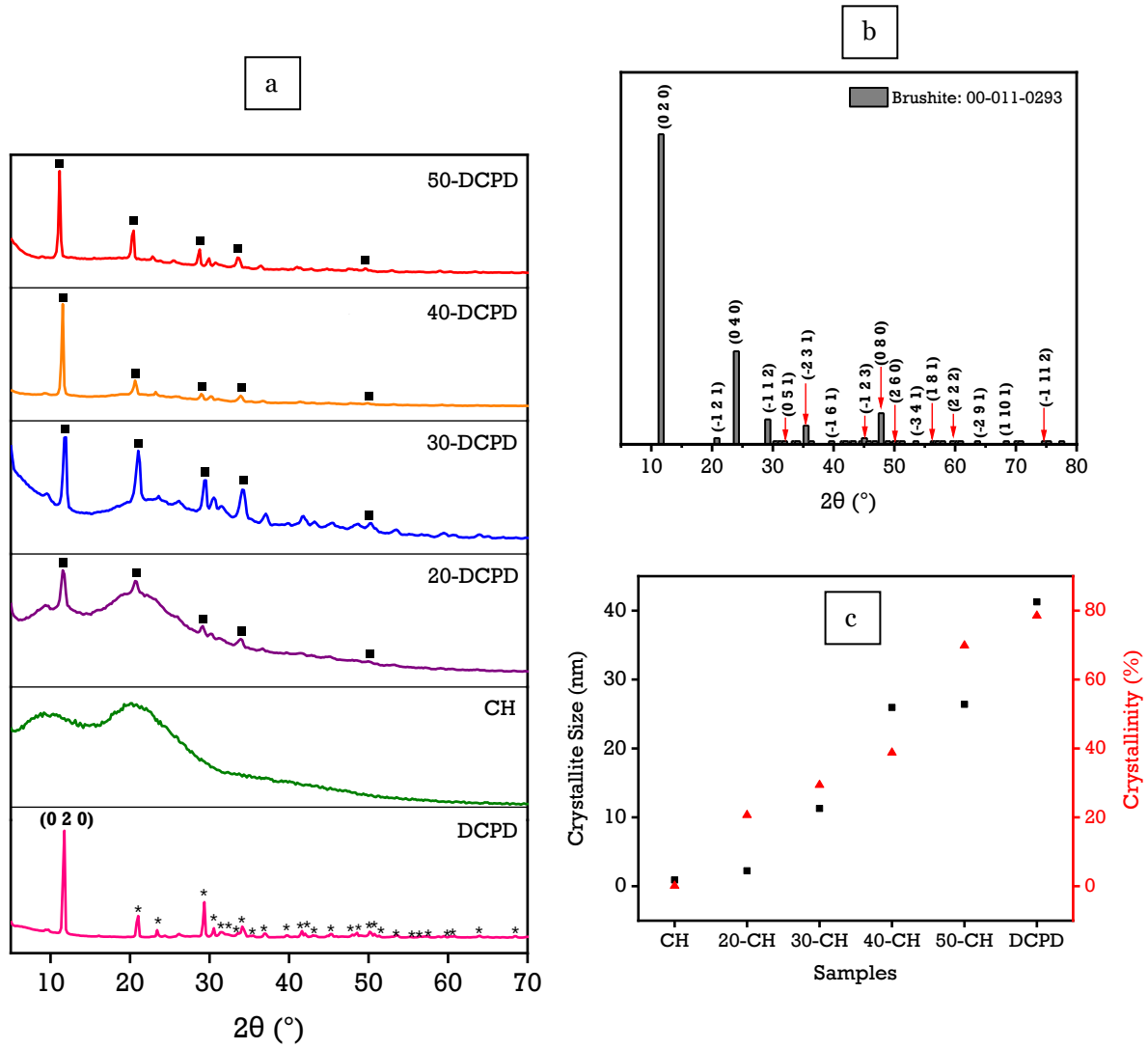

FIGURE 4.1 - Normalised X-ray diffraction data, (a) Experimental XRD spectra for DCPD, CH, 20, 30, 40 and 50-DCPD samples, (b) DCPD reference spectra and (c) graph depicting the relationship between crystallite size and crystallinity. * corresponds to Bragg 2θ diffraction peaks of DCPD while ■ corresponds to miller indices (0 2 0), (0 4 0), (-1 1 2), (-2 3 1) and (0 8 0) diffraction planes, respectively.

Rietveld Refinement was performed, and the crystallinity % of the scaffolds was calculated by subtracting the area of crystalline peaks from the total area of all peaks. The overall crystallinities of the freeze-dried scaffolds are displayed in Table 4.1. The crystallite size range for the synthesised scaffolds is determined from X-ray line broadening data using Scherrer's equation (Equation 3.9). The crystallite size is independent of crystallinity; however, based on the results displayed in Figure 4.1, both the crystallite size and crystallinity increase with increasing DCPD mineral concentration.

TABLE 4.1 - Summary of freeze-dried scaffolds with corresponding crystallite size and crystallinity %.

	Diffraction plane (h k l)			
Sample	(0 2 0)	(0 4 0)	Crystallite Size (nm)	Crystallinity (%)
CH	-	-	0.9059	0.1104
20-DCPD	11.53°	20.64°	2.2404	20.6399
30- DCPD	11.93°	21.04°	11.2882	29.3773
40- DCPD	11.53°	20.64°	25.9477	38.7656
50- DCPD	11.14°	20.44°	26.4008	69.8635
DCPD	10.97°	22.75°	41.2679	78.5123

4.0.2 Raman Spectroscopy

Raman spectroscopy was utilised to identify the characteristic bands relating to functional groups in the unloaded and DCPD mineral loaded freeze-dried scaffolds (20, 30, 40 and 50-DCPD); the spectra are displayed in Figure 4.2. There are

significant phosphate (PO_4^{3-}) vibrational modes associated with DCPD mineral [289] (Figure 4.2(a)). The highest frequency vibrational mode is located at 988 cm^{-1}, which relates to the P-O symmetric stretching of the PO_4^{3-} ion. The Raman peaks at 882 cm^{-1} and 1147 cm^{-1} [290] are assigned to the antisymmetric stretching modes of HPO_4^{2-}. Lower frequency vibrations of PO_4^{3-} are seen at 385 cm^{-1} to 420 cm^{-1}, and the 436 cm^{-1} to 590 cm^{-1} bands correspond to symmetric bending of P-O. Similar DCPD mineral Raman data are observed in the literature [289-291].

The following Raman peaks are associated with CS and are depicted in all the freeze-dried scaffolds; the -NH_2 symmetric and asymmetric stretching are displayed at 3200 cm^{-1} to 3450 cm^{-1}. The broad -OH stretching is observed at 3100cm^{-1} to 3200 cm^{-1}, and the -CH stretching is displayed in the 2880 cm^{-1} to 2990 cm^{-1} region. The Raman spectra of mineral loaded freeze-dried scaffolds (Figure 4.2(b-d)) depict a similar shape to the mineral free CH scaffold; notably, the main difference displayed is related to the peak broadenings and peak intensities in the 2800 and 3800 cm^{-1} range. As already confirmed by XRD in section 4.0.1, crystallinity is proportional to DCPD concentration; thus, the Raman peak broadening is likely to be attributed to the scaffolds increase in crystallinity [290]. The presence of the DCPD mineral peaks for the freeze-dried scaffolds (Figure 4.2(c)) is not entirely clear. Therefore, to further examine the structural changes occurring with increasing DCPD mineral concentrations, specifically the bands relating to the mineral phase, FTIR is utilised as described in section 4.0.3.

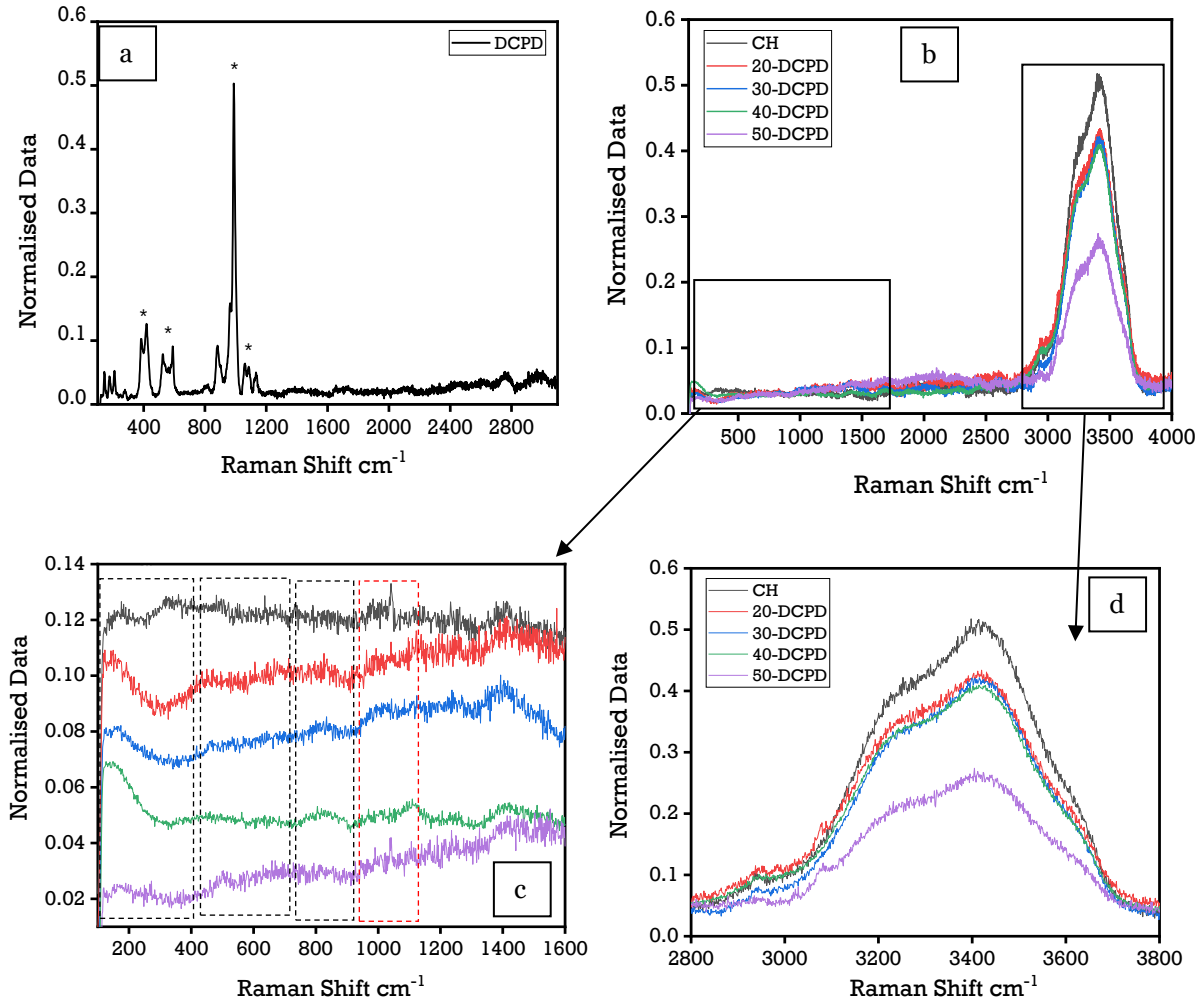

FIGURE 4.2 - Normalised Raman spectra, (a) Dicalcium Phosphate Dihydrate mineral (DCPD), (b) comparison of synthesised freeze-dried scaffolds in the 100 to 4000 cm^{-1} regions, (c) 100 to 2800 cm^{-1} region with 0.2 offset to observe the spectra individually and (d) 2800 to 3800 cm^{-1} region.

4.0.3 Fourier Transform Infrared Spectroscopy

The FTIR spectra of synthesised unloaded and DCPD mineral loaded freeze-dried scaffolds are presented in Figure 4.3(a). The FTIR bands associated with DCPD mineral are located at 511 cm^{-1}, 989 cm^{-1} and 1075 cm^{-1} which relate to PO_4^{3-} contributions. The bands located at 857 cm^{-1}, 1117 cm^{-1} and 1217 cm^{-1} correspond to the

contributions of HPO_4^{2-}. The freeze-dried CH scaffold presents broad transmission bands in the 3290 cm^{-1} and 2993 cm^{-1} regions, which are attributed to N-H and O-H bond stretching of the saccharide ring, respectively. The peak located at 2913 cm^{-1} relates to CH_2 symmetric/asymmetric pyranose ring vibrations. The amide stretching vibration C=O (amide I) depicted at 1625 cm^{-1} is directly related to the backbone conformation. The N-H bending vibration (amide II) is displayed at 1541 $cm^{-1,}$ and the C-N stretching vibration (amide III) corresponds to 1396 cm^{-1}. The peak at 1457 cm^{-1} relates to CH_3 deformation mode [292]. In contrast, the 1059cm^{-1} region correlates to C-O-C stretching vibration, which is dependent upon the crystallinity of chitosan. The saccharide structure of chitosan also exhibits a general reflection which may be associated with the > 846 cm^{-1} regions. The observations agree with previously reported data [293-296].

The DCPD mineral loaded freeze-dried scaffolds present similar FTIR spectra to the unloaded CH scaffold; this may be attributed to the CS amide (I, II and III), CH_3 and saccharide bands overlapping the HPO_4^{2-} and PO_4^{3-} peaks associated with DCPD mineral. The literature suggests that the CS protonated amino groups (NH_3^+) can form strong intermolecular interactions with the DCPD mineral phosphate groups (divalent HPO_4^{2-}, trivalent PO_4^{3-}) [297, 298]. Figure 4.3(b) displays the calculated areas of the amide I, II and III peaks, where a clear decreasing area trend is observed with increasing DCPD mineral concentrations (see Appendix II for peak analysis and further graphical representations). As the concentration of DCPD mineral increases, the number of divalent HPO_4^{2-} and trivalent PO_4^{3-} groups also increases, leading to a greater probability of interactions with protonated CS amino groups forming ionic crosslinking leading to the reduction of the calculated areas [299].

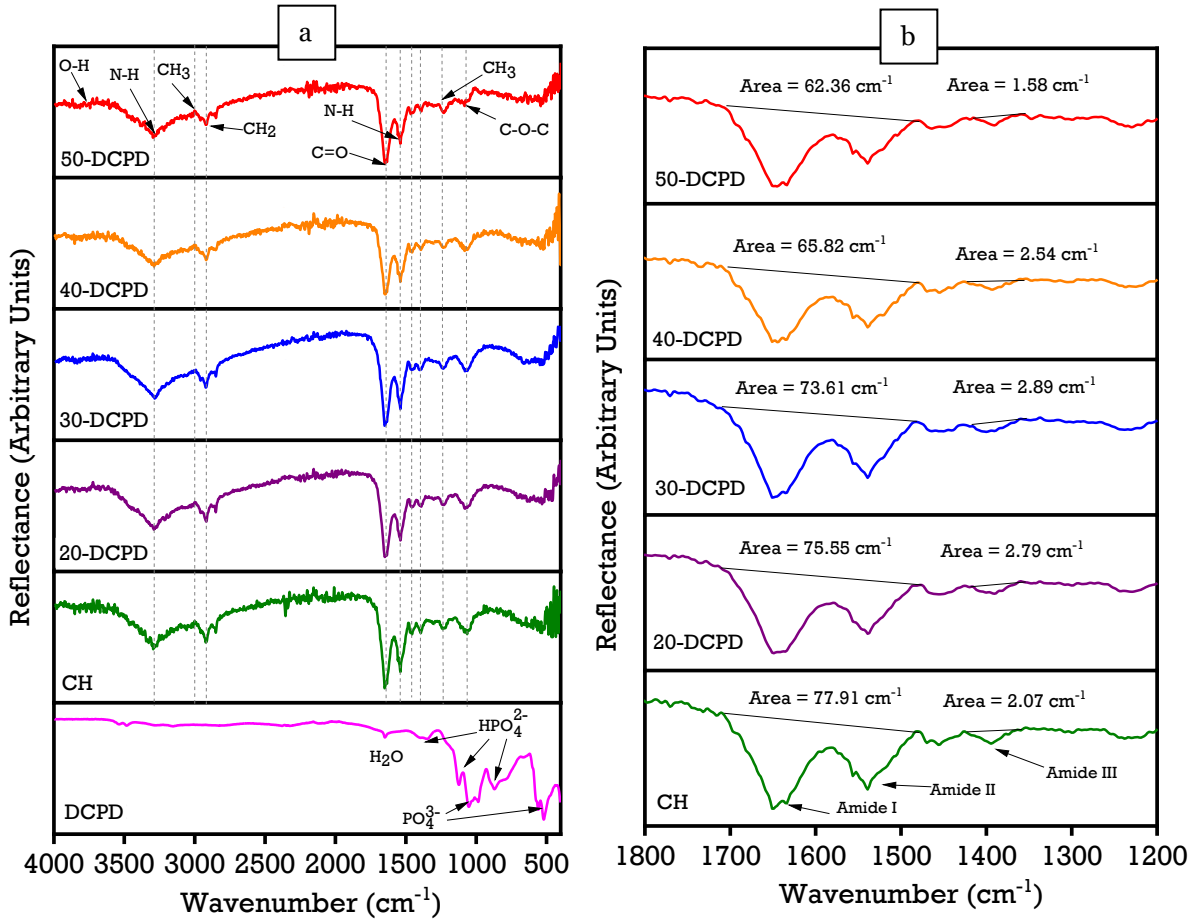

FIGURE 4.3 - Comparison of synthesised freeze-dried chitosan (CS) scaffolds containing varying concentrations of Dicalcium Phosphate Dihydrate (DCPD) mineral (CH, 20, 30, 40 and 50-DCPD), (a) Data obtained in the 400 cm^{-1} to 4000 cm^{-1} regions at a resolution of 4 cm^{-1} using the Vertex 70 FTIR spectrometer in attenuated total reflection mode, (b) comparison of the amide I, II and III peaks determined using OriginPro software.

4.0.4 Scanning Electron Microscopy

Figure 4.4 displays the SEM images porous architecture of the freeze-dried scaffolds fabricated using various concentrations of DCPD mineral (20, 30, 40 and 50 wt %). As depicted, increasing the DCPD mineral content affected the morphology and structural features of the scaffolds (See Appendix III for SEM images related to pore size measurements). The CH scaffold containing no DCPD mineral displays relatively

thick lamellae with a broad pore size distribution; the pore sizes range from 20 μm to 180 μm. The incorporation of DCPD mineral caused the pore size distribution and the lamellae thickness to decrease while the number of pores increased. Smaller pore size distributions enhance the surface areas of scaffolds by providing increased sites for cellular attachment. However, pore sizes < 50 μm have been found to limit cell migration, form cellular capsules, and in severe cases, lead to necrotic regions as the diffusion of nutrients and waste is restricted [28, 29]. Large pores > 1500 μm can lead to the reduction of the scaffold surface area, which has been found to limit the adhesion of cells [15]. Hence, pore size must be large enough to allow for the migration of cells throughout the scaffold but also small enough to allow cell binding to the scaffold [6, 300]. Furthermore, scaffolds containing larger pores exhibit limited mechanical properties due to an increase in the void volume.

The structural difference and increase in the number of pores are especially visible in comparison with the 20 and 30-DCPD scaffolds. The 30-DCPD scaffolds exhibits > 70 % more pores when compared to the 20-DCPD scaffold, with the majority of pores ranging from 20 μm to 160 μm. As the DCPD mineral concentration increased to $\geq$ 40 wt %, the shape of the pores became less defined, and the lamellae thickness further decreased, as demonstrated in Figure 4.4 (e). The reduction of lamellae sizes consequently caused many of the pores to combine; hence individual pores are no longer visible, as depicted in Figure 4.4 (f) for the 50-DCPD scaffold. Pore interconnectivity is essential as it encourages advanced cell seeding, growth, proliferation and cell migration of osteoblast cells into the entire polymeric scaffold [54, 119]. The 50-DCPD scaffold presents reduced pore interconnectivity due to the coalesces of many pores in addition to the creation of closed-ended pores which are

unfavourable to cell growth. Within the tissue engineering industry, the mean pore size for bone scaffolds has been investigated to be between 50 µm and 1500 µm [301, 302] with a minimum pore size range of 50 µm to 100 µm required to exhibit adequate bone and tissue regeneration [54, 303, 304].

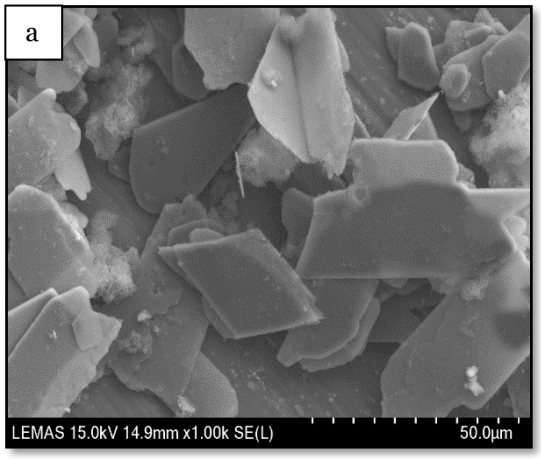

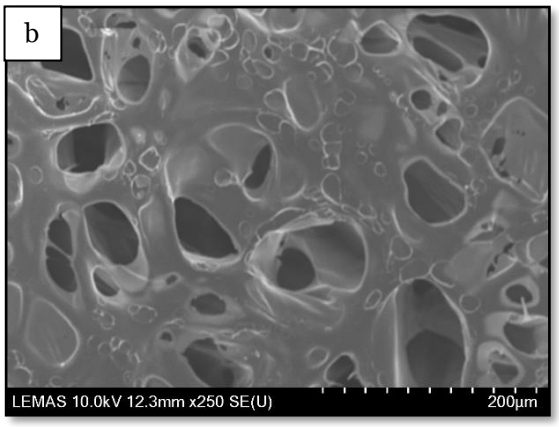

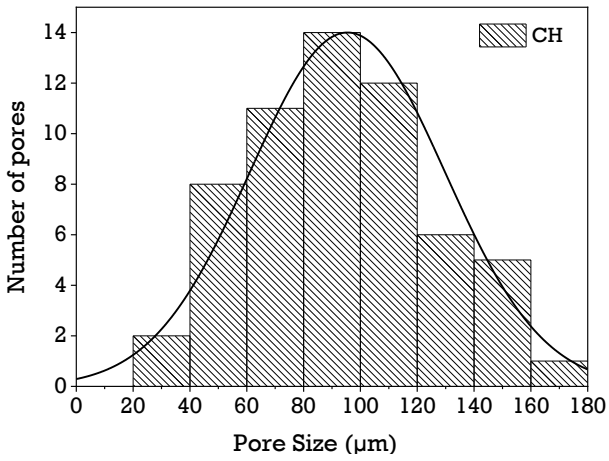

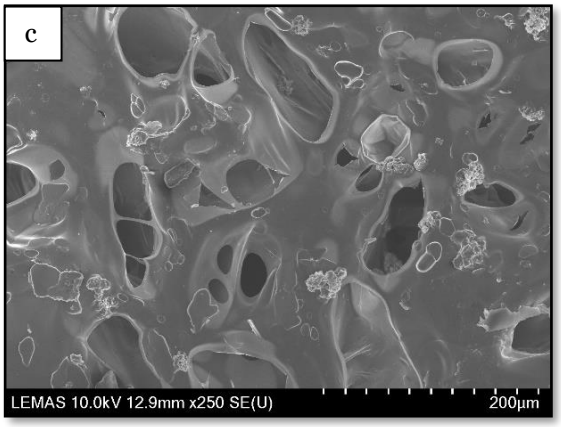
c
LEMAS 10.0kV 12.9mm x250 SE(U)
200µm

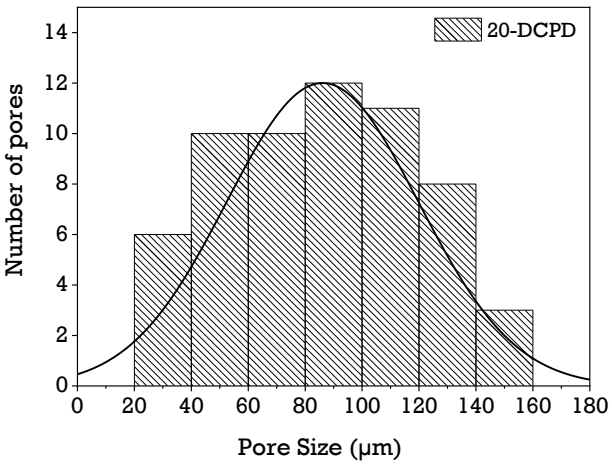
20-DCPD
Number of pores
Pore Size (µm)
0
2
4
6
8
10
12
14
0
20
40
60
80
100
120
140
160
180

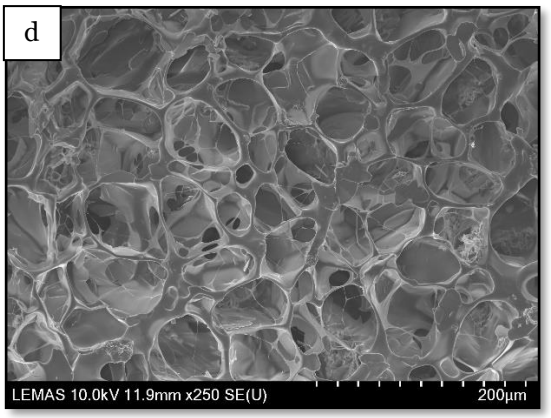
d
LEMAS 10.0kV 11.9mm x250 SE(U)
200µm

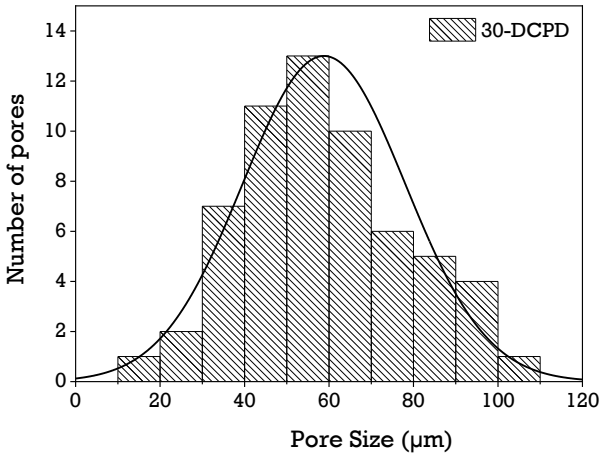
30-DCPD
Number of pores
Pore Size (µm)
0
2
4
6
8
10
12
14
0
20
40
60
80
100
120

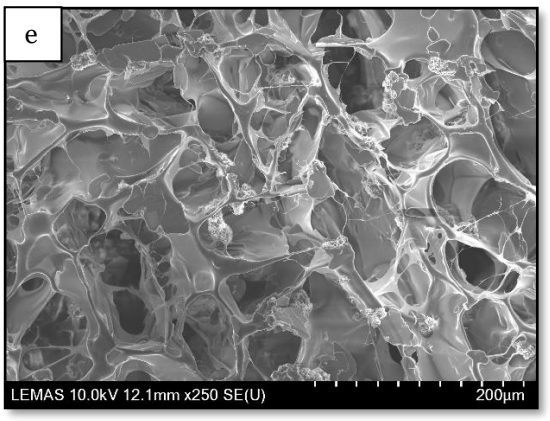
e
LEMAS 10.0kV 12.1mm x250 SE(U)
200µm

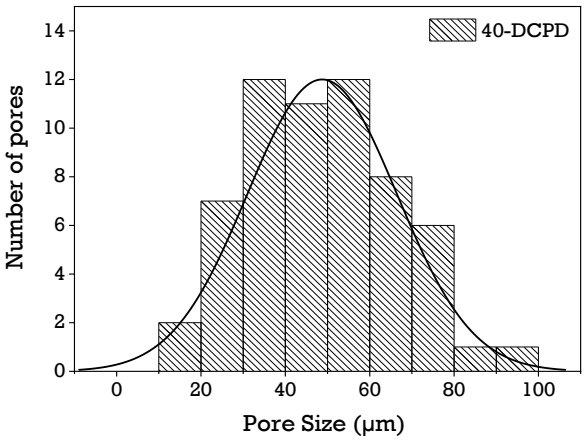
40-DCPD
Number of pores
Pore Size (µm)
0
2
4
6
8
10
12
14
0
20
40
60
80
100

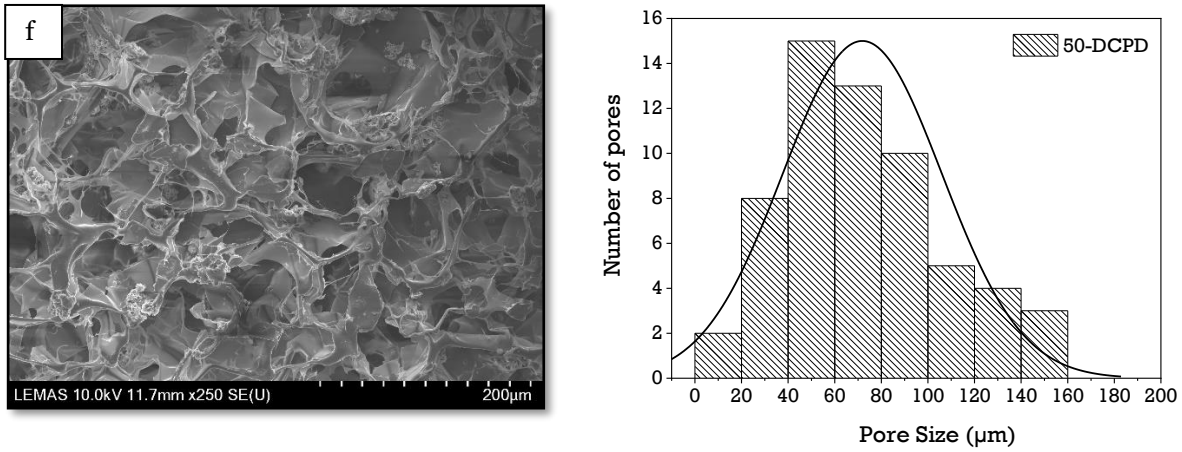

FIGURE 4.4 - Comparison of Hitachi SU8230 SEM images of freeze-dried chitosan (CS) samples containing Dicalcium Phosphate Dihydrate (DCPD) minerals, (a) DCPD mineral, (b) CH, (c) 20-DCPD, (d) 30-DCPD, (e) 40-DCPD, and (f) 50-DCPD.

4.1 Testing Results

4.1.1 Thermal Properties

Figure 4.5 displays the thermal analysis data of the all synthesised freeze-dried scaffolds. The observed initial temperature weight loss below 100 ˚C is attributed to the evaporation of moisture (water) from hydrophilic groups in the samples. The shoulder at approximately 120 ˚C expressed in all samples corresponds to the loss of adsorbed and bound water [55, 305, 306]. The CH, 20 and 30-DCPD scaffolds present similar downward slopes from 100 ˚C to 160 ˚C representing the beginning of the thermal degradation of CS, and the second weight loss observed at 160 ˚C to ~ 300 ˚C is attributed to the decomposition of the CS biopolymer chains [306]. With increasing DCPD mineral concentration, the weight loss % increases (Table 4.2). The CH scaffold presented the lowest total weight loss of 25 % compared to the DCPD mineral loaded scaffolds, while the 50-DCPD scaffold presents the highest weight loss of 50 % as

displayed in Table 4.2. High M_w CS is regarded as thermally stable [307, 308] due to the presence of extensive amount hydrogen bonding as compared with low/intermediate M_w CS. Therefore, the increase in weight loss for the DCPD mineral loaded scaffolds is likely attributed to the increasing presence of phosphate ions, forming electrostatic interactions with the protonated CS amino groups thus leading to more significant thermal degradation.

TABLE 4.2 - The thermal degradation of freeze-dried CS scaffolds from 30 ˚C to 310 ˚C.

Sample	Weight Loss (%)
CH	25
20-DCPD	30
30-DCPD	45
40-DCPD	48
50-DCPD	50

Monetite, also known as Dicalcium Phosphate Anhydrous, is formed via the dehydration of DCPD. Therefore, the endothermic peaks observed for the 40 (152 ˚C) and 50-DCPD (165 ˚C) scaffolds are attributed to the transformation of DCPD mineral to monetite (Equation 4.1).

$$2CaHPO_4\ 2H_2O\ (DCPD) \rightarrow 4H_2O + 2CaHPO_4\ (Monetite) \qquad \text{eq (4.1)}$$

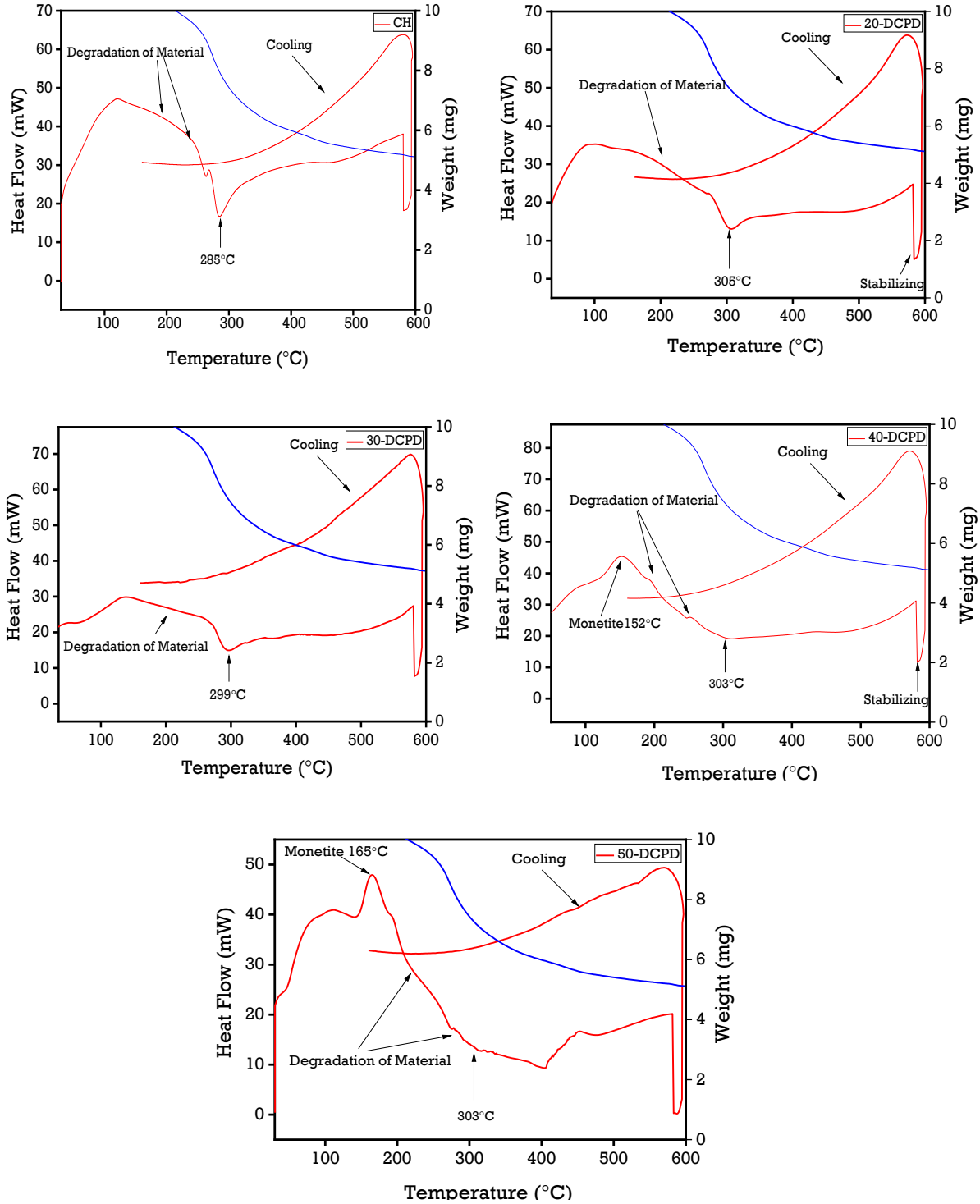

FIGURE 4.5 - Thermal analysis of high molecular weight freeze-dried chitosan scaffolds using the Perkin Elmer STA 8000 from 30 to 600 ˚C at a heating rate and cooling rate of 20 ˚C/min. The red line refers to the heat flow, while the blue line refers to the mass of the sample.

4.1.2 Water Uptake (Swelling)

The ability of freeze-dried scaffolds to swell and retain a certain amount of water/liquid within their structure is essential for applications of controlled release, i.e., drugs or minerals [309]. The swelling behaviour of the freeze-dried CS scaffolds containing various concentrations of DCPD mineral at different time intervals is displayed in Figure 4.6. The patterns observed indicate an initial rapid swelling increase from 0 to 25 minutes for all the scaffolds. There is a collective gradual increase between 25 and 175 minutes, followed by mass stabilisation from 175 to 350 minutes. The results reveal that the DCPD mineral concentrations strongly influenced the swelling % as it varies from 934.7 ± 23.3 % for un-loaded DCPD mineral CH freeze-dried scaffolds to 557.4 ± 29.8 % for 50-DCPD mineral freeze-dried scaffolds. The equilibrium swelling % is lower for scaffolds containing DCPD mineral and is likely to be attributed to the reduction of the hydrophilic functional groups in the cationic CS structure, i.e., amine (NH_2) and amide (-CONH, -$CONH_2$) groups [310].

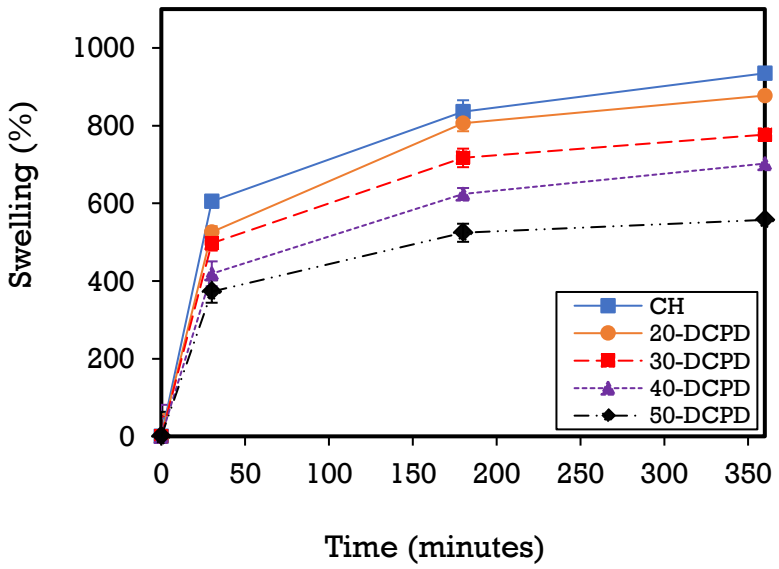

FIGURE 4.6 - Swelling kinetics of CH, 20, 30, 40 and 50-DCPD freeze-dried scaffolds submerged in phosphate saline buffer (pH 7.4) at physiological temperature 37 ˚C. Experiments were carried out in triplicates. The error bars are equivalent to the mean ± standard deviation (SD) (n = 3 in each group).

Thus, reducing the number of hydrophilic groups in the CS structure, which is unfavourable to the swelling rate [311]. The hydrophilic groups are water-binding sites [310, 312], resulting in the expansion and occupation of a larger volume, the process known as swelling. Furthermore, the addition of DCPD mineral stabilised the CS structure, where inter and intramolecular chain interactions occurred between the mineral and the polymeric CS chains. Potential bone scaffolds must have the ability to absorb inflammation liquids during the wound healing in a timely manner to avoid infection of the wound [313], and adequate water absorption capability has been found to promote cell adhesion, but lower mechanical properties of scaffolds [306, 314, 315]. The swelling % experiments confirm that all the polymer matrixes of the synthesised scaffolds can swell and store water similarly to living tissues [314]. The swelling % decreased with increased DCPD mineral content; thus, a balance between mechanical stability and surfaces which promote cellular adhesion will need to be established.

4.1.3 Degradation

The degradation behaviour of the synthesised freeze-dried scaffolds is displayed in Figure 4.7. Increasing DCPD mineral concentration promoted a reduction in the mass loss of the scaffolds, whereby 50-DCPD scaffolds exhibited the lowest mass loss of 22.7 ± 1.2 % in comparison to CH freeze-dried scaffolds, which expressed 40.3 ± 1.7 mass loss. The 20, 30 and 40-DCPD scaffolds presented mass losses of 36.3 ± 1.5 %, 30.2 ±

1.3 % and 28.6 ± 1.0 % respectively at four weeks. Scaffolds that exhibited higher crystallinity, i.e., 40 and 50-DCPD, as investigated using XRD analysis displayed in Figure 4.1, expressed lower equilibrium swelling and degradation degrees. The reduced degradation is likely attributed to the restriction of the biopolymer CS chains due to increased hydrogen bonding and intermolecular forces. Therefore reducing the water molecules accessibility to the hydrophilic groups [316]. The scaffold degradation must be tuned to ensure it lasts long enough for cellular regeneration to occur; hence, it was critical to study the structural stability in an aqueous environment.

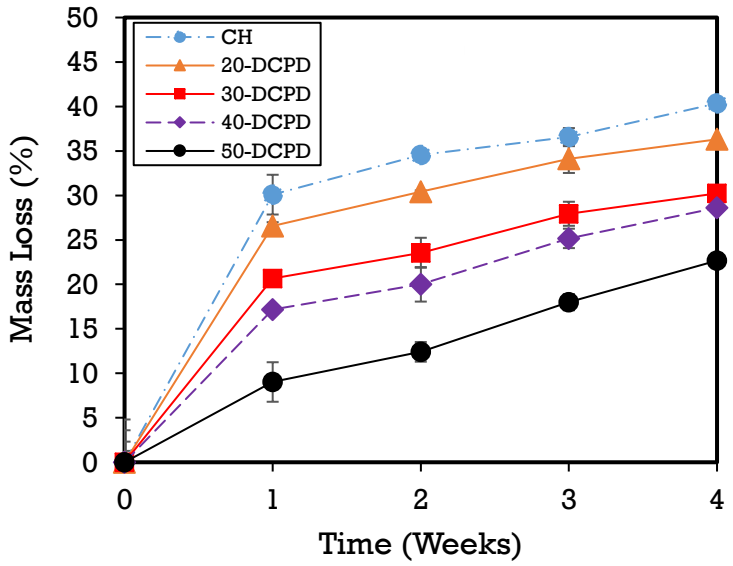

FIGURE 4.7 - Degradation results for CH, 20, 30, 40 and 50-DCPD freeze-dried scaffolds submerged in phosphate saline buffer (pH 7.4) at physiological temperature 37 ˚C. The experiments were carried out in triplicate over a 4-week process. The error bars are equivalent to the mean ± standard deviation (SD) (n = 3 in each group).

4.1.4 Porosity

Porosity is essential for synthetic bone scaffolds utilised for bone and tissue regeneration, particularly since the inner architecture of porous scaffolds is tailored by influencing the size and distribution of pores. Higher porosity and interconnected pores encourage cell attachments to facilitate 3D cell regeneration, diffusion of nutrients and the removal of waste products [6]. The porosity is related to the amount of pore space present in the structure; thus, the physical properties, i.e. material or bulk density, can be used to estimate the total porosity of the freeze-dried scaffolds. The porosity results of the freeze-dried scaffolds determined via the Gravimetric Principle and the Liquid Displacement method (determined via equation 3.18) are displayed in Figure 4.8.

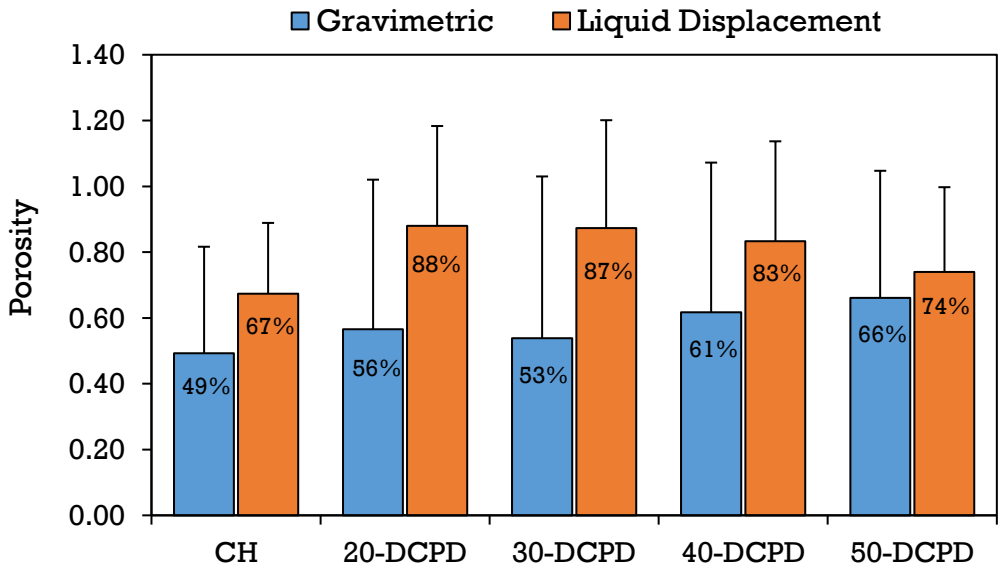

FIGURE 4.8 - Determination of porosity of the synthesised freeze-dried scaffolds via gravimetric and liquid displacement method. The error bars are equivalent to the mean ± standard deviation (SD) (n = 3 in each group).

The scaffold porosities determined via the gravimetric approach only takes into account the mass and volume while the size and the number of pores are not considered. Therefore, the porosity results obtained via the gravimetric approach are not accurate; however, the results have been included as a comparison to the results obtained from the liquid displacement method (Figure 4.8).

The porosity for all freeze-dried scaffolds is over 70 % except for the CH scaffold, where the porosity is 67.33 $\pm$ 10.78 % as determined via the Liquid Displacement method. An increasing porosity trend is observed from the CH to the 30-DCPD scaffolds. The increasing trend is attributed to the increase in the number of pores as already confirmed from SEM analysis (Figure 4.4). Conversely, the decreasing porosity trend observed from 30-DCPD to the 50-DCPD scaffolds can be attributed to the majority of pores combining creating larger pores leading to reduced interconnectivity, as observed from the pore size distribution data displayed in Figure 4.4 (d-e). The larger pores fundamentally alter the internal scaffold structures containing $\geq$ 40 wt% DCPD minerals, causing the overall surface areas to reduce, which is unbeneficial for cellular growth.

4.1.5 Zeta Potential

The zeta potential, i.e., $\pm$ 30 mV, is considered stable for colloidal systems due to the surface charge particle repulsions. The agglomeration tendency is conveyed by the Derjaguin Landau Verwey Overbeek (DLVO) theory which, corresponds the sum of the electrostatic repulsive and Van Der Waals forces thus, determining the total interaction energy at a particular separation distance [317]. The zeta potential of DCPD

mineral is -12.44 ± 0.4 mV indicating the agglomeration potential [318, 319]. Agglomeration of the synthesised DCPD mineral is also confirmed from the SEM characterisation shown in Figure 4.4 (a). The negative surface charge density value for DCPD is related to the presence of phosphate groups (PO_4^{3-}) within the structure. Conversely, the zeta potential values for all freeze-dried scaffolds are positive, confirming the protonation of the amino groups, which gave rise to the overall positive charge. However, the charge decreases with increasing DCPD mineral concentration where the average zeta potential decreased (Table 4.3) from +43.5 ± 0.4 mV to +20.2 ± 0.5 mV for DCPD free and 50-DCPD mineral loaded freeze-dried scaffolds respectively. The interaction of DCPD phosphate groups (PO_4^{3-}) with the protonated CS scaffold amino groups ($-NH_3^+$) likely attributed to the decrease of overall positive charge exhibited by the scaffolds.

TABLE 4.3 - Zeta potential measurements of the unloaded and Dicalcium Phosphate Dihydrate loaded freeze-dried scaffolds

Sample	Zeta Potential (mV)	Standard Deviation
DCPD	-12.44	0.41
CH	+43.47	0.35
20-DCPD	+39.57	0.31
30-DCPD	+34.53	0.38
40-DCPD	+28.23	0.25
50-DCPD	+20.23	0.47

4.1.6 Mechanical Testing

Pore size distribution, homogeneity and the heterogeneity of pores play a vital role with regards to the mechanical stability. Scaffolds containing smaller pore sizes exhibit enhanced mechanical properties due to the compact structure as compared with scaffolds containing larger pore sizes [320]. Several investigations have reported that heterogeneous pores (containing both large and small pores) produced increased mechanical properties [321, 322]. The mechanical property data for the synthesised scaffolds are presented in Table 4.4.

TABLE 4.4 - Mechanical property data obtained from tensile testing freeze-dried scaffolds (n=3).

	CH	20-DCPD	30-DCPD	40-DCPD	50-DCPD
Youngs Modulus (kN/m^2)	5.38 ± 0.03	7.26 ± 0.06	20.92 ± 0.11	22.73 ± 2.10	25.50 ± 0.54
Tensile Strength (kPa)	7.07 ± 0.03	9.86 ± 0.05	26.84 ± 0.08	23.21 ± 0.63	27.13 ± 0.25

As expected, the Youngs modulus and the tensile strength both increased with increasing DCPD mineral concentrations. The most significant modulus and strength increase is exhibited for the 30-DCPD scaffolds compared with the 20-DCPD scaffolds where the Youngs modulus increased by 65.29 ± 17.0 % and the tensile strength increased by 63.26 ± 13.0 %. The incorporation of DCPD mineral increased scaffold crystallinity as confirmed via XRD analysis (Figure 4.1), thus stabilising and restricting the CS biopolymer chains. Hence increased force is required to pull part the biopolymer chains, which consequently corresponds to enhanced mechanical properties with increasing DCPD concentrations.

4.2 Freeze-dried Scaffold Double Layer

Double-layered freeze-dried scaffold containing DCPD mineral is displayed in Figure 4.9. The first layer consists of pure CS, while the second layer contains 30 wt % DCPD mineral. The two layers were successfully fully incorporated, presenting a continuous freeze-dried structure containing no gaps between the layers via a novel construction technique (see Appendix IV and Appendix V for further SEM images relating to the 30-DCPD and double layer respectively). The synthesis of the double layer scaffold consisted of forming the initial freeze-dried CS layer (0.5 cm diameter) via the freeze-drying procedure described in section 3.1.4. The creation of the second layer consisted of placing the initial freeze-dried layer onto a 1 cm diameter cylindrical container where 2 ml CS solution containing DCPD mineral was added to the surrounding area. The samples were frozen at – 80 C, freeze-dried for 24 hours, and the resulting scaffold consisted of the successful interconnection of the two layers as confirmed by SEM and EDS analysis shown in Figure 4.9. The synthesis of the double layer scaffold is the initial test to confirm that the novel construction technique is successful where both materials are fully integrated.

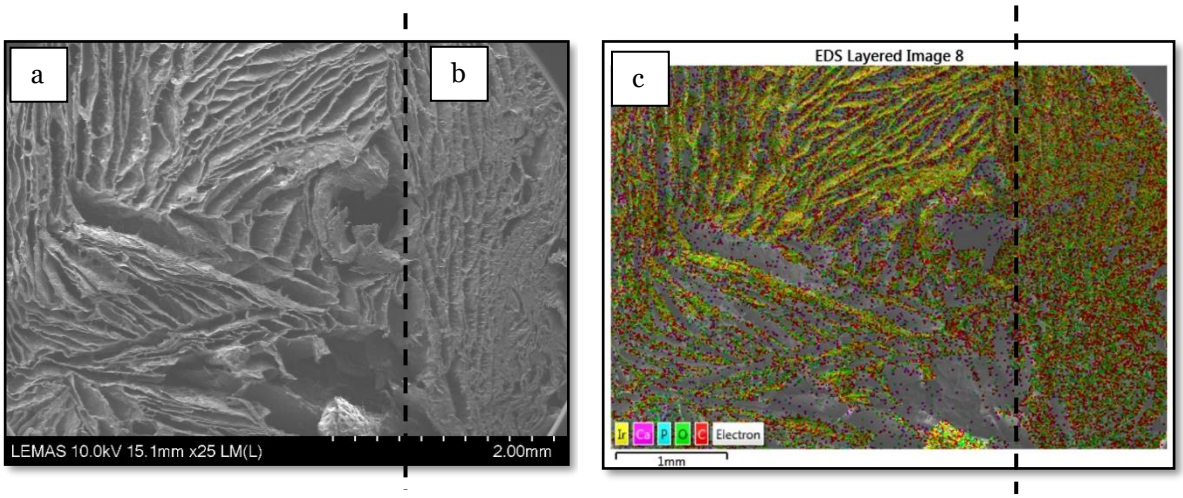

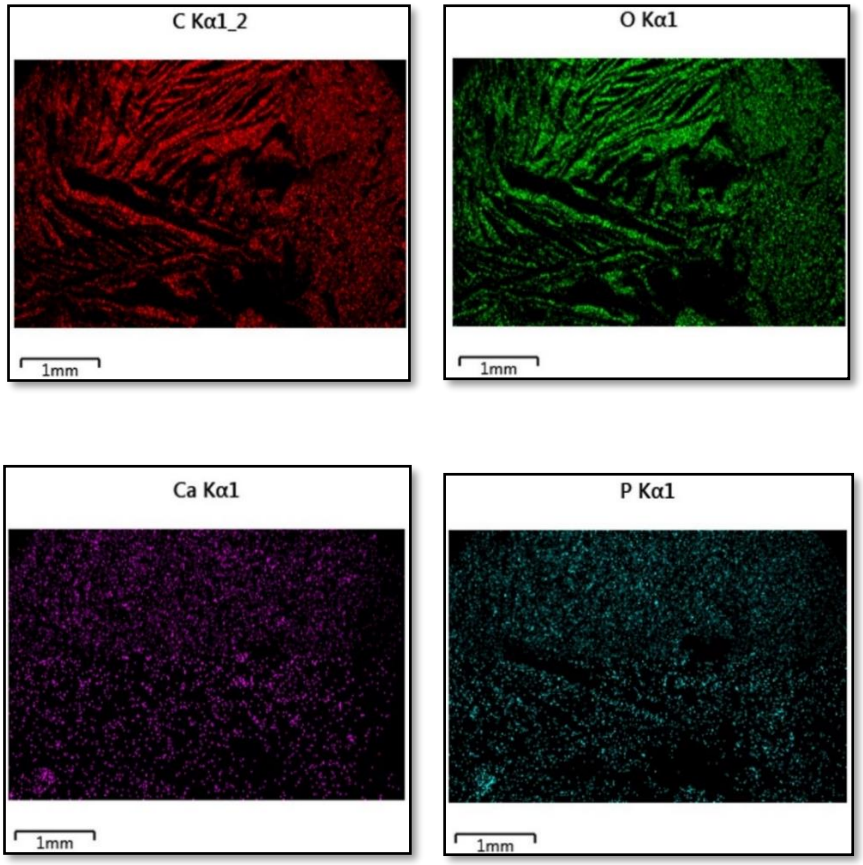

FIGURE 4.9 - Double-layered freeze-dried scaffold, (a) layer 1 contains pure chitosan, (b) layer 2 contains 30 wt % DCPD mineral and (c) corresponding EDS elemental analysis (carbon (C), oxygen (O), calcium (Ca) and phosphorus (P)).

4.3 In vitro Osteoblast Results

4.3.1 Contact Cytotoxicity Assay

Cytotoxicity assay testing is a qualitative assessment of cytotoxicity via microscopic observations to determine any changes to the osteoblast cells morphology and reactivity zones. Therefore, contact cytotoxicity testing is essential to assess and characterise any potentially toxic or harmful effects corresponding to the freeze-dried scaffolds [323]. The freeze-dried scaffolds seeded with 5 x 10^3 G292 osteoblast cells

were cultured for 24 hours to achieve 80 % confluency, i.e. the end of the logarithmic phase of growth. The *in vitro* cytotoxic effects of the freeze-scaffolds were evaluated by qualitative means, as depicted in Figure 4.10. Microscopic examinations of the osteoblast cells proliferated on or near to the samples in terms of general morphology, membrane integrity, and cell attachment shows little or no cytotoxic effect. The negative control (Figure 4.10(a)) consisting of DMSO resulted in a lack of cell growth due to cell lysis. The purpose of the positive control is to demonstrate an appropriate test system response, thus; the freeze-dried samples present similar results to the positive control (Figure 4.10(b)) due to osteoblast cells successfully proliferated entirely around each scaffold. The morphology of the osteoblast cells seems to be consistent throughout all of the freeze-dried scaffold samples, i.e. CH, 20, 30, 40 and 50-DCPD, and the lack of cell lysis indicates the biocompatible nature of the materials.

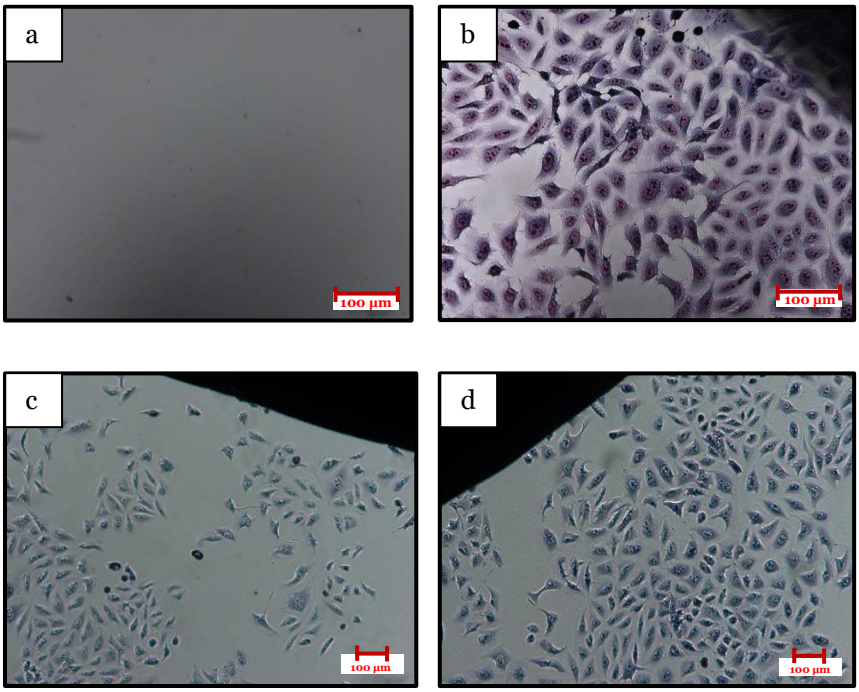

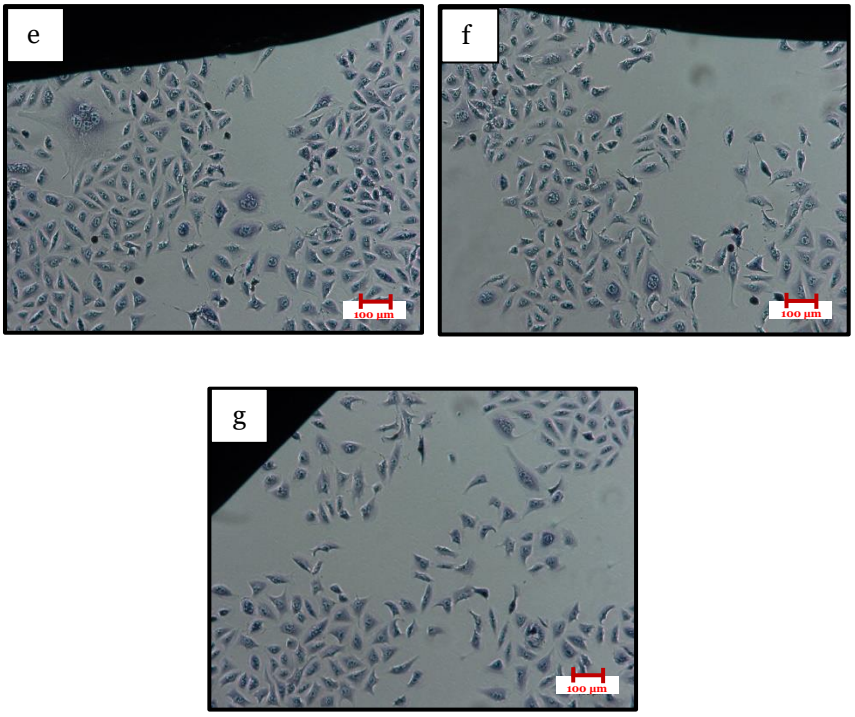

FIGURE 4.10 - Brightfield illumination images of undoped and mineral doped freeze-dried chitosan scaffolds to determine the presence of cytotoxicity, (a) negative controls; (b) positive control; (c) 20-DCPD, (d) 30-DCPD, (e) 40-DCPD and (f) 50-DCPD.

4.3.2 DNA Quantification Assay

The quantitative approach used to assess cellular viability of freeze-dried scaffolds, i.e. CH, 20, 30, 40 and 50-DCPD, confirmed successful cell proliferation at 1, 3 and 7 days, as shown in Figure 4.11. The general trend depicted for the CH, 20, 30 and 40-DCPD at each time point presents an increase in the number of cells proliferated. Calcium and phosphate ions released during DCPD degradation likely stimulated cellular growth by increasing cell adhesion, consequently enhancing proliferation. The porosity of freeze-dried scaffolds plays a vital role in cellular growth as the porous structure enhances nutrient exchange and enables the significant release of minerals to stimulate proliferation. For the 50-DCPD scaffold, a reduction of osteoblast

proliferation is observed at 3 and 7 days. The reduced proliferation is likely attributed to the reduction of scaffold porosity, as confirmed by the SEM analysis in section 4.04 and the porosity analysis in section 4.1.4. The coalesces and the formation of closed-ended pores likely reduced the flow of nutrients, thus reducing the osteoblast growth.

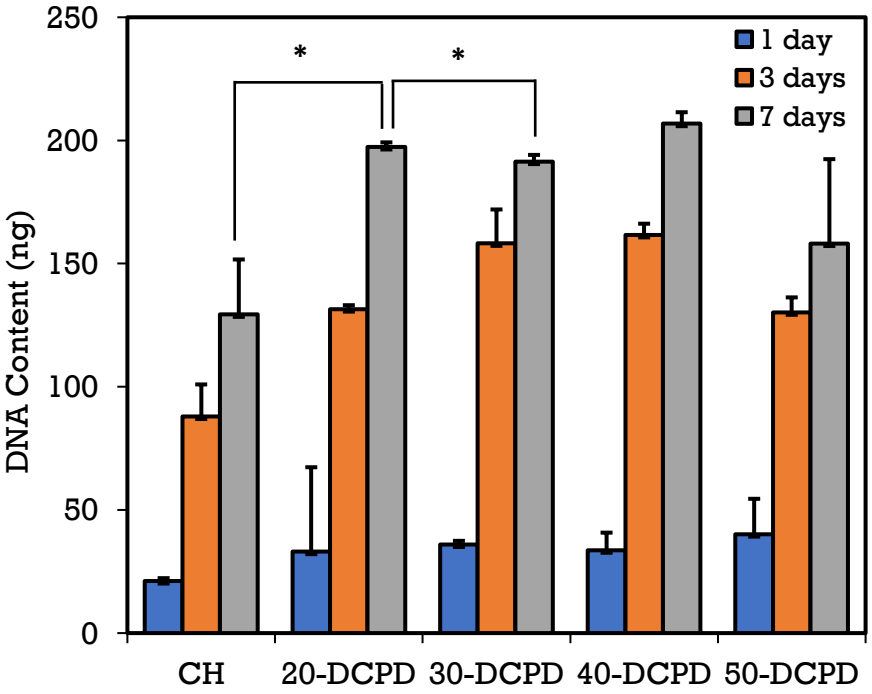

FIGURE 4.11 - Cell proliferation of undoped and mineral doped freeze-dried scaffold evaluated using PicoGreen assay. The error bars are equivalent to the mean ± standard deviation (SD) (n = 3 in each group).

4.4 Chapter 4 Summary

Porous freeze-dried unloaded and DCPD mineral loaded scaffolds were successfully fabricated. Increasing the mineral concentration led to the enhancement of the scaffold's crystallinity, porosity and mechanical properties while a reduction in zeta potentials was observed. The synthesised scaffolds did not exhibit any cytotoxicity to

the osteoblast growth. However, the 50-DCPD scaffold exhibited reduce porosity and osteoblast proliferation at 3 and 7 days compared to the CH, 20, 30 and 40-DCPD scaffolds.

Chapter 5
NANOPARTICLES RESULTS

5.0 Characterisation and Testing Results

5.0.1 Thermal Analysis

The simultaneous thermal analysis results for the synthesised scaffolds are displayed in Figure 5.1. The FUNP nanoparticles revealed gradual weight loss from 100 ˚C due to the removal of trapped moisture and atmospheric gases, i.e. water and carbon dioxide [324]. The three endothermic peaks (i) 280˚C, (ii) 385˚C and (iii) 815˚C are likely to be associated with the combustion of organic residues, e.g. NaOH and C_2H_5OH [325] as calcination allows for the removal of any impurities leading to the formation of crystalline nanoparticles. No weight loss is observed above 815 ˚C, suggesting the formation of crystalline nanoparticles as confirmed by sample C815 X-ray diffraction pattern depicted in Figure 5.4. Temperature plays a significant role with regards to nanoparticle structural changes, i.e. higher calcination temperatures often lead to larger nanoparticle sizes [326] but also affects the Ce^{3+} and Ce^{4+} ionic ratio.

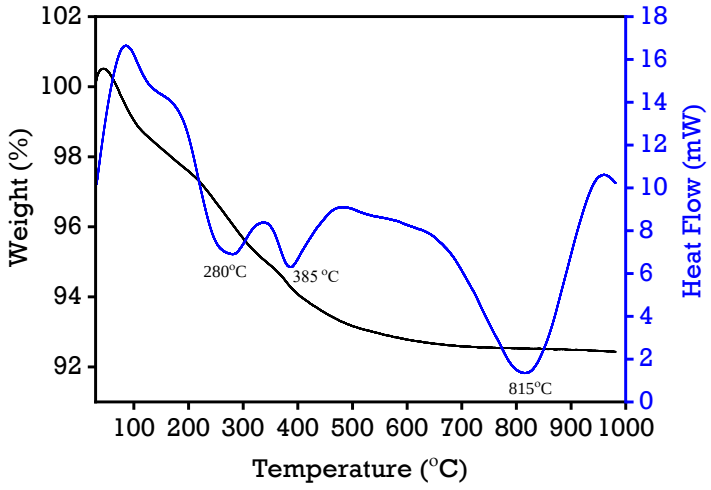

FIGURE 5.1 - Simultaneous Thermal Analysis spectrum of FUNP nanoparticles depicting critical exothermic peaks at 280, 385 and 815 ˚C. The blue line represents the heat flow, while the black line represents the mass of the sample.

The literature mentions that the antibacterial properties of nanoparticles are dependent upon ionic ratio and particle size, i.e. the smaller the particle size, the better the overall antibacterial properties [327-329]. Ostwald Ripening [325] or the coalescence of smaller particles (agglomeration) could lead to a temperature-dependent particle size increase. The structural changes occurring at the endothermic peaks are investigated by heat-treating the FUNP nanoparticles at calcined at 280˚C, 385˚C and 815˚C.

5.0.2 Fourier Transform Infrared Spectroscopy

FTIR results for the cerium oxide nanoparticles present similar spectra, as shown in Figure 5.2. The broad reflectance peak at 3500 cm^{-1} to 4000 cm^{-1} relates to the O-H stretching associated with the presence of adsorbed H_2O. The significant peaks located at 2050 cm^{-1} are likely related to ceria bound gasses, i.e. carbon dioxide and magnification of the 2050 cm^{-1} region as depicted in Figure 5.2(b) highlights the doublet rotational gas phase. The ceria bound gas peak for the FRNP nanoparticles has a lower intensity than the calcined nanoparticles, suggesting that atmospheric CO_2 was readily trapped during the furnace heat-treatment process. The bands related to Ce-O stretching vibrations are located in the region of 500 cm^{-1} to 750 cm^{-1}. Similar FTIR results relating to cerium oxide nanoparticles are described in the literature [252, 330-332].

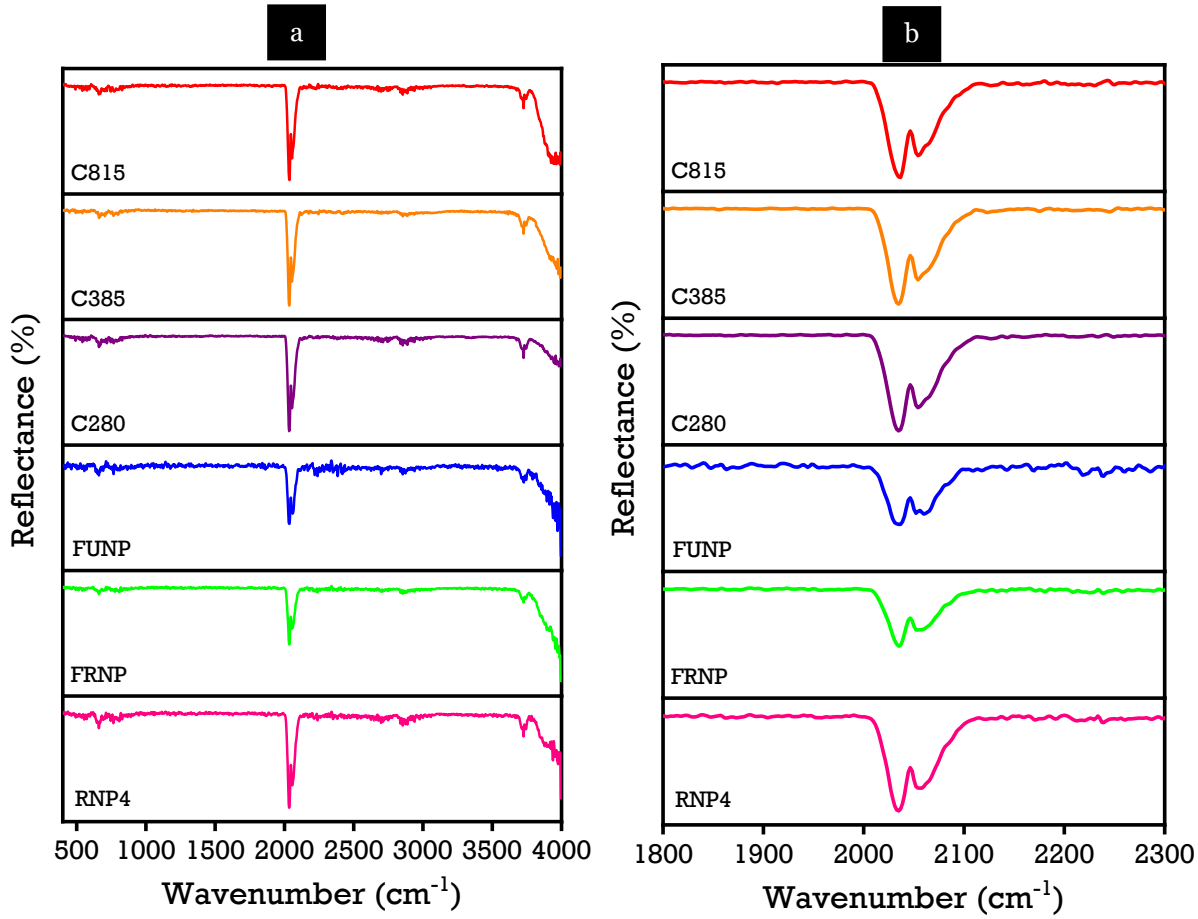

FIGURE 5.2 - Vertex 70 FTIR patterns for cerium oxide nanoparticles. The operating parameters consisted of a total of 32 scans at a resolution of 4 cm^{-1}, (a) FTIR spectrum from 400 cm^{-1} to 4000 cm^{-1}, (b) FTIR spectrum 1800 cm^{-1} to 2300 cm^{-1}.

5.0.3 Ultraviolet-Visible Spectroscopy

Absorbance spectra for the cerium oxide nanoparticles are shown in Figure 5.3, where the maximum absorbance is located in the 210 nm regions. The electronic behaviour, oxygen defects, particle size and the bivalence of the cerium oxide nanoparticles affects the optical properties of the nanoparticles. Also, an increase in the heat treatment temperatures likely affected the size distribution of the cerium oxide nanoparticles as confirmed from SEM images analysis depicted in Figure 5.5. Bandgap energies E_g of the synthesised nanoparticles are investigated from the absorption spectra and

calculated via The Tauc equation (equation 5.1), which determines the bandgap energy between valence and conduction bands of the nanoparticles spectrophotometrically:

$$\alpha h \upsilon = A (h \upsilon - E_g)^{0.5} \qquad \text{eq (5.1)}$$

With A being the absorption, α refers to the absorption coefficient, hυ is the photon energy (1240/λ), and E_g relates to the bandgap. Therefore, the bandgap energies are determined from the x-axis intersections of $(\alpha h\upsilon)^2$ vs hυ plots (Figure 5.3 (b-f)). The absorption maxima for samples calcined at 280, 385 and 815 ˚C exhibited a slight blue shift as absorption shifted to smaller wavelengths for calcined nanoparticles (C280, C385 and C815) [333]. The blue shift implies that the optical band gap energy decreases as the nanoparticle sizes increase, which has also been confirmed by other researchers [334, 335]. The direct optical band gap energies for the FRNP, FUNP, C280, C385 and C815 nanoparticles were found to be 5.6 eV, 5.5 eV, 5.2 eV, 4.7 eV and 3.4 eV, respectively. The difference in the band energies is related to the presence of different oxidation states (Ce^{3+} and Ce^{4+}) on the outer nanoparticles' surfaces, where the Ce^{3+} : Ce^{4+} ratio is known to be affected by oxygen vacancies and surface defects [326, 336, 337].

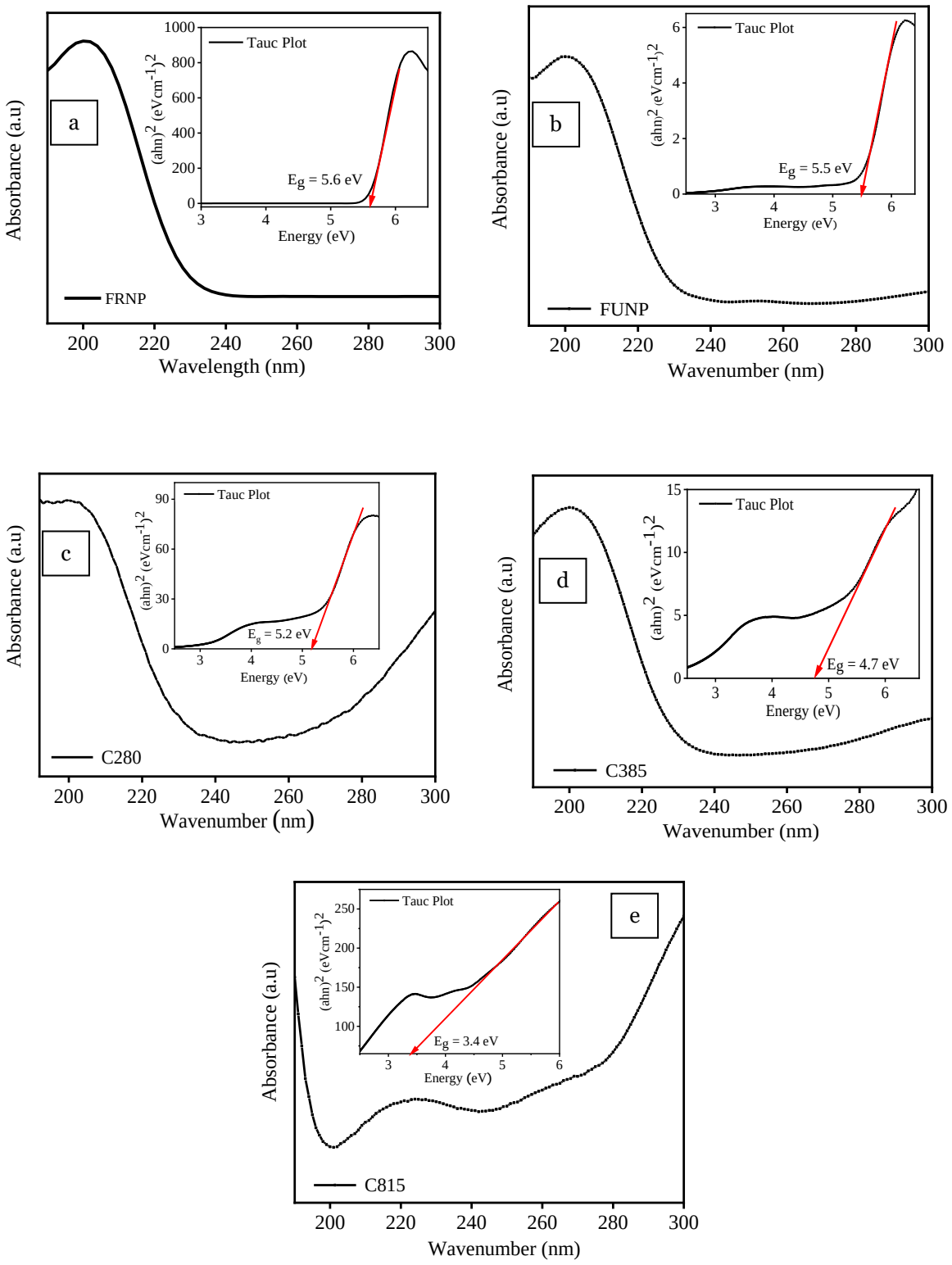

FIGURE 5.3 - UV-Vis absorbance spectra obtained from cerium oxide nanoparticles concentrations of 0.5 mg/ml and corresponding Tauc Plots, (a) FRNP, (b) FUNP, (c) C280, (d) C385 and (e) C815.

5.0.4 X-ray Diffraction

The crystalline structure, i.e. composition, crystallite size and microstrain of the nanoparticles, have been determined from the diffraction patterns (Figure 5.4). The XRD diffraction spectra for the synthesised nanoparticles exhibit eight major characterisation peaks located at 28.49, 33.00, 47.38, 56.12, 58.96, 69.45, 76.51 and 78.89˚, which corresponds to (111), (200), (220), (311), (222), (400), (331) and (420) Miller Indices respectively. The depicted synthesised nanoparticles are single phased and agree with the phase fluorite type CeO_2 JCPDS 00-067-0123 reference with a lattice parameter of 0.5423 nm. Notably, the (111) peaks shift to slightly higher 2θ with increasing calcination temperatures and are likely to be attributed to the removal of possible crystal lattice expansions resulting from nanoparticles coarsening.

The intensities of the calcined nanoparticles increased with increasing calcination temperatures from 280 ˚C to 815 ˚C and can be attributed to the crystallinity improvement of the nanoparticles confirmed from crystallite measurements displayed in Table 5.1. Consequently, the full width at half maximum (FWHM) of XRD peaks decreased as the crystallinity of the nanoparticles increased with temperature hence the reduction of FWHM peaks confirm that the calcination temperature affects the size and morphology of synthesised nanoparticles.

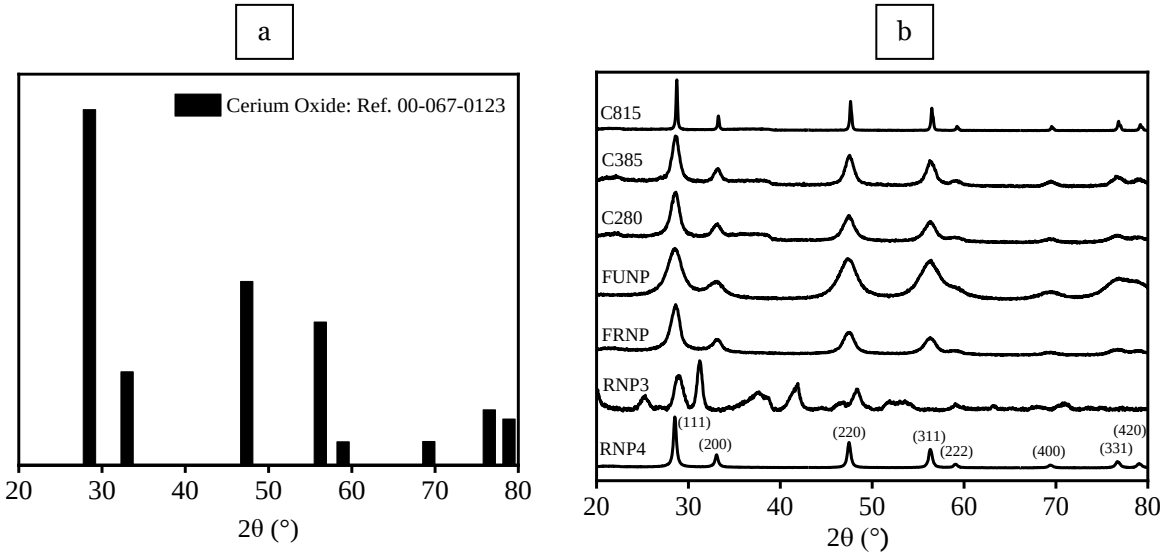

FIGURE 5.4 - X-ray diffraction patterns of nanoparticles, 2θ scanning range was 20° to 80° at a scan speed of 5s and increment of 0.03˚; (a) reference pattern of cerium oxide nanoparticles JCPDS 00-067-0123; (b) commercial and synthesised nanoparticles calcined at 280 ˚C, 385 ˚C and 815 ˚C.

The interplanar spacing 'd' was calculated via Bragg's equation (Equation 3.4) and the lattice cell parameter 'a' are determined for all samples using the following formula:

$$a = \frac{d}{(h^2 + k^2 + l^2)^{1/2}} \qquad \text{eq (5.2)}$$

where 'a' refers to the FCC lattice parameter, 'd' corresponds to the crystalline face spacing and 'hkl' are the crystalline face indexes. The results are displayed in Table 5.1. The comparison of the crystallite sizes determined via the Scherrer and Williamson-Hall methods are also displayed in Table 5.1, where significant differences are observed between the values. The crystallite size noticeably increases with increasing

calcination temperature, which is consistent with increasing particles size as confirmed from TEM analysis in Figure 5.5 and by the decreasing Brunauer Emmett Teller (BET) surface area results as displayed in Table 5.1.

TABLE 5.1 - XRD data obtained from prepared nanoparticles, crystallite sizes calculated via Scherrer and Williamson-Hall methods.

				Scherrer Method	***Williamson-Hall Method***
Sample	Lattice Cell Parameter (Å)	Unit Cell Volume ($Å^3$)	BET Surface Area (m^2/g)	Crystallite Size (nm)	Crystallite Size (nm) Error: $\times 10^{-2}$
RNP4	5.41	158.73	36.72 ± 0.14	21.56 ± 6.47	16.25 ± 0.09
FRNP	5.42	159.52	71.63 ± 0.47	4.29 ± 1.29	5.38 ± 1.37
FUNP	5.40	158.16	36.40 ± 0.15	6.70 ± 2.01	8.09 ± 0.42
C280	5.41	158.37	35.40 ± 0.11	6.59 ± 1.97	8.48 ± 0.69
C385	5.39	157.37	46.37 ± 0.15	7.87 ± 2.37	10.69 ± 0.70
C815	5.37	155.52	4.27 ± 0.04	32.59 ± 9.78	45.31 ± 0.22

5.0.5 Transmission Electron Microscopy

TEM is commonly utilised to characterise the size, shape and morphology of samples as shown in Figure 5.5, the majority of synthesised nanoparticles are spherical except RNP4 and the C815 nanoparticles. The smaller the size of the nanoparticles, the higher the agglomeration thus, makes it difficult to observe individual particles. The particles

size for RNP4, FRNP, FUNP, C280, C385 and C815, deduced from High-Resolution TEM (HRTEM) images, were estimated to be 25, 4, 6, 8, 11 and 53 nm, respectively (See Appendix VI for HRTEM and EELS images of the synthesised nanoparticles). The three principle low index planes for nanoparticles are (111), (110) and (100). The (111) planes for the FUNP nanoparticles are observed in the HRTEM image (Figure 5.5 (g)). The presence of lattice fringes is an indication of the crystalline nature of the synthesised nanoparticles (Figure 5.5(g)). The Selected Area Electron Diffraction (SAED) patterns for all samples except RNP4 and C815 nanoparticles depict continuous ring patterns (Figure 5.5(h)). The presence of discrete rings is an indication of the polycrystalline structure of the nanoparticles but also the relatively small size of the nanoparticles. All the obtained SAED rings are in good agreement with the XRD diffraction patterns.

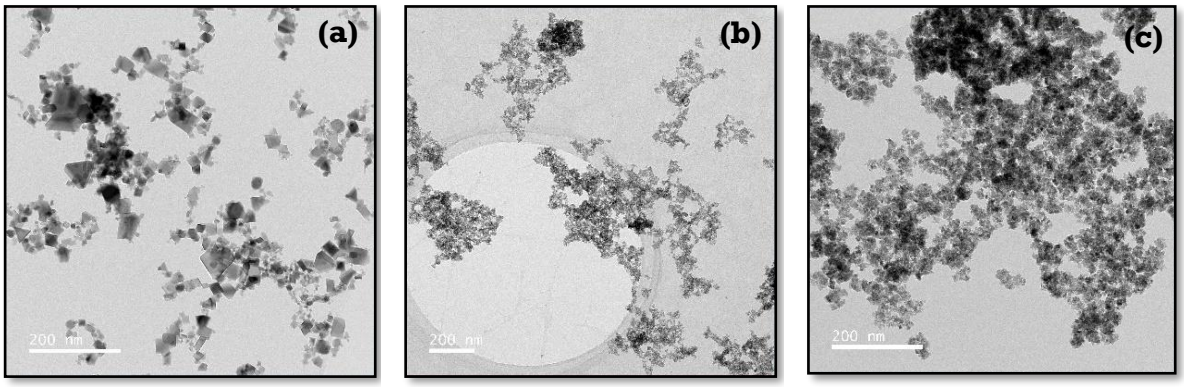

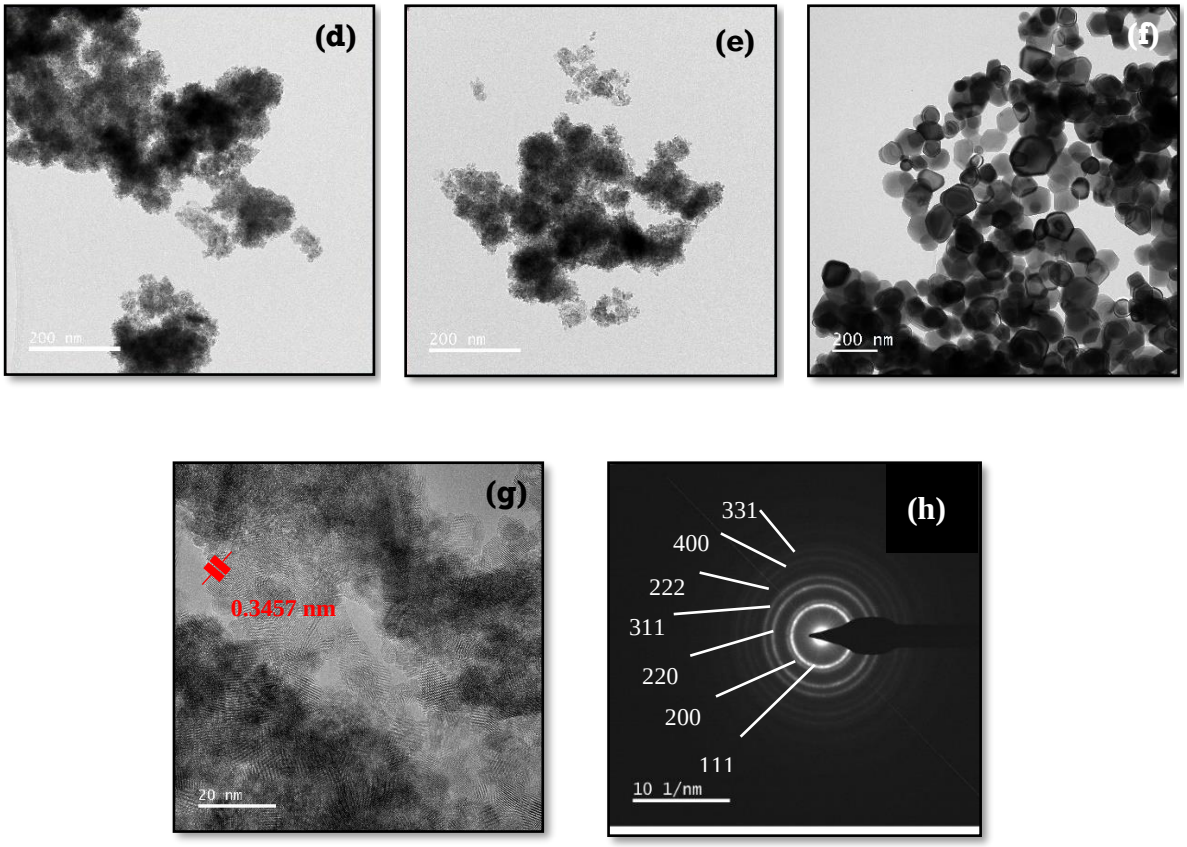

FIGURE 5.5 - Comparison of Titan Themis Cubed 300 TEM images of nanoparticles calcined at various temperatures (a) RNP4, (b) FRNP, (c) FUNP, (d) C280, (e) C385, (f) C815, (g) HRTEM image of FUNP and (h) SAED of FRNP.

TABLE 5.2 - Calculated d Spacing by (i) Bragg Equation, (ii) HRTEM images, (iii) From the (111) face index of SAED Transmission Electron Microscopy Diffraction Images.

Sample	Bragg Equation (nm)	Interplanar Spacing (nm)	Crystalline Face Index (nm) Error: $\times 10^{-3}$
RNP4	0.3126	0.3629	0.3225 ± 6.450

FRNP	0.3131	0.3423	0.3205 ± 6.410
FUNP	0.3122	0.3457	0.3196 ± 6.392
C280	0.3124	0.3630	0.3191 ± 6.382
C385	0.3117	0.3084	0.3216 ± 6.432
C815	0.3105	0.3249	0.3229 ± 6.458

5.0.6 X-ray Photoelectron Spectroscopy

The XPS measurements revealed significant differences in surface chemistry of the synthesised nanoparticles likely related to the drying method (furnace or freeze-drying) and calcination temperatures. It should be noted that XPS analyses the surface charge of the nanoparticles, whereas EELS analyses' the subsurface thus, is likely to differ regarding the Ce^{3+} : Ce^{4+} ratio. Figure 5.6 depicts the Ce 3d spectra for the FRNP, FUNP, C280, C385 and C815 cerium oxide nanoparticles. The spin-orbit doublet peaks associated with all the Ce 3d spectrums are **Ce $3d_{5/2}$** located between ~870 eV to 895 eV, and **Ce $3d_{3/2}$** located between ~895 eV to 915 eV. Additionally, multiple shake-up and shake-down satellite peaks are also present [338].

TABLE 5.3 - XPS peak data for synthesis cerium oxide nanoparticles (FRNP, FUNP, C280, C385 and C815).

		FRNP (eV)	FUNP (eV)	C280 (eV)	C385 (eV)	C815 (eV)
Ce^{4+}	u	906.1	905.9	911.1	911.6	903.9
	v	887.3	887.2	891.8	891.7	885.1

	u''	910.3	912.2	915.8	916.2	909.8
	v''	892.4	892.2	897.3	896.7	890.9
	u'''	921.4	920.9	926.1	925.5	918.9
	v'''	903.1	903.2	908.1	908.2	900.9
Ce^{3+}	u^0	905.5	905.2	904.9	904.7	903.1
	v^0	882.1	881.9	881.7	881.8	878.7
	u'	909.1	908.9	908.1	907.6	906.1
	v'	890.2	893.4	894.3	897.1	887.9

The XPS spectra indicate the co-existence of Ce^{3+} and Ce^{4+} due to the presence of satellite peaks linked to each oxidation state. Table 5.3 displays the XPS data regarding the energy peaks of the synthesised nanoparticles. Analysing the XPS measurements for the FRNP nanoparticles, the highest binding Ce 3d energy peaks u''' (921.4) and v''' (903.1) correspond to the Ce^{4+} valence state from the $Ce(3d^9\ 4f^0)\ O(2p^6)$ final states [339]. The remaining four lower energy peaks i.e., u (906.1), v (887.3), u'' (910.3) and v'' (892.4) are attributed to the mixing of $Ce(3d^9 4f^2)O(2p^4)$ and $Ce(3d^9\ 4f^1)O(2p^5)$ final states. Contributions related to the Ce^{3+} valence are labelled as u^0 (905.5), v^0 (882.1), u' (909.1) and v' (890.2) where the peaks are due to the mixing of $Ce(3d^9\ 4f^1)\ O(2p^6)$ and $Ce(3d^9\ 4f^2)\ O(2p^5)$ final states [339-342]. Figure 5.6 indicates with increasing calcination temperature, the Ce^{3+} doublet peaks (u', v', u^0 and v^0) decline, thus, suggesting that Ce^{3+} decreases with increasing calcination temperatures. Similar results were obtained by other researchers [339].

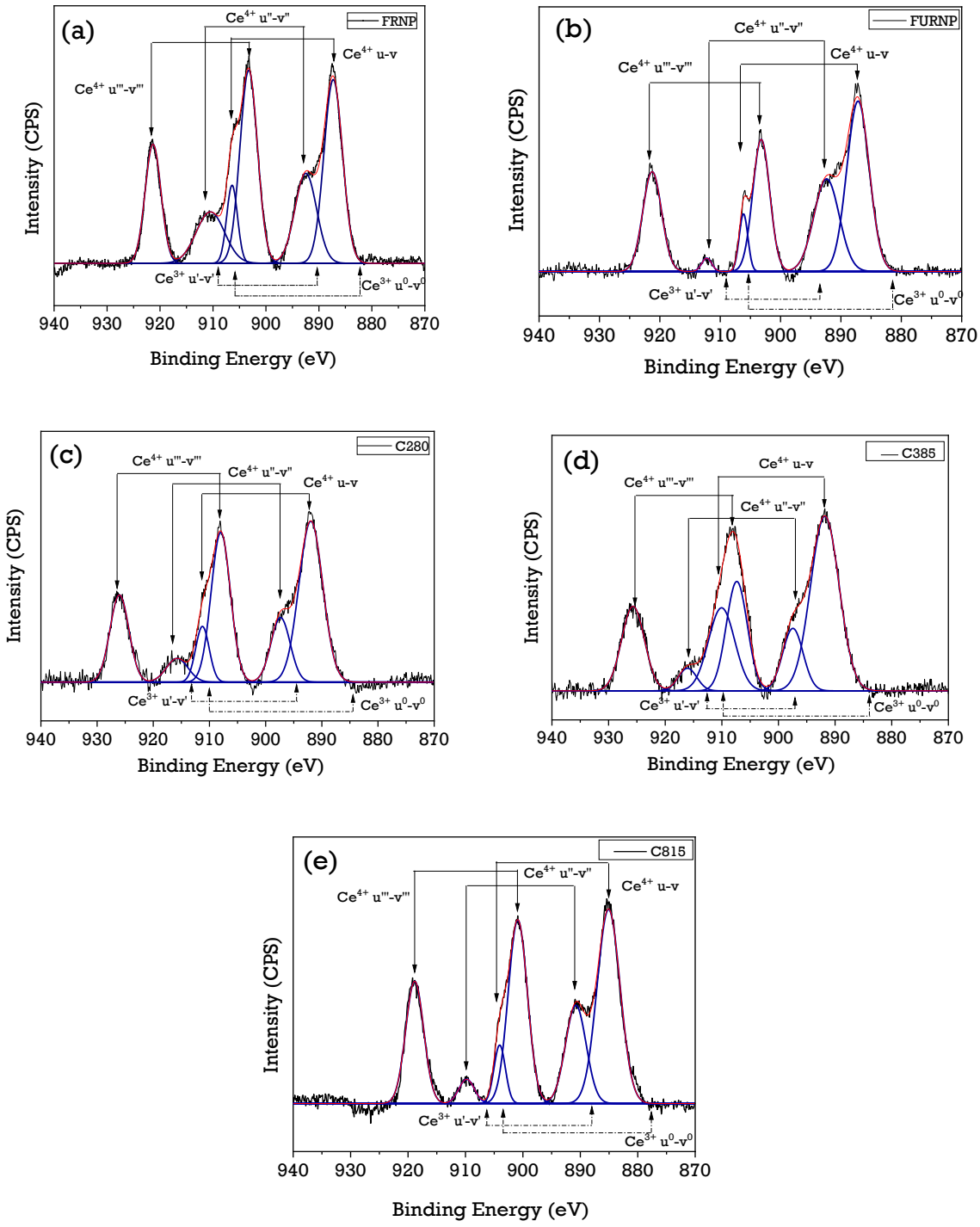

FIGURE 5.6 - Normalized XPS spectra for cerium oxide nanoparticles (FRNP, FUNP, C280, C385 and C815).

5.0.7 Electron Energy Loss Spectroscopy

Cerium oxide is electropositive and can exist in two oxidation modes, i.e. Ce^{3+} and Ce^{4+}. The EELS measurements were acquired by rastering the beam across several locations for each nanoparticle sample. EELS spectra from two controls (Ce^{3+} and Ce^{4+}) and five synthesised nanoparticles are shown in Figure 5.7. In each case, the background was removed, and Fourier-Ratio Deconvolution routines were applied prior to fitting. From the EELS spectra, the Ce $M_{4,5}$ edges of FRNP, FUNP, C280, C385 and C815 spectra are shown where the black lines represent the sample data, the red lines represent the Ce^{4+} ion spectra, and the grey lines represent the Ce^{3+} ion spectra.

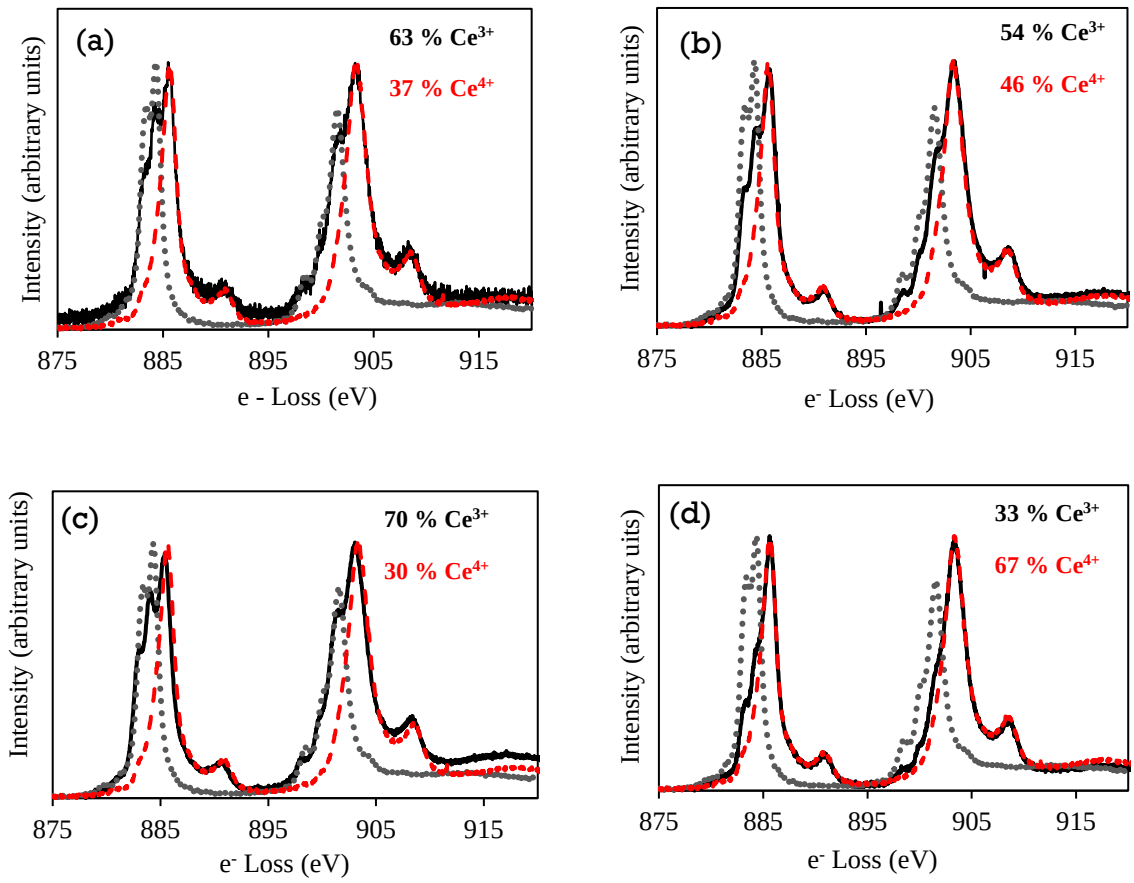

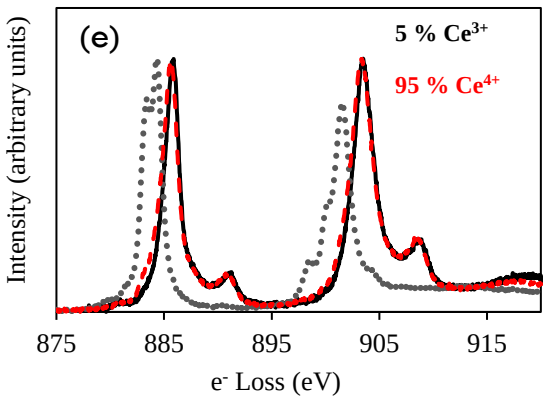

FIGURE 5.7 - Normalized EELS spectra depicting the presence of dual oxidation states. (a) FRNP, (b) FUNP, (c) C280, (d) C385 and (e) C815. Compared with Ce^{3+} (grey) and Ce^{4+} (red) standards.

It is evident as the size of the nanoparticles increases for calcined samples the Ce^{3+} : Ce^{4+} ratio decreases as the C815 sample contains 95 % majority of Ce^{4+} ions. The presence Ce^{4+} in the FRNP, FUNP, C280 and C385 is 37 %, 46 %, 30 %, and 67 % respectively. The obtained results confirm that the Ce^{3+} : Ce^{4+} ratio is temperature-dependent; therefore, the optimal calcination temperature must be characterised to ensure optimal Ce^{3+} : Ce^{4+}, which provides the highest antibacterial efficacy. Based on the XPS and EELS results, the FRNP, C385 and C815 nanoparticles are selected due to the range of particle size and Ce^{3+} : Ce^{4+} ratio to be further investigated.

5.1 Antibacterial Testing Results

5.1.1 Optical Density Measurements without Nanoparticles

The optical density (OD) measurements of bacteria growth can be used to assess the antibacterial properties of nanoparticles. Firstly, it is essential to characterise the

growth of the bacteria without the addition of the synthesised nanoparticles. Figure 5.8 displays the OD_{600} growth of *Escherichia coli, Pseudomonas aeruginosa* and *Staphylococcus epidermidis,* over 48 hours.

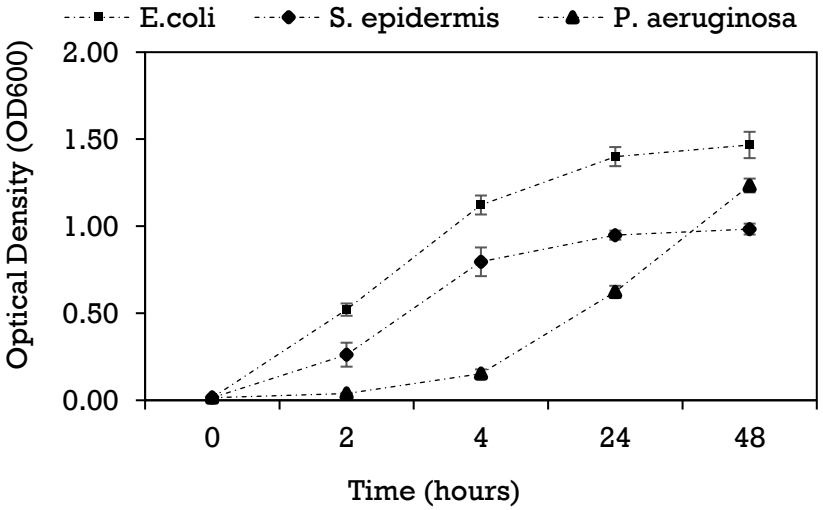

FIGURE 5.8 - Optical Density measurements characterising the growth of bacteria for 48 hours. The error bars are equivalent to the mean ± standard deviation (SD) (n = 3 in each group).

5.1.2 Optical Density Measurements with Nanoparticles

To investigate the antibacterial properties of nanoparticles with varying Ce^{3+} : Ce^{4+} ratio and particle size distribution FRNP, C385 and C815 nanoparticles have been selected. All three types of nanoparticles exhibited antibacterial properties against Gram-positive, and Gram-negative bacteria with the greatest antibacterial activity was observed against Gram-negative bacteria for the highest FRNP concentration (200 µg/ml) 38.8 ± 6.4 % reduction was observed against *Escherichia coli.* In contrast, a reduction of 28.7 ± 10.2 % was observed against *Pseudomonas aeruginosa* after 48

hours of incubation (**Figure 8**). The C385 nanoparticles exhibited 33.5 ± 5.8 %, 20.7 ± 8.1 % and 13.9 ± 1.1 % reduction of *Escherichia coli, Pseudomonas aeruginosa* and *Staphylococcus epidermidis,* respectively. The lowest antibacterial activity was observed for C815 nanoparticles with 20.3 ± 7.6 %, 18.2 ± 5.8 % and 6.4 ± 9.9 % bacterial reduction expressed against *Escherichia coli, Pseudomonas aeruginosa* and *Staphylococcus epidermidis*, respectively. Thus, confirming nanoparticles size and the ratio of oxidation states (Ce^{3+} : Ce^{4+}) plays a significant role in the antibacterial efficacy of cerium oxide nanoparticles. Several studies also found cerium oxide exhibited cytotoxic [229] and induced toxicity against *Escherichia coli* [229, 343]. Reduction of bacterial growth has been observed for coated nanoparticles which inhibited 50 % *Pseudomonas aeruginosa* growth [344]. Furthermore, cerium oxide nanoparticles have also exhibited moderate inhibitive activity against *Escherichia coli* and *Bacillus subtilis* [345-347] (see Appendix VII for relevant optical density plots).

TABLE 5.4 - The antibacterial effectiveness of the synthesised cerium oxide nanoparticles at a concentration of 200 μg/ml.

	E.*coli*	P.*aeruginosa*	S.*epidermis*
FRNP	38.8 ± 6.4 %,	28.7 ± 10.2 %	20.2 ± 4.1 %
C385	33.5 ± 5.8 %	20.7 ± 8.1 %	13.9 ± 1.1 %
C815	20.3 ± 7.56 %	18.2 ± 5.8 %	6.4 ± 9.9 %

The half-maximal inhibitory concentration (IC_{50}) calculated from linear regression models are shown in Table 5.5 (see Appendix VIII for regression plots). It is clear

smaller sized nanoparticles, i.e. < 10 nm, exhibit improved overall antibacterial efficacy against both Gram-positive and Gram-negative bacteria. The nanoparticles presented enhanced antibacterial activity against the Gram-negative bacteria, i.e. *Escherichia coli* and *Pseudomonas aeruginosa,* which is likely to be attributed to the structure of the bacterial cell wall. The cell wall of Gram-positive bacteria is composed of a relatively thick continuous peptidoglycan containing peptides and linear polysaccharide chains that is difficult for the nanoparticles to penetrate. However, the cell wall of Gram-negative bacteria is composed of a thin layer of peptidoglycan with a lipopolysaccharide surrounding the bacteria. Therefore, allowing the nanoparticles to possibly damage the wall causing the release of the contents, thus causing cell death; other studies [14, 348] also found similar results.

TABLE 5.5 - The half-maximal inhibitory concentration (IC_{50}) values of FRNP, C385 and C815.

IC_{50} (µg/ml)	*E.coli*	*P.aeruginosa*	*S.epidermis*
FRNP	340 ± 4.0	558 ± 3.9	580 ± 4.6
C385	365 ± 6.6	619 ± 5.2	741 ± 5.6
C815	563 ± 8.2	663 ± 9.4	785 ± 5.8

5.2 Chapter 5 Summary

The synthesis of cerium oxide nanoparticles was successful where the particles sizes ranged from 4 nm (FRNP) to 53 nm (C815). The nanoparticles drying and calcination temperatures affected the size, shape and Ce^{3+} : Ce^{4+} ratio. Increasing calcination

temperatures caused the size of the nanoparticles to increase as well as reducing the presence of Ce^{3+}. Enhanced antibacterial efficacy was observed in the FRNP nanoparticles compared to the C385 and C815 cerium oxide nanoparticles.

Chapter 6
DISCUSSION

6.0 Freeze-Dried Scaffolds

6.0.1 Pore Size Distribution and Porosity

The porosity of natural bone depends upon the bone type and ranges from 50 to 90 % [349]. Therefore, bone scaffold porosity and pore interconnectivity are essential for the adhesion, proliferation, and differentiation of bone cells and the transport of nutrients and waste removal. Adequate porosity subsequently aids revascularisation [2] when scaffolds are implanted *in vivo* [350]. The bone scaffolds fabricated via the freeze-drying approach exhibit highly interconnected porous structures, as confirmed via SEM analysis. The pore size distribution and amount of porosity are affected by the initial freezing temperatures of the scaffolds. Freezing temperatures, i.e. > - 60 ˚C, increase the cooling rate creating a lower freezing temperature of the CS suspensions, which induces a greater driving force for pore nucleation. Thus, the resulting structures contain a higher number of smaller pore sizes. Additionally, lower freezing temperatures often lead to the formation of fewer large ice crystals, which causes the microstructure to contain pores orientated in a particular direction.

Conversely, higher freezing temperatures, i.e. < - 60 ˚C, create a significant number of ice crystals where the resulting microstructure contains unoriented pores, which vary in size. The scaffold freezing rate also plays a significant role in terms of porosity formation, where rapid freezing, i.e. with liquid nitrogen, forms porosity of 91 % to 95 %. The rapid freezing rate creates pore sizes in the range of 13 to 35 μm [351], which is significantly too small for suitable osteoblast proliferation and differentiation [351]. Furthermore, the rapid freezing also has the potential to form scaffold structures with closed-pore morphology, which would hinder inter-pore connectivity [352]. Early tissue engineering methods such as solvent casting and particulate leaching

determined synthetic bone scaffold porosity was required to be at least 90 % to achieve high pore interconnectivity [140, 353]. However, researchers have developed scaffolds with porosities which range from 55 % to 90 % for potential bone regeneration [354, 355] due to increased mechanical properties at lower porosities [351]. The total porosity determined via the liquid displacement method for the CH, 20, 30 40, and 50-DCPD scaffolds are 67.33 $\pm$ 10.78 %, 88.01 $\pm$ 15.17 %, 87.33 $\pm$ 16.38 %, 83.34 $\pm$ 15.17 %, and 73.90 $\pm$ 12.87 % respectively. There is a lack of consensus regarding the optimal pore size required for bone regeneration where pore sizes in the range from 50 to 1500 μm are suggested [351]. The CH scaffold expresses the most extensive pore size distribution (20 to 180 μm); however, increasing DCPD mineral concentration led to a significant increase in the number of pores and a reduction in the pore size distributions, i.e., 10 μm to 160 μm (20-DCPD), 10 to 110 μm (30-DCPD), 10 to 100 μm (40-DCPD) and 10 to 150 μm (50-DCPD).

The number of pores associated with the 50-DCPD scaffold reduced significantly, where the majority of pores coalesced, subsequently forming a less defined microstructure with reduced pore interconnectivity. The DNA quantification results signify cellular growth increase with increasing DCPD mineral concentration for the CH, 20, 30 and 40-DCPD freeze-dried scaffolds. However, the structural environment plays a significant role in cellular attachment and proliferation, which is evident for the 50-DCPD scaffolds where the cellular growth reduced by 24.14 $\pm$ 6.06 % and 30.77 $\pm$ 17.13 % at 3 and 7 days, respectively in comparison to the 40-DCPD scaffolds. The cellular decline is likely attributed to the reduced surface area due to lack of individual pores and pore interconnectivity which likely led to a reduction in the flow of essential nutrients.

6.0.2 Bone Scaffold Mechanical Properties

Potential bone scaffolds must possess adequate mechanical strength to support cellular growth as well as the ability to maintain structural integrity during and after placement into the defect site [16]. CS alone does not possess the mechanical strength required for load-bearing applications. Thus, the addition of DCPD mineral with CS provided not only enhanced mechanical properties but also increased the osteoconductivity of the freeze-dried scaffolds. The overall strength of the synthesised scaffolds increased with increasing DCPD mineral concentration, where the 50-DCPD scaffold expressed a 20.1 $\pm$ 0.54 kNm^{-2} increase in Young's Modulus and a 20.1 $\pm$ 0.28 kPa increase of tensile strength in comparison to the DCPD mineral-free CH scaffold.

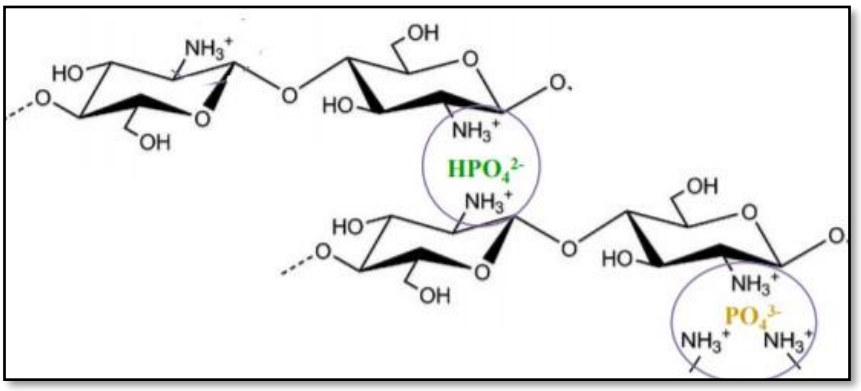

FIGURE 6.1 - Depiction of phosphate ion interaction with protonated amnio groups in the CS biopolymer chains.

The improvement of mechanical strength is likely attributed to the restriction of the CS biopolymer chains by the HPO_4^{2-} and PO_4^{3-} ions with increasing DCPD mineral concentration, as illustrated in Figure 6.1. The total porosity and the pore size distribution also has a significant effect on the mechanical properties of the

synthesised scaffolds [350]. The increase of DCPD mineral concentration led to a steady porosity increase for the CH, 20 and 30-DCPD scaffolds. Conversely, the 40 and 50-DCPD scaffolds exhibited a decline in the total porosity as determined via the liquid displacement method. The 50-DCPD scaffold presents the lowest total porosity (73.90 ± 12.87 %) for the DCPD mineral loaded scaffolds but the highest mechanical properties in comparison to the other scaffolds. The reduction of total porosity and the subsequent increase in mechanical properties is attributed to a decrease in the total void volume.

6.0.3 Biocompatibility and Degradation

Bone scaffolds must allow for adequate fluid absorption to avoid infection as inflammation liquids are often released during wound healing [313]. Synthetic scaffolds with increased water uptake capability are also found to promote the adhesion of cells; however, the mechanical scaffold properties are often reduced [306, 314, 315]. CS is a hydrophilic biopolymer [356] that facilitates the diffusion of water molecules due to the structural free volume and the ease of polymer chains mobility [357, 358]. Therefore, the DCPD mineral-free CH scaffolds presented the highest liquid uptake, while the 50-DCPD scaffolds exhibited the lowest swelling % increase. The increasing DCPD concentration restricted the mobility of the CS biopolymer chains, thus reducing the water molecules movement capability into the scaffolds. The swelling % experiments confirm all the polymer matrixes of the synthesised scaffolds can swell and store water which is favourable for living tissues [314]. Potential bone scaffolds and the scaffold degradation products must be biocompatible to ensure no cytotoxicity or inflammatory response is induced when implanted *in vivo* [359].

The term 'resorption' refers to the degradation of the implanted material from the cellular action of macrophages via phagocytosis [360]. While the term degradation' refers to the physical fragmentation and the disintegration of the material [163]. Calcium phosphates with relatively high crystallinity and Ca/P ratios, i.e. HA, exhibit delayed degradation and resorption rates within *in vitro* and *in vivo* applications, respectively. Porous cylindrical HA scaffolds demonstrated a 5.4 % volume reduction over six months when implanted into the cancellous bone of rabbits [361]. In contrast, under the same conditions, TCP minerals exhibited 85.4 % volume reduction [2, 361]. The Ca/P ionic ratio of DCPD mineral is lower compared to HA and so remains stable at lower pH values (acidic – pH 2 to 4.5). Conversely, at physiological pH, DCPD mineral is metastable [362] and undergoes resorption via osteoclastic activity as well as physiochemical dissolution [163, 179]. The mechanical stability of the scaffolds is directly affected by the rate of scaffold degradation. Increased degradation rates lead to the scaffold ceasing to provide the necessary mechanical support required by the tissue. Furthermore, the surrounding tissues may not be able to eliminate acid by-products; hence, leading to either a toxic or inflammatory response [351, 363, 364].

Conversely, the growth of new bone could be impeded if the degradation rate of the bone scaffold is too slow [351]. Therefore, potential bone scaffolds should be tuned to degrade at a similar rate to the regeneration rate of bone to ensure that the degraded scaffold material is replaced by the regenerated bone tissue [16]. The rate of bone regeneration is dependent upon the fracture size and can range from 50 to 100 μm/day for contact healing [365] and 3 to 8 weeks for gap healing [366]. The synthesised scaffold degradation results indicate increasing the DCPD mineral concentration reduces the scaffold mass loss. The mass loss reduction is related to the DD, M_w and

crystallinity as confirmed by other researchers [367]. The freeze-dried CH scaffold presented the most significant mass loss of 40.3 ± 1.7 % while the 50-DCPD scaffold exhibited the lowest mass loss at 22.7 ± 1.2 % after four weeks. The difference is likely attributed to the 50-DCPD exhibiting increased crystallinity as confirmed from the XRD analysis compared to the other scaffolds. Increased crystallinity leads to extensive hydrogen bonding and intermolecular forces between the CS biopolymer chains resulting in a more compact scaffold structure, thus reduces the water molecules accessibility to the hydrophilic groups.

6.0.4 Zeta Potential and Surface Chemistry

The zeta potential of CS is dependent upon the M_w. The structure of high M_w CS consists of longer polymeric chains indicating the presence of increased functional groups as compared to low M_w CS. Therefore, the relative positive charge (+ve) corresponds to the number of protonated amino groups present in the CS structure. As expected, the DCPD mineral-free DCPD scaffolds presented the highest zeta potential value of +43.47 ± 0.35 while the zeta potential for DCPD mineral was -12.44 ± 0.4 mV. The zeta potentials of the synthesised freeze-dried scaffolds follow a decreasing trend whereby increasing DCPD concentration caused a reduction in the positive zeta potential values. The reduction in the zeta potential is correlated to the presence of increasing DCPD phosphate ions, forming ionic bonds or electrostatic interactions with the protonated amino groups in CS. Other researchers report similar findings [368, 369].

6.0.5 Comparison to Commercial Bone Scaffolds

Table 6.1 compares the porosity and mechanical properties of commercially available bone scaffold such as Bio-Oss® (GeistlichPharma AG), Cerabone® (Botiss dental GmbH) and Maxresorb (Botiss dental GmbH) [370]. Unlike the synthesised DCPD mineral loaded scaffolds, where the primary constituent is chitosan, bovine mineral is the commercial scaffolds' primary component material. Increasing mineral content often leads to increased bone scaffolds mechanical properties, evidenced by the commercial scaffolds displayed in Table 6.1. Based on the proliferation results in section 4.3, the DCPD mineral loaded scaffolds have the correct structural environment to allow osteoblast proliferation; however, the freeze-dried scaffolds' mechanical properties are not comparable to the commercial scaffolds. Incorporating the synthesised DCPD mineral loaded scaffolds with other materials and structures, i.e., porous titanium dioxide scaffolds [370] will enable the synthesised scaffolds' mechanical properties to improve overall.

TABLE 6.1 - Examples of commercially available porous bone scaffolds and the corresponding properties.

Name	Composition Material	Porosity (%)	Mean Pore Diameter (μm)	Youngs Modulus (GPa)
Bio-Oss®	Bovine bone mineral	60.1 ± 3.4	320 ± 56.7	15 [370, 371]
Cerabone®	Bovine HA	69.0 ± 3.8	300 ± 43.2	83 [370, 372]

Maxresorb	60% HA and 40% ß-TCP	67.5 ± 3.6	140 ± 33.6	102 [370, 373]

6.1 Cerium Oxide Nanoparticles

6.1.1 Antibacterial Mechanism

The three main antibacterial mechanisms displayed by cerium oxide nanoparticles are:

- **cell wall adsorption -** Cerium oxide nanoparticles are positively charged, thus, via electrostatic interactions adsorb onto the negatively charged bacterial cell walls. The nanoparticles likely block the membrane and remain for a time impairing the viscosity of the cell wall, thus disrupting the transport exchange [374] between the solution and the bacterial cells [229].
- **Attack proteins or cell transport -** irregularly shaped nanoparticles are capable of causing damage to bacterial walls and has been demonstrated against Gram-positive bacteria [230, 375].
- **Induce oxidative stress –** cerium oxide nanoparticles have the potential to induce oxidative stress *in vivo* by the generation of reactive oxygen species (ROS). The ROS are developed on the bacterial cell wall surfaces from the reversible conversion of Ce^{3+} and Ce^{4+} [230]. The ROS are known to attack nucleic acids, proteins and polysaccharides, causing the loss of function, thus leading to the destruction and decomposition of bacteria [376].

Based on the results obtained, the relative size of the synthesised nanoparticles is also related to antibacterial effectiveness. Similar to positively charged particles, nanoparticles with relatively large surface areas can also adsorb tightly on the negatively charged bacterial cell walls disrupting the membrane integrity, causing cell lysis [377, 378]. As expected, the FRNP cerium oxide nanoparticles presented the highest antibacterial efficacy compared to the C385 and C815 nanoparticles. Therefore, the antibacterial results coincide with previously reported data which demonstrate that smaller particles size exhibit enhanced antibacterial properties due to increased surface area [368, 379].

6.1.2 Temperature-Dependent Particle Size

Based on the XRD results, increasing calcination temperature, i.e., from 80 ˚C to 815 ˚C, led to an increase in the calculated cerium oxide nanoparticles' crystallite sizes which, subsequently increased the size of the nanoparticles. The nanoparticles size was determined from the TEM images, where the FRNP, C385, and C815 nanoparticles are approximately 4 nm, 11 nm and 53 nm, respectively. Additionally, the surface area results determined via BET confirm the HRTEM findings whereby the surface area reduces as the particles size increases. The increase particles size with increasing treatment temperatures is contributed to two possible mechanisms, (i) Ostwald Ripening and (i) Oriented Attachment. Ostwald ripening is temperature-dependent as it influences the interfacial surface energies and the growth rate coefficients of the nanoparticles. Larger particles are more energetically stable as compared with smaller particles; thus, the possible dissolution of the smaller particles led to the growth of the larger sized nanoparticles. The oriented attachment mechanism is attributed to the aggregation of nanoparticles which reduces the total energy of the system and the

interphase boundaries, thus leading to increase particles size [380]. The aggregation/agglomeration of the synthesised cerium oxide nanoparticles is also confirmed from the obtained TEM analysis.

6.1.3 Antibacterial Properties of Cerium Oxide Nanoparticles

There is contradictory evidence in the literature regarding increased antibacterial effectiveness against Gram-positive and Gram-negative bacteria. Several studies have demonstrated superior action of cerium oxide nanoparticles against Gram-negative bacteria *Escherichia coli* as compared with Gram-positive bacteria *Bacillus subtilis* [381]. However, other studies expressed moderate antibacterial efficacy against Gram-negative bacteria, i.e. *Pseudomonas aeruginosa* and *Proteus vulgaris,* with increased activity against Gram-positive bacteria *Staphylococcus aureus* and *Streptococcus pneumoniae* [375, 382]. The variation of the cerium oxide antibacterial properties is likely related to possible oxygen defects in the nanoparticles, variation in the bandgap energies [383], the Ce^{3+} : Ce^{4+} ratio, irregular morphologies and possibly low dispersity [384].

The obtained antibacterial experimental results show that the most significant antibacterial activity is observed against Gram-negative bacteria *Escherichia coli* and *Pseudomonas aeruginosa* for the FRNP, C385 and C815 cerium oxide nanoparticles. During the synthesis of cerium oxide nanoparticles, it was observed that the drying method (i.e. freeze-drying or furnace drying) and calcination temperatures significantly affected the physicochemical properties, size, shape and the Ce^{3+}: Ce^{4+} ratio. XRD and TEM confirmed the formation of the spherical cerium oxide

nanoparticles. Also, the XPS and EELS data collected verified the presence of both Ce^{3+} and Ce^{4+} in all the synthesised nanoparticles. The presence of Ce^{3+} in the FRNP and C385 likely contributed to improved antibacterial effectiveness by the oxidative stress mechanism [230] compared with the C815 cerium oxide nanoparticles, which contains 95 % Ce^{4+} as confirmed from the EELS data.

6.1.4 Antibacterial Properties of Other Minerals and Nanoparticles

Fluorapatite doped with cerium (Ce^{3+}) and strontium (Sr^{2+}) [385] and Bioactive Glass has been found to exbibit antibacterial behaviour [386, 387]. Fluorapatite minerals at concentrations of 100 µg/ml tested against *Escherichia coli* (BL21) and *Staphylococcus aureus* (ATCC 25923) exhibited antibacterial behaviour with IC_{50} values of 110 $\pm$ 7.5 and 112 $\pm$ 6.2 respectively [385]. Also, antimicrobial activity was observed for bioactive glass S53P4 against aerobic and anaerobic bacteria in the planktonic and the sessile forms [386, 387]. The proposed bioglass antibacterial mechanism involves inducing changes in the cellular environmental pH, osmotic pressure and damaging the bacterial cell membranes leading to cellular death. Although cerium oxide nanoparticles also induce similar antibacterial actions, the presence of bivalency (Ce^{3+}/Ce^{4+}) presents additional antibacterial mechanisms, e.g., cell wall adsorption and inducing oxidative stress via generation of ROS. Therefore, increasing the antibacterial action of cerium oxide nanoparticles in comparison to single valance minerals/nanoparticles.

Chapter 7
CONCLUSIONS

7.0 Overview

The highly complex hierarchical structure of natural bone supports mechanical, biological and chemical functions simultaneously within the body. Current synthetic bone scaffolds lack the ability to address multiple requirements essential for the regeneration of bone tissue via a single construct. Research efforts focus on increasing the osteoconductive potential or improving the mechanical properties while overlooking the antibacterial efficacy of scaffolds. An ideal bone scaffold should exhibit: i) osteoconductive potential to aid the formation of new bone, ii) load-bearing properties, iii) appropriate microstructure to promote angiogenesis for nutrients circulation and iv) antibacterial efficacy to reduce or prevent infections which lead to failure of the surgery. This study aimed to investigate the osteoconductive and mechanical potential freeze-dried CS scaffolds embedded with different concentrations of DCPD mineral (0, 20, 30, 40 and 50 wt %) and the antibacterial potential of cerium oxide nanoparticles, respectively.

7.1 In-depth Conclusions

7.1.1 Freeze-Dried Scaffolds

The fabrication of porous freeze-dried CS scaffolds embedded with different concentrations of DCPD minerals (0, 20, 30, 40 and 50 wt%) was successful as confirmed from the XRD, FTIR and SEM characterisation results. CS alone does not possess the required mechanical properties for suitable bone scaffold synthesis; therefore, the incorporation of DCPD mineral improved the mechanical properties of the freeze-dried scaffolds. Increasing the DCPD mineral concentration from 0 to 50 wt % led to an increase in crystallinity of the scaffolds, thus enhancing the rigidity of the

structures. The Youngs Modulus and Tensile Strength were found to be proportional to the increasing DCPD concentrations where the 50-DCPD scaffolds presented five times greater mechanical strength as compared with the DCPD mineral-free scaffolds (CH).

Increasing the DCPD concentration also increases the hydrogen bonding and intermolecular forces between the CS biopolymer chains, thus, leading to a reduction in the scaffold liquid uptake and the rate of scaffold degradation. The CH scaffolds exhibited the most significant water uptake of 934.74 $\pm$ 29.87 %, while the 50-DCPD scaffolds exhibited a 557.36 $\pm$ 23.27 % increase, respectively. The initial scaffold degradation for 0 to 1 week was high; however, from week two to week four, a reduction in the scaffolds mass loss was observed. The reduction is related to increased scaffold crystallinity, causing restriction of the CS biopolymer chains, thus reducing the water molecules accessibility to the scaffold structures. The CH scaffolds mass loss determined after four weeks of phosphate buffer submersion at 37 $^{\circ}$C was 40.4 $\pm$ 1.7 %, while the 50-DCPD scaffolds presented mass losses of 22.7 $\pm$ 1.2 %. The ability to synthesise multilayered freeze-dried scaffolds based on the fundamentals of advanced manufacturing using freeze-drying was successful. The SEM analysis confirmed the interconnecting of two distinct layers via the described freeze-drying approach. **Layer-1** consisted of CS while **Layer-2** contained CS loaded with 30 wt % DCPD minerals, where the presence of the two distinct layers was confirmed from the EDS analysis. The scaffold porosity and pore size distribution were affected by the DCPD mineral concentration. The number of pores in the DCPD mineral loaded scaffolds were higher as compared with the CH scaffolds.

Additionally, the pore size distributed decreased with increasing DCPD mineral concentration (20 to 40 wt %). However, for scaffolds containing 50 wt % DCPD the porosity reduced and many of the pores coalesced, thus forming closed-ended pores. Since porosity and pore size plays an essential role in terms of osteoblast proliferation and differentiation, the negative effect of the reduced porosity is observed for the 50-DCPD scaffolds in terms of cellular growth. Increasing DCPD concentration led to increased osteoblast proliferation for the 20, 30 and 40-DCPD scaffolds. However, osteoblast reduction was observed at day 3 and 7 for the 50-DCPD scaffolds as compared with the 40-DCPD scaffolds. The reduction is attributed to the change in the scaffold architecture and reduced porosity.

7.1.2 Cerium Oxide Nanoparticles

The synthesis of cerium oxide nanoparticles was successful as confirmed from the XRD and TEM analysis. It has been demonstrated that the drying method (i.e. freeze-drying or furnace drying) and calcination temperature significantly affected the physicochemical properties, i.e. size, shape, agglomeration and the oxidation ratio Ce^{3+} : Ce^{4+}. Increased calcination temperatures from 280 ˚C to 815 ˚C caused the size of the synthesised nanoparticles to increase where the nanoparticles calcined at 815 ˚C (C815) were eight times larger as compared with FRNP nanoparticles. The nanoparticles size increase is temperature-dependent, thus related to Oswald ripening and oriented attachment. The synthesised cerium oxide nanoparticles exhibited agglomeration, causing a lack of individual particles as confirmed from the SEM analysis, which would have negatively impacted the antibacterial potential. Two oxidation states were detected for FRNP, FUNP, C280, C385 and C815 cerium oxide nanoparticles. However, with increasing calcination temperatures, the Ce^{3+} : Ce^{4+} ratio

reduced where the nanoparticles calcined at 815 ˚C consisted of only 5 % of Ce^{3+} ions with the remaining existing as Ce^{4+}. The antibacterial properties of nanoparticles are dependent upon two main factors, (i) the type of bacteria and (ii) the physicochemical properties of the nanoparticles.

The FRNP, C815 and C385 nanoparticles all exhibited antibacterial properties against *Escherichia coli*, *Pseudomonas aeruginosa* and *Staphylococcus epidermis*. The FRNP nanoparticles presented significant antibacterial efficacy as compared to the larger size C385 and C815 nanoparticles. Particles size influences the antibacterial potential, where relatively small-sized particles cerium oxide nanoparticles (< 10 nm) can cause more damage to bacteria compared to larger particle sizes. Additionally, increased antibacterial efficacy was observed towards the Gram-negative bacteria as compared with the Gram-positive bacteria. The reduced antibacterial potential against Gram-positive bacteria is attributed to the structural difference in thickness between Gram-positive and Gram-negative bacterial cell walls. As expected, the half-maximal inhibitory concentrations (IC_{50}) to reduce bacterial growth by 50 % were found to be lower for FRNP compared with the C385 and C815 nanoparticles.

7.2 Main Thesis Outcomes

The initial thesis research questions which were investigated have been addressed; the key findings are briefed below:

- The investigation confirmed the incorporation of DCPD mineral increases the mechanical properties of the mineral loaded porous freeze-dried scaffolds.

- The porosity of the scaffolds improved with increasing the DCPD concentrations for 20 wt % and 30 wt %.
- The osteoconductive potential was enhanced in the scaffolds containing 30 wt % to 40 wt % DCPD mineral.
- The freeze-drying approach successfully formed interconnected double-layered scaffolds.
- Increasing calcination temperature, particle size and Ce^{3+} : Ce^{4+} ratio altered the overall antibacterial efficacy of synthesised cerium oxide nanoparticles.
- The optimal Ce^{3+} : Ce^{4+} ratio, which observed more significant antibacterial efficacy, was found to be 63 % : 37 % (FRNP).

7.3 Future work

The possible future research pathways are summarised below:

1) Synthesise, characterise and evaluate whether freeze-dried CS scaffolds embedded with cerium oxide nanoparticles exhibit any cytotoxic effects to osteoblast cells by performing cytotoxicity experiments.
2) Investigate whether the scaffolds embedded with cerium oxide nanoparticles inhibit osteoblast growth and differentiation via proliferation experiments.
3) Fabricate and characterise the freeze-dried double-layered scaffold, where the outer layer contains CS with cerium oxide nanoparticles, and the inner layer contains DCPD mineral.
4) Cerium oxide has also been reported to exhibit angiogenetic potential (growth of blood vessels); thus, co-culture osteoblasts and endothelial cell experiments could be conducted.

5) Surface micropatterning on the surfaces of scaffolds could provide guided cellular growth if osteoblasts are seeded into the ablation channels. Initial experiments were conducted on DCPD mineral loaded CS films (Appendix VIIII).

REFERENCES

1. Dimitriou, R., et al., *Bone regeneration: current concepts and future directions.* BMC Med, 2011. **9**: p. 66.
2. Wang, W. and K.W.K. Yeung, *Bone grafts and biomaterials substitutes for bone defect repair: A review.* Bioactive Materials, 2017. **2**(4): p. 224-247.
3. Roberts, T.T. and A.J. Rosenbaum, *Bone grafts, bone substitutes and orthobiologics: the bridge between basic science and clinical advancements in fracture healing.* Organogenesis, 2012. **8**(4): p. 114-124.
4. Khan, S.N., et al., *The biology of bone grafting.* J Am Acad Orthop Surg, 2005. **13**(1): p. 77-86.
5. Bauer, T.W. and G.F. Muschler, *Bone Graft Materials: An Overview of the Basic Science.* Clinical Orthopaedics and Related Research®, 2000. **371**: p. 10-27.
6. Chocholata, P., V. Kulda, and V. Babuska, *Fabrication of Scaffolds for Bone-Tissue Regeneration.* Materials (Basel), 2019. **12**(4).
7. De Long, W.G., Jr., et al., *Bone grafts and bone graft substitutes in orthopaedic trauma surgery. A critical analysis.* J Bone Joint Surg Am, 2007. **89**(3): p. 649-58.
8. Jahangir, A.A., et al., *Bone-graft substitutes in orthopaedic surgery.* AAOS Now, 2008. **2**.
9. Turnbull, G., et al., *3D bioactive composite scaffolds for bone tissue engineering.* Bioactive Materials, 2018. **3**(3): p. 278-314.
10. Oh, S.-H., et al., *Growth of nano-scale hydroxyapatite using chemically treated titanium oxide nanotubes.* Biomaterials, 2005. **26**(24): p. 4938-4943.
11. Das, S., et al., *The induction of angiogenesis by cerium oxide nanoparticles through the modulation of oxygen in intracellular environments.* Biomaterials, 2012. **33**(31): p. 7746-7755.
12. Cheng, T., et al., *Osteogenic and antibacterial properties of vancomycin-laden mesoporous bioglass/PLGA composite scaffolds for bone regeneration in infected bone defects.* Artificial Cells, Nanomedicine, and Biotechnology, 2018. **46**(8): p. 1935-1947.
13. García-Quintanilla, M., et al., *Vaccines for Antibiotic-Resistant Bacteria: Possibility or Pipe Dream?* Trends Pharmacol Sci, 2016. **37**(2): p. 143-152.
14. Hajipour, M.J., et al., *Antibacterial properties of nanoparticles.* Trends in Biotechnology, 2012. **30**(10): p. 499-511.
15. Velasco, M.A., C.A. Narváez-Tovar, and D.A. Garzón-Alvarado, *Design, Materials, and Mechanobiology of Biodegradable Scaffolds for Bone Tissue Engineering.* BioMed Research International, 2015. **2015**: p. 729076.
16. Levengood, S.K.L. and M. Zhang, *Chitosan-based scaffolds for bone tissue engineering.* Journal of Materials Chemistry B, 2014. **2**(21): p. 3161-3184.
17. Martini, N., Bartholomew, *Fundamentals of Anatomy & physiology* 9ed. 2012, San Francisco: Pearson Education
18. Osborn, J.F. and H. Newesely, *The material science of calcium phosphate ceramics.* Biomaterials, 1980. **1**(2): p. 108-11.
19. Hench, L.L., et al., *Bonding mechanisms at the interface of ceramic prosthetic materials.* Journal of Biomedical Materials Research, 1971. **5**(6): p. 117-141.
20. LeGeros, R.Z., *Calcium phosphate-based osteoinductive materials.* Chemical Reviews, 2008. **108**(11): p. 4742-4753.
21. Jones, J.R., *19 - Scaffolds for tissue engineering*, in *Biomaterials, Artificial Organs and Tissue Engineering*, L.L. Hench and J.R. Jones, Editors. 2005, Woodhead Publishing. p. 201-214.

22. LeGeros, R.Z., *Properties of osteoconductive biomaterials: calcium phosphates.* Clin Orthop Relat Res, 2002(395): p. 81-98.

23. Daculsi, G., R.Z. LeGeros, and C. Deudon, *Scanning and transmission electron microscopy, and electron probe analysis of the interface between implants and host bone. Osseo-coalescence versus osseo-integration.* Scanning Microsc, 1990. **4**(2): p. 309-14.

24. Barrère, F., C.A. van Blitterswijk, and K. de Groot, *Bone regeneration: molecular and cellular interactions with calcium phosphate ceramics.* International journal of nanomedicine, 2006. **1**(3): p. 317-332.

25. Dhert, W.J.A., et al., *Integration of press-fit implants in cortical bone: A study on interface kinetics.* Journal of Biomedical Materials Research, 1998. **41**(4): p. 574-583.

26. Krieghoff, J., et al., *Increased pore size of scaffolds improves coating efficiency with sulfated hyaluronan and mineralization capacity of osteoblasts.* Biomaterials Research, 2019. **23**(1): p. 26.

27. Murphy, C.M., M.G. Haugh, and F.J. O'Brien, *The effect of mean pore size on cell attachment, proliferation and migration in collagen-glycosaminoglycan scaffolds for bone tissue engineering.* Biomaterials, 2010. **31**(3): p. 461-466.

28. Yannas, I.V., *Tissue regeneration by use of collagen-glycosaminoglycan copolymers.* Clin Mater, 1992. **9**(3-4): p. 179-87.

29. Karageorgiou, V. and D. Kaplan, *Porosity of 3D biomaterial scaffolds and osteogenesis.* Biomaterials, 2005. **26**(27): p. 5474-91.

30. Mikos, A. and J. Temenoff, *Formation of highly porous biodegradable scaffolds for tissue engineering.* Electronic Journal of Biotechnology (Chile) Num.2 Vol.3, 2000. **3**.

31. Eltom, A., G. Zhong, and A. Muhammad, *Scaffold Techniques and Designs in Tissue Engineering Functions and Purposes: A Review.* Advances in Materials Science and Engineering, 2019. **2019**: p. 1-13.

32. Sanz-Herrera, J.A., J.M. García-Aznar, and M. Doblaré, *On scaffold designing for bone regeneration: A computational multiscale approach.* Acta Biomater, 2009. **5**(1): p. 219-29.

33. Ji, C., et al., *Fabrication of porous chitosan scaffolds for soft tissue engineering using dense gas CO2.* Acta Biomaterialia, 2011. **7**(4): p. 1653-1664.

34. Nam, Y.S., J.J. Yoon, and T.G. Park, *A novel fabrication method of macroporous biodegradable polymer scaffolds using gas foaming salt as a porogen additive.* J Biomed Mater Res, 2000. **53**(1): p. 1-7.

35. Khairnar, S., et al., *A Review on Freeze Drying Process of Pharmaceuticals.* International Journal of Research in Pharmacy and science, 2012. **IJRPS 2013**: p. 76-94.

36. Garg, T., et al., *Scaffold: A Novel Carrier for Cell and Drug Delivery.* Critical reviews in therapeutic drug carrier systems, 2012. **29**: p. 1-63.

37. Liu, X. and P.X. Ma, *Polymeric Scaffolds for Bone Tissue Engineering.* Annals of Biomedical Engineering, 2004. **32**(3): p. 477-486.

38. Alizadeh, M., et al., *Microstructure and characteristic properties of gelatin/chitosan scaffold prepared by a combined freeze-drying/leaching method.* Materials Science and Engineering: C, 2013. **33**(7): p. 3958-3967.

39. Polo-Corrales, L., M. Latorre-Esteves, and J.E. Ramirez-Vick, *Scaffold design for bone regeneration.* Journal of nanoscience and nanotechnology, 2014. **14**(1): p. 15-56.

40. Anderson, J.M., *Biological Responses to Materials.* Annual Review of Materials Research, 2001. **31**(1): p. 81-110.

41. Navarro, M., et al., *Biomaterials in orthopaedics.* J R Soc Interface, 2008. **5**(27): p. 1137-58.

42. Bettinger, C.J., et al., *Three-dimensional microfluidic tissue-engineering scaffolds using a flexible biodegradable polymer.* Advanced Materials, 2006. **18**(2): p. 165-169.

43. Fidkowski, C., et al., *Endothelialized microvasculature based on a biodegradable elastomer.* Tissue Engineering, 2005. **11**(1-2): p. 302-309.

44. Rai, R., et al., *Synthesis, properties and biomedical applications of poly(glycerol sebacate) (PGS): A review.* Progress in Polymer Science, 2012. **37**(8): p. 1051-1078.

45. Wang, J., et al. *Biodegradable microfluidic scaffolds with tunable degradation properties from amino alcohol-based poly(ester amide) elastomers*. in *2010 MRS Fall Meeting, November 29, 2010 - December 3, 2010*. 2011. Boston, MA, United states: Materials Research Society.

46. Makadia, H.K. and S.J. Siegel, *Poly Lactic-co-Glycolic Acid (PLGA) as Biodegradable Controlled Drug Delivery Carrier.* Polymers, 2011. **3**(3): p. 1377-1397.

47. Mogosanu, D.E., et al., *Fabrication of 3-dimensional biodegradable microfluidic environments for tissue engineering applications.* Materials & Design, 2016. **89**: p. 1315-24.

48. Hench, L.L. and I. Thompson, *Twenty-first century challenges for biomaterials.* Journal of the Royal Society, Interface, 2010. **7 Suppl 4**(Suppl 4): p. S379-S391.

49. Rahman, S.U., et al., *Nanoscale and Macroscale Scaffolds with Controlled-Release Polymeric Systems for Dental Craniomaxillofacial Tissue Engineering.* Materials (Basel, Switzerland), 2018. **11**(8): p. 1478.

50. Hench, L.L. and J.M. Polak, *Third-generation biomedical materials.* Science, 2002. **295**(5557): p. 1014-7.

51. Place, E.S., N.D. Evans, and M.M. Stevens, *Complexity in biomaterials for tissue engineering.* Nature Materials, 2009. **8**(6): p. 457-470.

52. Dias, J.R., et al., *In situ Enabling Approaches for Tissue Regeneration: Current Challenges and New Developments.* Frontiers in Bioengineering and Biotechnology, 2020. **8**(85).

53. Abdulghani, S. and G.R. Mitchell, *Biomaterials for In Situ Tissue Regeneration: A Review.* Biomolecules, 2019. **9**(11): p. 750.

54. Reys, L.L., et al., *Revealing the potential of squid chitosan-based structures for biomedical applications.* Biomed Mater, 2013. **8**(4): p. 045002.

55. Leceta, I., et al., *Characterization and antimicrobial analysis of chitosan-based films.* Journal of Food Engineering, 2013. **116**(4): p. 889-99.

56. Kadokawa, J.-I., *Ionic Liquid as Useful Media for Dissolution, Derivatization, and Nanomaterial Processing of Chitin.* Green and Sustainable Chemistry, 2013. **03**: p. 19-25.

57. Rouhani Shirvan, A., M. Shakeri, and A. Bashari, *5 - Recent advances in application of chitosan and its derivatives in functional finishing of textiles*, in *The Impact and Prospects of Green Chemistry for Textile Technology*, I. Shahid ul and B.S. Butola, Editors. 2019, Woodhead Publishing. p. 107-133.

58. Luzi, F., D. Puglia, and L. Torre, *10 - Natural fiber biodegradable composites and nanocomposites: A biomedical application*, in *Biomass, Biopolymer-Based Materials, and Bioenergy*, D. Verma, et al., Editors. 2019, Woodhead Publishing. p. 179-201.

59. Roy, J., et al., *Solubility of Chitin: Solvents, Solution Behaviors and Their Related Mechanisms*. 2017.

60. Anitha, A., et al., *Chitin and chitosan in selected biomedical applications.* Progress in Polymer Science, 2014. **39**(9): p. 1644-1667.

61. Kurita, K., et al., *Reactivity characteristics of squid β-chitin as compared with those of shrimp chitin: High potentials of squid chitin as a starting material for facile chemical modifications.* Journal of Polymer Science Part A: Polymer Chemistry, 1994. **32**(6): p. 1027-1032.

62. Younes, I. and M. Rinaudo, *Chitin and chitosan preparation from marine sources. Structure, properties and applications.* Marine drugs, 2015. **13**(3): p. 1133-1174.

63. Rinaudo, M., *Chitin and chitosan: Properties and applications.* Progress in Polymer Science, 2006. **31**(7): p. 603-632.

64. Sagheer, F.A.A., et al., *Extraction and characterization of chitin and chitosan from marine sources in Arabian Gulf.* Carbohydrate Polymers, 2009. **77**(2): p. 410-419.

65. Dash, M., et al., *Chitosan - A versatile semi-synthetic polymer in biomedical applications.* Progress in Polymer Science (Oxford), 2011. **36**(8): p. 981-1014.

66. Roberts, G.A.F., *Chitin chemistry*. 1992, London: Macmillan.

67. Ibrahim, H.M. and E.M.R.E. Zairy. *Chitosan as a Biomaterial@ Structure, Properties, and Electrospun Nanofibers*. 2015.

68. Jayakumar, R., et al., *Biomedical applications of chitin and chitosan based nanomaterials—A short review.* Carbohydrate Polymers, 2010. **82**(2): p. 227-232.

69. Venkatesan, J. and S.K. Kim, *Chitosan composites for bone tissue engineering--an overview.* Mar Drugs, 2010. **8**(8): p. 2252-66.

70. Rodríguez-Vázquez, M., et al., *Chitosan and Its Potential Use as a Scaffold for Tissue Engineering in Regenerative Medicine.* BioMed Research International, 2015. **2015**: p. 821279.

71. Rodríguez-Vázquez, M., et al., *Chitosan and Its Potential Use as a Scaffold for Tissue Engineering in Regenerative Medicine.* BioMed research international, 2015. **2015**: p. 821279-821279.

72. Lee, D., et al., *Advances in Chitosan Material and its Hybrid Derivatives: A Review.* The Open Biomaterials Journal, 2009. **1**: p. 10-20.

73. Qasim, S.B., et al., *In-vitro and in-vivo degradation studies of freeze gelated porous chitosan composite scaffolds for tissue engineering applications.* Polymer Degradation and Stability, 2017. **136**: p. 31-38.

74. Ikeda, T., et al., *Fabrication and Characteristics of Chitosan Sponge as a Tissue Engineering Scaffold.* BioMed Research International, 2014. **2014**: p. 786892.

75. Chatelet, C., O. Damour, and A. Domard, *Influence of the degree of acetylation on some biological properties of chitosan films.* Biomaterials, 2001. **22**(3): p. 261-268.

76. Hirano, S., H. Tsuchida, and N. Nagao, *N-acetylation in chitosan and the rate of its enzymic hydrolysis.* Biomaterials, 1989. **10**(8): p. 574-576.

77. Aryaei, A., et al., *Cross-linked chitosan improves the mechanical properties of calcium phosphate-chitosan cement.* Materials science & engineering. C, Materials for biological applications, 2015. **54**: p. 14-19.

78. Freier, T., et al., *Controlling cell adhesion and degradation of chitosan films by N-acetylation.* Biomaterials, 2005. **26**(29): p. 5872-8.

79. Roberts, G.A.F., *Structure of Chitin and Chitosan*, in *Chitin Chemistry*, G.A.F. Roberts, Editor. 1992, Macmillan Education UK: London. p. 1-53.

80. Aranaz, I., et al., *Macroporous Calcium Phosphate/Chitosan Composites Prepared via Unidirectional Ice Segregation and Subsequent Freeze-Drying.* Materials (Basel, Switzerland), 2017. **10**(5): p. 516.

81. Jennings, J.A., *7 - Controlling chitosan degradation properties in vitro and in vivo*, in *Chitosan Based Biomaterials Volume 1*, J.A. Jennings and J.D. Bumgardner, Editors. 2017, Woodhead Publishing. p. 159-182.

82. Min, L.J., et al., *Chapter 6 - Biomaterials for Bioprinting*, in *3D Bioprinting and Nanotechnology in Tissue Engineering and Regenerative Medicine*, L.G. Zhang, J.P. Fisher, and K.W. Leong, Editors. 2015, Academic Press. p. 129-148.

83. Yuan, Y., et al., *Deacetylation of Chitosan: Material Characterization and in vitro Evaluation via Albumin Adsorption and Pre-Osteoblastic Cell Cultures.* Materials (Basel, Switzerland), 2011. **4**(8): p. 1399-1416.

84. Li, Q., et al., *Applications and Properties of Chitosan.* Journal of Bioactive and Compatible Polymers, 1992. **7**(4): p. 370-397.

85. Di Martino, A., M. Sittinger, and M.V. Risbud, *Chitosan: A versatile biopolymer for orthopaedic tissue-engineering.* Biomaterials, 2005. **26**(30): p. 5983-5990.

86. Goy, R., D. Britto, and O. Assis, *A Review of the Antimicrobial Activity of Chitosan.* Polimeros-ciencia E Tecnologia - POLIMEROS, 2009. **19**.

87. Peh, K., T. Khan, and H. Ch'ng, *Mechanical, bioadhesive strength and biological evaluations of chitosan films for wound dressing.* J Pharm Pharm Sci, 2000. **3**(3): p. 303-11.

88. Chen, X.-G., et al., *Molecular Affinity and Permeability of Different Molecular Weight Chitosan Membranes.* Journal of Agricultural and Food Chemistry, 2002. **50**(21): p. 5915-5918.

89. Croisier, F. and C. Jérôme, *Chitosan-based biomaterials for tissue engineering.* European Polymer Journal, 2013. **49**(4): p. 780-792.

90. Aljawish, A., et al., *Enzymatic synthesis of chitosan derivatives and their potential applications.* Journal of Molecular Catalysis B: Enzymatic, 2015. **112**: p. 25-39.

91. Zhang, M., et al., *Properties and biocompatibility of chitosan films modified by blending with PEG.* Biomaterials, 2002. **23**(13): p. 2641-8.

92. Lahiji, A., et al., *Chitosan supports the expression of extracellular matrix proteins in human osteoblasts and chondrocytes.* J Biomed Mater Res, 2000. **51**(4): p. 586-95.

93. Mi, F.-L., et al., *Fabrication and characterization of a sponge-like asymmetric chitosan membrane as a wound dressing.* Biomaterials, 2001. **22**(2): p. 165-173.

94. Rezwan, K., et al., *Biodegradable and bioactive porous polymer/inorganic composite scaffolds for bone tissue engineering.* Biomaterials, 2006. **27**(18): p. 3413-3431.

95. Garg, U., et al., *Current Advances in Chitosan Nanoparticles Based Drug Delivery and Targeting.* Advanced pharmaceutical bulletin, 2019. **9**(2): p. 195-204.

96. Rawal, T., et al., *Rifampicin loaded chitosan nanoparticle dry powder presents an improved therapeutic approach for alveolar tuberculosis.* Colloids Surf B Biointerfaces, 2017. **154**: p. 321-330.

97. Petkar, K.C., et al., *Development of Novel Octanoyl Chitosan Nanoparticles for Improved Rifampicin Pulmonary Delivery: Optimization by Factorial Design.* AAPS PharmSciTech, 2018. **19**(4): p. 1758-1772.

98. Oguido, A.P.M.T., et al., *Naringenin Eye Drops Inhibit Corneal Neovascularization by Anti-Inflammatory and Antioxidant Mechanisms.* Investigative Ophthalmology & Visual Science, 2017. **58**(13): p. 5764-5776.

99. Liu, S., S. Yang, and P.C. Ho, *Intranasal administration of carbamazepine-loaded carboxymethyl chitosan nanoparticles for drug delivery to the brain.* Asian Journal of Pharmaceutical Sciences, 2018. **13**(1): p. 72-81.

100. Sekar, V., et al., *Synthesis and characterization of chitosan ascorbate nanoparticles for therapeutic inhibition for cervical cancer and their in silico modeling.* Journal of Industrial and Engineering Chemistry, 2018. **62**: p. 239-249.

101. Esfandiarpour-Boroujeni, S., et al., *Fabrication and study of curcumin loaded nanoparticles based on folate-chitosan for breast cancer therapy application.* Carbohydr Polym, 2017. **168**: p. 14-21.

102. Kobayashi, N., et al., *The Roles of Peyer's Patches and Microfold Cells in the Gut Immune System: Relevance to Autoimmune Diseases.* Frontiers in Immunology, 2019. **10**(2345).

103. Illum, L., et al., *Chitosan as a novel nasal delivery system for vaccines.* Adv Drug Deliv Rev, 2001. **51**(1-3): p. 81-96.

104. Perinelli, D.R., et al., *Chitosan Loaded into a Hydrogel Delivery System as a Strategy to Treat Vaginal Co-Infection.* Pharmaceutics, 2018. **10**(1): p. 23.

105. Martínez-Pérez, B., et al., *Controlled-release biodegradable nanoparticles: From preparation to vaginal applications.* Eur J Pharm Sci, 2018. **115**: p. 185-195.

106. Sultankulov, B., et al., *Progress in the Development of Chitosan-Based Biomaterials for Tissue Engineering and Regenerative Medicine.* Biomolecules, 2019. **9**(9): p. 470.

107. Rousselle, P., M. Montmasson, and C. Garnier, *Extracellular matrix contribution to skin wound re-epithelialization.* Matrix Biol, 2019. **75-76**: p. 12-26.

108. Aguilar, A., et al., *Application of Chitosan in Bone and Dental Engineering.* Molecules (Basel, Switzerland), 2019. **24**(16): p. 3009.

109. Hu, Z., et al., *Chitosan-Based Composite Materials for Prospective Hemostatic Applications.* Mar Drugs, 2018. **16**(8).

110. Sagnella, S. and K. Mai-Ngam, *Chitosan based surfactant polymers designed to improve blood compatibility on biomaterials.* Colloids and Surfaces B: Biointerfaces, 2005. **42**(2): p. 147-155.

111. Khan, M.A. and M. Mujahid, *A review on recent advances in chitosan based composite for hemostatic dressings.* International Journal of Biological Macromolecules, 2019. **124**: p. 138-147.

112. Hu, Z., et al., *Investigation of the Effects of Molecular Parameters on the Hemostatic Properties of Chitosan.* Molecules, 2018. **23**(12).

113. Guo, X., et al., *Effects of Chitosan Oligosaccharides on Human Blood Components.* Frontiers in pharmacology, 2018. **9**: p. 1412-1412.

114. Mohamed, K.R., Z.M. El-Rashidy, and A.A. Salama, *In vitro properties of nano-hydroxyapatite/chitosan biocomposites.* Ceramics International, 2011. **37**(8): p. 3265-3271.

115. Zhang, J., et al., *Novel Mesoporous Hydroxyapatite/Chitosan Composite for Bone Repair.* Journal of Bionic Engineering, 2012. **9**(2): p. 243-251.

116. Takahashi, T., et al., *Characteristics of polyion complexes of chitosan with sodium alginate and sodium polyacrylate.* International Journal of Pharmaceutics, 1990. **61**(1): p. 35-41.

117. Kim, T.-H., et al., *Chemical modification of chitosan as a gene carrier in vitro and in vivo.* Progress in Polymer Science, 2007. **32**(7): p. 726-753.

118. Pavinatto, F.J., L. Caseli, and O.N. Oliveira, *Chitosan in Nanostructured Thin Films.* Biomacromolecules, 2010. **11**(8): p. 1897-1908.

119. Madihally, S.V. and H.W. Matthew, *Porous chitosan scaffolds for tissue engineering.* Biomaterials, 1999. **20**(12): p. 1133-42.

120. Seol, Y.-J., et al., *Chitosan sponges as tissue engineering scaffolds for bone formation.* Biotechnology Letters, 2004. **26**(13): p. 1037-1041.

121. Lee, J.S., et al., *In vivo study of chitosan-natural nano hydroxyapatite scaffolds for bone tissue regeneration.* International Journal of Biological Macromolecules, 2014. **67**: p. 360-366.

122. Kiuchi, H., W. Kai, and Y. Inoue, *Preparation and characterization of poly(ethylene glycol) crosslinked chitosan films.* Journal of Applied Polymer Science, 2008. **107**(6): p. 3823-3830.

123. Adekogbe, I. and A. Ghanem, *Fabrication and characterization of DTBP-crosslinked chitosan scaffolds for skin tissue engineering.* Biomaterials, 2005. **26**(35): p. 7241-7250.

124. Yin, Y., et al., *Preparation and characterization of macroporous chitosan-gelatin/beta-tricalcium phosphate composite scaffolds for bone tissue engineering.* J Biomed Mater Res A, 2003. **67**(3): p. 844-55.

125. Swetha, M., et al., *Biocomposites containing natural polymers and hydroxyapatite for bone tissue engineering.* Int J Biol Macromol, 2010. **47**(1): p. 1-4.

126. Zhang, Y. and M. Zhang, *Synthesis and characterization of macroporous chitosan/calcium phosphate composite scaffolds for tissue engineering.* Journal of Biomedical Materials Research, 2001. **55**(3): p. 304-312.

127. Zhang, Y. and M. Zhang, *Calcium phosphate/chitosan composite scaffolds for controlled in vitro antibiotic drug release.* Journal of Biomedical Materials Research, 2002. **62**(3): p. 378-386.

128. Lian, Q., et al., *Fabrication and In Vitro Evaluation of Calcium Phosphate Combined with Chitosan Fibers for Scaffold Structures.* Journal of Bioactive and Compatible Polymers - J BIOACT COMPAT POLYM, 2009. **24**: p. 113-124.

129. Li, H., et al., *Chitosan composite scaffolds for articular cartilage defect repair: a review.* RSC Advances, 2018. **8**(7): p. 3736-3749.

130. Comblain, F., et al., *Chitosan: A promising polymer for cartilage repair and viscosupplementation.* Bio-medical materials and engineering, 2017. **28**(s1): p. S209-S215.

131. Heath, C.A. and G.E. Rutkowski, *The development of bioartificial nerve grafts for peripheral-nerve regeneration.* Trends Biotechnol, 1998. **16**(4): p. 163-8.

132. Haipeng, G., et al., *Studies on nerve cell affinity of chitosan-derived materials.* Journal of Biomedical Materials Research, 2000. **52**(2): p. 285-295.

133. Yuan, Y., et al., *The interaction of Schwann cells with chitosan membranes and fibers in vitro.* Biomaterials, 2004. **25**(18): p. 4273-8.

134. Itoh, S., et al., *Effects of a laminin peptide (YIGSR) immobilized on crab-tendon chitosan tubes on nerve regeneration.* J Biomed Mater Res B Appl Biomater, 2005. **73**(2): p. 375-82.

135. Bellis, S.L., *Advantages of RGD peptides for directing cell association with biomaterials.* Biomaterials, 2011. **32**(18): p. 4205-4210.

136. Stashak, T.S., E. Farstvedt, and A. Othic, *Update on wound dressings: Indications and best use.* Clinical Techniques in Equine Practice, 2004. **3**(2): p. 148-163.

137. Kumirska, J., et al., *Application of spectroscopic methods for structural analysis of chitin and chitosan.* Marine drugs, 2010. **8**(5): p. 1567-1636.

138. Pillai, C., W. Paul, and C. Sharma, *Chitin and Chitosan Polymers: Chemistry, Solubility and Fiber Formation.* Progress in Polymer Science, 2009: p. 641-678.

139. Souza, M.P.C.d., et al., *Highlighting the impact of chitosan on the development of gastroretentive drug delivery systems.* International journal of biological macromolecules, 2020. **159**: p. 804-822.

140. Agrawal, P., G.J. Strijkers, and K. Nicolay, *Chitosan-based systems for molecular imaging.* Advanced Drug Delivery Reviews, 2010. **62**(1): p. 42-58.

141. Rong Huei, C. and H.-D. Hwa, *Effect of molecular weight of chitosan with the same degree of deacetylation on the thermal, mechanical, and permeability properties of the prepared membrane.* Carbohydrate Polymers, 1996. **29**(4): p. 353-358.

142. Zeng, L., et al., *Absorption and distribution of chitosan in mice after oral administration.* Carbohydrate Polymers, 2008. **71**: p. 435-440.

143. Muzzarelli, R.A., *Human enzymatic activities related to the therapeutic administration of chitin derivatives.* Cell Mol Life Sci, 1997. **53**(2): p. 131-40.

144. Tomihata, K. and Y. Ikada, *In vitro and in vivo degradation of films of chitin and its deacetylated derivatives.* Biomaterials, 1997. **18**(7): p. 567-575.

145. Yuan, Y., et al., *Mechanical property, degradation rate, and bone cell growth of chitosan coated titanium influenced by degree of deacetylation of chitosan.* J Biomed Mater Res B Appl Biomater, 2008. **86**(1): p. 245-52.

146. Yuan, Y., et al., *The effect of cross-linking of chitosan microspheres with genipin on protein release.* Carbohydrate Polymers, 2007. **68**: p. 561-567.

147. Pangburn, S.H., P.V. Trescony, and J. Heller, *Lysozyme degradation of partially deacetylated chitin, its films and hydrogels.* Biomaterials, 1982. **3**(2): p. 105-108.

148. Swoboda, J.G., et al., *Wall teichoic acid function, biosynthesis, and inhibition.* Chembiochem : a European journal of chemical biology, 2010. **11**(1): p. 35-45.

149. Raafat, D., et al., *Insights into the mode of action of chitosan as an antibacterial compound.* Applied and environmental microbiology, 2008. **74**(12): p. 3764-3773.

150. Silhavy, T.J., D. Kahne, and S. Walker, *The bacterial cell envelope.* Cold Spring Harbor perspectives in biology, 2010. **2**(5): p. a000414-a000414.

151. Kong, M., et al., *Preparation and antibacterial activity of chitosan microshperes in a solid dispersing system.* Frontiers of Materials Science in China, 2008. **2**(2): p. 214-220.

152. Yilmaz Atay, H., *Antibacterial Activity of Chitosan-Based Systems.* Functional Chitosan: Drug Delivery and Biomedical Applications, 2020: p. 457-489.

153. Helander, I.M., A. von Wright, and T.M. Mattila-Sandholm, *Potential of lactic acid bacteria and novel antimicrobials against Gram-negative bacteria.* Trends in Food Science & Technology, 1997. **8**(5): p. 146-150.

154. Prescott, L.M., J.P. Harley, and D.A. Klein, *Microbiology*. 2002: McGraw-Hill.

155. Green, D.W., *The bacterial cell wall as a source of antibacterial targets.* Expert Opin Ther Targets, 2002. **6**(1): p. 1-19.

156. Devlieghere, F., A. Vermeulen, and J. Debevere, *Chitosan: Antimicrobial activity, interactions with food components and applicability as a coating on fruit and vegetables.* Food Microbiology, 2004. **21**: p. 703-714.

157. Shahidi, F., J.K.V. Arachchi, and Y.J. Jeon, *Food applications of chitin and chitosans.* Trends in Food Science & Technology, 1999. **10**(2): p. 37-51.

158. Koilparambil, D., et al., *Antimicrobial Properties of Chitosan Nanoparticles: Mode of Action and Factors Affecting Activity.* Fibers and Polymers, 2017. **18**: p. 221-230.

159. Xiao, D., et al., *The role of calcium phosphate surface structure in osteogenesis and the mechanisms involved.* Acta Biomaterialia, 2020. **106**: p. 22-33.

160. Zhang, L., et al., *Three-dimensional (3D) printed scaffold and material selection for bone repair.* Acta Biomaterialia, 2019. **84**: p. 16-33.

161. Neacsu, I.A., et al., *Biomimetic Composite Scaffold Based on Naturally Derived Biomaterials.* Polymers, 2020. **12**(5): p. 1161.

162. van Vugt, T.A., et al., *3 - Biomaterials in treatment of orthopedic infections*, in *Management of Periprosthetic Joint Infections (PJIs)*, J.J.C. Arts and J. Geurts, Editors. 2017, Woodhead Publishing. p. 41-68.

163. Sheikh, Z., et al., *Mechanisms of in Vivo Degradation and Resorption of Calcium Phosphate Based Biomaterials.* Materials (Basel, Switzerland), 2015. **8**(11): p. 7913-7925.

164. Barney, V.C., M.P. Levin, and D.F. Adams, *Bioceramic implants in surgical periodontal defects. A comparison study.* J Periodontol, 1986. **57**(12): p. 764-70.

165. Sheikh, Z., C. Sima, and M. Glogauer, *Bone Replacement Materials and Techniques Used for Achieving Vertical Alveolar Bone Augmentation.* Materials, 2015. **8**(6): p. 2953-2993.

166. LeGeros, R.Z., *Calcium phosphate-based osteoinductive materials.* Chem Rev, 2008. **108**(11): p. 4742-53.

167. Müller, P., et al., *Calcium phosphate surfaces promote osteogenic differentiation of mesenchymal stem cells.* J Cell Mol Med, 2008. **12**(1): p. 281-91.

168. Yuan, H., et al., *Osteoinductive ceramics as a synthetic alternative to autologous bone grafting.* Proceedings of the National Academy of Sciences of the United States of America, 2010. **107**(31): p. 13614-13619.

169. Eliaz, N. and N. Metoki, *Calcium Phosphate Bioceramics: A Review of Their History, Structure, Properties, Coating Technologies and Biomedical Applications.* Materials (Basel, Switzerland), 2017. **10**(4): p. 334.

170. Brown, W.E., M. Mathew, and M.S. Tung, *Crystal chemistry of octacalcium phosphate.* Progress in Crystal Growth and Characterization, 1981. **4**(1): p. 59-87.

171. Chow, L.C., *Next generation calcium phosphate-based biomaterials.* Dent Mater J, 2009. **28**(1): p. 1-10.

172. Kay, M.I., R.A. Young, and A.S. Posner, *Crystal Structure of Hydroxyapatite.* Nature, 1964. **204**(4963): p. 1050-1052.

173. Habraken, W., et al., *Calcium phosphates in biomedical applications: materials for the future?* Materials Today, 2016. **19**(2): p. 69-87.

174. Samavedi, S., A.R. Whittington, and A.S. Goldstein, *Calcium phosphate ceramics in bone tissue engineering: A review of properties and their influence on cell behavior.* Acta Biomaterialia, 2013. **9**(9): p. 8037-8045.

175. Bohner, M. and J. Lemaître, *Can Bioactivity be Tested in vitro with SBF Solution?* Biomaterials, 2009. **30**: p. 2175-2179.

176. Jeong, J., et al., *Bioactive calcium phosphate materials and applications in bone regeneration.* Biomater Res, 2019. **23**: p. 4.

177. Douglas, T., et al., *Porous polymer/hydroxyapatite scaffolds: characterization and biocompatibility investigations.* J Mater Sci Mater Med, 2009. **20**(9): p. 1909-15.

178. Guo, H., et al., *Biocompatibility and osteogenicity of degradable Ca-deficient hydroxyapatite scaffolds from calcium phosphate cement for bone tissue engineering.* Acta Biomater, 2009. **5**(1): p. 268-78.

179. Tamimi, F., Z. Sheikh, and J. Barralet, *Dicalcium phosphate cements: Brushite and monetite.* Acta Biomaterialia, 2012. **8**(2): p. 474-487.

180. Mathew, M., et al., *The crystal structure of α-Ca3(PO4)2.* Acta Crystallographica Section B, 1977. **33**(5): p. 1325-1333.

181. Dickens, B., L.W. Schroeder, and W.E. Brown, *Crystallographic studies of the role of Mg as a stabilizing impurity in β-Ca3(PO4)2. The crystal structure of pure β-Ca3(PO4)2.* Journal of Solid State Chemistry, 1974. **10**(3): p. 232-248.

182. Strub, J.R., T.W. Gaberthüel, and A.R. Firestone, *Comparison of tricalcium phosphate and frozen allogenic bone implants in man.* Journal of periodontology, 1979. **50**(12): p. 624-629.

183. Baldock, W.T., et al., *An Evaluation of Tricalcium Phosphate Implants in Human Periodontal Osseous Defects of Two Patients.* Journal of Periodontology, 1985. **56**(1): p. 1-7.

184. Ronda, M., et al., *Expanded vs. dense polytetrafluoroethylene membranes in vertical ridge augmentation around dental implants: a prospective randomized controlled clinical trial.* Clin Oral Implants Res, 2014. **25**(7): p. 859-66.

185. Sakae, T., H. Nakada, and J. Legeros, *Historical Review of Biological Apatite Crystallography.* Journal of Hard Tissue Biology, 2015. **24**: p. 111-122.

186. Mathew, M. and S. Takagi, *Structures of Biological Minerals in Dental Research.* Journal of research of the National Institute of Standards and Technology, 2001. **106**(6): p. 1035-1044.

187. Pompe, W., et al., *Octacalcium phosphate – a metastable mineral phase controls the evolution of scaffold forming proteins.* Journal of Materials Chemistry B, 2015. **3**(26): p. 5318-5329.

188. Suzuki, O., et al., *Bone regeneration by synthetic octacalcium phosphate and its role in biological mineralization.* Curr Med Chem, 2008. **15**(3): p. 305-13.

189. Suzuki, O., *Octacalcium phosphate (OCP)-based bone substitute materials.* Japanese Dental Science Review, 2013. **49**(2): p. 58-71.

190. Brown, W.E., et al., *Octacalcium Phosphate and Hydroxyapatite: Crystallographic and Chemical Relations between Octacalcium Phosphate and Hydroxyapatite.* Nature, 1962. **196**(4859): p. 1050-1055.

191. Fernández, M., et al., *New model for the hydroxyapatite-octacalcium phosphate interface.* Acta crystallographica. Section B, Structural science, 2003. **59**: p. 175-81.

192. Zhan, J., et al., *Biomimetic Formation of Hydroxyapatite Nanorods by a Single-Crystal-to-Single-Crystal Transformation.* Advanced Functional Materials, 2005. **15**(12): p. 2005-2010.

193. Nelson, D.G.A. and J.D. McLean, *High-resolution electron microscopy of octacalcium phosphate and its hydrolysis products.* Calcified Tissue International, 1984. **36**(1): p. 219-232.

194. Tseng, Y.-H., C.-Y. Mou, and J.C.C. Chan, *Solid-State NMR Study of the Transformation of Octacalcium Phosphate to Hydroxyapatite: A Mechanistic Model for Central Dark Line Formation.* Journal of the American Chemical Society, 2006. **128**(21): p. 6909-6918.

195. Hughes, J.M., *Structure and Chemistry of the Apatites and Other Calcium Orthophosphates By J. C. Elliot (The London Hospital Medical College). Elsevier: Amsterdam. 1994. xii + 389 pp. ISBN 0-444-81582-1.* Journal of the American Chemical Society, 1996. **118**(12): p. 3072-3072.

196. Rubini, K., E. Boanini, and A. Bigi, *Role of Aspartic and Polyaspartic Acid on the Synthesis and Hydrolysis of Brushite.* Journal of functional biomaterials, 2019. **10**(1): p. 11.

197. Dorozhkin, S.V., *Calcium orthophosphates (CaPO4): occurrence and properties.* Progress in Biomaterials, 2016. **5**(1): p. 9-70.

198. Bigi, A. and E. Boanini, *Calcium Phosphates as Delivery Systems for Bisphosphonates.* J Funct Biomater, 2018. **9**(1).

199. Zhang, Z.-L., et al., *Identification of dicalcium phosphate dihydrate deposited during osteoblast mineralization in vitro.* Journal of Inorganic Biochemistry, 2014. **131**: p. 109-114.

200. Anastasiou, A.D., et al., *Sintering of calcium phosphates with a femtosecond pulsed laser for hard tissue engineering.* Materials and Design, 2016. **101**: p. 346-354.

201. Redepenning, J., et al., *Characterization of electrolytically prepared brushite and hydroxyapatite coatings on orthopedic alloys.* Journal of Biomedical Materials Research, 1996. **30**(3): p. 287-294.

202. Fulmer, M.T. and P.W. Brown, *Hydrolysis of dicalcium phosphate dihydrate to hydroxyapatite.* Journal of Materials Science: Materials in Medicine, 1998. **9**(4): p. 197-202.

203. Boanini, E., M. Gazzano, and A. Bigi, *Ionic substitutions in calcium phosphates synthesized at low temperature.* Acta Biomaterialia, 2010. **6**(6): p. 1882-1894.

204. Laskus, A., A. Zgadzaj, and J. Kolmas, *Selenium-Enriched Brushite: A Novel Biomaterial for Potential Use in Bone Tissue Engineering.* International journal of molecular sciences, 2018. **19**(12): p. 4042.

205. Theiss, F., et al., *Biocompatibility and resorption of a brushite calcium phosphate cement.* Biomaterials, 2005. **26**(21): p. 4383-94.

206. Xia, Z., et al., *In vitro biodegradation of three brushite calcium phosphate cements by a macrophage cell-line.* Biomaterials, 2006. **27**(26): p. 4557-4565.

207. Tamimi, F., et al., *Brushite–collagen composites for bone regeneration.* Acta biomaterialia, 2008. **4**: p. 1315-21.

208. Kuemmerle, J.M., et al., *Assessment of the suitability of a new brushite calcium phosphate cement for cranioplasty – an experimental study in sheep.* Journal of Cranio-Maxillofacial Surgery, 2005. **33**(1): p. 37-44.

209. Barinov, S. and V. Komlev, *Calcium phosphate based bioceramics for bone tissue engineering*. 2008.

210. Lu, J., et al., *The biodegradation mechanism of calcium phosphate biomaterials in bone.* Journal of Biomedical Materials Research, 2002. **63**(4): p. 408-412.

211. Wang, L. and G.H. Nancollas, *Calcium Orthophosphates: Crystallization and Dissolution.* Chemical Reviews, 2008. **108**(11): p. 4628-4669.

212. Pulcini, C., et al., *Adverse effects of parenteral antimicrobial therapy for chronic bone infections.* European Journal of Clinical Microbiology & Infectious Diseases, 2008. **27**(12): p. 1227-1232.

213. Lew, D.P. and F.A. Waldvogel, *Osteomyelitis.* The Lancet, 2004. **364**(9431): p. 369-379.

214. Bernard, L., et al., *Trends in the treatment of orthopaedic prosthetic infections.* Journal of Antimicrobial Chemotherapy, 2004. **53**(2): p. 127-129.

215. Ribeiro, M., F.J. Monteiro, and M.P. Ferraz, *Infection of orthopedic implants with emphasis on bacterial adhesion process and techniques used in studying bacterial-material interactions.* Biomatter, 2012. **2**(4): p. 176-194.

216. Johnson, C.T. and A.J. Garcia, *Scaffold-based anti-infection strategies in bone repair.* Ann Biomed Eng, 2015. **43**(3): p. 515-28.

217. Anastasiou, A.D., et al., *Antibacterial properties and regenerative potential of Sr(2+) and Ce(3+) doped fluorapatites; a potential solution for peri-implantitis.* Sci Rep, 2019. **9**(1): p. 14469.

218. Knetsch, M.L.W. and L.H. Koole, *New Strategies in the Development of Antimicrobial Coatings: The Example of Increasing Usage of Silver and Silver Nanoparticles.* Polymers, 2011. **3**(1): p. 340.

219. Wang, L., C. Hu, and L. Shao, *The antimicrobial activity of nanoparticles: present situation and prospects for the future.* International journal of nanomedicine, 2017. **12**: p. 1227-1249.

220. Holmes, N.E., et al., *Genetic and molecular predictors of high vancomycin MIC in Staphylococcus aureus bacteremia isolates.* Journal of clinical microbiology, 2014. **52**(9): p. 3384-3393.

221. Parsons, B. and E. Strauss, *Surgical management of chronic osteomyelitis.* The American Journal of Surgery, 2004. **188**(1): p. 57-66.

222. Mahmoudi, M. and V. Serpooshan, *Silver-Coated Engineered Magnetic Nanoparticles Are Promising for the Success in the Fight against Antibacterial Resistance Threat*. Vol. 6. 2012. 2656-64.

223. Høiby, N., et al., *Antibiotic resistance of bacterial biofilms.* Int J Antimicrob Agents, 2010. **35**(4): p. 322-32.

224. Hall-Stoodley, L. and P. Stoodley, *Evolving concepts in biofilm infections.* Cell Microbiol, 2009. **11**(7): p. 1034-43.

225. Qiu, Z., et al., *Nanoalumina promotes the horizontal transfer of multiresistance genes mediated by plasmids across genera.* Proceedings of the National Academy of Sciences of the United States of America, 2012. **109**(13): p. 4944-4949.

226. Poole, K., *Mechanisms of bacterial biocide and antibiotic resistance.* J Appl Microbiol, 2002. **92 Suppl**: p. 55s-64s.

227. Raza, M.A., et al., *Size- and Shape-Dependent Antibacterial Studies of Silver Nanoparticles Synthesized by Wet Chemical Routes.* Nanomaterials (Basel, Switzerland), 2016. **6**(4): p. 74.

228. Hajipour, M.J., et al., *Antibacterial properties of nanoparticles.* Trends Biotechnol, 2012. **30**(10): p. 499-511.

229. Thill, A., et al., *Cytotoxicity of CeO2 nanoparticles for Escherichia coli. Physico-chemical insight of the cytotoxicity mechanism.* Environ Sci Technol, 2006. **40**(19): p. 6151-6.

230. Zhang, M., et al., *Antibacterial mechanism and activity of cerium oxide nanoparticles.* Science China Materials, 2019. **62**(11): p. 1727-1739.

231. Shrivastava, S., et al., *Characterization of enhanced antibacterial effects of novel silver nanoparticles.* Nanotechnology, 2007. **18**(22): p. 225103.

232. Usman, M.S., et al., *Synthesis, characterization, and antimicrobial properties of copper nanoparticles.* International journal of nanomedicine, 2013. **8**: p. 4467-4479.

233. Jones, N., et al., *Antibacterial activity of ZnO nanoparticle suspensions on a broad spectrum of microorganisms.* FEMS Microbiol Lett, 2008. **279**(1): p. 71-6.

234. Cho, M., et al., *Linear correlation between inactivation of E. coli and OH radical concentration in TiO2 photocatalytic disinfection.* Water Res, 2004. **38**(4): p. 1069-77.

235. Ramalingam, B., T. Parandhaman, and S.K. Das, *Antibacterial Effects of Biosynthesized Silver Nanoparticles on Surface Ultrastructure and Nanomechanical Properties of Gram-Negative Bacteria viz. Escherichia coli and Pseudomonas aeruginosa.* ACS Appl Mater Interfaces, 2016. **8**(7): p. 4963-76.

236. AshaRani, P.V., et al., *Cytotoxicity and Genotoxicity of Silver Nanoparticles in Human Cells.* ACS Nano, 2009. **3**(2): p. 279-290.

237. Johnston, H.J., et al., *A review of the in vivo and in vitro toxicity of silver and gold particulates: Particle attributes and biological mechanisms responsible for the observed toxicity.* Critical Reviews in Toxicology, 2010. **40**(4): p. 328-346.

238. Shareena Dasari, T.P., Y. Zhang, and H. Yu, *Antibacterial Activity and Cytotoxicity of Gold (I) and (III) Ions and Gold Nanoparticles.* Biochemistry & pharmacology : open access, 2015. **4**(6): p. 199.

239. Sawai, J., et al., *Antibacterial characteristics of magnesium oxide powder.* World Journal of Microbiology and Biotechnology, 2000. **16**(2): p. 187-194.

240. Sawai, J., et al., *Antibacterial Characteristics of Magnesium Oxide Powder.* World Journal of Microbiology and Biotechnology, 2000. **16**: p. 187-194.

241. Qing, Y.a., et al., *Potential antibacterial mechanism of silver nanoparticles and the optimization of orthopedic implants by advanced modification technologies.* International journal of nanomedicine, 2018. **13**: p. 3311-3327.

242. Dong, Y., et al., *Antibacterial activity of silver nanoparticles of different particle size against Vibrio Natriegens.* PLOS ONE, 2019. **14**(9): p. e0222322.

243. Wang, L., C. Hu, and L. Shao, *The antimicrobial activity of nanoparticles: Present situation and prospects for the future.* International Journal of Nanomedicine, 2017. **Volume 12**: p. 1227-1249.

244. Pal, S., Y.K. Tak, and J.M. Song, *Does the Antibacterial Activity of Silver Nanoparticles Depend on the Shape of the Nanoparticle? A Study of the Gram-Negative Bacterium <em>Escherichia coli</em&gt.* Applied and Environmental Microbiology, 2007. **73**(6): p. 1712.

245. Reed, K., et al., *Exploring the properties and applications of nanoceria: is there still plenty of room at the bottom?* Environmental Science: Nano, 2014. **1**(5): p. 390-405.

246. Lv, G., et al., *The application of nanoceria in the bio-antioxidation.* Scientia Sinica Chimica, 2013. **43**: p. 1309.

247. Hirst, S.M., et al., *Anti-inflammatory Properties of Cerium Oxide Nanoparticles.* Small, 2009. **5**(24): p. 2848-2856.

248. Perez, J.M., et al., *Synthesis of biocompatible dextran-coated nanoceria with pH-dependent antioxidant properties.* Small, 2008. **4**(5): p. 552-6.

249. Tarnuzzer, R., et al., *Vacancy Engineered Ceria Nanostructures for Protection from Radiation-Induced Cellular Damage.* Nano letters, 2006. **5**: p. 2573-7.

250. Tsai, Y.Y., et al., *Novel synthesis of cerium oxide nanoparticles for free radical scavenging.* Nanomedicine (Lond), 2007. **2**(3): p. 325-32.

251. Park, B., et al., *Hazard and risk assessment of a nanoparticulate cerium oxide-based diesel fuel additive - a case study.* Inhal Toxicol, 2008. **20**(6): p. 547-66.

252. De Marzi, L., et al., *Cytotoxicity and genotoxicity of ceria nanoparticles on different cell lines in vitro.* Int J Mol Sci, 2013. **14**(2): p. 3065-77.

253. Das, M., et al., *Auto-catalytic ceria nanoparticles offer neuroprotection to adult rat spinal cord neurons.* Biomaterials, 2007. **28**(10): p. 1918-1925.

254. Babu, K.S., et al., *Cytotoxicity and antibacterial activity of gold-supported cerium oxide nanoparticles.* International journal of nanomedicine, 2014. **9**: p. 5515-5531.

255. Channei, D., et al., *Aqueous and Surface Chemistries of Photocatalytic Fe-Doped CeO2 Nanoparticles.* Catalysts, 2017. **7**(2): p. 45.

256. Korsvik, C., et al., *Superoxide dismutase mimetic properties exhibited by vacancy engineered ceria nanoparticles.* Chemical Communications, 2007(10): p. 1056-1058.

257. Celardo, I., et al., *Pharmacological potential of cerium oxide nanoparticles.* Nanoscale, 2011. **3**(4): p. 1411-20.

258. Heckert, E.G., et al., *The role of cerium redox state in the SOD mimetic activity of nanoceria.* Biomaterials, 2008. **29**(18): p. 2705-9.

259. Pelletier, D.A., et al., *Effects of Engineered Cerium Oxide Nanoparticles on Bacterial Growth and Viability.* Applied and Environmental Microbiology, 2010. **76**(24): p. 7981-7989.

260. Limbach, L.K., et al., *Removal of oxide nanoparticles in a model wastewater treatment plant: influence of agglomeration and surfactants on clearing efficiency.* Environ Sci Technol, 2008. **42**(15): p. 5828-33.

261. Van Hoecke, K., et al., *Fate and effects of CeO2 nanoparticles in aquatic ecotoxicity tests.* Environ Sci Technol, 2009. **43**(12): p. 4537-46.

262. Lin, W., et al., *Toxicity of Cerium Oxide Nanoparticles in Human Lung Cancer Cells.* International Journal of Toxicology, 2006. **25**(6): p. 451-457.

263. Zhang, W., et al., *Progress in Drying Technology for Nanomaterials AU - Wang, Baohe.* Drying Technology, 2005. **23**(1-2): p. 7-32.

264. Aguilera-Correa, J.J., et al., *A New Antibiotic-Loaded Sol-Gel Can Prevent Bacterial Prosthetic Joint Infection: From in vitro Studies to an in vivo Model.* Frontiers in Microbiology, 2020. **10**(2935).

265. Crémet, L., et al., *Orthopaedic-implant infections by Escherichia coli: Molecular and phenotypic analysis of the causative strains.* Journal of Infection, 2012. **64**(2): p. 169-175.

266. Olivares, E., et al., *Clinical Impact of Antibiotics for the Treatment of Pseudomonas aeruginosa Biofilm Infections.* Frontiers in Microbiology, 2020. **10**(2894).

267. Mahdi, A.A., T.S. Al-Salmani, and M.M. Al-Qaisi, *The Novel Role of Healing from Bacterial Infections of Lower Limb Open Fractures by X-Ray Exposure.* International Journal of Microbiology, 2020. **2020**: p. 3129356.

268. Davidson, D.J., D. Spratt, and A.D. Liddle, *Implant materials and prosthetic joint infection: the battle with the biofilm.* EFORT Open Reviews, 2019. **4**(11): p. 633-639.

269. Clark, J. *THE BEER-LAMBERT LAW*. 2007 [cited 2020 10/09/2020]; Available from: https://www.chemguide.co.uk/analysis/uvvisible/beerlambert.html.

270. Nassar, A., *ENHANCING THE PERFORMANCE OF COLD BITUMEN EMULSION MIXTURE USING SUPPLEMENTARY CEMENTITIOUS*. 2016.

271. Bumbrah, G.S. and R.M. Sharma, *Raman spectroscopy – Basic principle, instrumentation and selected applications for the characterization of drugs of abuse.* Egyptian Journal of Forensic Sciences, 2016. **6**(3): p. 209-215.

272. Jones, R.R., et al., *Raman Techniques: Fundamentals and Frontiers.* Nanoscale Research Letters, 2019. **14**(1): p. 231.

273. Ember, K.J.I., et al., *Raman spectroscopy and regenerative medicine: a review.* npj Regenerative Medicine, 2017. **2**(1): p. 12.

274. Instruments, N. *How a Scanning Electron Microscope Works*. 2020 [cited 2020 10/09/2020]; Available from: https://www.nanoscience.com/techniques/scanning-electron-microscopy/#:~:text=A%20scanning%20electron%20microscope%20(SEM,the%20surface%20topography%20and%20composition.

275. Physics, W.D.o. *Transmission Electron Microscopy (TEM)*. 2020 [cited 2020 10/09/2020]; Available from: https://warwick.ac.uk/fac/sci/physics/current/postgraduate/regs/mpagswarwick/ex5/techniques/structural/tem/.

276. Corporation, H.H.-T. *Principle of Differential Thermal Analysis (DTA)*. 2001 13/09/2020]; Available from: https://www.hitachi-hightech.com/global/products/science/tech/ana/thermal/descriptions/dta.html.

277. Loh, Q.L. and C. Choong, *Three-dimensional scaffolds for tissue engineering applications: role of porosity and pore size.* Tissue engineering. Part B, Reviews, 2013. **19**(6): p. 485-502.

278. Guarino, V., et al., *Polylactic acid fibre-reinforced polycaprolactone scaffolds for bone tissue engineering.* Biomaterials, 2008. **29**(27): p. 3662-3670.

279. Zhao, F., et al., *Preparation and histological evaluation of biomimetic three-dimensional hydroxyapatite/chitosan-gelatin network composite scaffolds.* Biomaterials, 2002. **23**(15): p. 3227-3234.

280. Lu, G.W. and P. Gao, *CHAPTER 3 - Emulsions and Microemulsions for Topical and Transdermal Drug Delivery*, in *Handbook of Non-Invasive Drug Delivery Systems*, V.S. Kulkarni, Editor. 2010, William Andrew Publishing: Boston. p. 59-94.

281. Energy, U.o.C.f.t.U.D.o. *XPS Works*. 2000 17/09/2020]; Available from: https://www.lanl.gov/orgs/nmt/nmtdo/AQarchive/04summer/XPS.html#:~:text=It%20can%20detect%20all%20of,%2D9%20millibar%20(mbar).

282. Baer, D.R. and S. Thevuthasan, *Chapter 16 - Characterization of Thin Films and Coatings*, in *Handbook of Deposition Technologies for Films and Coatings (Third Edition)*, P.M. Martin, Editor. 2010, William Andrew Publishing: Boston. p. 749-864.

283. Mather, R.R., *13 - Surface modification of textiles by plasma treatments*, in *Surface Modification of Textiles*, Q. Wei, Editor. 2009, Woodhead Publishing. p. 296-317.

284. Greczynski, G. and L. Hultman, *X-ray photoelectron spectroscopy: Towards reliable binding energy referencing.* Progress in Materials Science, 2020. **107**: p. 100591.

285. Clais, S., et al., *Comparison of viable plate count, turbidity measurement and real-time PCR for quantification of Porphyromonas gingivalis.* Letters in Applied Microbiology, 2015. **60**(1): p. 79-84.

286. Gritsch, L., et al., *Fabrication and characterization of copper(II)-chitosan complexes as antibiotic-free antibacterial biomaterial.* Carbohydr Polym, 2018. **179**: p. 370-378.

287. Lapa, A., et al., *Correction: Ga and Ce ion-doped phosphate glass fibres with antibacterial properties and their composite for wound healing applications.* Journal of Materials Chemistry B, 2019. **7**.

288. Gritsch, L., et al., *Chitosan/hydroxyapatite composite bone tissue engineering scaffolds with dual and decoupled therapeutic ion delivery: copper and strontium.* Journal of Materials Chemistry B, 2019. **7**(40): p. 6109-6124.

289. Rey, C., et al., *Characterization of Calcium Phosphates Using Vibrational Spectroscopies*. 2014. p. 229-266.

290. Alsubhe, E., et al., *Analysis of the osteogenic and mechanical characteristics of iron (Fe2+/Fe3+)-doped β-calcium pyrophosphate.* Materials Science and Engineering: C, 2020. **115**: p. 111053.

291. Alsubhe, E.H., *The influence of iron-doped calcium phosphate with different concentration in bone tissue engineering*, in *School of Chemical & Processing Engineering* 2016, Leeds University p. 54.

292. Yasmeen, S., et al., *Chromium (VI) Ions Removal from Tannery Effluent using Chitosan-Microcrystalline Cellulose Composite as Adsorbent.* International Research Journal of Pure and Applied Chemistry, 2016. **10**: p. 1-14.

293. Mandel, S. and A.C. Tas, *Brushite (CaHPO(4)·2H(2)O) to octacalcium phosphate (Ca(8)(HPO(4))(2)(PO(4))(4)·5H(2)O) transformation in DMEM solutions at 36.5°C.* Mater Sci Eng C Mater Biol Appl, 2010. **30**(2): p. 245-254.

294. Lee, D. and P.N. Kumta, *Chemical synthesis and stabilization of magnesium substituted brushite.* Materials Science and Engineering: C, 2010. **30**(7): p. 934-943.

295. Singh, S., et al., *Synthesis of brushite nanoparticles at different temperatures.* Chemical Papers, 2010. **64**(4): p. 491.

296. Mai, T., et al., *Anionic Polymer Brushes for Biomimetic Calcium Phosphate Mineralization-A Surface with Application Potential in Biomaterials.* Polymers, 2018. **10**(10): p. 1165.

297. Fadeeva, I.V., et al., *Interactions of calcium phosphates with chitosan.* Doklady Chemistry, 2011. **441**(2): p. 387-390.

298. Wan, Y., et al., *Synthesis, Characterization and Ionic Conductive Properties of Phosphorylated Chitosan Membranes.* Macromolecular Chemistry and Physics, 2003. **204**(5-6): p. 850-858.

299. MJ, L.D., et al., *The Impact of the Ionic Cross-Linking Mode on the Physical and In Vitro Dexamethasone Release Properties of Chitosan/Hydroxyapatite Beads.* Molecules, 2019. **24**(24).

300. Yu, J., H. Xia, and Q.-Q. Ni, *A three-dimensional porous hydroxyapatite nanocomposite scaffold with shape memory effect for bone tissue engineering.* Journal of Materials Science, 2018. **53**.

301. Lee, S.J., et al., *Macroporous biodegradable natural/synthetic hybrid scaffolds as small intestine submucosa impregnated poly(D,L-lactide-co-glycolide) for tissue-engineered bone.* J Biomater Sci Polym Ed, 2004. **15**(8): p. 1003-17.

302. Yu, J., H. Xia, and Q.-Q. Ni, *A three-dimensional porous hydroxyapatite nanocomposite scaffold with shape memory effect for bone tissue engineering.* Journal of Materials Science, 2017. **53**: p. 4734-4744.

303. Oliveira, J.M., et al., *Novel hydroxyapatite/chitosan bilayered scaffold for osteochondral tissue-engineering applications: Scaffold design and its performance when seeded with goat bone marrow stromal cells.* Biomaterials, 2006. **27**(36): p. 6123-6137.

304. Klawitter, J.J., et al., *An evaluation of bone growth into porous high density polyethylene.* Journal of Biomedical Materials Research, 1976. **10**(2): p. 311-323.

305. Lewandowska, K., *Miscibility and thermal stability of poly(vinyl alcohol)/chitosan mixtures.* Thermochimica Acta, 2009. **493**(1): p. 42-48.

306. Ruini, F., et al., *Chitosan membranes for tissue engineering: comparison of different crosslinkers.* Biomedical Materials, 2015. **10**(6): p. 065002.

307. Mucha, M. and A. Pawlak, *Complex study on chitosan degradability.* Polimery, 2002. **47**: p. 509-516.

308. Szymańska, E. and K. Winnicka, *Stability of chitosan-a challenge for pharmaceutical and biomedical applications.* Marine drugs, 2015. **13**(4): p. 1819-1846.

309. Mallika, P., A. Himabindu, and D. Shailaja, *Modification of chitosan towards a biomaterial with improved physico-chemical properties.* Journal of Applied Polymer Science, 2006. **101**(1): p. 63-69.

310. Ahmadi, F., et al., *Chitosan based hydrogels: characteristics and pharmaceutical applications.* Research in pharmaceutical sciences, 2015. **10**(1): p. 1-16.

311. Costa-Júnior, E.S., et al., *Preparation and characterization of chitosan/poly(vinyl alcohol) chemically crosslinked blends for biomedical applications.* Carbohydrate Polymers, 2009. **76**(3): p. 472-481.

312. Kim, S.J., et al., *Swelling characterizations of chitosan and polyacrylonitrile semi-interpenetrating polymer network hydrogels.* Journal of Applied Polymer Science, 2003. **87**(12): p. 2011-2015.

313. Yang, L., et al., *The Properties of Chitosan-Gelatin Scaffolds by Once or Twice Vacuum Freeze-Drying Methods.* Polymer-Plastics Technology and Engineering, 2013. **52**(11): p. 1154-9.

314. Shanmugasundaram, N., et al., *Collagen-chitosan polymeric scaffolds for the in vitro culture of human epidermoid carcinoma cells.* Biomaterials, 2001. **22**(14): p. 1943-51.

315. Peter, M., et al., *Preparation and characterization of chitosan–gelatin/nanohydroxyapatite composite scaffolds for tissue engineering applications.* Carbohydrate Polymers, 2010. **80**(3): p. 687-694.

316. Silva, R.M., et al., *Preparation and characterisation in simulated body conditions of glutaraldehyde crosslinked chitosan membranes.* Journal of Materials Science: Materials in Medicine, 2004. **15**(10): p. 1105-1112.

317. Adair, J.H., E. Suvaci, and J. Sindel, *Surface and Colloid Chemistry*, in *Encyclopedia of Materials: Science and Technology*, K.H.J. Buschow, et al., Editors. 2001, Elsevier: Oxford. p. 1-10.

318. Asghar, W., et al., *PLGA Micro and Nanoparticles Loaded Into Gelatin Scaffold for Controlled Drug Release.* IEEE Transactions on Nanotechnology - IEEE TRANS NANOTECHNOL, 2012. **11**: p. 546-553.

319. Couvreur, P., et al., *Nanocapsule technology: a review.* Critical reviews in therapeutic drug carrier systems, 2002. **19 2**: p. 99-134.

320. Ma, P.X. and J.W. Choi, *Biodegradable polymer scaffolds with well-defined interconnected spherical pore network.* Tissue Eng, 2001. **7**(1): p. 23-33.

321. Abbasi, N., et al., *Porous scaffolds for bone regeneration.* Journal of Science: Advanced Materials and Devices, 2020. **5**(1): p. 1-9.

322. Gaharwar, A.K., et al., *2D Nanoclay for Biomedical Applications: Regenerative Medicine, Therapeutic Delivery, and Additive Manufacturing.* Advanced Materials, 2019. **31**(23): p. 1900332.

323. Gola, J., *Chapter 10 - Quality Control of Biomaterials—Overview of the Relevant Technologies*, in *Stem Cells and Biomaterials for Regenerative Medicine*, M.J. Łos, A. Hudecki, and E. Wiecheć, Editors. 2019, Academic Press. p. 143-161.

324. Phoka, S., et al., *Synthesis, structural and optical properties of CeO2 nanoparticles synthesized by a simple polyvinyl pyrrolidone (PVP) solution route.* Materials Chemistry and Physics, 2009. **115**(1): p. 423-428.

325. Baqer, A.A., et al., *Effect of polyvinylpyrrolidone on cerium oxide nanoparticle characteristics prepared by a facile heat treatment technique.* Results in Physics, 2017. **7**: p. 611-619.

326. Sifontes, A.B., et al., *Effect of calcination temperature on structural properties and photocatalytic activity of ceria nanoparticles synthesized employing chitosan as template.* Journal of Nanomaterials, 2013.

327. Alpaslan, E., et al., *pH-Controlled Cerium Oxide Nanoparticle Inhibition of Both Gram-Positive and Gram-Negative Bacteria Growth.* Scientific reports, 2017. **7**: p. 45859-45859.

328. Sirelkhatim, A., et al., *Review on Zinc Oxide Nanoparticles: Antibacterial Activity and Toxicity Mechanism.* Nano-Micro Letters, 2015. **7**(3): p. 219-242.

329. Thakur, N., P. Manna, and J. Das, *Synthesis and biomedical applications of nanoceria, a redox active nanoparticle.* Journal of Nanobiotechnology, 2019. **17**(1): p. 84.

330. Farahmandjou, M., M. Zarinkamar, and T. Firoozabadi, *Synthesis of Cerium Oxide (CeO2) nanoparticles using simple CO-precipitation method.* Revista Mexicana de Fisica, 2016. **62**: p. 496-499.

331. Prabaharan, D., et al., *Structural, Optical, Morphological and Dielectric Properties of Cerium Oxide Nanoparticles.* Materials Research-ibero-american Journal of Materials, 2016. **19**: p. 478-482.

332. Caputo, F., et al., *A novel synthetic approach of cerium oxide nanoparticles with improved biomedical activity.* Scientific Reports, 2017. **7**(1): p. 4636.

333. Dao, N.N., et al., *UV absorption by cerium oxide nanoparticles/epoxy composite thin films.* Advances in Natural Sciences: Nanoscience and Nanotechnology, 2011. **2**(4): p. 045013.

334. Ren, Z., et al., *Morphology-Dependent Properties of Cu/CeO2 Catalysts for the Water-Gas Shift Reaction.* Catalysts, 2017. **7**: p. 48.

335. Tsunekawa, S., et al., *Blueshifts in the ultraviolet absorption spectra of cerium oxide nanocrystallites.* Journal of Applied Physics, 2003. **94**: p. 3654-3656.

336. Gillen, R., S. Clark, and J. Robertson, *Nature of the electronic band gap in lanthanide oxides.* Physical Review B, 2012. **87**.

337. Skorodumova, N., et al., *Electronic, bonding, and optical properties of CeO2 and Ce2O3 from first principles.* Phys. Rev. B, 2001. **64**: p. 1-9.

338. Burroughs, P., et al., *Satellite structure in the X-ray photoelectron spectra of some binary and mixed oxides of lanthanum and cerium.* Journal of the Chemical Society, Dalton Transactions, 1976(17): p. 1686-1698.

339. Janoš, P., et al., *Thermal Treatment of Cerium Oxide and Its Properties: Adsorption Ability versus Degradation Efficiency.* Advances in Materials Science and Engineering, 2014. **2014**: p. 706041.

340. Zhang, J., et al., *X-ray photoelectron spectroscopy study of high-k CeO2/La2O3 stacked dielectrics.* AIP Advances, 2014. **4**(11): p. 117117.

341. Holgado, J.P., et al., *XPS study of oxidation processes of CeOx defective layers.* Applied Surface Science, 2000. **158**(1): p. 164-171.

342. Holgado, J.P., R. Alvarez, and G. Munuera, *Study of CeO ₂ XPS spectra by factor analysis: reduction of CeO ₂.* Applied Surface Science, 2000. **161**: p. 301.

343. Shah, V., et al., *Antibacterial activity of polymer coated cerium oxide nanoparticles.* PLoS One, 2012. **7**(10): p. e47827.

344. Wang, Q., J.M. Perez, and T.J. Webster, *Inhibited growth of Pseudomonas aeruginosa by dextran- and polyacrylic acid-coated ceria nanoparticles.* International journal of nanomedicine, 2013. **8**: p. 3395-3399.

345. Xia, T., et al., *Comparison of the abilities of ambient and manufactured nanoparticles to induce cellular toxicity according to an oxidative stress paradigm.* Nano Lett, 2006. **6**(8): p. 1794-807.

346. Xia, T., et al., *Comparison of the mechanism of toxicity of zinc oxide and cerium oxide nanoparticles based on dissolution and oxidative stress properties.* ACS Nano, 2008. **2**(10): p. 2121-34.

347. Burello, E. and A.P. Worth, *A theoretical framework for predicting the oxidative stress potential of oxide nanoparticles.* Nanotoxicology, 2011. **5**(2): p. 228-35.

348. Farias, I.A.P., et al., *Antimicrobial Activity of Cerium Oxide Nanoparticles on Opportunistic Microorganisms: A Systematic Review.* BioMed Research International, 2018. **2018**: p. 14.

349. Stevens, B., et al., *A review of materials, fabrication methods, and strategies used to enhance bone regeneration in engineered bone tissues.* J Biomed Mater Res B Appl Biomater, 2008. **85**(2): p. 573-82.

350. Le Huec, J.C., et al., *Influence of porosity on the mechanical resistance of hydroxyapatite ceramics under compressive stress.* Biomaterials, 1995. **16**(2): p. 113-118.

351. Kramschuster, A. and L.-S. Turng, *17 - Fabrication of Tissue Engineering Scaffolds*, in *Handbook of Biopolymers and Biodegradable Plastics*, S. Ebnesajjad, Editor. 2013, William Andrew Publishing: Boston. p. 427-446.

352. Nam, Y.S. and T.G. Park, *Porous biodegradable polymeric scaffolds prepared by thermally induced phase separation.* Journal of Biomedical Materials Research, 1999. **47**(1): p. 8-17.

353. Agrawal, C.M. and R.B. Ray, *Biodegradable polymeric scaffolds for musculoskeletal tissue engineering.* Journal of Biomedical Materials Research, 2001. **55**(2): p. 141-150.

354. Sherwood, J.K., et al., *A three-dimensional osteochondral composite scaffold for articular cartilage repair.* Biomaterials, 2002. **23**(24): p. 4739-4751.

355. Shao, X.X., et al., *Evaluation of a hybrid scaffold/cell construct in repair of high-load-bearing osteochondral defects in rabbits.* Biomaterials, 2006. **27**(7): p. 1071-80.

356. Liuyun, J., L. Yubao, and X. Chengdong, *A novel composite membrane of chitosan-carboxymethyl cellulose polyelectrolyte complex membrane filled with nano-hydroxyapatite I. Preparation and properties.* Journal of Materials Science: Materials in Medicine, 2009. **20**(8): p. 1645-1652.

357. Farag, R.K. and R.R. Mohamed, *Synthesis and characterization of carboxymethyl chitosan nanogels for swelling studies and antimicrobial activity.* Molecules (Basel, Switzerland), 2012. **18**(1): p. 190-203.

358. Unagolla, J.M., T.E. Alahmadi, and A.C. Jayasuriya, *Chitosan microparticles based polyelectrolyte complex scaffolds for bone tissue engineering in vitro and effect of calcium phosphate.* Carbohydrate polymers, 2018. **199**: p. 426-436.

359. Forman, S., et al., *The effect of different solvents on the ATP/ADP content and growth properties of HeLa cells.* J Biochem Mol Toxicol, 1999. **13**(1): p. 11-5.

360. Rae, T., *The macrophage response to implant materials-with special reference to those used in orthopedics.* Crc Critical Reviews in Biocompatibility, 1986. **2**(2): p. 97-126.

361. Eggli, P.S., W. Müller, and R.K. Schenk, *Porous hydroxyapatite and tricalcium phosphate cylinders with two different pore size ranges implanted in the cancellous bone of rabbits. A comparative histomorphometric and histologic study of bony ingrowth and implant substitution.* Clin Orthop Relat Res, 1988(232): p. 127-38.

362. Ginebra, M.-P., et al., *Calcium phosphate cements as drug delivery materials.* Advanced Drug Delivery Reviews, 2012. **64**(12): p. 1090-1110.

363. Martina, M. and D.W. Hutmacher, *Biodegradable polymers applied in tissue engineering research: a review.* Polymer International, 2007. **56**(2): p. 145-157.

364. Lanza, R., R. Langer, and J. Vacanti, *Principle of Tissue Engineering*. 2007.

365. Marsell, R. and T.A. Einhorn, *The biology of fracture healing.* Injury, 2011. **42**(6): p. 551-555.

366. Kaderly, R.E., *Primary bone healing.* Semin Vet Med Surg Small Anim, 1991. **6**(1): p. 21-5.

367. Islam, N., I. Dmour, and M.O. Taha, *Degradability of chitosan micro/nanoparticles for pulmonary drug delivery.* Heliyon, 2019. **5**(5): p. e01684.

368. Ing, L.Y., et al., *Antifungal activity of chitosan nanoparticles and correlation with their physical properties.* International journal of biomaterials, 2012. **2012**: p. 632698-632698.

369. Katas, H. and H.O. Alpar, *Development and characterisation of chitosan nanoparticles for siRNA delivery.* Journal of Controlled Release, 2006. **115**(2): p. 216-225.

370. Zhang, X., H. Tiainen, and H.J. Haugen, *Comparison of titanium dioxide scaffold with commercial bone graft materials through micro-finite element modelling in flow perfusion.* Medical & Biological Engineering & Computing, 2019. **57**(1): p. 311-324.

371. Miranda, P., A. Pajares, and F. Guiberteau, *Finite element modeling as a tool for predicting the fracture behavior of robocast scaffolds.* Acta Biomaterialia, 2008. **4**(6): p. 1715-1724.

372. Birmingham, E., et al., *Mechanical stimulation of bone marrow in situ induces bone formation in trabecular explants.* Ann Biomed Eng, 2015. **43**(4): p. 1036-50.

373. Ebrahimian-Hosseinabadi, M., et al., *Evaluating and Modeling the Mechanical Properties of the Prepared PLGA/nano-BCP Composite Scaffolds for Bone Tissue Engineering.* Journal of Materials Science & Technology, 2011. **27**(12): p. 1105-1112.

374. Li, X., et al., *Surface treatments on titanium implants via nanostructured ceria for antibacterial and anti-inflammatory capabilities.* Acta Biomaterialia, 2019. **94**: p. 627-643.

375. Arunachalam, T., M. Karpagasundaram, and N. Rajarathinam, *Ultrasound assisted green synthesis of cerium oxide nanoparticles using Prosopis juliflora leaf extract and their structural, optical and antibacterial properties.* Materials Science-Poland, 2017. **35**(4): p. 791.

376. Li, Y., et al., *Mechanism of Photogenerated Reactive Oxygen Species and Correlation with the Antibacterial Properties of Engineered Metal-Oxide Nanoparticles.* ACS Nano, 2012. **6**(6): p. 5164-5173.

377. Qi, L., et al., *Preparation and antibacterial activity of chitosan nanoparticles.* Carbohydrate Research, 2004. **339**(16): p. 2693-2700.

378. Ma, Z. and L.-Y. Lim, *Uptake of Chitosan and Associated Insulin in Caco-2 Cell Monolayers: A Comparison Between Chitosan Molecules and Chitosan Nanoparticles.* Pharmaceutical Research, 2003. **20**(11): p. 1812-1819.

379. Martinez-Gutierrez, F., et al., *Synthesis, characterization, and evaluation of antimicrobial and cytotoxic effect of silver and titanium nanoparticles.* Nanomedicine: Nanotechnology, Biology and Medicine, 2010. **6**(5): p. 681-688.

380. Jiang, H., et al., *Variable Frequency Microwave Synthesis of Silver Nanoparticles.* Journal of Nanoparticle Research, 2006. **8**: p. 117-124.

381. Patil, S.N., et al., *Bio-therapeutic Potential and Cytotoxicity Assessment of Pectin-Mediated Synthesized Nanostructured Cerium Oxide.* Applied Biochemistry and Biotechnology, 2016. **180**(4): p. 638-654.

382. Qi, M., et al., *Cerium and Its Oxidant-Based Nanomaterials for Antibacterial Applications: A State-of-the-Art Review.* Frontiers in Materials, 2020. **7**(213).

383. Arunachalam, T., M. Karpagasundaram, and N. Rajarathinam, *Ultrasound assisted green synthesis of cerium oxide nanoparticles using Prosopis juliflora leaf extract and their structural, optical and antibacterial properties.* Materials Science Poland, 2018. **35**: p. 791.

384. Reddy Yadav, L.S., et al., *Fruit juice extract mediated synthesis of CeO2 nanoparticles for antibacterial and photocatalytic activities.* The European Physical Journal Plus, 2016. **131**(5): p. 154.

385. Anastasiou, A.D., et al., *Antibacterial properties and regenerative potential of Sr2+ and Ce3+ doped fluorapatites; a potential solution for peri-implantitis.* Scientific Reports, 2019. **9**(1): p. 14469.

386. Drago, L., M. Toscano, and M. Bottagisio, *Recent Evidence on Bioactive Glass Antimicrobial and Antibiofilm Activity: A Mini-Review.* Materials (Basel, Switzerland), 2018. **11**(2): p. 326.

387. Leppäranta, O., et al., *Antibacterial effect of bioactive glasses on clinically important anaerobic bacteria in vitro.* J Mater Sci Mater Med, 2008. **19**(2): p. 547-51.

APPENDICES

FREEZE-DRIED SCAFFOLDS

Appendix I – Osteoblast Culture Protocols

Thawing the Cells

1) Take the frozen cryovial [Sigma-Aldrich, CAS: CLS431421] from the – 80 ˚C freezer and wrap an ethanol-soaked tissue around the lid to prevent contamination of the vial contents.
2) Suspend the vial in a water bath (37 ˚C) until the vial content is completely thawed.
3) Using the smallest stripette [Sigma-Aldrich, CAS: CLS4485] remove the suspension from the vial and place into a small falcon tube, add 4 ml of medium.
4) Centrifuge the falcon tube [Sigma-Aldrich, CAS: CLS430791] (1200 rpm for 5 minutes).
5) Once centrifuged, aspirate the supernatant using a glass pipette [Sigma-Aldrich, CAS: CLS9016].
6) Add 2 ml to 5 ml of medium [Sigma-Aldrich, CAS: D5796] to the centrifuged pellet to re-suspend the cells.
7) Add 15 ml to 20 ml (dependent on the flask's size) of medium to each flask [Sigma-Aldrich, CAS: SIAL1080]. For example, if re-suspended the cells in 2 ml then add between 13 ml and 18 ml of medium.

Detaching the Cells

1) Place medium, PBS and trypsin into a water bath to warm.

2) If preparing a new bottle of medium, then warm up FBS and PenStrep in the water bath. DMEM medium > add 10 % FBS > add 1 % PenStrep. If using Alpha medium, then add 5 ml of Glutamine.
3) Switch on the Hood > Blower ON > Light ON. Spray the workspace with 70 % ethanol solution and wipe clean.
4) Remove the flask with the seeded cells from the incubator and check their morphology under the microscope.
5) Aspirate the medium using a glass pipette > wash the flask using 10 ml of Phosphate Buffered Saline (PBS) [Sigma-Aldrich, MDL: MFCD00131855] and repeat if necessary. Remove the PBS by tilting the flask and aspirating.
6) Add between 3 ml and 5 ml of trypsin and ensure all the cells are covered. Then close the flask and place into the incubator for 5 minutes.

Collecting the Cells

1) Remove the flask for the incubator and gently tap once. View the cells under the microscope to ensure the cell have detached (should look circular and floating in the medium).
2) Add between 12 ml and 15 ml of medium to the flask, then take out all the solution using a stripette and aliquot into a falcon tube. At this point re-suspend the cells by mixing up and down using the stripette.
3) Centrifuge the falcon tube (1200 rpm for 5 minutes).
4) Remove the supernatant from the falcon tube, leaving behind the pelleted cells.
5) Add between 3 ml and 10 ml (dependant on the number of cells required) of medium into the falcon tube and re-suspend the cells.

Splitting the Cells

1) Add between 12 ml to 20 ml of medium into two flasks.
2) Next, add between 1 ml and 5 ml of cell suspension into each flask. Close the lids and gently tilt from side to side.
3) Check each flask under the microscope to ensure the flasks contain cells, then place into the incubator.
4) The cells will attach to the flask within a few hours.

Cell Counting

1) Remove 45 µl of cell suspension using a micropipette and place in an Eppendorf vial [Sigma-Aldrich, CAS: EP0030119460].
2) Add 5 µl of Trypan Blue to the vial (the ratio should be 1:10)
3) Re-suspend the cells using the micropipette set to 10 ul, then remove 10 ul of the solution and dispense into a haemocytometer.
4) Place the haemocytometer under a microstructure to count the cells. The average of three different 'squares' should be counted and averaged. **NOTE:** Live cells should be visible as white dots while the dead cells are visible as blue dots (membrane was broken, and the dye stained the cells).

Averaged number of counted cells

$$\textbf{Cell concentration} = N_{av} * 10^4 * 1.1$$

Convert to ml

Gives the cell concentration in cell/ml

5) The cell concentration must be multiplied by the total volume of the re-suspension medium.

Appendix II – FTIR Peak Analysis

Attenuated Fourier Transform Infrared Spectroscopy: Determination of the amide I, II and III peak areas regarding the CH, 20, 30, 40 and 50-DCPD freeze-dried scaffolds. OriginPro software was utilised to determine the baselines, peak centres and base markers to calculate the area of the amide (I, II and III) three peaks.

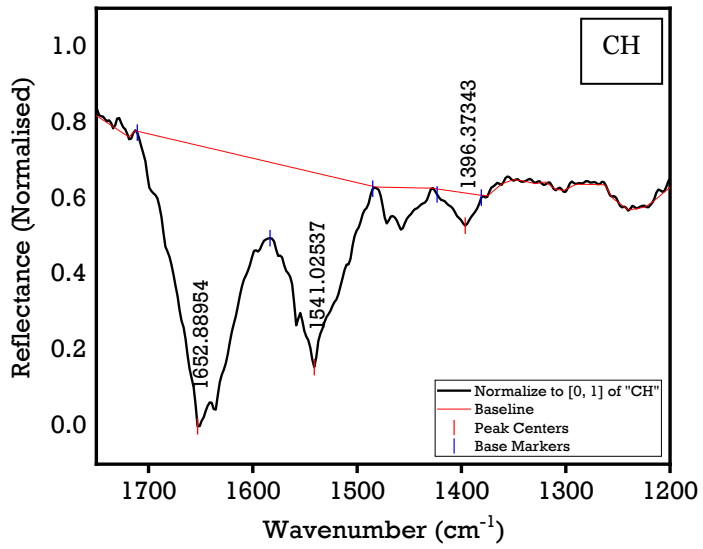

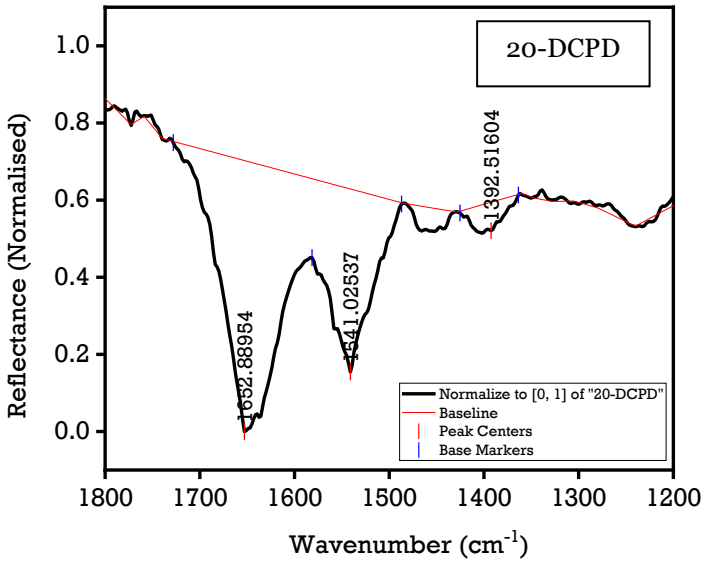

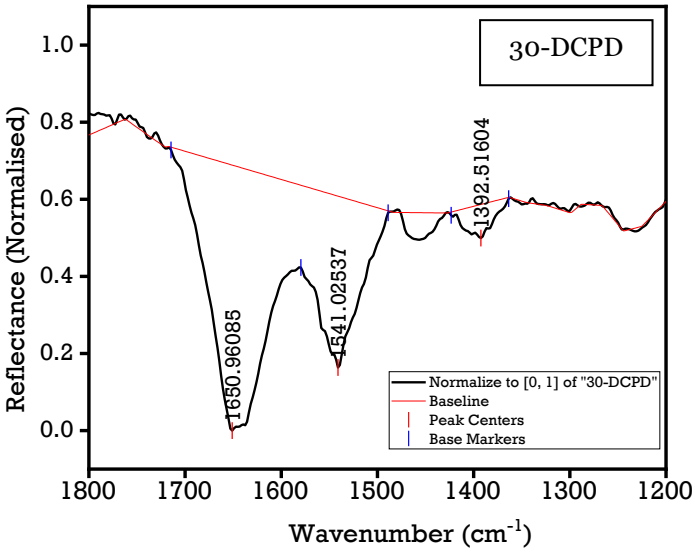
30-DCPD
Reflectance (Normalised)
Wavenumber (cm-1)
1650.96085
1541.02537
1392.51604
Normalize to [0, 1] of "30-DCPD"
Baseline
Peak Centers
Base Markers

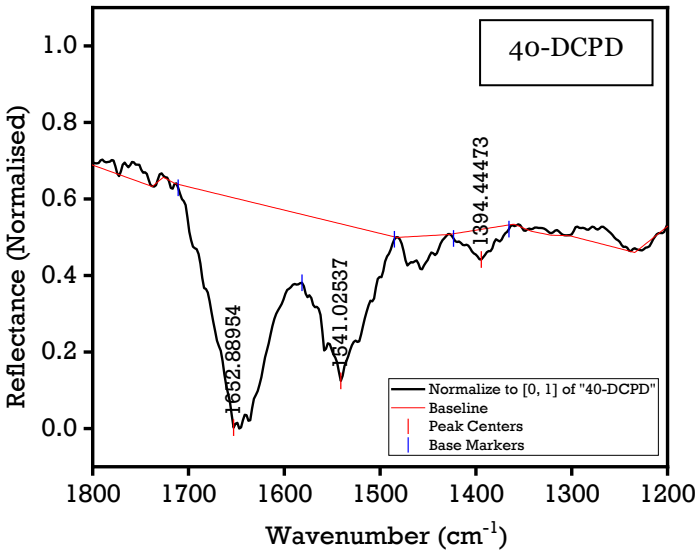
40-DCPD
Reflectance (Normalised)
Wavenumber (cm-1)
1652.88954
1541.02537
1394.44473
Normalize to [0, 1] of "40-DCPD"
Baseline
Peak Centers
Base Markers

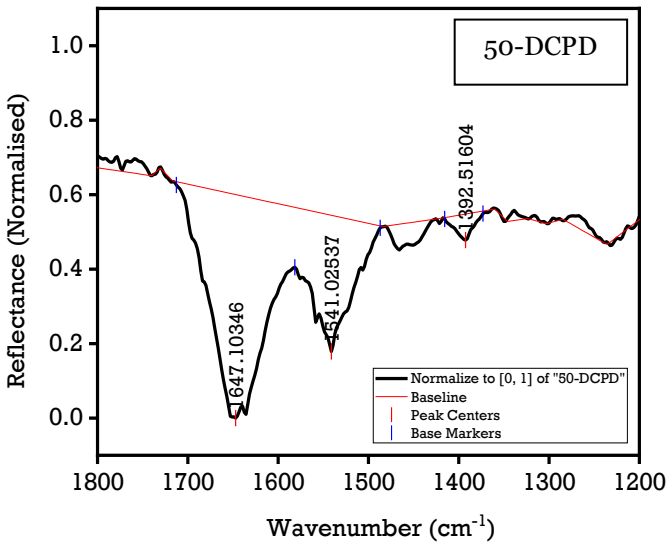
50-DCPD
Reflectance (Normalised)
Wavenumber (cm-1)
1647.10346
1541.02537
1392.51604
Normalize to [0, 1] of "50-DCPD"
Baseline
Peak Centers
Base Markers

Appendix III – SEM images

(a) CH, (b) 20-DCPD, (c) 30-DCPD, (d) 40-DCPD, and (e) 50-DCPD where the pore size distribution was determined by using the ImageJ software.

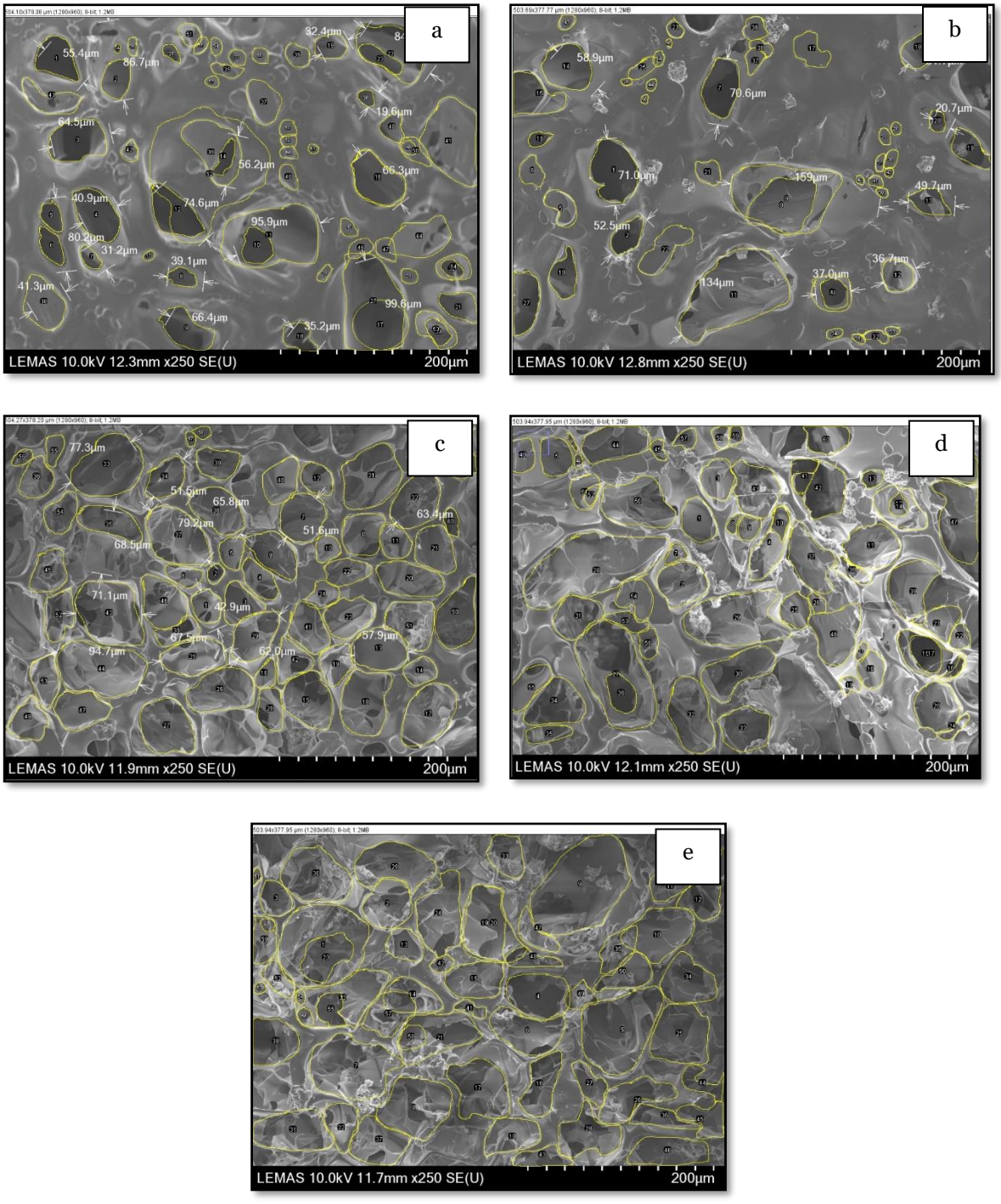

Appendix IV – Hitachi SEM and EDS analysis

30-DCPD freeze-dried scaffold

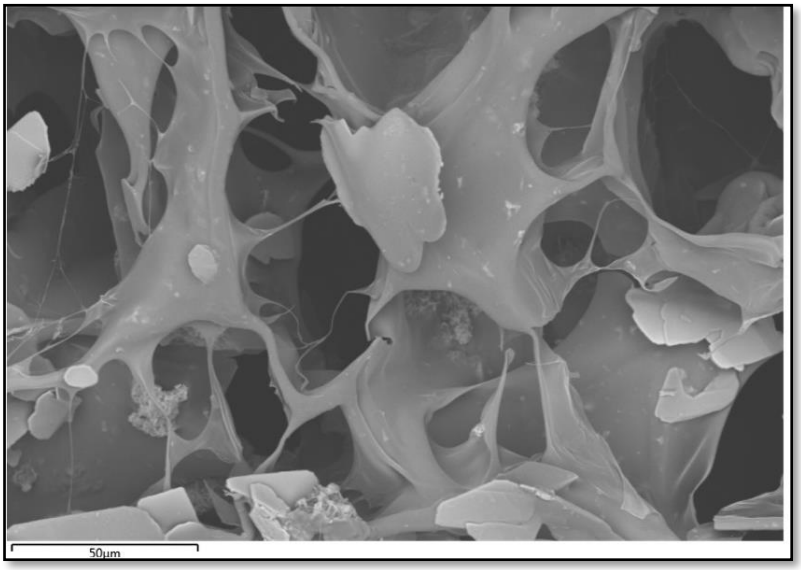

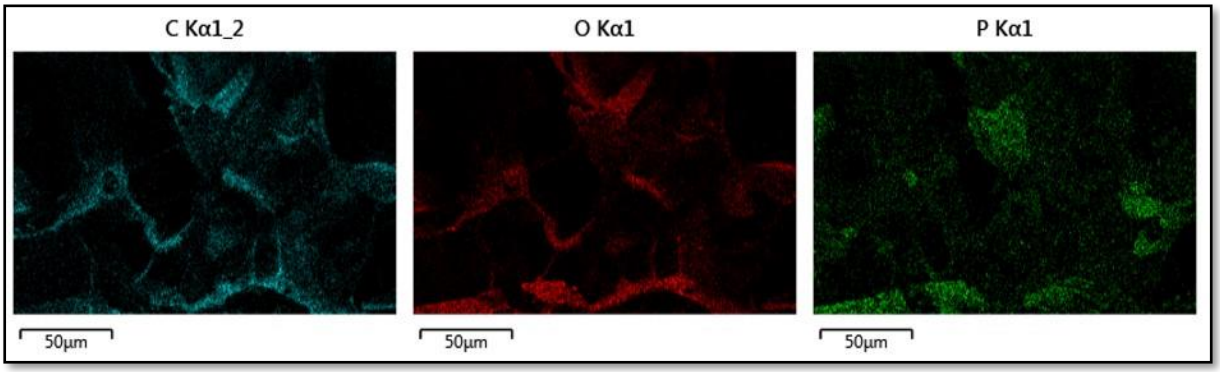

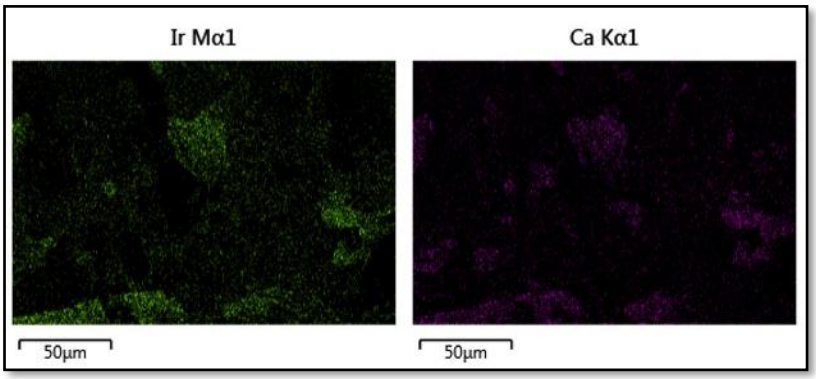

Appendix V – Double Layer SEM images

Double-layered freeze-dried scaffold, layer-1 = CS AND layer-2 contain 30 wt% DCPD embedded in CS. Image (d) is a close up of DCPD mineral.

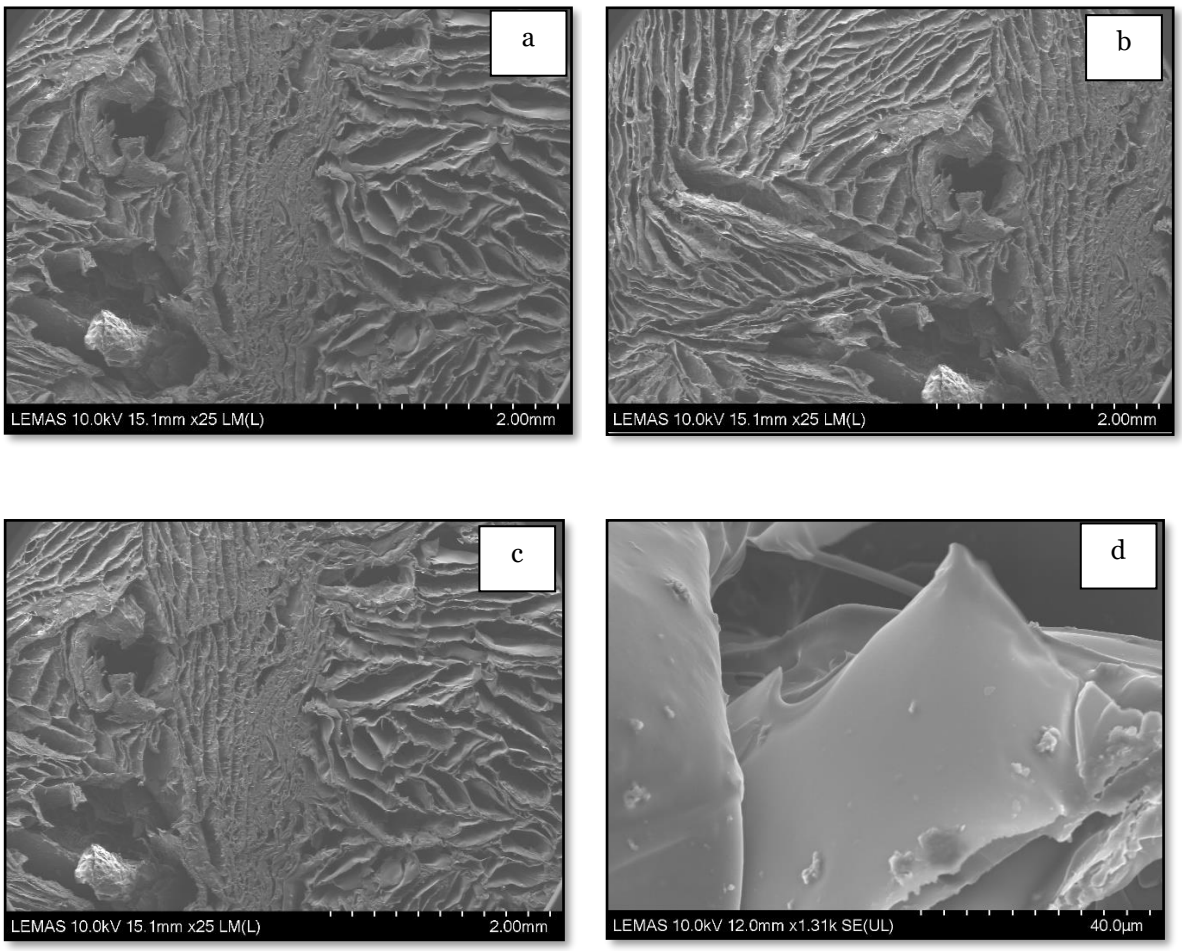

CERIUM OXIDE NANOPARTICLES

Appendix VI – High-resolution TEM images and EELS Analysis

RNP4

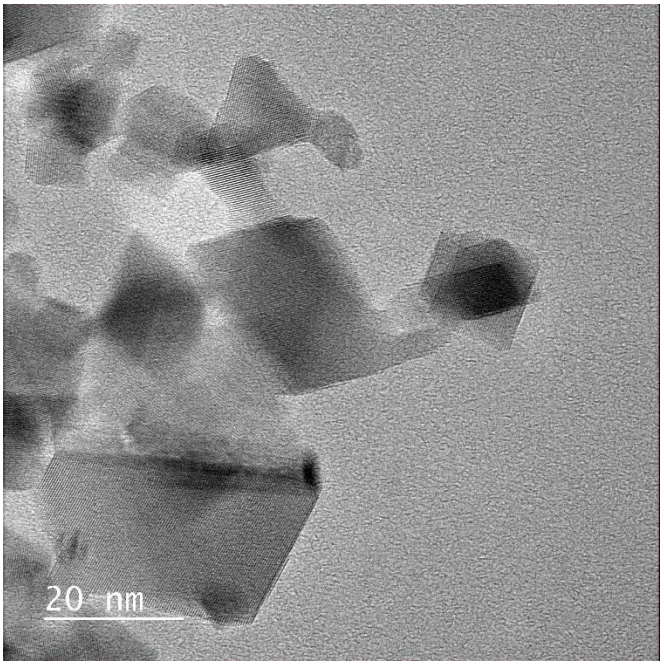

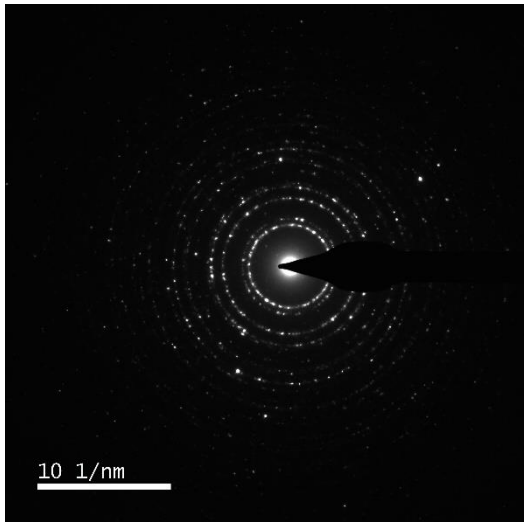

RNP3

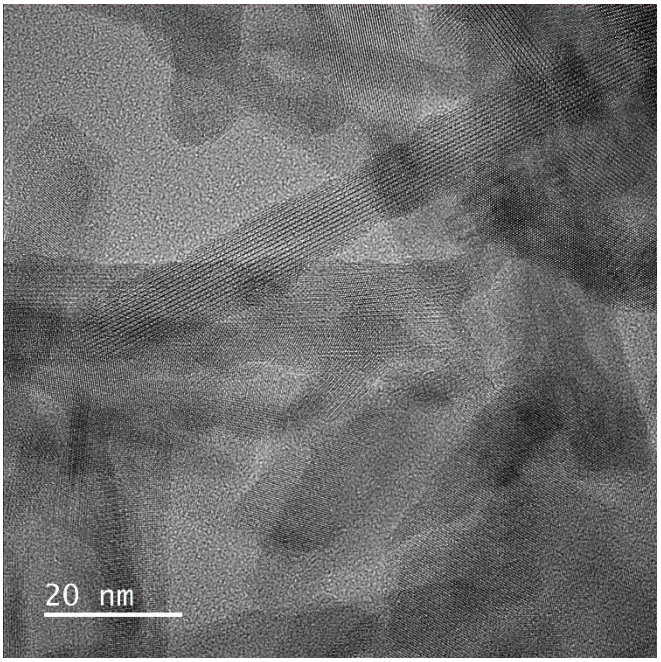

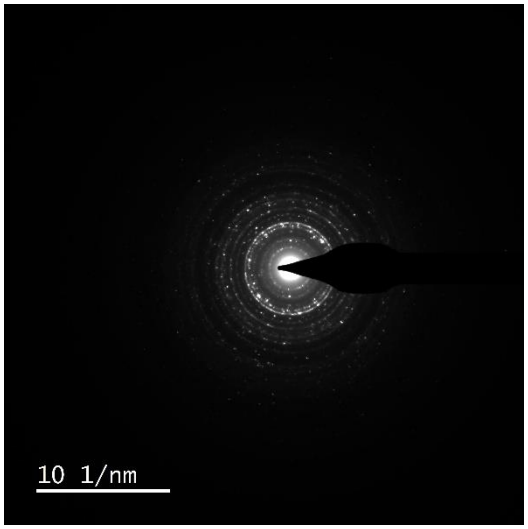

FRNP

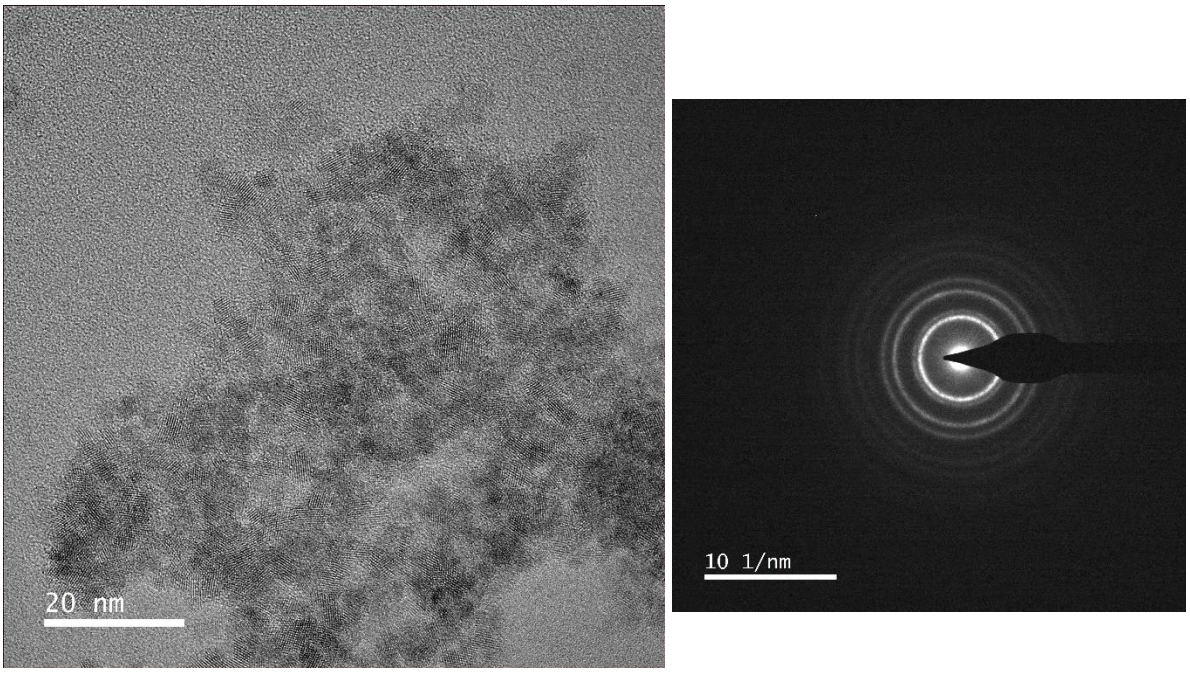

FUNP

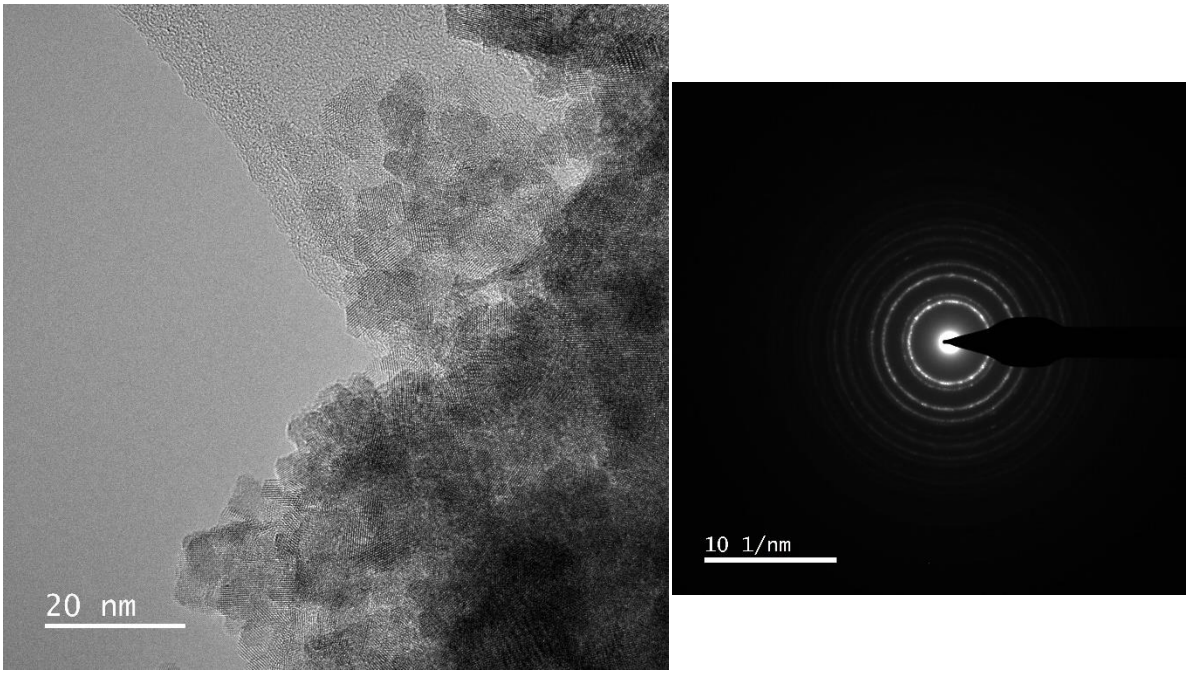

C280

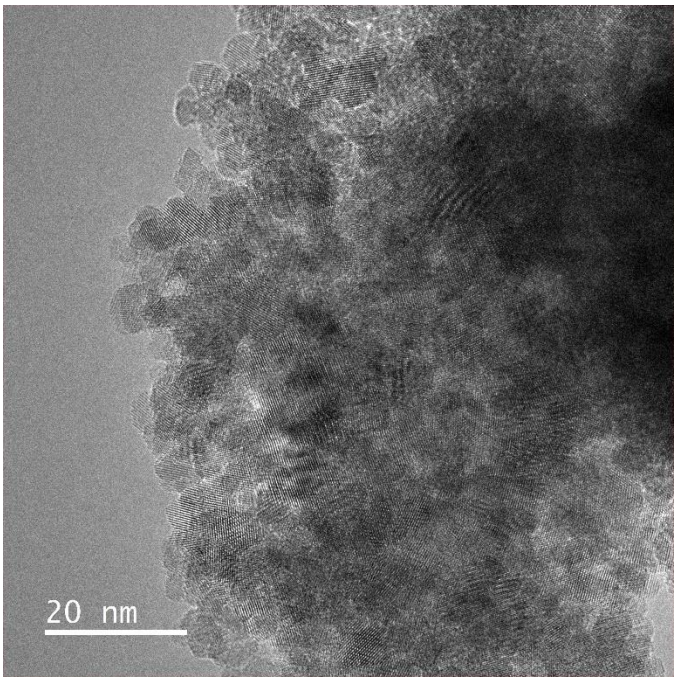

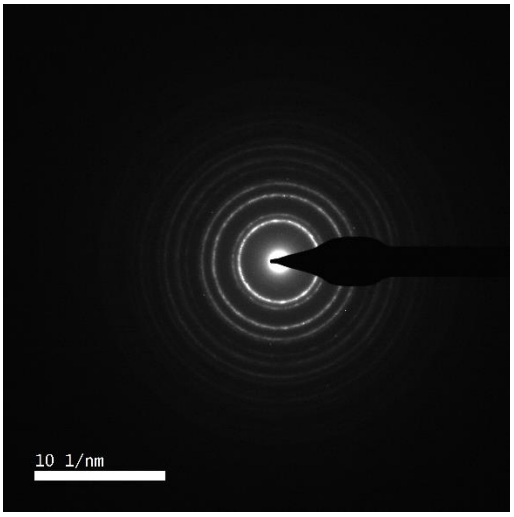

C385

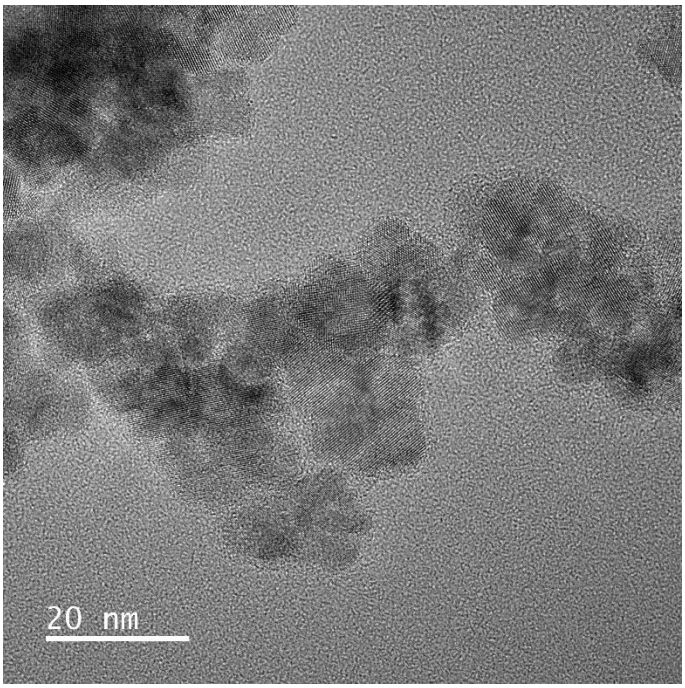

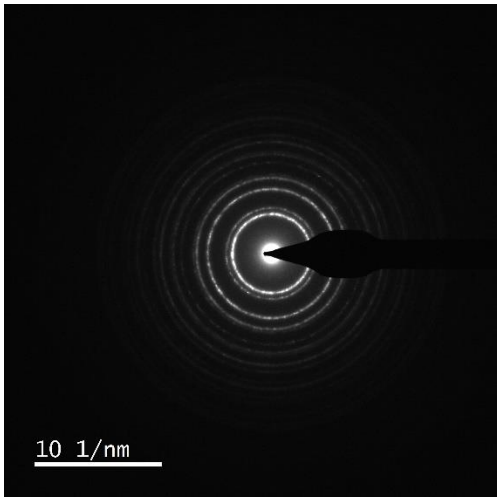

C815

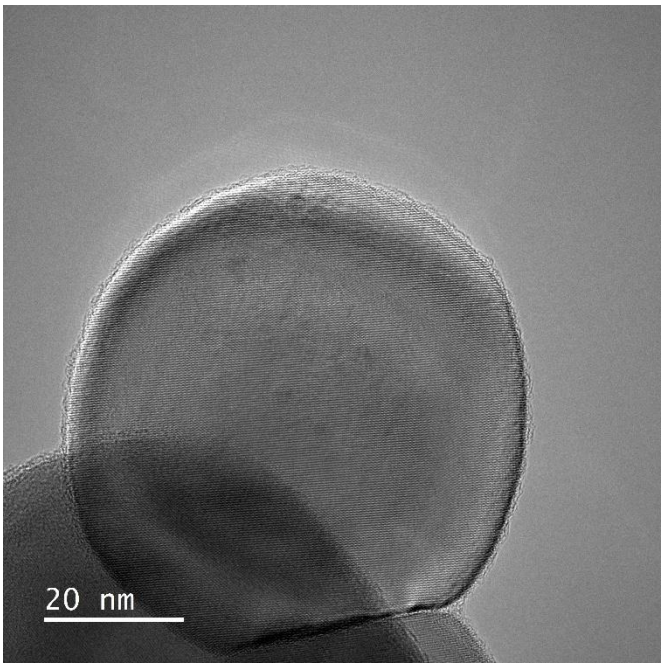

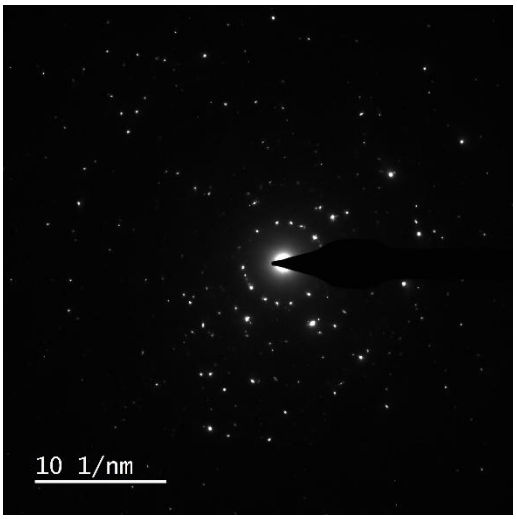

Appendix VII – Optical Density Plots

Optical density measurements characterising the antibacterial properties of C385 and C815 cerium oxide nanoparticles after direct incubation with *Escherichia coli*, *Staphylococcus epidermidis* and *Pseudomonas aeruginosa* for 48 hours.

SAMPLE - FRNP

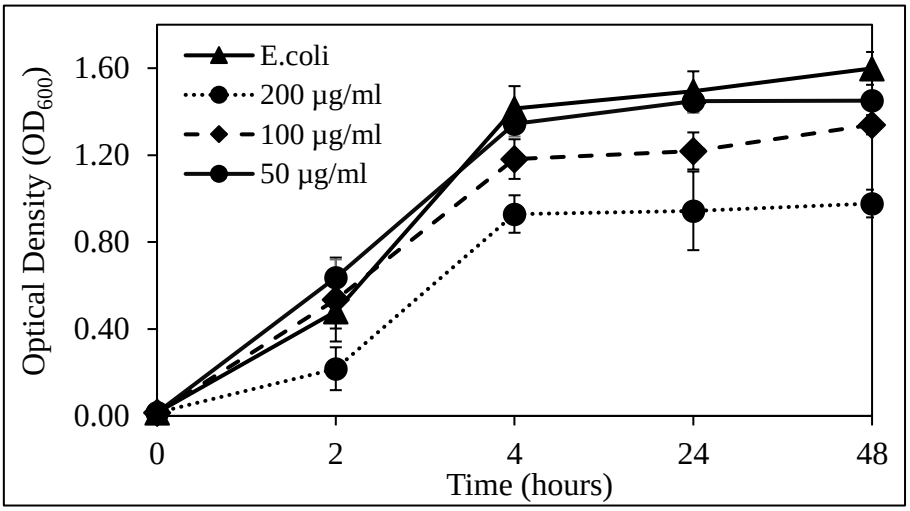

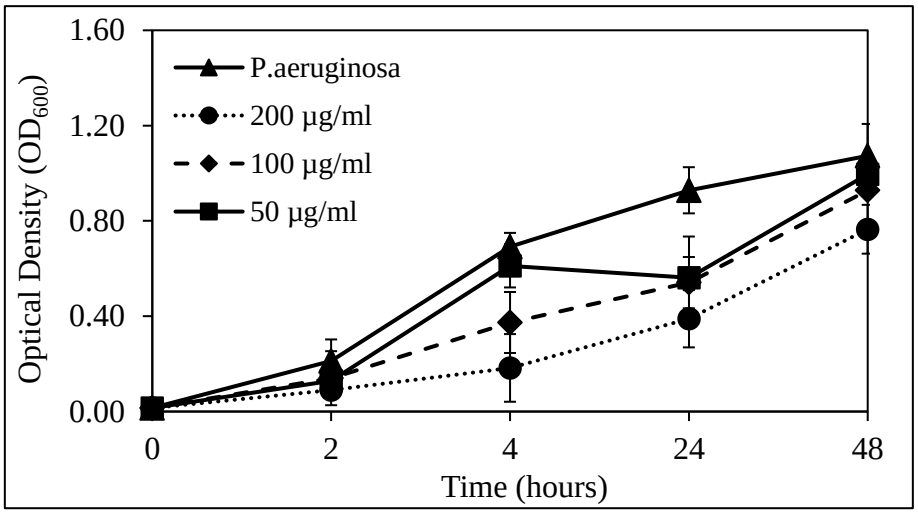

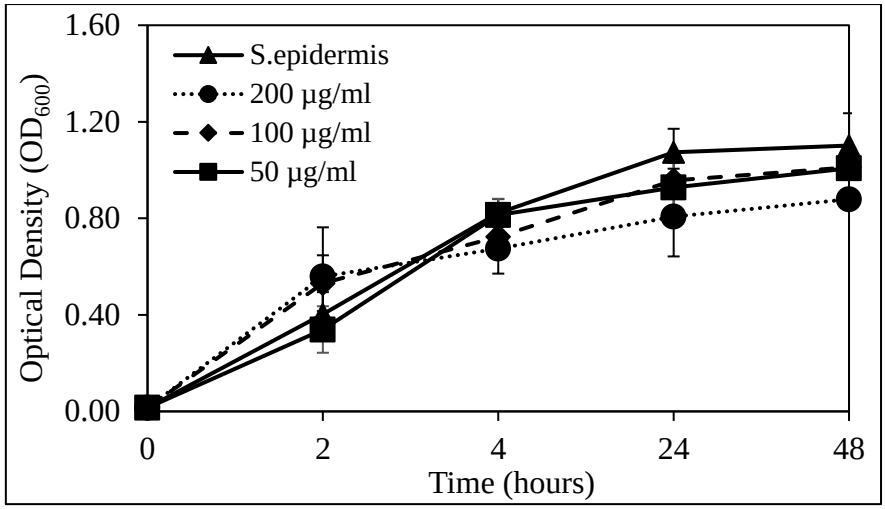
1.60
1.20
0.80
0.40
0.00
Optical Density (OD600)
S.epidermis
200 µg/ml
100 µg/ml
50 µg/ml
0
2
4
24
48
Time (hours)

SAMPLE - C383

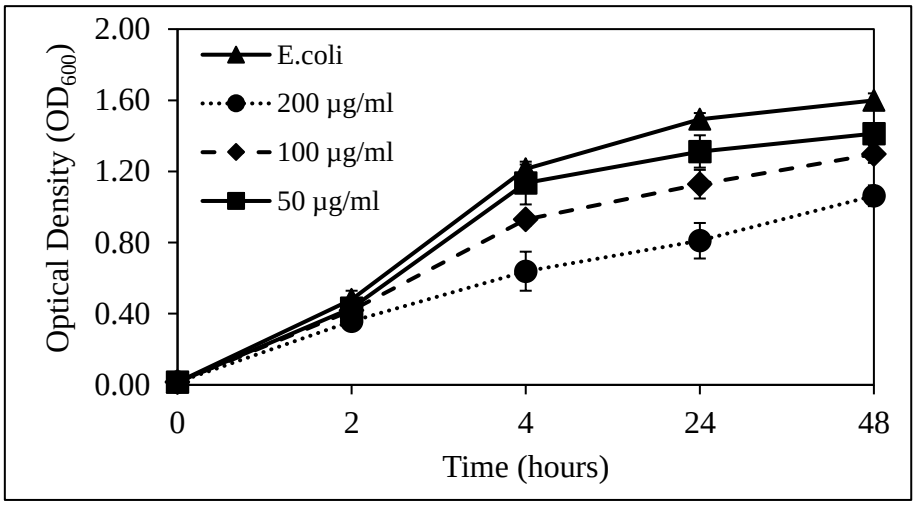
2.00
1.60
1.20
0.80
0.40
0.00
Optical Density (OD600)
E.coli
200 µg/ml
100 µg/ml
50 µg/ml
0
2
4
24
48
Time (hours)

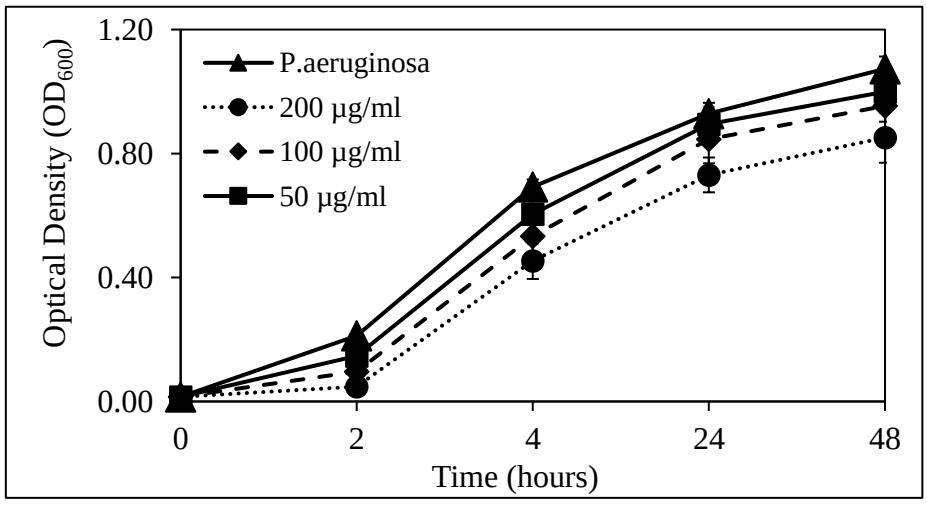
1.20
0.80
0.40
0.00
Optical Density (OD600)
P.aeruginosa
200 µg/ml
100 µg/ml
50 µg/ml
0
2
4
24
48
Time (hours)

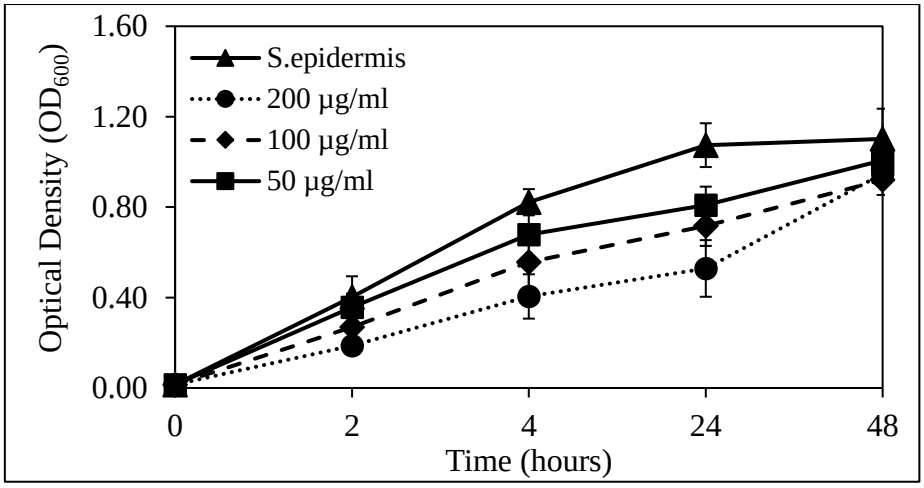
1.60
1.20
0.80
0.40
0.00
Optical Density (OD600)
S.epidermis
200 µg/ml
100 µg/ml
50 µg/ml
0
2
4
24
48
Time (hours)

SAMPLE - C815

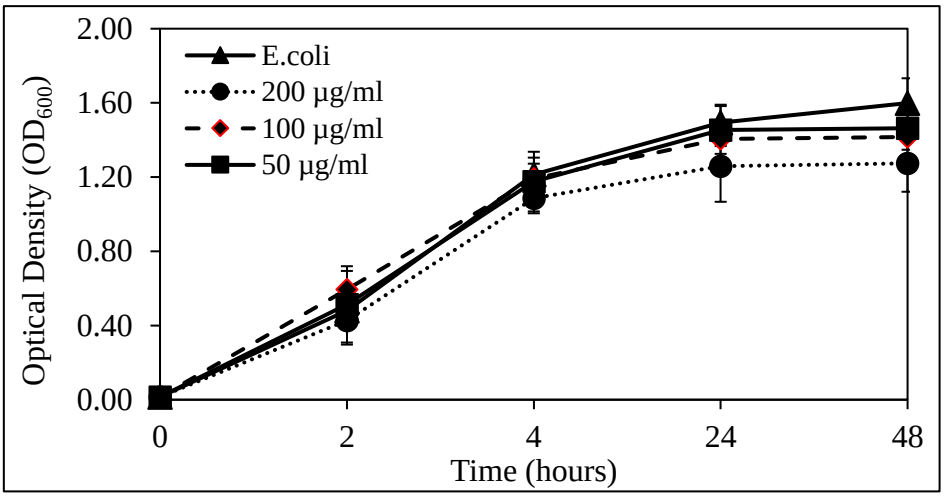
2.00
1.60
1.20
0.80
0.40
0.00
Optical Density (OD600)
E.coli
200 µg/ml
100 µg/ml
50 µg/ml
0
2
4
24
48
Time (hours)

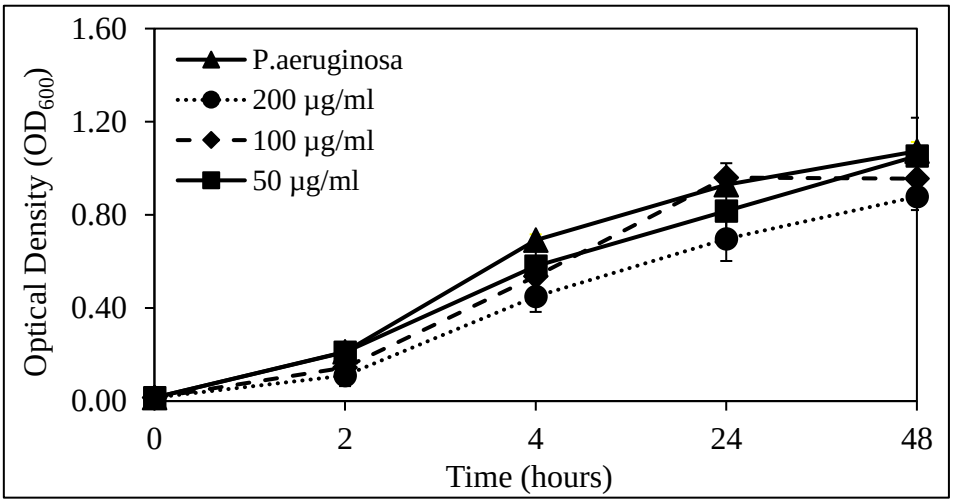
1.60
1.20
0.80
0.40
0.00
Optical Density (OD600)
P.aeruginosa
200 µg/ml
100 µg/ml
50 µg/ml
0
2
4
24
48
Time (hours)

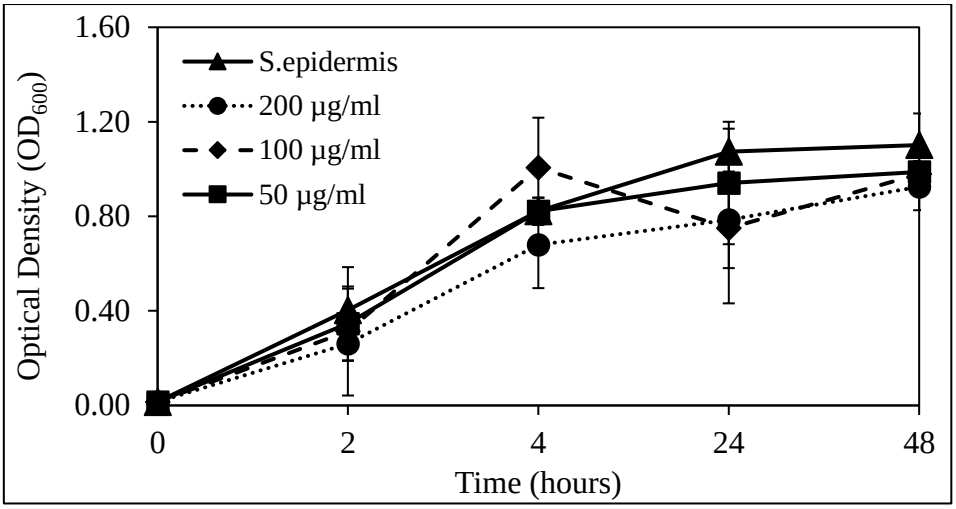
1.60
1.20
0.80
0.40
0.00
Optical Density (OD600)
S.epidermis
200 µg/ml
100 µg/ml
50 µg/ml
0
2
4
24
48
Time (hours)

Appendix VIII – Linear regression plots

Various concentration of nanoparticles tested against *Escherichia coli*, *Staphylococcus epidermidis* and *Pseudomonas aeruginosa*. The plots were used to calculate the IC_{50}

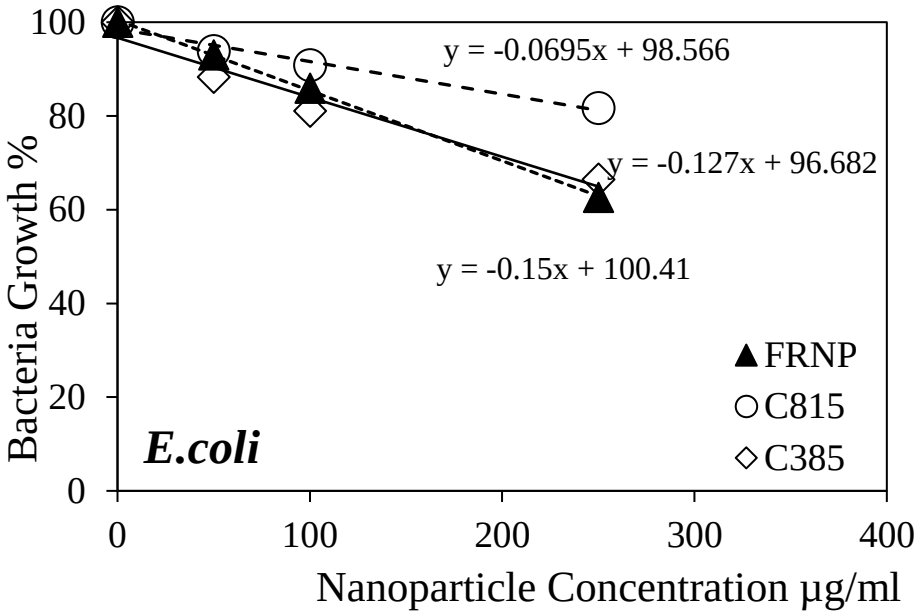

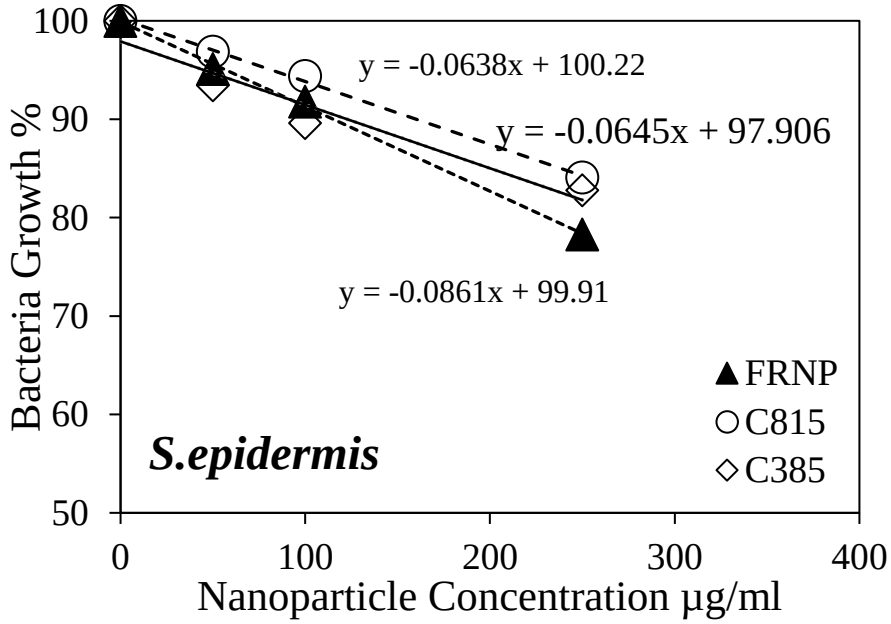

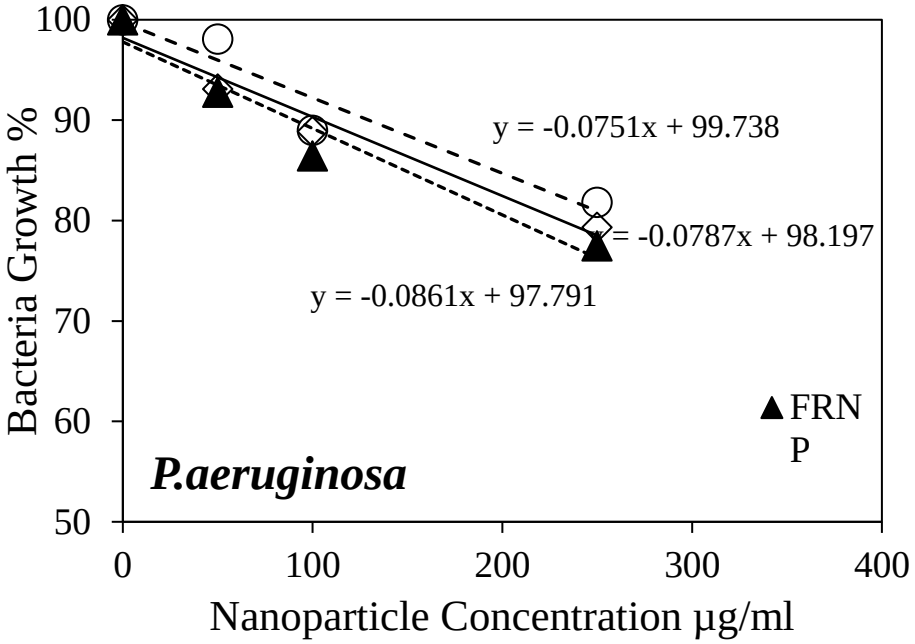
100
90
80
70
60
50
Bacteria Growth %
0
100
200
300
400
Nanoparticle Concentration µg/ml
y = -0.0751x + 99.738
= -0.0787x + 98.197
y = -0.0861x + 97.791
FRNP
P.aeruginosa

Appendix VIIII – Initial Ablation Channels and Micropatterning

Micropatterning and microchannels are expected to promote guided cellular growth leading eventually to the formation of vasculature. The channels were created using a Coherent Libra-S-1K (100fs) femtosecond laser (1 kHz repetition rate), at a wavelength of 800 nm.